Sivert Vist

Two-phase Flow Distribution in Heat Exchanger Manifolds

Dr.ing.-thesis

Faculty of Engineering Science and Technology
Department of Energy and Process Engineering

NTNU

Two-phase Flow Distribution in Heat Exchanger Manifolds

by
Sivert Vist

Thesis submitted in partial fulfilment of the requirements for the
Degree of Doktor Ingeniør

NTNU - Norwegian University of Science and Technology
Faculty of Engineering Science and Technology
Department of Energy and Process Engineering

December, 2003

Foreword

This thesis is submitted for the Degree of Doktor Ingeniør at NTNU - Norwegian University of Science and Technology. The thesis is based on studies carried out at the Department of Energy and Process Engineering (formerly Department of Refrigeration and Air Conditioning). The close relationship with the contract research institute SINTEF Energy Research has been of invaluable importance in terms of funding, infrastructure and supporting personnel.

I would like to thank Hydro Alunova in Tønder, Denmark, for initiating and funding this project and for the production of the prototype heat exchanger manifolds that have been tested.

Many people have contributed and helped me during the four years of study, thank you:

- *Jostein Pettersen,* for initiating the project with Hydro Alunova and for being my main supervisor.
- *Geir Owren,* for being my co-supervisor and for offering inspiration and recreation through other SINTEF projects.
- *Ole Jørgen Nydal,* for being my second co-supervisor and the ”chairman” of our very nice group of PhD students at the third floor.
- *Arvid Espedal and Helge Reimer Hansen,* for being my contacts in Alunova and for keeping the project economy healthy.
- *Tore Rye,* for construction, reconstruction and reconstruction in the lab.
- *Gunnar Lohse*, for always giving good advise when problems appear in the lab. And they do!
- *Arvid Almenning,* for precise work with the test section construction.

- *Johannes Zilly, Christian Andreas Schorn, Stephane Ringenbach, Samuel Houry and Aurélien Théard,* for spending their practical semester in Norway, conducting experiments in the lab.
- *Colleagues at the department,* for making this a joyful place to work.

A warm thanks goes to Donald E. Knuth and Leslie Lamport for inventing the fantastic typesetting environment LaTeX, saving me from the clammy hands of another widely used system.

Last but not least I want to express my gratitude to my wife, Siri Helene, and to my wonderful two daughters Lovise and Julie, for great patience and tolerance. I apologize to you and to my friends for any neglect while I single-mindedly pursued my goal.

Trondheim,
December 15, 2003

Sivert Vist

Summary and Conclusions

The current study has investigated two-phase refrigerant flow distribution in heat exchanger manifolds. Experimental data have been acquired in a heat exchanger test rig specially made for measurement of mass flow rate and gas and liquid distribution in the manifolds of compact heat exchangers. Twelve different manifold designs were used in the experiments, and CO_2 and HFC-134a were used as refrigerants.

Experimental data is compared to existing semi-empirical models for phase split in T-junctions and a new empirical model has been developed to describe the current data. A simulation model has been built to analyse the consequences of two-phase maldistribution, and comparisons to the experimental results has been conducted.

A summary highlighting the content of the main chapters of the report follows, before conclusions drawn from the present investigations on two-phase refrigerant distribution are listed.

Introduction

The use of compact heat exchangers with reduced channel hydraulic diameter and flow channel length has increased over the last years. To keep the pressure loss at acceptable levels, an implication of the diameter down-scaling is an increase in the number of parallel flow channels through the heat exchanger. The growing number of parallel flow channels increases the challenge of distributing two-phase flow equally among the channels.

Two-phase flow maldistribution[1] can significantly reduce the performance of heat exchangers. Different physical properties (density, viscosity and surface tension)

[1] Flow maldistribution is defined as nonuniform distribution of the mass flow rate, and/or nonuniform distribution of the individual phases in a multiphase flow, on either fluid side of the heat exchanger.

affects the inertial, gravitational, shear and capillary forces of the vapour and liquid phases. The interaction of these forces determines the distribution of the two phases in the heat exchanger manifold.

Capacity degradation due to two-phase flow maldistribution is most detrimental to evaporators, because heat transfer is degraded in tubes receiving less liquid. The heat transfer coefficient is lower in single-phase vapour flow and the temperature difference between the refrigerant and the secondary fluid (e.g. air) is reduced as the refrigerant superheats. Non-uniform refrigerant distribution in air/refrigerant heat exchangers will produce non-uniform wall temperatures, giving non-uniform air outlet temperature. This can reduce the dehumidification effect of the heat exchanger and produce uneven frosting on the heat exchanger surface.

Background and Literature Review

Several authors have found a degradation of 20 to 30% of heat exchanger capacity due to maldistribution of two-phase flow in compact evaporators. The two-phase flow pattern at the inlet of the manifold and throughout the manifold was claimed to be of great importance for the distribution into the individual flow channels.

Few publications have been published with experimental measurements of manifold two-phase flow distribution. Because of the large number of geometrical and operational parameters involved, it is difficult to make overall conclusions based on the published results. However, gravity has been reported to be an important force affecting the two-phase distribution in horizontal manifolds with vertical branch tubes[2]. In upward branch tubes, the vapour phase entered the first branch tubes, while the liquid was distributed to the last tubes of the manifold. In experiments performed with manifolds consisting of transparent material, the liquid level was seen to rise along the length of the manifold (liquid pooling). In downward flow configuration, the liquid entered the first branch tubes, while vapour entered the last tubes of the manifold. None of the authors claimed to measure even two-phase manifold distribution. A simple drawing of a heat exchanger with inlet and outlet manifolds and branch tubes with counterflowing water is shown in Figure 1.

Extensive work has been done on analysing two-phase flow distribution in T-junctions. The difference in momentum flux of the phases in the inlet tube was seen to be very important for the phase separation in the T-junction. Generally, the phase with lowest momentum flux was taken off in the branch tube. The flow pattern affected the phase separation for all branch tube angles. Also, gravity in-

[2]Branch tubes are the parallel heat exchanger tubes connecting the inlet and outlet manifold of the heat exchanger.

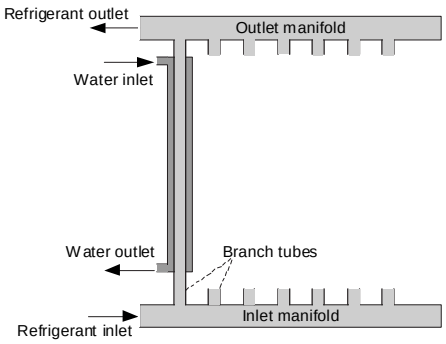

Figure 1: Simple drawing of a heat exchanger with six branch tubes between an inlet and an outlet manifold. Counterflow water is shown on the first branch tube.

fluenced the phase separation to a large degree. For upward branch tube flow, separation of the phases was very distinct because the momentum flux difference between the phases and gravity acted in the same direction. For downward flow the effects of momentum flux difference and gravity acted in opposite directions, hence the phase separation was generally more uniform than in the case of upward oriented branch tubes.

Based on the limited knowledge base on distribution of two-phase flow in manifolds, and the wide variety in geometrical and operational factors involved, the necessity for further experimental measurements was obvious. It was the intention of the current work to contribute to a broadening this knowledge base.

Experimental methods

A test rig based on new concepts for measurement of two-phase distribution in heat exchanger manifolds was erected in the laboratories at NTNU. The test rig was built with the possibility of running experiments at flow rates and inlet vapour fractions encountered in car air-conditioning systems. Because of the large influence of geometry on two-phase distribution, emphasis was put on the importance of using realistic manifold geometries. The test rig was constructed such that the heat exchanger branch tubes could be directed both upward and downward from a horizontal manifold. Both low pressure refrigerants (e.g. HFC-134a) and high pressure refrigerants (e.g. CO_2) could be used in the refrigerant circuit.

Because two-phase maldistribution is most detrimental in evaporators, the test section heat exchanger was equipped with heating water jackets. But the test rig principle can also be applied for condensers (water cooling). Water was chosen

instead of air as secondary fluid, because of the possibility to measure the heat load on each branch tube. Much effort was put in creating a reliable system for measurement of two-phase flow distribution in the manifold without disturbing the flow while conducting the measurements.

A data reduction scheme was developed to find the vapour fraction at the inlet of the manifold and at the inlet of each single branch tube. Uncertainties in the test rig instrumentation gave an overall uncertainty in manifold inlet vapour fraction, x_{mIn}, of ± 0.0023 to ± 0.0036 for HFC-134a and ± 0.0031 to ± 0.0041 for CO_2. Maximum uncertainty in the calculation of the branch tube inlet vapour fraction, $x_{t,i}$, was ± 0.06 for both the HFC-134a and the CO_2 measurements.

The measurement procedure with switching individual channels to a tap-off circuit added extra uncertainty to the measurement results. The extent of the total measurement uncertainty was estimated by mass flow rate and vapour fraction continuity calculations. 94.8% of the measurements gave less than 5% deviation between measured mass flow rate in and out of the inlet manifold. For the vapour fraction continuity, 96% of the measurements gave less than 10% deviation between vapour fraction at the inlet and outlet of the inlet manifold.

Experimental results

Two-phase distribution measurements were run in twelve different manifold designs to investigate how the distribution was affected by changes in geometry parameters. First, some experiments were run in a hand-made glass manifold to gain visual observations of flow in the manifold. In experiments with upward directed branch tubes, the two-phase flow was separated, and pooling of liquid was seen in the end of the manifold. Severe maldistribution with gas feeding of the first tubes and liquid feeding the last tubes was seen for the full range of inlet vapour fractions tested. In experiments with downward directed branch tubes, liquid at the bottom of the inlet tube was mixed into the gas flow because of the protrusion of branch tubes into the manifold, resulting in a more homogeneous two-phase distribution.

Experiments were run in three generic round tube manifolds with ID 8 mm, ID 12 mm and ID 16 mm, respectively. A prototype MPE-tube[3] heat exchanger manifold was constructed, such that several geometry parameters could be varied (MPE-tube pitch, MPE-tube protrusion, baffle inserts and progressive insert in the manifold). Finally, experiments with a novel star manifold design were run to investigate two-phase distribution in a manifold with shorter longitudinal length.

[3]MPE-tube: MultiPort Extruded-tube. The MPE-tube consists of several parallel flow channels (ports).

Generally, the measurements showed that with upward directed branch tubes from the manifold, gas was taken off in the first tubes, while liquid was taken off in the last tubes of the manifold. More liquid was taken off in the first branch tubes when the hydraulic diameter of the manifold was reduced, and when introducing mixed flow at the inlet of the manifold. In experiments with downward directed branch tubes, liquid was preferentially taken off in the first tubes of the manifold and gas was transported to the last tube. However, when reducing the hydraulic diameter of the manifold and introducing tube protrusion into the manifold, more gas entered the first tubes and more of the liquid was transported to the last tubes.

The uniformity in branch tube heat transfer rates was used as a measure of the two-phase distribution uniformity in the inlet manifold. Large deviations in branch tube heat transfer was measured, with a standard deviation ranging from 12.42% in the ID 8 mm round tube manifold with short inlet tube in downward configuration, to 69.23% in the MPE-tube manifold with 15 mm tube pitch in upward configuration. The ID 8 mm round tube manifold with short inlet tube provided the most uniform heat transfer rates both in upward and downward configuration. In most manifolds, the heat transfer rate was most uniform in downward configuration. In upward configuration, the branch tube heat transfer rate distribution was more uniform in experiments with CO_2 than in experiments with HFC-134a. With exception of the experiments with spiral mixer at the manifold insert, the measurements in downward configuration showed more homogeneous branch tube heat transfer rate with HFC-134a than with CO_2. The only geometric modification to the MPE-tube manifold showing significant improvement in branch tube heat transfer uniformity in upward configuration was the introduction of a spiral mixer at the manifold inlet. In downward configuration, only minor changes were seen in branch tube heat transfer rate uniformity due to the MPE-tube manifold geometry modifications. The branch tube heat transfer rate in the star manifold was more uniform than in the MPE-tube manifold with upward configuration, but in the same range as in the MPE-tube manifolds with downward configuration.

Analysis and discussion of experimental results

In order to adapt the information from experimental measurements to computer simulations of refrigerant maldistribution in heat exchangers, correlations were developed for the manifold phase split. The correlations were based on a T-junction modelling approach, handling each separate manifold branch tube off-take as a separate T-junction.

Based on experimental results from the large number of manifold designs it was possible to analyse several geometrical and flow property effects on the two-phase distribution. Separate empirical correlations were developed for distribution in

horizontal manifolds with vertical upward and downward oriented branch tubes. In upward flow configuration, the phase split correlation was divided into a ”low manifold mass flux” and a ”high manifold mass flux” region by a transition criterion, which dependents on the manifold cross-sectional area and the flow regime transition line between stratified and intermittent flow in the Kattan et al. (1998) flow map. In the ”low manifold mass flux” region, the branch tube vapour fraction could be correlated to the manifold gas mass flux, while in the ”high manifold mass flux” region the branch tube liquid take-off fraction was correlated to a dimensionless manifold mass flux. The new model was able to predict the branch tube vapour fraction within a mean absolute deviation of 0.04 to 0.20 for the different manifold geometries. In downward flow configuration, the branch tube liquid take-off was correlated against a dimensionless manifold mass flux. The new model for downward flow configuration predicted the branch tube vapour fraction within a mean absolute deviation of 0.03 to 0.14.

The only geometrical parameter that was taken into account when developing the phase split correlations, was the manifold cross-sectional area. Hence, the phase split in manifolds with protruded MPE-tubes could be predicted using general correlations, only correcting for the reduction in free flow cross sectional area because of tube inserts.

Two main factors affected the phase split in manifolds, both in upward and downward configuration. First, gravitational forces acted on the fluid in the two-phase flow split. Second, the momentum difference between the phases, provoking low-momentum gas to be taken off in the branch tubes, had a pronounced effect on flow distribution. In manifolds having upward directed branch tubes, both gravitational forces and the effect of momentum flux difference favoured gas off-take in the branch tubes. Hence, the first branch tubes of the manifold received most of the gas, while the liquid was distributed to the last tubes. In downward orientation, gravity favoured liquid off-take, while the difference in momentum flux favoured gas off-take in the branch tubes. Therefore, more even distribution could be obtained compared to upward flow distribution.

A static mixing device at the inlet of the manifold reduced the effect of gravity and momentum flux difference in the first part of the manifold. The larger momentum flux difference between the gas and liquid phase in HFC-134a, compared to CO_2, was seen to provide higher take-off of low momentum gas in the first tubes. This provided improved two-phase distribution in downward branch tube configuration, while it provided poorer two-phase distribution in upward configuration.

Heat exchanger simulations

A heat exchanger model was developed that provided means of calculating the distribution of an inlet two-phase flow through a manifold system, given only the inlet conditions and the geometry. In order to efficiently take into account the local pressure losses in the inlet and outlet manifold and in the heat exchanger branch tubes, a network simulation model was developed. In the network model, the heat exchanger was divided into nodes and units, where pressure and enthalpy were defined in the nodes connecting the pipe units. An implicit simultaneous solver was used to calculate node pressures while the mass flows through the pipe units were calculated based on the inlet and outlet pressures.

A model case was constructed with geometry equal to the present test rig, where two manifolds were joined with ten branch tubes. A discretized model of the heat exchanger branch tubes with counterflow water in outside jackets, was solved simultaneously. The branch tube model was tested against the experimental measurements on the single branch tubes. The RMS (Root Mean Square) error in the predicted heat transfer rate was 4.4%.

Three different two-phase split models for the inlet manifold were implemented. First, the traditional method used in heat exchanger simulations, with homogeneous two-phase distribution, was implemented in order to find the maximum heat transfer rate of the heat exchanger. Second, a worst-case scenario with complete separation of liquid and gas was modelled. Third, the developed two-phase flow correlations were implemented in the network simulation model.

Generally, the model showed less reduction in heat exchanger capacity caused by two-phase distribution for CO_2, than for HFC-134a. The difference was due to the smaller differences in pressure gradient through the two-phase region, providing less difference in branch tube mass flow rates among tubes fed with different vapour fractions.

By comparing the total heat exchanger capacity of the three distribution models, the consequences of maldistribution in the inlet manifold could be calculated. Within the operating conditions used in the current test rig experiments with the ID 16 mm round tube manifold, the model showed a potential increase in capacity of 12% both for CO_2 and HFC-134a, if homogeneous two-phase distribution could be obtained. At reduced temperature difference between refrigerant and water, and lower vapour fraction at the branch tube outlets, as will be the case in a heat exchanger with several passes, the potential drop in heat exchanger capacity could be more than 30% due to maldistribution of two-phase flow in the inlet manifold.

Conclusions

The most important conclusions from the study are highlighted in the following text.

- A new measurement concept has been developed, such that two-phase refrigerant distribution can be measured in the inlet manifold of compact heat exchangers under realistic operating conditions and using relevant manifold geometries.
- The understanding of mechanisms affecting two-phase manifold distribution has been improved by analysis of measurements of mass flow rate and phase distribution in twelve different manifold geometries. The two-phase flow was in general not evenly distributed. Gravity and difference in momentum flux between gas and liquid was important factors, affecting the distribution. Only minor differences between HFC-134a and CO_2 were found, with HFC-134a performing best in downward branch tube configuration, while CO_2 performed best in upward branch configuration.
- The tested geometry modifications to the MPE-tube manifold did not show significant improvements in two-phase flow distribution. However, a static mixer insert at the inlet of the manifold showed some improvement.
- The length of the inlet tube to the manifold was important for distribution in the ID 8 mm manifold. A short inlet tube of 50 mm (compared to the original 250 mm) improved the distribution quite significantly, showing that the two-phase flow regime at the manifold inlet was important for two-phase distribution.
- Measurements in the star manifold showed maldistribution of the two-phase flow, comparable to the MPE-tube manifolds in downward branch tube configuration.
- A set of correlations for the manifold two-phase flow distribution, based on a T-junction modelling concept, were developed. The new correlations were able to predict the measured two-phase distribution better than the selected T-junction correlations from the literature.
- A network modelling concept was implemented in order to analyse the consequences of two-phase maldistribution. The model was verified against experimental data. The possible reduction in heat exchanger capacity, due to maldistribution, was found to be over 30% in cases with low temperature differences between the refrigerant and the water.

- Further experimental work should focus on the connection between flow pattern at the inlet of the manifold and two-phase distribution to the branch tubes. A glass tube section at the inlet of the manifold would be of high value, such that the manifold inlet flow regime could be visually observed. By using a pump with more static head, or an extra pump in series with the existing one, the test rig could be modified such that a throttle valve could be inserted at the inlet of the manifold. This would introduce mist flow at the inlet of the manifold, with the possibility of improved two-phase distribution compared to the current results.

- To enhance the understanding of the connection between manifold two-phase distribution and pressure losses in the heat exchanger branch tubes, it would be valuable to measure pressure profiles in the manifold. The estimation of frictional and deceleration pressure losses are today very uncertain in manifolds with e.g. branch tube inserts and developing two-phase flows.

- Further work on the model development should be focused on verification against experimental data. A unit model for air/refrigerant heat exchangers should be developed such that the model could be verified against secondary air-side measurements from e.g. Hafner (2003). The reduction in heat exchanger capacity, due to two-phase maldistribution, could be analysed for several types of heat exchangers.

Contents

Nomenclature

Latin letters

A	Area	m^2
A_c	Manifold free flow cross-sectional area	m^2
A	Parameter	-
A_{gd}	Dimensionless gas cross-sectional area	-
a	Parameter	-
b	Parameter	-
C	Parameter in the Chisholm two-phase multiplier	-
CF	Correction factor	-
C_D/D_B	Coeff. in Hench's drag model	-
$CLTF$	Constant Liquid Take-off Fraction	-
COP	Coefficient Of Performance	-
c_p	Specific heat capacity at constant pressure	J/(kgK)
c_v	Specific heat capacity at constant volume	J/(kgK)
C_0	Void concentration parameter	m^2
D	Diameter	m
D_H	Hydraulic diameter, $4A/P_f$	m
F	Empirical coefficient	-
f	Darcy-Weisbach friction factor	-
F_d	Gas volumetric interfacial drag	N
Fr	Froude number	-
F_w	Wall volumetric drag on the gas	N
G	Mass flux	$kg/(m^2s)$
g	Acceleration due to gravity	m/s^2
H	Enthalpy	J
h	Specific enthalpy	J/kg
h	Height	m
h	Heat transfer coefficient	$W/(m^2K)$
h_{lim}	Parameter	-
h_b	Height at beginning of entrainment	m

h	Dimensionless liquid height	-
j	Volumetric flux	m/s
K	Hydraulic loss coefficient	-
k	Flow ratio	-
k'	Parameter	-
k''	Parameter	-
k^*	Parameter	-
L_J	Vapour path length in junction	m
$MMFTC$	Manifold Mass Flux Transition Criterion	-
$\dot{m}$	Mass flow rate	kg/s
N_t	Number of manifold branch tubes	
n	Constant	-
n	Number of measurements	-
p	Pressure	Pa
P_f	Friction perimeter	m
$\dot{Q}$	Heat load	W
q	Heat flux	W/m^2
R	Gas constant	J/(kgK)
R	Parameter	-
Re	Reynolds number	-
S	Slip ratio	-
STD	Standard deviation	
T	Temperature	K
t	Time	s
U_r	One-dimensional averaged relative velocity	m/s
U	Heat transfer coefficient	$W/(m^2K)$
u	Velocity	m/s
u	Internal energy	J/kg
v	Specific volume	m^3/kg
V	Volume	m^3
V_{Gj}	Drift velocity	m/s
We	Weber number	-
X_{tt}	Martinelli parameter	-
x	Vapour (mass) fraction (quality)	-
y	Protrusion length	m
z	Deviation parameter	-
z	Length	-

Greek letters

α	Void fraction	-

β	Pressure reduction factor	-
γ	Angle of inclination from the horizontal	-
γ	Parameter	-
λ	Thermal conductivity	W/(mK)
μ	Dynamic viscosity	Pa s
Φ	Two-phase local loss multiplier	-
ϕ	Angle	rad
ϕ_{Lo}^2	Two-phase friction loss multiplier	-
ρ	Density	kg/m^3
ρ_h	Homogeneous (no-slip) density	kg/m^3
ρ_m	Momentum density	kg/m^3
ρ_e	Energy density	kg/m^3
σ	Surface tension	N/m
θ	Angle	-
τ	Time constant	s

Subscripts

0	Initial
acc	Acceleration
b	Continuous phase at beginning of entrainment
c	Critical
c	Condenser
cIn	Condenser inlet
cOut	Condenser outlet
d	Drag
fric	Friction
g	Gas
grav	Gravity
i	Grid number index
i	Branch tube index
I	Inlet
in	Inlet
J	Junction
l	Liquid
lg	Difference between liquid and gas phase
m	Manifold
mIn	Manifold inlet
p	Phase
ph	Preheater
phIn	Preheater inlet

v	At constant volume
vd	Dimensionless vapour area
ref	Refrigerant
T	At constant temperature
T	Total
t	Branch tube
tp	Two-phase
ts	Test section
$tsIn$	Test section inlet
$tsOut$	Test section outlet
w	Wall
w	Water
$wavy$	Trasition line for stratified-wavy flow regime area

Superscripts

$pred$	Predicted value
m	Exponent
$meas$	Measurement
n	Exponent
s	superficial
sat	Saturated

Chapter 1

Introduction

1.1 Background

The use of compact heat exchangers has increased over the last years due to the need for higher efficiency equipment in smaller package volumes. Lower operating costs because of rising energy prices has justified the larger initial cost of such heat exchangers. Making heat exchangers more compact involves reduction of channel hydraulic diameters and length of the flow channels. Heat exchangers with MPE-tubes are now utilized in a growing number of applications, e.g. mobile and residential air conditioning. The good air and refrigerant-side performance of such heat exchangers has been documented extensively in the literature (Jacobi, 2001). Another advantage of microchannel heat exchangers (MCHE) is the possible charge reduction, often important in systems with flammable or poisonous refrigerants.

Generally, an implication of down-scaling the tube diameter is an increase in the number of parallel flow channels through the heat exchanger to keep the pressure loss at acceptable levels. The heat exchanger pressure losses affects the COP (Coefficient Of Performance) of the system. Because of the increasing number of parallel flow channels, the issue of fluid distribution has received growing attention. One of the common assumptions in basic heat exchanger design theory has been that the fluids are distributed uniformly. In practice, a flow maldistribution often occurs, which can significantly reduce the performance of heat exchangers with parallel flow circuits.

The complex issue of flow distribution in heat exchangers have been studied by

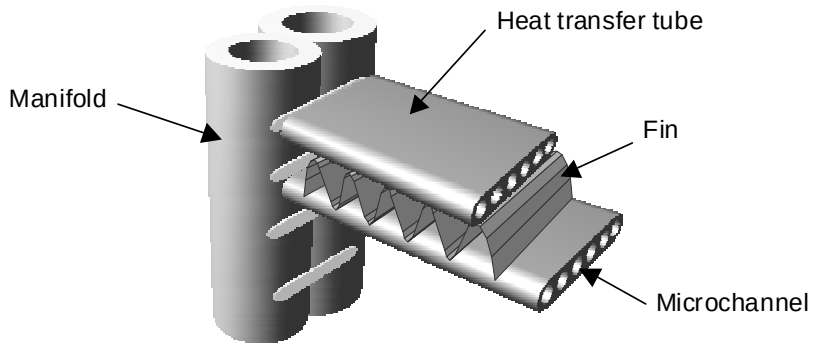

Figure 1.1: Principles of heat exchanger geometry for high operating pressures using MPE-tubes, folded fins, and a compact ”double barrel” manifold (Pettersen, 2002). The heat exchanger is assembled by brazing in a furnace.

many authors. Mueller (1987) and Mueller and Chiou (1988) reviewed various types of flow maldistribution in heat exchangers. They concluded that maldistribution could be caused by geometric factors (manifold cross-sectional design, branch couplings, location and orientation of the tubes) or operating factors (mass flow rate, flow regime and vapour fraction at the inlet of the manifold and heat load on the tubes). The current work is an investigation of the second type of flow maldistribution, with emphasis on the distribution resulting from two-phase flow at the inlet of the heat exchanger manifold. The differences in physical properties between the liquid and the vapour phase (density, viscosity and surface tension) affects the inertial, gravitational, shear and capillary forces. The interaction of these forces determines the phase split in the heat exchanger manifold.

Evaporators are particularly sensitive to uneven distribution of two-phase refrigerant. This is because heat transfer is degraded in liquid-starved tubes, not only because the heat transfer coefficient is lower in single-phase vapour flow compared to two-phase flow, but the temperature difference between the refrigerant and the secondary fluid (e.g. air) is reduced as the refrigerant superheats. In addition to reduction in capacity because of two-phase maldistribution, the operation of the evaporator can be affected in a number of ways. Non-uniform refrigerant distribution in air heat exchangers will produce non-uniformity in the air outlet temperature. Also, the surface temperature of superheated tubes will rise and may exceed the dew-point temperature of the air, which will reduce the dehumidification effect of the heat exchanger. The same problem arises in evaporators operating in cold climate where frosting occurs. Unequal surface temperatures will then produce uneven frosting of the heat exchanger (Hrnjak, 2003), which

will provide differences in the airflow resistance through the heat exchanger and reducing the heat transfer of the evaporator even further. Another problem due to maldistribution of the refrigerant flow is due to flooding of evaporator tubes, which may allow liquid to enter the evaporator outlet and thereby influencing the control stability of the thermal expansion valve.

1.2 Objective

To avoid the problems arising from maldistribution of refrigerant flow in heat exchanger manifolds, the behaviour of the fluid distribution must be understood. Capabilities of computer models for two-phase flows have been steadily improved over the last decades. However, it is not possible to achieve the necessary understanding of the complex two-phase flow involved in the manifold distribution problem without an experimental foundation.

As a basis for developing new manifold designs to improve the heat exchanger performance, a better understanding of the flow within the manifold is of great importance. It was the intention of the current study to contribute to the understanding of the fundamental aspects involved in two-phase flow distribution.

Specific objectives of the work were to:

- Measure two-phase flow distribution in compact heat exchanger manifolds, with focus on manifolds in MPE-tube heat exchangers, at a range of realistic operating conditions.
- Investigate the performance of several manifold geometries, to enhance the understanding of the connection between two-phase flow distribution and the manifold geometry.
- analyse results, observations and findings in relation to other published models for two-phase flow distribution.
- Develop a model for two-phase flow distribution, which could be used in heat exchanger simulation models taking into account the performance reduction of flow maldistribution.
- Develop and demonstrate a heat exchanger simulation model and verify the modelling results against the laboratory experiments.

1.3 Outline of the thesis

Chapter 2 contains a literature review on the subject of two-phase distribution in compact heat exchanger manifolds. As a basis for understanding the manifold distribution issue, an introduction to flow regime maps in small diameter tubes are presented and a thorough review of experimental and theoretical work on two-phase flow distribution in T-junctions is given.

The test rig that was built for the purpose of investigating manifold two-phase distribution is described in Chapter 3. The data reduction procedure used for deducing the vapour fraction at the inlet of the manifold and at the inlet of each branch tube is also described. The chapter is finalized with an uncertainty propagation analysis and a description of the measurement procedures.

Measurement results are presented graphically in Chapter 4, as well as a comparison of the two-phase distribution performance of the different manifold geometries.

In Chapter 5 the measurement results are compared to existing correlations for flow split in manifolds and T-junctions. A new model is developed and the flow phenomena affecting the two-phase distribution in the manifold is analysed.

Chapter 6 provides a description of the simulation model developed for the purpose of analysing the effect of two-phase maldistribution on the heat exchanger performance. Simulation results are shown and compared to the experimental results.

Parts of the experimental work has earlier been presented at the Compact Heat Exchanger Symposium in Grenoble (Vist and Pettersen, 2002) and at the 2nd International Conference on Heat Transfer, Fluid Mechanics and Thermodynamics in Zambia (Vist and Pettersen, 2003). The first paper is also published in *Experimental Thermal and Fluid Science* (Vist and Pettersen, 2004). A paper presenting the initial work on correlating the experimental data has been accepted for publication at the symposium ”Air-to-Carbon Dioxide Heat Exchangers” at the 2004 ASHRAE winter meeting in Anaheim, USA.

Chapter 2

Background and Literature Review

2.1 Chapter overview

The current Chapter provides an overview of previous work relevant for the understanding of two-phase flow distribution in heat exchanger manifolds. First, studies that have quantified the significance of two-phase flow maldistribution are outlined in Section 2.2. Then, an overview of experimental work done on two-phase distribution in manifolds is given in Section 2.3. Emphasis is put on results obtained with horizontal manifolds and vertical branch tubes, which is of relevance for the current study.

As will be shown, the two-phase flow pattern at the inlet of the manifold and throughout the manifold is of great importance for the distribution to the individual flow channels of the heat exchanger. Therefore, a short introduction to flow patterns in horizontal tubes is given in Section 2.4.

Extensive work is done on two-phase flow distribution in T-junctions. Due to the fact that the manifolds studied in the current report geometrically can be regarded as a series of T-junctions, a review of the experimental and theoretical work done on T-junctions is given in Sections 2.5 and 2.6, respectively.

Based on the principles developed in the analysis of two-phase flow in T-junctions, some authors have presented models for two-phase flow in heat exchanger manifolds. These approaches are described in Section 2.7.

Finally, a review of suggested geometrical designs and principles for improvement of two-phase flow distribution is provided in Section 2.8.

2.2 Heat exchangers - significance of maldistribution

To determine the limit of the effect of two-phase flow maldistribution, Beaver et al. (2000) set up a system with two alternative methods for feeding the evaporator in an air-conditioning system operating with CO_2 in transcritical mode. First, the evaporator was connected in conventional mode with an expansion valve at the inlet and a low pressure receiver at the outlet of the evaporator. Second, the evaporator was fed with pure liquid from a separator located upstream the evaporator. The flash gas from the separator was bypassed the evaporator to the suction line of the compressor. The air outlet temperatures showed a much more uniform distribution in the second setup, indicating an improved two-phase distribution. The system COP (Coefficient Of Performance) was claimed to be increased by 20%.

Choi et al. (2003) conducted experiments with R-22 in a three-circuit finned tube evaporator to determine the capacity degradation due to non-uniform refrigerant and air flow distributions. The refrigerant distribution between the three circuits was controlled individually and the superheat at the exit was measured. The study showed that refrigerant maldistribution between the three circuits could cause an evaporator capacity degradation of 30%. Two of the circuits were run with an elevated superheat of 11.1°C, while the third was flooded to keep the overall superheat at the exit unchanged compared to the base-case. Tests with forced air maldistribution were found to cause a capacity degradation up to 8.7%. A 4% capacity recovery was obtained by controlling refrigerant mass flow rate in each circuit to maintain equal exit superheat. More details from this study were presented by Payne and Domanski (2002), where also a simulation model, taking into account the distribution issues, was outlined. The simulation model was verified against the experimental measurements.

Tests by Wu and Webb (2002) showed serious maldistribution in the third pass of an evaporator having a horizontal header with upward branch tube configuration. An 8% reduction in capacity of the tested brazed aluminum evaporator was estimated due to refrigerant maldistribution.

Lalot et al. (1999) investigated fluid maldistribution in an electrically heated heat exchanger. They developed a numerical model of the fluid flow in the heater and found a 7% reduction in calculated heat exchanger performance due to mald-

istribution in condensers and counterflow heat exchangers, and more than 25% reduction for cross flow heat exchangers. The authors also found that backward flow in some channels could occur for certain manifold geometries.

Pettersen et al. (2000) modelled the effect of separated flow distribution on heat transfer in the last pass of an HFC-134a multiport extruded tube (MPE-tube) evaporator, with an inlet vapour fraction, $x = 0.8$. Equal pressure drops were assumed for the tubes filled with liquid and those filled with vapour. A capacity reduction of 30% was calculated compared to the case of uniform two-phase flow feeding.

Even in single-phase flow distribution serious performance reduction have been observed due to manifold maldistribution. Heggs and Scheidat (1992) studied performance of plate heat exchangers as function of plate flow arrangements. A thermal performance reduction of up to 15% was observed in a 60 channel exchanger due to maldistribution of single-phase flow.

2.3 Manifold flow distribution - experimental investigations

Only a limited number of publications in the open literature are dealing with the problem of two-phase distribution in manifolds. In light of the large number of variables that come into play, e.g. manifold and branch tube geometry, number of branch tubes, orientation of the manifold and the branch tubes, as well as operating conditions and physical properties of the test fluid, it is difficult to make definite conclusions regarding the two-phase distribution in heat exchanger manifolds. Also, only some authors have used heat load on the branch tubes, while measuring the two-phase flow distribution in the manifold. In the following sections, an overview of the published literature containing experimental results on two-phase distribution in round tube heat exchangers, plate heat exchangers and MPE-tube heat exchangers is given.

2.3.1 Round tube heat exchanger manifolds

Asoh et al. (1991) studied two-phase R113 distribution in a simulated automobile air conditioning system using downward flow into three vertical branch tubes (ID 7.9 mm, center distance 50 mm) from a horizontal manifold (ID 13.9 mm). The manifold was made out of glass, and the authors could observe the two-phase flow in the manifold. The flow pattern at the inlet of the manifold during the

experiments was slug or froth flow. Copper branch tubes were heated by electrical cables and the evolution of static pressure in the manifold and in the branch tubes was measured. The authors found that refrigerant maldistribution appeared due to two-phase fluid dynamics and non-uniform thermal load. Also, the flow rates of both phases entering the branch tubes were controlled more by the liquid flow rate in the manifold than that of the vapour.

Watanabe et al. (1995) studied distribution of refrigerant R11 in a horizontal manifold (ID 20 mm) with four upward heat exchanger tubes (ID 6 mm), simulating an automobile air-conditioning evaporator. Several geometrical factors that affected the two-phase flow distribution in the manifold were identified: cross-sectional area ratio of branches and manifold, location and branch orientation. In addition, operational parameters such as total mass flow rate and vapour fraction in the manifold and the heat load on the branch tubes, were found to be important for the two-phase distribution in the manifold. The authors found that the vapour phase was preferentially distributed to the first branch tubes and that the liquid level in the horizontal manifold was rising further downstream in the manifold due to the vapour take-off. The last tube of the manifold was always the one with the lowest vapour fraction. Reducing the number of branch tubes changed only the quantitative results. Qualitatively, the two-phase distribution results were almost unchanged. Adding heat load to the branch tubes reduced the maldistribution of the two-phase flow in the manifold. The authors pointed out the necessity of conducting further research on the two-phase flow development along the length of the manifold because of the absence of work in this field (except a few publications in Japanese between 1988 and 1992) and that the experimental results obtained in T-junctions, mostly derived from geometries and operational parameters relevant for cooling systems of nuclear power plants, could not be directly applied to manifolds with several branch tubes. However, a T-junction modelling approach was found to be applicable in the analysis of the flow distribution in the inlet manifold. The model developed by Watanabe et al. (1995) is described in detail in Section 2.7.1.

Osakabe et al. (1999) studied single-phase (air) and two-phase (air-water) distribution in a horizontal manifold (40 mm $\times$ 40 mm in cross-section) with four vertical branch tubes (ID 10 mm) in upward configuration. Air and water flow rates in each branch tube were recorded. When introducing a small amount of bubbles in the manifold, the water distribution rate to the first branch tube increased as in an airlift pump, while the flow rates to the other branch tubes decreased. Increasing the inlet air flow rate, the water flow rate to the first branch tube reached a maximum and tended to decrease. At even larger inlet air flow rates, the flow pattern at the manifold inlet became stratified and the first two branch tubes were starved

with water. In a further study by Horiki and Osakabe (1999), the branch tubes protruded into the manifold, and the effect of protrusion length on the water distribution was studied. By increasing the protrusion length, maldistribution of the water was reduced because the gas-phase was distributed more evenly. The best result was obtained when the four branch tubes were protruded into the center of the manifold.

Unpublished experimental tests at Penn State University, referred by Wu and Webb (2002), showed that flow maldistribution was more severe in upward than in downward branch tube configuration. Stratification was seen in the manifold with a resulting poor two-phase distribution, especially in upward flow configuration.

2.3.2 Plate heat exchanger manifolds

Some experimental work has been done on two-phase distribution in plate heat exchanger manifolds. Rong et al. (1995) studied distribution of air and water in a heat exchanger simulating a plate evaporator with seven 75 mm wide flow passages, both in vertical upward and downward orientation. Measured values of air and water flow rates in each passage were reported for varying inlet flow rates and adiabatic conditions. The authors found that the manifold geometry was a critical factor, because it determined the two-phase flow characteristics, which had a strong influence on the distribution. At low air and high water flow rates (low vapour fraction), the inlet flow pattern was slug flow and air and water in the manifold tended to separate due to gravity, resulting in severe maldistribution among the channels. At higher air flow rates, annular flow was observed in the distribution manifold. In these experiments, the first branches received most water while the last branches of the manifold received most air, both in upward and downward configuration. Flow blockages at the inlet of the heat exchanger channels were tested to manipulate the two-phase distribution. One of the blockage designs showed significant improvement and was recommended for actual application. Rong et al. (1996) identified the phase distribution at the manifold inlet and especially the liquid momentum as an important factor determining the two-phase distribution in the manifold. At low liquid momentum in downward configuration, the water flow was almost homogeneously distributed, while at higher momentum the liquid could skip the first channel entrances and reach channels further downstream.

Bernoux (2000) conducted experiments with two-phase distribution in a horizontal plate heat exchanger manifold with transparent walls. The test section consisted of eight vertical downward rectangular channels (2×50 mm) with R113

as working fluid. The author observed that the distribution was never uniform, regardless of flow patterns in the manifold or at the inlet of the manifold. At low inlet vapour fraction the liquid phase was more uniformly distributed and at high inlet vapour fraction the vapour was more uniformly distributed. The inlet flow patterns were visually observed and the relation to the manifold distribution was studied. At low inlet vapour fraction, the incoming jet of liquid filled the channels upon which it was impinging. At medium inlet vapour fractions the liquid jet hit the end wall of the manifold and filled the last channels of the heat exchanger. At the highest inlet vapour fraction ($x = 0.8$) droplets in the inlet flow collided with the end wall and was predominantly collected in the last channel.

Fei et al. (2002) conducted experiments with HFC-134a in a generic plate evaporator manifold (0.3 m long and square cross section 25 $\times$ 25 mm) with distribution to five round tube branches in downward orientation from the horizontal manifold. The manifold was transparent, such that the developing flow could be observed in side-view. Further work from this ongoing project was described by Hrnjak (2003). It was found that the inlet flow conditions to the manifold significantly affected the flow regime and the liquid distribution in the manifold. Standard deviation from the average value was used as a measure of uniformity in liquid distribution to the branch tubes. Best liquid distribution was found at small droplet sizes and slip velocities close to unity, where the droplets followed the vapour flow. The authors constructed flow regime maps for developing flow in the manifold.

2.3.3 MPE-tube heat exchanger manifolds

Yoo et al. (2002) conducted air-water experiments on a horizontally and vertically oriented manifold with fifteen MPE-tubes (this work was also partially published by Tompkins et al. (2002b)). The MPE-tubes were 6-port aluminum tubes with a flow cross sectional area of 1.669×10^{-5} m^2. The tubes did not protrude into the manifold. Air flow distribution, water distribution and pressure profiles along the manifold were measured. The area ratio, defined as the sum of the branch tube cross-sectional area divided by the cross-sectional area of the manifold, was changed by adjusting the height of the rectangular tube manifold. Four different entrance locations were employed to the manifold. Maldistribution was generally seen to increase at increasing inlet mass flux. At low inlet mass fluxes, the flow pattern in the manifold was stratified-wavy, and the water was preferentially distributed to the first tubes in the manifold. At high mass fluxes, annular flow was observed in the manifold and the liquid film at the bottom entered the first MPE-tube, while the remaining liquid film around the periphery of the manifold reached

the end of the manifold and entered the last MPE-tubes. Generally, the air flow distribution was inversely related to the water flow distribution. The authors cited that the liquid film on the walls was moved along the manifold by the vapour drag. No correlation was found between the pressure profile along the manifold and the air/water distribution. Various parameters were utilized in an attempt of reducing the experimental data, but no universal trends were discovered. However, it was seen that the tests with short inlet lengths to the manifold produced more maldistribution than the tests with longer inlet lengths. Vapour fraction and mass flux at the inlet of the manifold did not have big impact on the normalized standard deviation values of the air/water distributions. Tompkins et al. (2002a) developed a mathematical model based on the data given in Yoo et al. (2002). This model is outlined in Section 2.7.2.

Stott et al. (2002) used a MPE-tube evaporator with feeding of the two-phase flow at four locations along the inlet manifold. Measurement of superheat at the outlet of the tubes were used to quantify maldistribution. Capacity reduction due to maldistribution in the evaporator was estimated to 13% at dry conditions and 19% at wet-coil conditions.

Song and Bullard (2002) observed frosting patterns as a qualitative indicator of maldistribution of CO_2 in a multipass MPE-tube evaporator with vertical manifolds and horizontal branch tubes. The tubes at the bottom or at the top of the manifold usually received less liquid than the others. Location of these tubes was determined by a balance between inertial, gravitational and shear forces. In the first passes, containing most liquid, the gravitational forces were dominant, while moving downstream the inertia forces became more important in determining the flow distribution. It was seen that the refrigerant maldistribution created non-uniform frost deposition, which increased air velocity through the regions where the surface was unfrosted.

Cho et al. (2002) studied two-phase R-22 maldistribution in a vertical manifold with fifteen horizontal MPE-tubes. Two solutions for the inlet to the manifold were tested. First, in the inline configuration (Figure 2.1 a)) the inlet tube had the same direction as the manifold, with vertical upward flow. Second, in parallel configuration (Figure 2.1 b)), the vertical manifold was fed with a horizontal inlet pipe at the middle of the manifold. The inlet pipe was then parallel to the heat exchanger MPE-tubes. The flow maldistribution improved when changing from parallel to inline configuration. For both configurations, the mass flow rate was largest in branch tubes at the bottom of the manifold. The difference in phase separation ratios for the MPE-tubes decreased as the inlet vapour fraction increased.

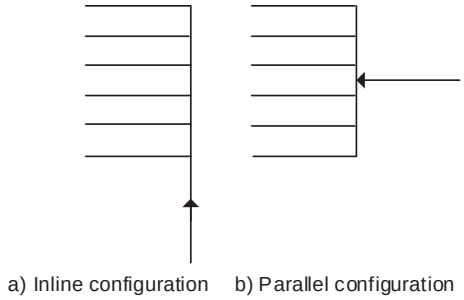

Figure 2.1: Inline and parallel manifold inlet configuration used by Cho et al. (2002).

Lee and Lee (2002) investigated two-phase distribution in a vertical manifold (24 mm $\times$ 24 mm) with six horizontal flat branch tubes (22 mm $\times$ 1.8 mm). The branch tube protrusion depth could be varied from 0 to 12 mm into the manifold. Air and water were used as test fluid. Deeper protrusion prevented the water from entering the first branch tubes of the manifold. A protrusion depth of 3 mm was found to give most uniform liquid distribution.

Zietlow et al. (2002) presented an experimental setup with the purpose to measure liquid distribution in a MPE-tube manifold. Further details regarding the measurement concept is given in Section 3.2.1.

2.4 Two-phase flow patterns in horizontal pipe flow

As pointed out in the previous Section, several authors mentioned that the flow pattern at the inlet of the manifold and along the manifold length was of great importance for the two-phase distribution. Therefore, it is useful to consider the flow patterns which occur in two-phase flow in pipes as a basis for understanding the flow patterns of the developing flow in the manifold. One complication in the analysis of horizontal pipe flow compared to vertical flow is that the flow is not symmetrical around the axial centre axis. The flow patterns that can be observed in horizontal two-phase flow are shown in Figure 2.2.

Bubbly flow: At low gas flow rates, the gas is distributed in discrete bubbles in a continuous liquid phase. The bubbles tend to flow in the upper part of the tube due to buoyancy.

Plug flow (elongated bubble flow): An increase in gas flow rate cause the bubbles to coalescence into large elongated plug-type bubbles, which flow in a continuous liquid phase in the upper part of the tube.

Slug flow: The liquid flow is contained in liquid slugs, separating successive gas bubbles. The length of the gas bubbles can vary considerably and contain liquid droplets. Gas bubbles may be dispersed in the liquid slug.

Stratified flow: The liquid is flowing in the lower part of the tube with a relatively smooth interface to the gas in the upper part.

Wavy flow: At increasing gas velocity, the interface between the gas and the liquid becomes wavy.

Annular Flow: At even higher velocities, a liquid film will form a continuous annulus along the tube wall with the gas flowing in the core. Due to gravity, the film will be thicker at the bottom of the tube ("crescent" liquid interface).

Dispersed mist flow: The liquid is transported as droplets in the continuous gas phase.

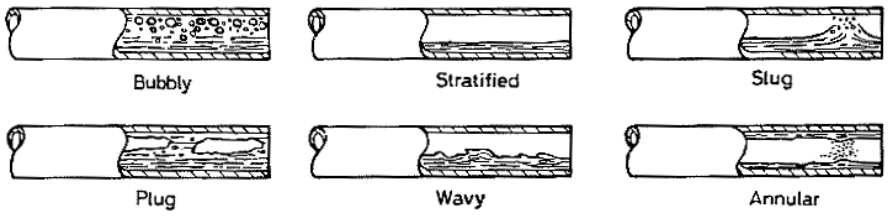

Figure 2.2: Flow patterns in horizontal flow. Reproduced from Collier and Thome (1994).

Flow pattern maps are often used in predicting two-phase flow patterns, which are represented as areas on the map separated by transition lines. The coordinates of the flow pattern maps can be the actual superficial gas and liquid velocities or generalized parameters containing these velocities. The flow pattern map of Baker (1954), widely used in the petrochemical industry, is purely empirically developed for horizontal adiabatic flow, using superficial gas and liquid velocities, together with scaling parameters for fluid properties as coordinates. Taitel and Dukler (1976) and Taitel (1990) developed a comprehensive set of methods for the prediction of flow pattern transitions. Kattan et al. (1998) developed a diabatic

two-phase flow pattern map based on the methods of Taitel and Dukler (1976) and the work of Steiner (1993). The Kattan et al. (1998) flow pattern map can be plotted with gas fraction (x) and mass flux (G) as axis legends, given specific fluid properties, pipe diameter and wall heat flux (q). Intermittent flow is a term covering both plug and slug flow. Zürcher et al. (2002) introduced the effect of void fraction on the flow transition and flow pattern on the void fraction. Thome and El Hajal (2002) simplified the methods to calculate the transition lines in the flow pattern map of Kattan et al. (1998) by using a simpler method to get the equivalent results. The void fraction method of Rouhani and Axelsson (1970) was used to avoid the iteration calculation procedure necessary in the originally used void fraction method of Taitel and Dukler (1976). An example of such a map, generated with the transition equations given by Kattan et al. (1998), with the extensions Zürcher et al. (1999), is shown in Figure 2.3. The transition lines in the flow pattern map are used in the correlation of the experimental data in Chapter 5.

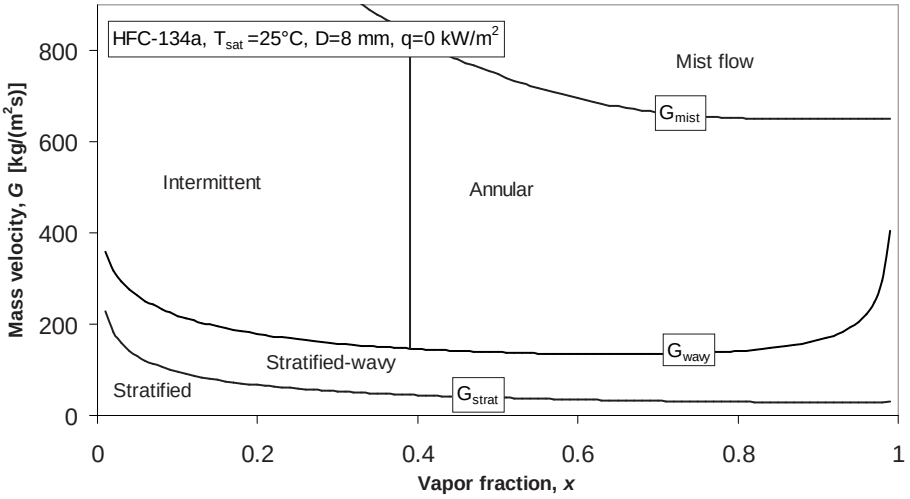

Figure 2.3: Horizontal flow pattern map, from Kattan et al. (1998) with extensions of Zürcher et al. (1999). Symbols are S: Stratified, SW: Stratified-Wavy, I: Intermittent, A: Annular, MF: Mist.

2.5 Two-phase flow splitting in T-junctions

Manifolds, which are the focus of the current study, can be regarded as a series of T-junctions. Even if measurement data from T-junction experiments cannot be

applied to manifolds directly (Moura, 1990), it is believed that the fundamental knowledge gained by studying two-phase flow split in T-junctions can be valuable in the investigation of two-phase distribution in manifolds. This Section contains a general overview of the experimental work done on two-phase flow in T-junctions, with a special focus on data and models relevant for flow distribution in heat exchanger manifolds. The phenomena affecting the two-phase split, both those observed and those deduced from the trends in T-junction measurements are reviewed in a systematic manner. Some analytical models developed for flow split in T-junctions are reviewed in Section 2.6. The following review surveys provide a good starting point for further reading: Müller and Reimann (1991), Azzopardi and Hervieu (1994) and Azzopardi (2000).

2.5.1 Definitions

When studying the available literature on two-phase split in T-junctions, it is useful to first establish some definitions, Figure 2.4.

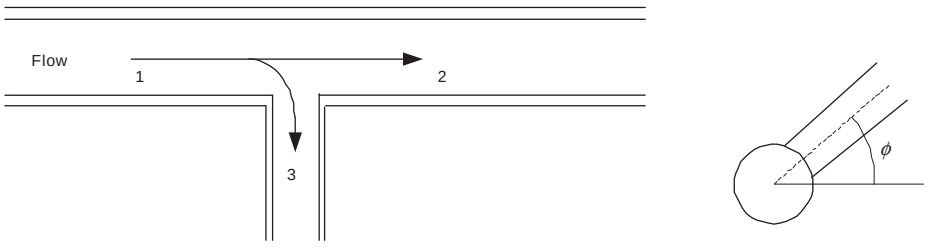

Figure 2.4: T-junction conventions.

The T-junctions considered in the present survey has one inlet pipe and two outlet pipes. One of the outlet pipes is in line with the inlet pipe, and the third pipe, often denoted as the branch or the side arm, meet the main pipe in a right angle. The diameter of the branch, D_3, is generally not equal to D_1. The angle ϕ denotes the angle between the axial direction of the branch and the horizontal plane, see Figure 2.4. Most T-junctions used in research have been machined from solid material and therefore have no rounding of the T-junction corners.

In addition to the geometry variables, the fluid physical properties and the two-phase flow rates are also important variables in determining the flow distribution in the T-junction. The flow distribution in the T-junction is strongly dependent upon the pressures in the two downstream systems. Clearly, lower outlet pressure gives more powerful suction and higher fluid flow. In addition to the pressure drop due

to friction etc. downstream the T-junction, there are pressure drops (rises) related to the flow in the T-junction, as illustrated in Figure 2.5. The upper diagram shows the pressure undershoot and recovery that occurs when the fluid turns a sharp 90° bend. In contrast, the lower diagram shows the sudden pressure recovery that occurs in the main pipe due to fluid retardation when the mass flux is reduced. By extrapolating the fully developed pressure profiles in the main pipe and the branch tube downstream the junction, the pseudo axial pressure rise, $p_{1J} - p_{2J}$, and branch tube pressure drop $p_{1J} - p_{3J}$ are obtained.

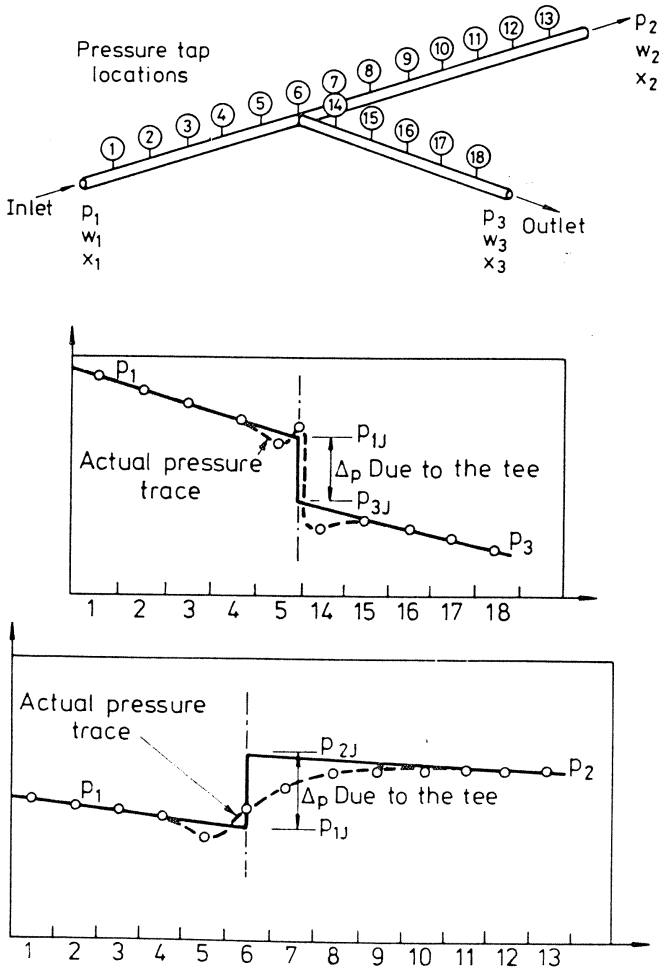

Figure 2.5: Typical pressure distribution in a T-junction (Lahey, 1986).

2.5.2 Experimental work

2.5.3 General overview

Dividing and combining pipe junctions commonly occur in many types of process and power plants. Observation has shown that when multiphase flows divide at such junctions, there is almost inevitably a maldistribution of the phases. This phase separation is studied in detail because it can have a profound effect on system performance. Examples of cases which illustrate the problems caused by maldistribution at junctions include:

- The effect of phase separation in the main coolant piping on the effectiveness of the core cooling of a Light Water Nuclear Reactor (LWR), during a hypothetical loss-of-coolant accident (LOCA).
- Condensate accumulation in reserve lines of gas distribution networks during winter season.
- The effectiveness of wet stream injection systems for enhanced oil recovery.
- The design of slug catchers and phase separators in natural gas and oil well lines.
- Two-phase distribution between parallel equipment units in refrigeration systems and in chemical industrial applications.

Due to the critical function of the water cooling in a LWR much of the research on two-phase flow splitting in T-junctions has been conducted with these systems in mind. Given the importance of the phase separation phenomenon, this has been an area of fairly active research. The most significant experimental research, with T-junctions having a horizontal main pipe, is summarized in Table 2.1.

Several factors affect the phase separation T-junctions with horizontal main pipes:

- Difference in momentum fluxes of the phases due to velocity and density differences
- Mass flow split ratio, $\dot{m}_3/\dot{m}_1$
- Fluid physical properties
- Geometry of the T-junction

Table 2.1: Details of sources for experimental data on T-junctions with horizontal main pipe and 90° angle between the main pipe and the branch tube.

Sources	D_1 (m)	D_1/D_3	ϕ (deg)	p_1 (bar)	u_g^s (m/s)	u_l^s (m/s)
Oranje (1973)	0.076	0.67,1.0	0°	30	3-14	0.00018
Fouda and Rhodes (1974)	0.051	0.5	+90°	1.5	24-51	0.046-0.077
Collier (1976)	0.038	0.67	0°	3.0	0.8-18.5	0.066-0.13
Hong (1978)	0.0095	1.0	0° ±45° ±90°	1.2-1.6	9-43	0.0023-0.047
Henry (1981)	0.1	0.2	0°	1.0	25-100	0.1-0.8
Azzopardi and Whalley (1982)	0.032	0.4	0° ±30° ±60° ±90°	2.5	21	0.08
Saba and Lahey (1984) Hwang and Lahey (1988)	0.038	1.0	0°	1.3-1.9	0.8-6.5	1.35-2.7
Reimann and Kahn (1984)	0.206	0.03-0.15	-90°	5	0-1.65	0.02-0.3
Seeger et al. (1985) Seeger et al. (1986)	0.05	1	0° ±90°	4-100	4-40	0.5-4
Smoglie and Reimann (1986)	0.206	0.03-0.1	0° ±90°	5.0		
Shoham and Brill (1987) Shoham et al. (1989)	0.051	0.5, 1.0	0°	3.0	2.7-26	0.011-0.055
Katsaounis (1987)	0.203	0.26	+90°	1.0	0.03-2	0.025-1.7
Rubel et al. (1988)	0.038	1.0	0°	1-2.5		
Reimann et al. (1988)	0.05	0.08 1.0	0° ±90°	4-100		
Ballyk et al. (1988) Peng et al. (1996) Shoukri et al. (2002)	0.026	0.5 0.82 1.0	0° -45° -90°	1.1-2.1		
Azzopardi and Memory (1989) Azzopardi and Smith (1992) Azzopardi (1999)	0.038	0.33	+90° 0°	1.5-3.0	0.7-31	0.008-0.078
Hart et al. (1991a) Hart et al. (1991b) Ottens et al. (1999)	0.05	0.75	0° +0.25° +0.5°	1.0	7-10	0.00007- 0.031
Mudde et al. (1993)	0.23	0.43	+90°	1.0	0.01-0.19	0.5-1.5
Buell et al. (1994) Walters et al. (1998)	0.038	0.206 0.5	0°	1.5-3.0	2.7-40	0.002-0.18
Roberts et al. (1995) Rea (2001) Wren et al. (1999)	0.127	0.6 1.0	0° +90°	1.0	4-43	0.0045- 0.558
Penmatcha et al. (1996) Marti and Shoham (1997)	0.5	0.5 1.0	-60° - +35°	3.0	6.1	0.003- 0.059
Peng et al. (1998)	0.076	0.33-1.0	0° -90°	1.1-1.6	1.5-5	0.05-0.9
Stacey et al. (2000)	0.005	1.0	0°	1.5	46-60	0.1-0.2
Tae and Cho (2003)	0.00812	0.61, 1	0° ±90°	6.5	0.74-7.4	0.09-3.58

In Figures 2.6 to 2.9 examples of results from (Seeger et al., 1985) are shown. Phase separation was presented by plotting the ratio of branch tube to main tube inlet vapour fraction, x_3/x_1, against the total flow split, G_3/G_1. Equal phase distribution was then represented by the horizontal line $x_3/x_1 = 1.0$.

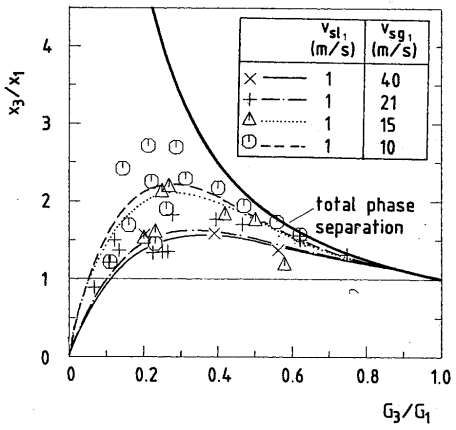

Figure 2.6: Phase separation for horizontal branch tube. Air-water, $D_1 = D_3 = 50$ mm, $P_1 \approx 0.7$ MPa, $u_l^s = \text{const}$. Reproduced from (Seeger et al., 1985).

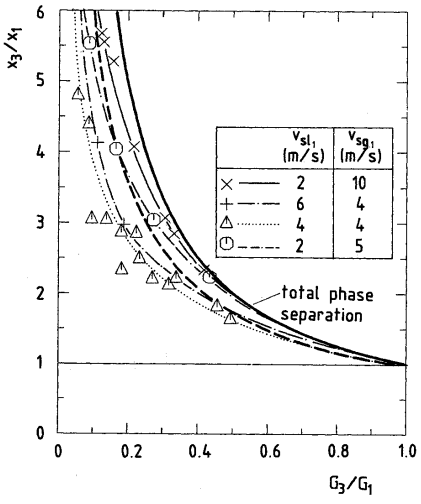

Figure 2.7: Phase separation for upward branch tube. Air-water, $D_1 = D_3 = 50$ mm, $P_1 \approx 0.7$ MPa. Reproduced from (Seeger et al., 1985).

2.5.3.1 Horizontal branch tube experiments

Experiments conducted with a horizontal branch tube, Figure 2.6, showed that the phase split $x_3/x_1$was smaller than 1.0 for very small values of G_3/G_1. This was due to the fact that at small extraction ratios mainly the fluid close to the wall, having a high liquid fraction, was extracted. These observations were consistent with the concept of dividing streamlines, introduced by McCreery (1984), which proposed that the liquid and the gas going into the branch tube did not come from the same segment of the main pipe. Especially in annular flow regime, this favoured the take-off of liquid flowing at low speed close to the wall.

At increasing G_3/G_1, more gas was deflected into the branch tube and x_3/x_1reached values considerably above 1.0 (Figure 2.6). A further increase in G_3/G_1 was obtained only by increasing the liquid take-off until the value of x_3/x_1=1.0 at $G_3/G_1 = 1.0$. For the superficial gas velocity of 10 m/s and $G_3/G_1 > 0.4$ the

phase distribution measurements were very close to the curve of total phase separation (only gas was taken off in the T-junction).

Based on air/water experiments Saba and Lahey (1984) explained the separation effect in the T-junction by the axial momentum difference between the air and the water in the inlet tube. Water, having the larger momentum, tended to maintain its rectilinear speed across the T-junction while the low-momentum gas was taken off into the branch tube. Azzopardi and Whalley (1982) came to the same conclusions, studying the effect of flow pattern on phase separation. In annular or churn flow the liquid phase was preferentially taken off due to the low momentum liquid film flowing along the walls. In contrast, for bubbly flow the gas phase entered the branch tube as it generally had lower momentum flux than that of the liquid. In order to quantify the variations in phase separation with varying liquid and vapour flow rates Azzopardi (2000) examined phase split data in terms of local momentum fluxes of the phases. A separated flow model, including the Chisholm (1972) void fraction expression was used to calculate the phase momentum fluxes at the inlet of the T-junction. Although the experimental data were scattered, there was a clear trend of reduced liquid take-off when the liquid to gas momentum flux ratio increased. The pressure rise in the main tube created an adverse pressure field (illustrated in Figure 2.5) that the vapour with relatively low momentum flux had to overcome. Thus, the vapour was encouraged to flow in the direction of the branch. Indeed, Saba and Lahey (1984) observed vapour flowing past the T-junction and making a 180° return, caused by the adverse pressure field, and then flowing into the branch tube. Lahey (1986) stated that the local pressure field in the T-junction together with the axial momentum of the phases approaching the junction were two prime parameters deciding the two-phase flow distribution. The local pressure field in the T-junction was strongly dependent on the total flow split ratio $\dot{m}_3/\dot{m}_1$, the diameter ratio D_1/D_3, the flow pattern upstream the T-junction and the orientation of the T-junction.

2.5.3.2 Upward branch tube experiments

Figure 2.7 shows results from the pioneering work by Seeger et al. (1985) with a horizontal main pipe and an upward branch tubes. The authors found that for upward branch tubes and stratified flow at the T-junction inlet, the measured $x_3/x_1$was close to the curve of total separation. Only gas entered the branch tube if the distance from the top of the pipe to the liquid surface was sufficiently large. For smaller distances, the liquid interface was raised due to the pressure drop produced by the gas acceleration near the branch tube exit (Bernoulli effect). A considerable amount of liquid could be torn away from the interface and enter the

tube. The authors explained that the severe separation in upward branch tube flow was due to the impact of gravity forces on the fluid. Work had to be done to lift a liquid particle from the main pipe into the higher level branch tube. In addition, the void fraction in the upper part of the main pipe was higher than in the lower part, especially in stratified flow.

2.5.3.3 Downward branch tube experiments

Experiments with downward branch tube by Seeger et al. (1985) are shown in Figures 2.8 and 2.9. More liquid was taken off in the branch tube, as expected, compared to the results with horizontal and upward branch tube. When the influence of the difference in momentum flux between the phases exceeded the influence of gravity, values of x_3/x_1larger than one was observed. Stratification was most pronounced at the lowest inlet velocities and therefore, liquid tended to enter the branch tube. Shoukri et al. (2002) found that the liquid was preferentially taken off through the whole flow split range in experiments with downward branch tube. At low branch tube flow ratios, G_3/G_1, only liquid was extracted in the branch tube. The gas phase had to be pulled through the liquid film to be extracted through the branch tube. It was seen that a higher vapour flow rate, producing a thinner liquid layer in the main tube, resulted in onset of vapour extraction at lower flow split ratios. Smoglie and Reimann (1986) found that the gas pull-through could occur due to vortex formation or the gas could be pulled through the liquid layer in vortex-free flow.

Figure 2.8 shows the results from Seeger et al. (1985) with constant superficial liquid velocity. In general, x_3/x_1increased with increasing superficial gas velocity, u_g^s. However, the effect of increasing u_l^s at constant u_g^s, Figure 2.9, was much more distinct. The authors explained that this was due to the fact that the flow regime changed more significantly for changes in u_g^s. Seeger et al. (1986) observed a change from stratified/slug flow to a more homogeneous bubble flow regime at u_l^s =4 m/s. Similar to the flow reversal effect in upward branch tubes, which had been observed due to gravity effects, bubbles contained in the liquid taken off in downward branches could be recirculated due to buoyancy at small values of G_3 (Seeger et al., 1985).

2.5.3.4 Variation in physical properties

There are few studies that have varied the fluid physical properties systematically. The gas density in air-water experiments has been changed by altering the system

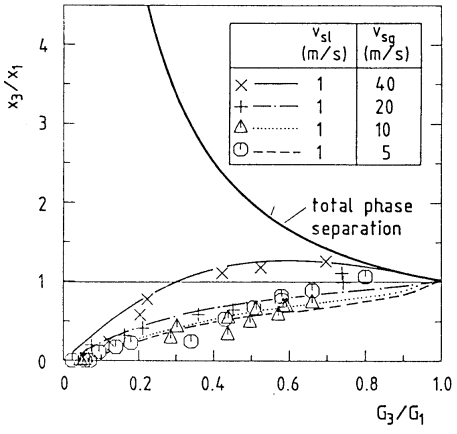

Figure 2.8: Phase separation for downward branch tube. Air-water, $D_1 = D_3 = 50$ mm, $P_1 \approx 0.7$ MPa and $u_l^s =$const. Reproduced from (Seeger et al., 1985).

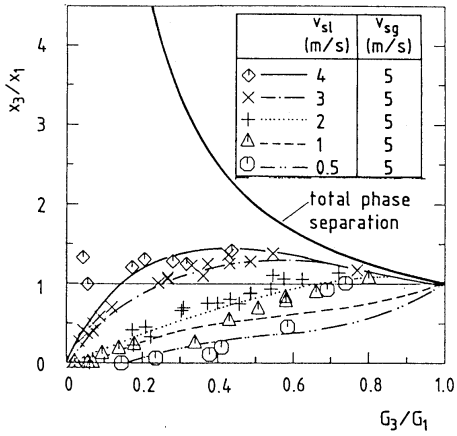

Figure 2.9: Phase separation for downward branch tube. Air-water, $D_1 = D_3 = 50$ mm, $P_1 \approx 0.7$ MPa and $u_g^s =$ const. Reproduced from (Seeger et al., 1985).

pressure. In single fluid experiments all properties vary with the pressure, and the evaluation of phase distribution changes caused by individual properties are difficult. Hong (1978) varied liquid viscosity and found that increasing the liquid viscosity from 1 to 5 cP increased the liquid take-off. The behaviour was explained by changes in the annular film thickness which results in lower liquid momentum flux making it easier for the liquid phase to be extracted into the branch tube. However, increasing further to 10 cP only produced minor differences.

The studies of Seeger et al. (1986), Reimann and Seeger (1986) and Hwang and Lahey (1988) showed that phase separation and pressure distribution measurements for steam-water flows had characteristics similar to those demonstrated in previous air-water studies. (Ballyk and Shoukri, 1990) concluded that condensation and flashing had small effects on the separation process in the T-junction. The flow dynamics was therefore taken to be the dominant mechanism for phase separation in single component two-phase flow. Tae and Cho (2003) studied phase separation in a T-junction using R-22 as fluid. Experiments were run using both horizontal and vertical main tube. Pressure losses from main tube to branch tube and from main tube to main run were predicted within $\pm 25\%$ using pressure loss coefficients suggested by Chisholm and Sutherland (1969).

2.5.3.5 Diameter effects

Many publications listed in Table 2.1 reported the effect of branch tube to main pipe diameter ratio on the phase distribution. The results of Ballyk et al. (1991) showed a decrease in liquid take-off when the diameter ratio was decreased. In contrast, Walters et al. (1998) found that the liquid take-off was greater in a T-junction with diameter ratio of 0.2, compared to a T-junction with a diameter ratio of 0.5. The higher vapour velocity in smaller pipes produced a greater suction on the liquid phase in the T-junction. The effect of rounding of the T-junction was seen to have only a minimal effect on the phase split (Hart et al., 1991a). The effect of varying pipe diameters, holding $D_1 = D_3$, was studied by Stacey et al. (2000). Smaller pipe diameters gave higher liquid take-off values, which was explained by less liquid entrainment in smaller diameter pipes. Additionally, the distance the liquid had to travel to enter the branch tube was smaller in a smaller pipe. The asymmetry in annular flow was also increasing with increasing pipe diameters, resulting in higher momentum liquid which was more difficult to divert into upward branch tubes.

2.5.3.6 Other geometry effects

The effect of downstream geometry on the phase split in a T-junction with horizontal main pipe and horizontal and vertical upward branch tube was studied by Azzopardi and Smith (1992). The geometry downstream of the junction affected the liquid fraction taken off in the branch tube when the flow in the main pipe was stratified. Restrictions in the main pipe downstream the T-junction could then increase the liquid level in the main pipe and therefore affect the phase split in the T-junction. No effect of downstream geometry on two-phase split in the T-junction was found in annular flow.

Wren et al. (1999) studied the effect of branch tube protrusion into the main pipe and branch tube cut off angle (see Figure 2.10 a) and b)). The branch tube was positioned $D_1/2$ and $3D_1/4$ into the main pipe, and a cut off of 30° and 45° was studied. Forward facing branch tube opening and increasing branch tube protrusion increased the liquid take-off in annular flow compared to the T-junction without any insert. Backward facing branch tube reduced the liquid take-off. Changing the branch tube cut off angle from 30° to 45° had little effect on the phase distribution both in forward and backward facing position. Due to the restriction in free cross-sectional flow area in the main pipe, the fluid velocity was increased substantially. The liquid being dragged through the restriction would have a higher momentum and hence it was more difficult to divert the liquid into the branch tube when the

branch tube cut was facing backward. Similar results of branch tube protrusion were reported by the limited tests performed by Butterworth (1980).

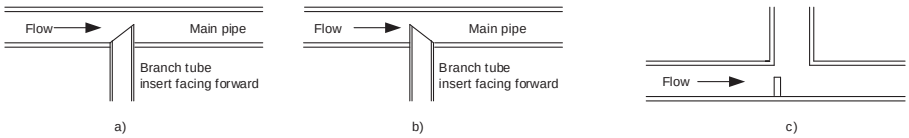

Figure 2.10: Inserts in T-junctions, a) and b) branch tube protrusion used by Butterworth (1980) and Wren et al. (1999), c) baffle insert used by Fouda and Rhodes (1974).

Fouda and Rhodes (1974) tried to obtain equal phase distribution by inserting baffles and homogenizers before the T-junction. The baffles were a quarter, half and three-quarters of the pipe diameter and were placed just at the base of the T-junction (see Figure 2.10c)). Severe maldistribution, with the vapour phase preferentially taken off, was observed in the case without baffles. Only when the largest baffle was used, the flow maldistribution was significantly reduced. The liquid was stopped by the baffle and diverted upward into the branch tube, but for the smaller baffles, the vapour stream in the pipe centre atomized the liquid and transported it down the main pipe run.

2.6 Analytical models for flow split in T-junctions

Although extensive work on the phenomena of flow splitting in T-junctions has been published, no generally applicable model for prediction of the two-phase flow split has been presented. However, due to the request for such models within one-dimensional codes for calculation of two-phase flow phenomena in large hydraulic systems, e.g. nuclear reactor water cooling systems, a number of models have been developed. These models are based on empirical closure relations, and therefore applicable only within the ranges of operational parameters and geometries which they are based upon.

In the development of predictive methods for phase split in T-junctions, three main types of analytical approaches have been used:

- Completely empirical approaches
- Mechanistic (fluid mechanics based) models

- Phenomenological flow regime based models

Initially, various investigators tried to resolve the problem with empirical correlations developed from laboratory measurements (e.g. Zetzmann (1982)). Due to the large number of parameters involved, purely empirical models with general applicability would be impractical to develop. Later, physically based mechanistic models improved the prediction capabilities and the range where the models were valid. These models tried to identify the governing mechanisms involved and applied the appropriate conservation laws and closing with experimentally based constitutive relationships. The mechanistic models provided valuable insight into the fundamental mechanisms involved. However, none of the developed models have shown to have general applicability.

In the next sections, the main models developed for T-junctions with horizontal inlet pipes will be outlined. The Saba and Lahey (1984) model provides a good overview of the mechanical forces involved in the fluid-mechanical problem. Later, three models developed especially for horizontal inlet tube and vertical branch tubes are described.

2.6.1 The Saba and Lahey model

Saba and Lahey (1984) and Lahey et al. (1985) presented a general method for calculation of the separation of phases in a T-junction. There were eight variables in addition to the geometry that defined the flow split. These were the total flow rate, vapour fraction for the inlet and the two outlet pipes, together with the two pressure drops associated with the T-junction ($\dot{m}_1, \dot{m}_2, \dot{m}_3, x_1, x_2, x_3$, Δp_{12}, Δp_{13}). The authors stated that three parameters were normally known in pipeline systems (e.g. $\dot{m}_1, x_1$ and Δp_{12}). The remaining five parameters became the dependent variables of the problem and five equations were needed to ensure closure. For steady state conditions, Saba and Lahey (1984) used these equations:

1. The mixture continuity equation
2. The vapour phase continuity equation
3. The main pipe mixture linear momentum equation
4. The branch tube linear momentum equation
5. Vapour phase momentum equation for the branch tube

The model of Saba and Lahey (1984) is outlined in detail in Appendix A.

The five equations can be used to solve the phase separation problem in T-junctions. However, even though the Saba and Lahey (1984) model is based on fluid mechanics of the phase separation process, the fifth equation, which constituted the closure equation, was based on low pressure bubbly/churn air/water data in 25 mm tubes ($D_1 = D_3$) and $0.3 \leq \dot{m}_3/\dot{m}_1 \leq 1.0$. The derivation of the closure equation has been criticised as not being rigourous and containing several coefficients adjusted to the authors specific data. Clearly, a careful evaluation is needed when using the model in other applications. The following Section will describe closure relations that can be used instead of the fifth equation in the Saba and Lahey (1984) model in other geometries and for lower mass take-off ratios.

2.6.2 Models for phase split in junctions with vertical branch tube

Some authors have developed correlations to describe the two-phase flow split in T-junctions with vertical branch tubes. First, Seeger et al. (1985) developed a purely empirical model which is described in Section 2.6.2.1. Smoglie et al. (1987), Maciaszek and Micaelli (1990) and Castiglia and Giardina (2002a) developed semi-empirical models taking into account the phenomena of gas-pull through and liquid entrainment. These models are outlined in Sections 2.6.2.2, 2.6.2.3 and 2.6.2.4. The branch tube vapour fraction x_3 was often expressed in terms of the ratio $r = h/h_b$, where h was the distance from the branch tube off take to the liquid interface and h_b was the corresponding critical distance at the beginning of liquid entrainment or gas pull-through (critical distance). Notations used in the following models are given in Figure 2.11. The models will be compared to the experimental data of the current project in Chapter 5.

2.6.2.1 The model of Seeger et al. (1985)

Seeger et al. (1985) proposed models for flow split in horizontal pipes with vertical upward or vertical downward branch tubes. For vertical upward branch tubes the authors recommended as a rule of thumb,

$$\frac{x_3}{x_1} = \left(\frac{\dot{m}_3}{\dot{m}_1}\right)^{-0.8} \tag{2.1}$$

Equation 2.1 was developed based on a large set of experiments with $D_1 = D_3 =$ 50 mm, $\dot{m}_3/\dot{m}_1 > 0.15$, and inlet flow conditions in the dispersed bubble, slug,

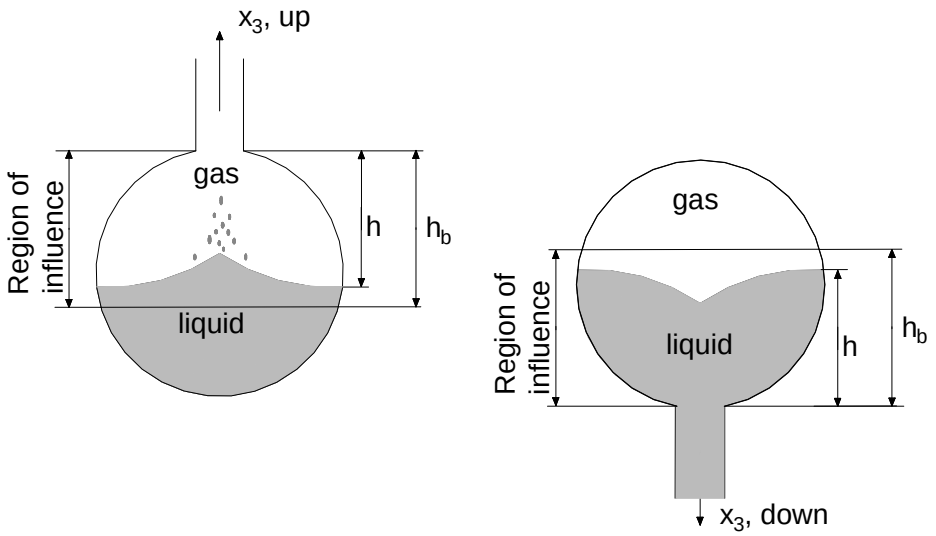

Figure 2.11: Liquid entrainment in stratified flow with upward branch tube (a) and gas pull-through in stratified flow and downward branch tube. Reproduced from Castiglia and Giardina (2002b).

stratified and annular flow regime. Equation 2.1 is not valid for low values of G_3 because in this range only gas entered the branch tube. The maximum value of G_3 with pure gas take-off was given by,

$$G_{3max,x_3=1} = 0.23A\left(gD\rho_g\left(\rho_l-\rho_g\right)\right)^{0.5} \tag{2.2}$$

with $A = 0.5$ for inlet conditions in the dispersed bubble flow regime and $A = 1$ for other inlet conditions. Similar relationships were earlier used to describe flow regime transitions in upward flow (Wallis, 1969).

To fit the experiments on downward branch tubes Seeger et al. (1986) proposed the correlation,

$$x_3/x_1 = 5\eta - 6\eta^2 + 2\eta^3 + a\eta\left(1-\eta\right)^b \tag{2.3}$$

where the parameter a was dependent on the flow regime (given in Figure 2.25 in Reimann et al. (1988)) and η was given by

$$\eta = \left(\frac{G_3}{G_1} - \frac{G_{3max,x=0}}{G_1}\right) / \left(1 - \frac{G_{3max,x=0}}{G_1}\right) \tag{2.4}$$

and

$$b = 3 + 2.2\tanh\left(0.5\left(G_{1l} - 3000\right)\right) \tag{2.5}$$

The maximum mass flux, G_{3max}, where $x_3 = 0$ was described by a relationship similar to the rise velocity of bubbles given by Wallis (1969).

$$G_{3max,x_3=0} = 0.52\rho_l^{0.5}\left(\sigma g\left(\rho_l - \rho_g\right)\right)^{0.25} \tag{2.6}$$

2.6.2.2 The model of Smoglie et al. (1987)

Based on extensive experimental measurements at the Nuclear Research Centre Karlsruhe (KfK) with air/water and steam/water at varying pressures and different diameter ratios, Smoglie et al. (1987) developed a correlation for phase distribution in upward branch tubes and smooth stratified flow at the inlet,

$$x_3 = 1 - \left(\frac{1.15}{1+\left(\rho_l/\rho_g\right)^{0.5}}\right)^{2\frac{h}{h_b}}\left[1 - \frac{1}{2}\frac{h}{h_b}\left(1+\frac{h}{h_b}\right)\left(\frac{1.15}{1+\left(\rho_l/\rho_g\right)^{0.5}}\right)^{\left(1-\frac{h}{h_b}\right)}\right]^{0.5} \tag{2.7}$$

and subsequently for downward branch tubes,

$$x_3 = 1 - \left(\frac{1.15}{1+\left(\rho_l/\rho_g\right)^{0.5}}\right)^{2.5\frac{h}{h_b}}\left[1 - \frac{1}{2}\frac{h}{h_b}\left(1+\frac{h}{h_b}\right)\left(\frac{1.15}{1+\left(\rho_l/\rho_g\right)^{0.5}}\right)^{\left(1-\frac{h}{h_b}\right)}\right]^{0.5} \tag{2.8}$$

Seeger et al. (1986) observed that below a critical height parameter, h_b (see Figure 2.11), only gas would enter in upward branch tubes and liquid in downward branch tubes. The value of h_b was proposed to be calculated using the expression from Smoglie (1984) where the correlation between the Froude number and h_b was fitted to experimental data.

$$h_b = \frac{k^* \dot{m}_{b3}^{0.4}}{\left[g\rho_b\left(\rho_l - \rho_g\right)\right]^{0.2}} \tag{2.9}$$

The parameters ρ_b and $\dot{m}_{b3}$ represented the density and the mass flow rate of the continuous phase at beginning of entrainment (gas for upward branch tube and liquid for downward branch tube). By fitting the model to experimental data, Smoglie et al. (1987) found the values for the nondimensional constant $k^* = 1.67$ for upward branch tubes. For downward branch tubes the value of k^* was found to be 2.0 and 1.17 for vortex flow and vortex-free flow, respectively. Smoglie (1984) demonstrated that vortices were rather unstable and disappeared in the case of quite small transverse liquid velocities in the main tube.

It should be noted that Smoglie et al. (1987) only considered the a range of very low liquid extraction in the upward branch tube configuration ($0.95 < x_3 < 1.0$).

2.6.2.3 The model of Maciaszek and Micaelli (1990)

Maciaszek and Micaelli (1990) developed a model for phase split in T-junctions to be used in the thermo-hydraulic code CATHARE. Following the same reasoning as Smoglie et al. (1987), they used the formulation given by Smoglie (1984), Equation 2.9, to model the critical height parameter h_b. However, data obtained by Maciaszek and Memponteil (1986) showed that for gas entrainment in downward branch tube configuration, the parameter k^* was strongly dependent upon the liquid velocity in the main pipe for $\rho_l u_{l2}^2/\rho_l u_{l3}^2 \sim 10^{-1}$. This trend was not taken into account in the Smoglie et al. (1987) model since their data were limited to $\rho_l u_{l2}^2/\rho_l u_{l3}^2 < 10^{-3}$. Maciaszek and Micaelli (1990) explained this behaviour by the balance between horizontal and vertical inertial forces, while the gas core was penetrating the liquid layer to initiate gas entrainment. This balance was characterized by the dimensionless number,

$$R = \frac{\rho_l u_{l2}^2}{\rho_l u_{l3}^2} \tag{2.10}$$

The parameter k^* in the model for beginning of gas entrainment in downward branch tubes was then fitted to the experimental data and the following formulation was obtained,

$$k^* = \left(1 - R^{0.2}\right) \tag{2.11}$$

In the case of upward branch tube configuration, Maciaszek and Micaelli (1990) used a more general formulation of Equation 2.9 from Smoglie (1984) to model the critical height for beginning of entrainment,

$$h_b = k_l^* \left[\frac{\dot{m}_{b3}^{0.4}}{g\rho_b\left(\rho_l - \rho_g\right)d^a}\right]^{\frac{1}{5-a}} \tag{2.12}$$

Fitted to data from Reimann et al. (1988) the values used were $k^* = 0.88$ and $a = 2.0$.

The phase split in case of downward branch tube was modelled by,

$$x_3 = \frac{\alpha_3}{\alpha_3 + \sqrt{\rho_l/\rho_g}\,(1-\alpha_3)} \tag{2.13}$$

where

$$\alpha_3 = \left(1 - \frac{h}{h_b}\right) \tag{2.14}$$

In case of upward branch tube geometry, Maciaszek and Micaelli (1990) developed a model that covered a wide range of branch tube vapour fractions compared to the Smoglie et al. (1987) model, which were limited to ($0.95 < x_3 < 1.0$). Maciaszek and Micaelli (1990) observed that if the distance h decreased below a critical value h_{lim}, the waves at the interface reached the branch tube entrance with a subsequently sharp increase in liquid extraction. The authors therefore distinguished the phase split model in three separate domains,

- $h < h_b$, there is no liquid entrainment, $x_3 = 0$
- $h_{lim} < h < h_b$, there is low entrainment, linear variation in x_3 between 1 and x_0 =0.98 when h decreases from h_b to h_{lim}
- $h < h_{lim}$, the entrainment rate is assumed to be given by,

$$x_3 = x_0 \frac{\alpha_3}{\alpha_3 + \sqrt{\rho_l/\rho_g}\,(1-\alpha_3)} \tag{2.15}$$

where,

$$\alpha_3 = \frac{h}{h_{lim}} \tag{2.16}$$

Maciaszek and Micaelli (1990) proposed the following correlation for h_{lim},

$$h_{lim} = 2.5 \left(\frac{d}{D}\right)^{0.666} h_b \left(1 - R^{0.15}\right) \tag{2.17}$$

where,

$$R = \frac{\rho_g u_{g2}^2}{G_{3T}^2/\rho_{3m}} \tag{2.18}$$

The parameter R was modelling the reduction of the entrainment efficiency due to the transverse flow in the main pipe.

2.6.2.4 The model of Castiglia and Giardina (2002a)

Castiglia and Giardina (2002a) introduced a new semi-empirical model, producing a single expression for the evaluation of the branch tube vapour fraction, x_3, valid both for vertically upward and downward branch tubes. The model was based on the assumption of a *region of branch interest* in the main pipe, outlined by Skorek (1995), from which the liquid and the gas phases were separated into the branch

tube. The region was bounded by the horizontal surface at a distance h_b from the branch inlet and the pipe wall (see Figure 2.11). Castiglia and Giardina (2002a) proposed an expression for the void fraction in the branch tube, α_3, dependent on the portion of vapour and liquid in the *region of branch interest*:

$$\frac{\alpha_3}{1-\alpha_3} = k' \left(\frac{h}{h_b - h} \right)^{\frac{1}{n}} \tag{2.19}$$

k and n were nondimensional constants, dependent on the orientation of the branch tube. The authors introduced a slip parameter to denote the velocity difference between the gas and liquid phase. The slip parameter was included in the new parameter k'' and Equation 2.19 was reformulated:

$$\frac{h}{h_b - h} = k'' \left(\frac{x_3}{1-x_3} \right)^{n} \tag{2.20}$$

Using Equation 2.20, the model was compared to experimental data where the liquid level in the inlet tube was measured. Table 2.2 shows the values of k'' and n fitted to data from four separate sources.

Table 2.2: Parameters in the Castiglia and Giardina (2002a) model, fitted to data from Reimann and Kahn (1984), Schrock et al. (1986), Smoglie et al. (1987) and Reimann et al. (1988).

branch tube orientation	k''	n
upward	0.62	0.30
downward	0.12	-0.65

The Castiglia and Giardina (2002a) model gave better correspondence with experimental results with downward branch tubes from Anderson and Benedetti (1986) and Maciaszek and Memponteil (1986) than the Smoglie et al. (1987) model. Using the model on data obtained in other flow regimes than stratified flow, also showed remarkably good results. The model of Castiglia and Giardina (2002a) was implemented in the multi-fluid version of the dynamic thermal-hydraulic code RELAP5 (Franchello et al., 1993).

In Castiglia and Giardina (2002b) the authors also fitted the model to experimental data with horizontal branch tubes.

2.7 Analytical models for two-phase distribution in manifolds

2.7.1 The model of Watanabe et al. (1995)

Watanabe et al. (1995) published an empirical model for the prediction of liquid and vapour distribution in an ID 20 mm manifold with four upward ID 6 mm branch tubes. A correlation for the gas extraction in the branch tube *No i* was proposed,

$$G_{g,t,i} = 6.07 G_{g,m,i} \tag{2.21}$$

According to the Watanabe et al. (1995) correlation, the gas mass flux in branch tube *No i* only depended on the gas mass flux in the manifold at the inlet of the junction *i*. The fraction of liquid taken off in the branch tube was found only to be dependent on the gas Reynolds number in the manifold at the inlet of the corresponding branch tube junction,

$$\frac{\dot{m}_{l,t,i}}{\dot{m}_{l,m,i}} = 2.74 \times 10^{-5} Re_{g,m,i} - 0.0124 \sqrt{Re_{g,m,i}} + 1.37 \tag{2.22}$$

The experimental results in the current report are compared to the model of Watanabe et al. (1995) in Chapter 5.

2.7.2 The model of Tompkins et al. (2002a)

Tompkins et al. (2002a) formulated an one-dimensional steady flow two-phase model, using a mechanical integral-type approach, which was compared to experimental data reported in Yoo et al. (2002). The two-phase void fraction model, denoted TP-a, was a modified separated flow model. In a fully separated flow model, the interfacial interactions must be considered, while in the TP-a model the void fraction correlation was used to provide information about the cross-sectional area occupied by the liquid and by the gas phase. Figure 2.12 shows the discretization of the manifold used by Tompkins et al. (2002a).

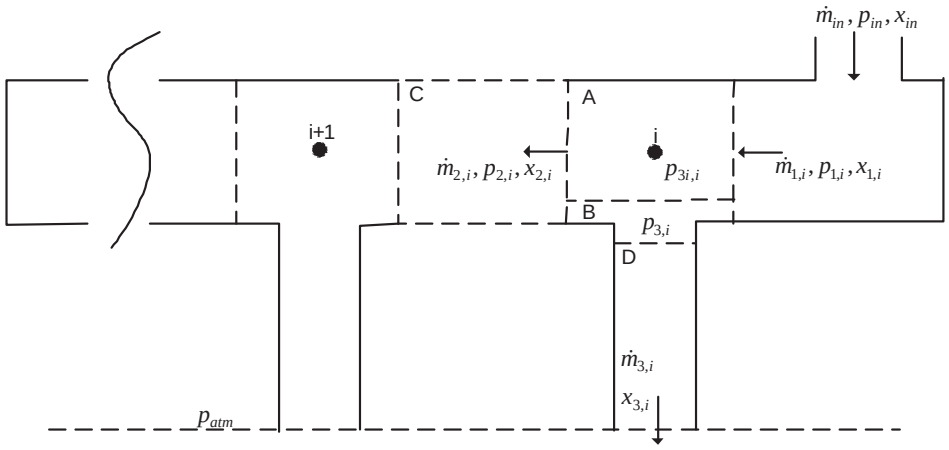

Figure 2.12: Control volume discretization used in the TP-a model of Tompkins et al. (2002a).

The two-phase flow with quantities $\dot{m}_{in}$, p_{in} and x_{in} entered the manifold and was distributed to a number of branch tubes. Four different types of control volumes *A*, *B*, *C* and *D* were used in the model (Figure 2.12). The phase separation between the manifold main flow and the branch tube occured in control volume *A*, with the imaginary junction point in the middle of the volume. The control volume *B*, with an infinitesimal height, was defined to account for the pressure drop, $p_{3i,i} - p_{3,i}$, due to the abrupt change in area from the manifold to the branch inlet. The exit pressure of all branch channels was set to p_{atm} and the resulting set of equations for all control volumes were solved simultaneously.

Following the procedure of Saba and Lahey (1984) (see Section 2.6.1 and Appendix A), five equations were used to define the flow split in control volume *A*. Instead of using a gas momentum equation for the branch tube as the closure equation (the fifth equation in the Saba and Lahey (1984) model), Tompkins et al. (2002a) used a force-momentum balance around the *entire* control volume (Bajura, 1971):

$$p_1 - p_2 = -\rho \left[u_2^2 - u_1^2 + sin(\theta) cos(\theta) u_3^2 \frac{A_3}{A_1} \right] \tag{2.23}$$

with

$$\rho = \rho_g \alpha + \rho_l (1 - \alpha) \tag{2.24}$$

θ was the angle with respect to the horizontal that the initial stream bent into

the branch tube. Tompkins et al. (2002a) used the void fraction at the inlet of the control volume to calculate the two-phase density of the volume based on the assumption that the initial void fraction would have the greatest impact on a change in mixture density, and changes in α_2 and α_3 would affect the density only to a minor degree.

An area-contraction pressure equation formulated by Giot (1981) was used for the control volume *B* in Figure 2.12, while a conventional two-phase pressure drop equation accounting for both frictional and acceleration pressure losses was used to calculate the static pressure losses in control volumes *C* and *D*.

The model was compared to experimental tests with varying manifold cross sectional area and inlet stream properties. The model predictions were quite good in some cases but produced great deviations to the sample sets in other. Especially, the ability to predict the mass flow distribution between the branch tubes was poor. ”Pressure reduction factors”, β_1, β_2 and β_3 were introduced to tune the static pressure profile in the manifold, such that the outlet mass flows were better predicted. β_1 and β_3 were correction factors applied to the branch tube linear momentum equation for control volume *A* of the first and the last tube junction in the manifold, respectively. Likewise, β_2 was a correction factor applied to control volumes of the intermediate junctions. The values of the pressure reduction factors had to be changed from test case to test case. The authors cited that a likely explanation for the need of the β-factors was the inability of the model to take into account changes in flow regimes in the manifold. Running the model without the pressure reduction factors resulted in a flat profile of the branch mass flow rates, compared to the experimental values with a sharp decrease in mass flow rate from branch 1 to branch 2 and a sharp increase in mass flow rate in the last branch.

Another challenge with the model of Tompkins et al. (2002a) was reported to be the solution procedure. Stability and convergence of the solution of the large set of equations was a problem and good initial values had to be provided.

2.8 Component design and applications to improve two-phase distribution

A number of literature references and patents are directly related to the problem of two-phase distribution in heat exchanger manifolds. The proposed concepts for reducing the penalties of two-phase maldistribution can be divided in four main groups:

- Manifold design modifications
- Phase mixing and controlled mixture distribution
- Phase separation and remixing into each branch tube
- Phase separation and liquid feeding of the evaporator

The different options for distribution improvement are shortly outlined in the next Sections, while a more detailed overview of available patents is given in Appendix B.

2.8.1 Manifold design modifications

Depending on the manifold design and the refrigerant flow conditions inside it, the manifold may be modified e.g. by inserts or geometrical modifications that facilitate the two-phase distribution. Geometrical features such as guide vanes, baffles, twisted tapes, folded strips of metal etc. may improve the two-phase distribution performance. An overview of patents aimed at improving the two-phase distribution by modifying the manifold geometry is given in Section B.1.

A homogeneous mist or dispersed droplet flow is easier to distribute than a separated vapour/liquid flow (Fei et al., 2002). The use of mixers as integrated components in the heat exchanger manifold, or placing the expansion valve at the inlet of the inlet manifold of the evaporator may therefore improve the two-phase distribution. In general, large pressure drops are needed to produce small liquid droplets and homogeneous two-phase flow. The strategy of mixing is therefore best suited for the inlet manifold, not for intermediate manifolds inside the evaporator, where pressure drops give penalties in reduced heat transfer temperature difference or increased compressor power input.

2.8.2 Phase mixing and controlled mixture distribution

One possible option for improvement of two-phase distribution is to mix the two-phase flow and then divide the homogeneous mixture into the heat exchanger branch tubes. Numerous two-phase flow distributors have been shown in the general literature and in patents. Some proposed methods for obtaining ”homogeneous distribution” can be summarized:

- Impingement at a normal angle against a surface, and radial distribution into tubes
- Flow against the tip of a cone with axis corresponding to the inlet tube axis, and into an annular space around the cone, eventually leading into distributing tubes (also denoted as the ”venturi” distributor).
- Flow into a swirl cyclone with guide vanes that distribute the two-phase flow into the branch tubes.

An overview of patents aimed at improving two-phase distribution by phase mixing and controlled mixture distribution is given in Section B.2. Some patents describing remedies for mixing two-phase flow are described in Section B.3.

2.8.3 Phase separation and remixing into each branch tube

Improved two-phase distribution can be realized by first separating the liquid and the gas and then remix the phases into each branch tube. Figure 2.13 shows a sketch of a combined separator and distributor. Slits in the branch tubes that protrude into the separator ensures quite equal distribution of the liquid phase.

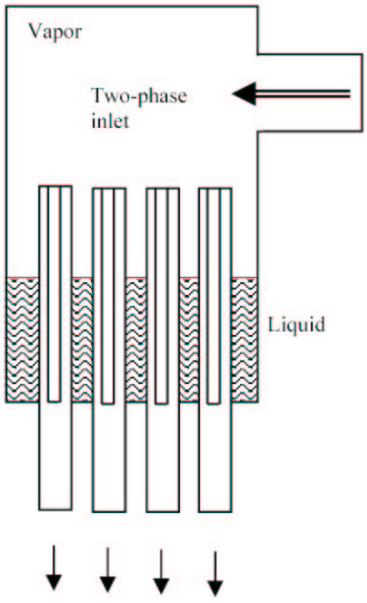

Figure 2.13: Two-phase distributor (Küba mixer - commercial product) based on phase separation and equal distribution of each phase (Hrnjak, 2003).

2.8.4 Phase separation and liquid feeding of the evaporator

Since single-phase liquid is easier to distribute homogeneously in a manifold than a two-phase flow, the evaporator may be fed with refrigerant liquid only. This can be achieved in at least two ways:

- Separation of the liquid and vapour after the expansion valve, and bypassing the flash vapour around the evaporator into the compressor suction line. Single-phase liquid is distributed in the evaporator inlet manifold.
- Cooling of the refrigerant either before expansion or after expansion, thereby establishing liquid conditions at the evaporator inlet.

Flash vapour from the expansion valve does not contribute to the refrigerating capacity in the evaporator. However, the flash vapour increases the refrigerant mass flux through the heat exchanger, which normally improves the heat transfer coefficient.

As described in Section 2.2, Beaver et al. (2000) used a separator to split the two-phase flow after the expansion valve in an air conditioning system operating with CO_2 in transcritical mode. The liquid phase was feeding the evaporator, while the vapour phase was bypassed to the outlet of the evaporator.

Hafner (2003) performed experiments on a system similar to that used by Beaver et al. (2000) and observed more uniform air outlet temperatures when the vapour bypassed the evaporator. However, no increase in system performance was observed, most likely because of the decrease in refrigerant side heat transfer coefficient due to reduced mass flux. It was noted that an increase in mass flux would be necessary to derive an advantage from the improved refrigerant distribution. This could be obtained by reducing the number of refrigerant tubes in the evaporator, or by increasing the evaporator circulation rate by a pump.

Some patents, described in Section B.4, are related to the issue of liquid feeding of the evaporator. A short description of devices for two-phase separation is also given.

Chapter 3

Experimental Methods

3.1 Chapter overview

This Chapter starts by discussing some general principles for measurement of two-phase distribution in heat exchanger manifolds. Different options described in the literature are outlined and the choice of measurement concepts for the test rig built within the current project is substantiated. Design details of the test rig and the test section are discussed. Principles of data reduction of the two-phase distribution measurements are shown and finally, uncertainty data for all test results are given.

3.2 Concepts for measuring two-phase distribution

3.2.1 Available measurement concepts

Different approaches for evaluation of two-phase distribution in heat exchanger manifolds can be used. In practice, the methods can be divided in two main groups:

Direct measurements: The two-phase flow parameters are measured by direct measurement on the refrigerant flow circuit. This implies an intrusion into the real heat exchanger geometry, to be able to measure the mass flow rate and vapour fraction in each branch tube.

Indirect measurements: The two-phase refrigerant distribution can be indirectly

evaluated by measurements on the secondary side of the heat exchanger. Measurement of wall temperatures or the secondary fluid temperature distribution at the outlet of the heat exchanger will give qualitative information of the refrigerant distribution at the primary side of the heat exchanger.

Measurement of air temperature uniformity at the outlet of a refrigerant evaporator has been used to obtain a qualitative measurement of the distribution of the refrigerant flow at the primary side of the heat exchanger by e.g. Hafner (2003) and Beaver et al. (2000). Song and Bullard (2002) observed frosting patterns as an indicator of refrigerant flow maldistribution. Thermal imaging of the heat exchanger surface could also be used to measure surface temperatures. However, as both the mass flow rate and the vapour fraction can vary between the parallel flow channels of the heat exchanger, the indirect method cannot be used to quantify the two-phase flow distribution.

The discussion of test rig principles thus becomes a matter of choosing between the options for direct measurements of two-phase flow in the heat exchanger. Alternative methods have been proposed in the literature. Bernoux (2000) measured the mass flow rate in each individual branch tube of the heat exchanger. Each branch tube was connected to individual flow circuits with condensers equipped for calorimetric measurements on the water side. In this way, both the refrigerant mass flow rate and the vapour fraction at the inlet of each branch tube could be deduced. Watanabe et al. (1995) used five parallel separators with measurement devices for both the liquid and vapour phase, to measure the two-phase distribution in an evaporator with heat load on the branch tubes. Zietlow et al. (2002) used two-phase air and water in a multiport tube manifold with nineteen parallel heat exchanger branch tubes. The water flow rate was measured in batches by load cells connected to a collection tank. The air flow rate was not measured, which means that the vapour fraction at the inlet of the branch tubes could not be calculated. Yoo et al. (2002) used refrigerant HFC-134a in a multiport tube manifold with fifteen branch tubes. They measured the liquid flow rate by using a stop watch for measurement of accumulation of liquid in separator tanks, while the vapour flow rate was measured by a flow meter. The same principle for measurement of the two-phase HFC-134a distribution in a plate heat exchanger with five branch tubes was used by Fei et al. (2002).

3.2.2 Discussion and choice of test rig principles

Some major factors influencing the choice of test rig principles for the present study can be summarized:

- A realistic heat exchanger manifold deviates significantly from the simplified designs used in most of the previous studies. Since the two-phase flow distribution is greatly affected by geometry (as shown in Chapter 2), it is important to use realistic manifold geometries and tube insert designs.
- Manifolds in real heat exchangers have both horizontal and vertical position. In horizontal position, the heat exchanger tubes can be directed both upward and downward from the manifold.
- According to T-junction literature outlined in Section 2.5, the fluid properties, especially liquid and vapour densities, are important for the behaviour of the two-phase flow distribution.
- Watanabe et al. (1995) reported that heat load on the branch tubes had significant effect on the two-phase distribution. Also, mass flow and vapour fraction at the manifold inlet were important factors affecting the distribution results.

A new concept for measurement of two-phase flow distribution was designed considering the above mentioned factors. The test rig was built with the possibility to use real refrigerant fluids, e.g. HFC-134a and CO_2, at flow rates and inlet vapour fractions encountered in mobile air-conditioning units. Due to the possible influence of the heat exchanger load on the manifold two-phase distribution, a heat exchanger test section with countercurrent water as secondary fluid was constructed. Water was chosen instead of air because of the possibility to measure the heat load (temperature and water mass flow measurements) on the secondary fluid side of each refrigerant branch tube. Watanabe et al. (1995) utilized electrical heating on the branch tubes. The use of electrical heating is a simple measurement principle, but the constant heat flux boundary condition is not quite relevant for evaporators that are heated by a fluid, as in air coolers and water chillers. The electrical heater can elevate the wall temperatures in regions of poor heat transfer to levels that are physically impossible in fluid-heated heat exchangers (Pettersen, 2002).

The test rig was designed such that different manifold geometries easily could be tested and the orientation of the test rig could be changed to measure distribution in both horizontal and vertical positions.

3.3 Description of the experimental test rig

In order to measure two-phase flow distribution under different operating conditions, an experimental test rig was built in the laboratories of the Department of

Energy and Process Engineering. This Section provides an overview of the test rig and its components.

3.3.1 Overview

Figure 3.1 shows a layout of the test rig and a description of the main components. The test rig consists of four main parts:

- Main refrigerant circuit.
- Tap-off circuit to measure the flow parameters in a single heat exchanger branch tube.
- Test section with inlet manifold and ten parallel branch tubes, which were heated by water.
- Heating water circuit.

The flow in the refrigerant loop was driven by a variable speed gear pump (1). Refrigerant flow ($\dot{m}_{mIn}$) was measured by a coriolis flow meter (2) and an electrical heater (3) was used to heat the subcooled liquid refrigerant to the desired vapour fraction at the inlet of the test section. In the inlet manifold (4) of the evaporator, the flow was divided into ten parallel branch tubes, which were heated by counter-flowing water in double-tube jackets. The refrigerant flow in a single tube in the evaporator could be redirected by three-way valves (5) to the outlet manifold of the tap-off circuit (9). The refrigerant in the tap-off circuit was condensed in the condenser (11), and the mass flow ($\dot{m}_{t,i}$) was measured by a coriolis flow meter (12). The heat added to the water in the condenser was calculated using the temperature difference ($T_{w,cOut} - T_{w,cIn}$) and the water mass flow rate ($\dot{m}_{w,c}$), which was measured by a coriolis mass flow meter (13). The main refrigerant flow was condensed in the main condenser (8), before it was mixed with the tap-off flow and led back to the pump (1). The operating pressure in the refrigerant loop was controlled by regulating the pressure in the refrigerant tank (19). A constant water flow through a water heated coil inside the tank was used to heat the refrigerant liquid in the tank. A regulator, operating on the tank pressure, was attached to a 2 kW electrical heater (20) on the inlet water stream. A constant refrigerant condensation was provided by a cooling coil on the outside of the gas filled top of the tank. By this control system, the refrigerant pressure could be adjusted with a tolerance of ± 1 kPa.

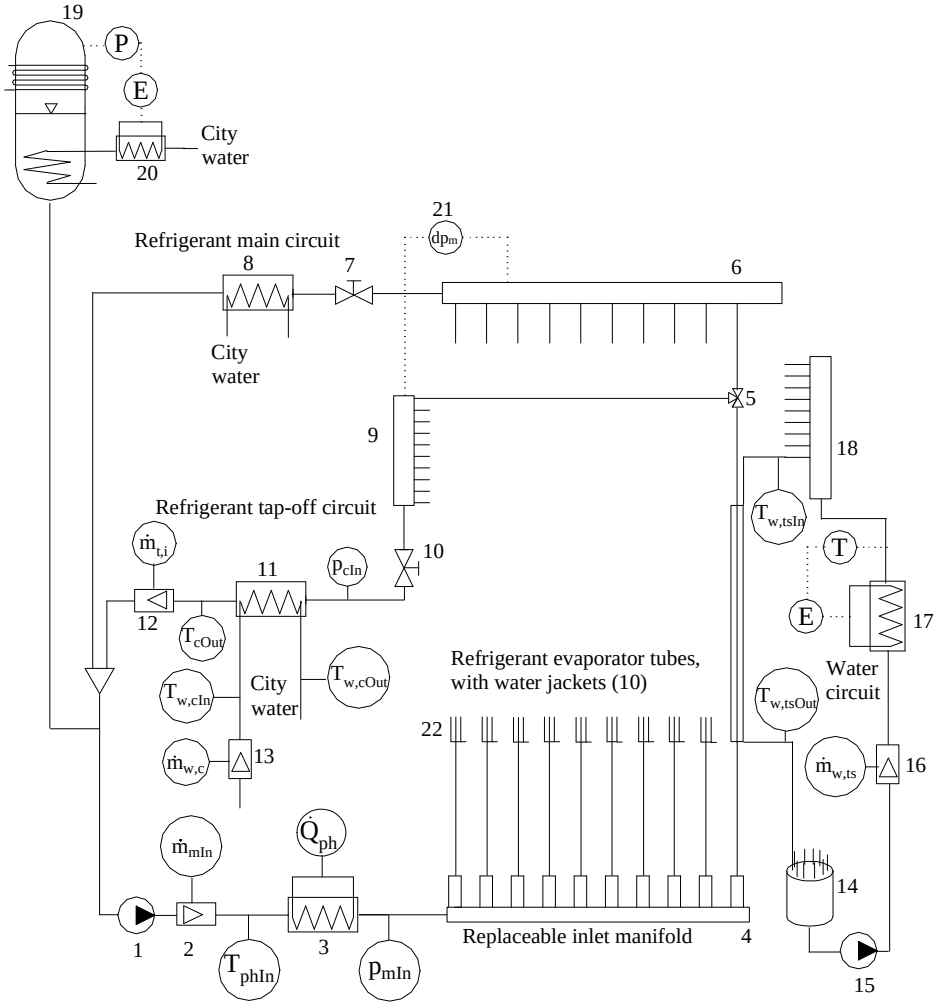

1 Refrigerant pump	12 Tap-off mass flow meter
2 Mass flow meter	13 Water mass flow meter
3 Electrical preheater	14 Water tank
4 Inlet manifold	15 Water pump
5 Three-way valves (10)	16 Water mass flow meter
6 Main outlet manifold	17 Electrical water heater
7 Valve	18 Water inlet manifold
8 Main condenser	19 Refrigerant tank
9 Tap-off outlet manifold	20 Electrical water heater
10 Valve	21 Differential pressure cell
11 Tap-off condenser	22 Water jackets (10)

Figure 3.1: Schematic diagram of the experimental apparatus with main instrumentation locations.

3.3.2 Evaporator test section

The test section consisted of an inlet manifold (4) and ten parallel 4 mm inner diameter (ID) evaporator tubes (Figure 3.3.2). Section 4.1.1 contains a description of the different manifold geometries used in the present study. Couplings between the manifold and the test section heat transfer tubes made it possible to change the orientation of the manifold. Measurements were conducted with horizontal manifold, and vertical upward and downward heat exchanger tubes.

The evaporator tubes were heated with water flowing counter-currently in an annulus outside the refrigerant tube. A 0.9 mm wire was coiled outside the refrigerant tubes to ensure that the water flow was distributed equally around the circumference of the tube. The total water flow ($\dot{m}_{w,ts}$), measured with the coriolis flow meter (16), was divided in a manifold (18) into the ten annuli outside the refrigerant tubes (22). The portion of the total flow in each annuli was found by calibration measurements (described in Appendix C). The measured water temperature difference ($T_{w,tsIn} - T_{w,tsOut}$) was used in the calculation of the heat transfer in each evaporator section.

At the outlet of each evaporator tube, there was a three-way valve (7), which allowed one tube at a time to be redirected to the separate tap-off circuit. The pressure drops in the symmetric three-way valves were equal when the flow was diverted in either of the two directions. Pressure taps were mounted on the two outlet manifolds to measure the differential pressure (21). This differential pressure was used to adjust the mass flow in the tap-off circuit. Due to unsteadiness of the two-phase flow, time-averaged measurements had to be used. For a measurement series at a single operating condition, one time-averaged measurement was taken for each tube redirected to the tap-off circuit. The measurements were taken when the time-averaged differential pressure between the outlet manifolds had been adjusted to approximately zero by the manually controlled needle valve (10). When the pressures in the two outlet manifolds were equal, the mass flow in the tube directed to the tap-off circuit was taken to be equal to the mass flow in the tube when it was connected to the main outlet manifold. Mass and phase continuity balances over the inlet manifold were used to check the uncertainty in the measurement procedure (see Section 3.7).

The inlet pipe to the manifold had the same diameter as the manifold and had a length of 250 mm between a horizontal 90° bend and the first heat exchanger tube. In this way, fully developed flow at the inlet of the manifold was obtained. However, some results are reported using a shorter inlet tube to quantify the effect of the inlet flow pattern on two-phase distribution in the manifold (Chapter 4).

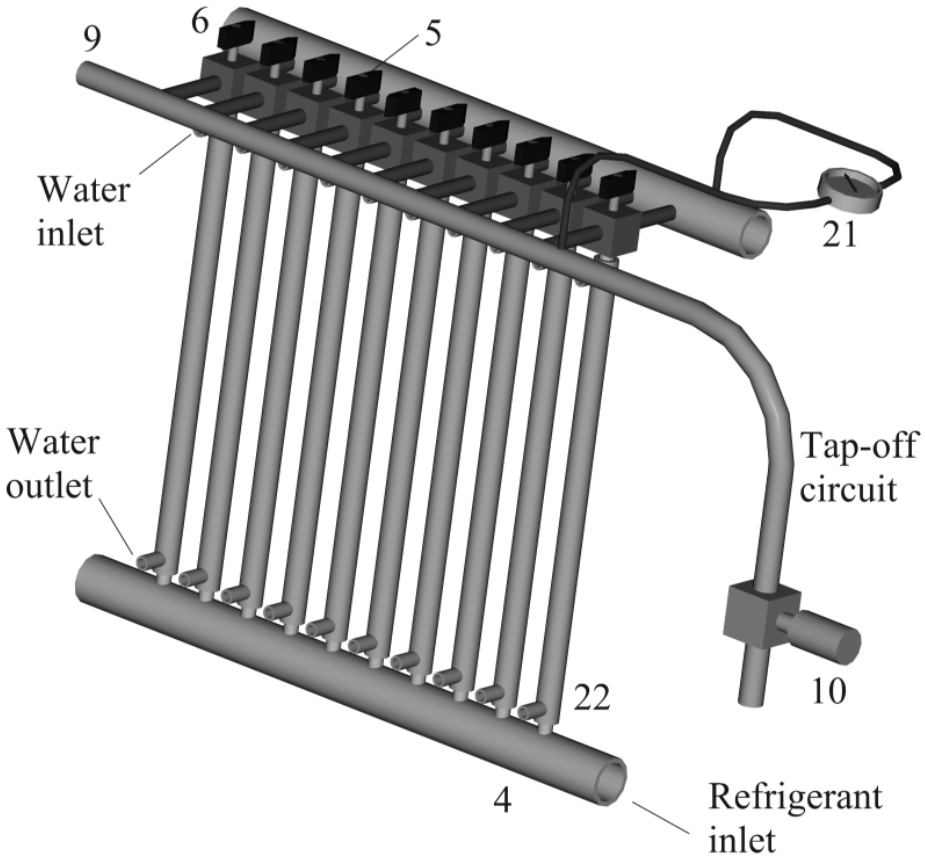

4 Inlet manifold
5 Three-way valves
6 Main outlet manifold
9 Tap-off outlet manifold
10 Needle valve
21 Differential pressure cell
22 Water jackets

Figure 3.2: Simplified drawing of the test section with the principles of two-phase flow distribution measurements.

Initially, the test section could be rotated, such that the flow in the tubes could be horizontal, vertical downward or vertical upward. Because of the 0.9 m length of the test section, the pressure in the outlet manifolds fluctuated very much when the test section was placed in vertical position due to interaction between gravity and friction in the two-phase flow in the parallel vertical channels. It was therefore necessary to permanently fix the evaporator tubes in horizontal position and use 90° elbows from the inlet manifold to the evaporator tubes. For the MPE tube manifolds, the 90° turn was combined with the coupling as shown in e.g. Figure 4.3.

3.3.3 Refrigerant fluid

The fluids utilized in the framework of this study were CO_2 and HFC-134a. Today, HFC-134a is commonly used in refrigeration and air-conditioning systems. The evaporation temperature of these systems varies greatly, dependent on the application. Changes in evaporation temperature gives corresponding changes in physical properties of the fluid, which could influence the two-phase distribution in the inlet manifold. CO_2 is receiving growing attention as an efficient and environmentally safe refrigerant.

The saturation temperature at the inlet of the test section was limited by the operational limits of the test rig. Especially the temperature of the cooling water in the condenser restricted the condensing temperature of the refrigerant. From initial experiments it was found that the condensing temperature had to be kept above 15°C (cooling water temperature: 5-7°C). To obtain stable regulation of the pressure at the test section with the needle valve (10) a total pressure drop of at least 2.5 bar from the test section inlet to the outlet of the condenser had to be maintained. This implied a saturation pressure of 55.6 bar (18.7°C) for CO_2 and 7.6 bar (29.5°C) for HFC-134a. For CO_2 it was not possible to increase the pressure to obtain variations in fluid properties because of the maximum design pressure of the test rig (70 bar). Also, the plastic tubing in the water circuit restricted the temperature level on the high temperature side of the test rig. It was therefore decided to keep the saturation pressure of the refrigerant constant and use the difference in physical properties between CO_2 and HFC-134a as basis for an evaluation of the effect of fluid physical properties on two-phase distribution.

3.3.4 Water circuit

The flow in the water circuit was driven by a centrifugal GRUNDFOS CHI2-30 water pump (15) with a capacity of 30 litres per minute at 0.6 MPa differential pressure. The pump was driven by a 220 V AC motor. Two valves in the water circuit, one in the main cycle and one in a bypass circuit were used to control the mass flow of water to the test section. Before entering the test section, the water was heated using a 6 kW Sønnico electrical heater (17). The power input to the heater was adjusted from 0 V to 230 V by a West Regulator operating on the water outlet temperature.

3.3.5 Preheater

An electrical heater (3) was used to heat the subcooled liquid refrigerant to the desired state at the inlet of the test section. A 10 meter long Philips SEI 30-1000 heating cable was wrapped bifilar around a 12 mm OD inner tube, which had a length of 1.2 metres. The refrigerant was flowing over the heating cable restricted by a ID 19 mm outer tube. The heating cable had a resistance of 14 Ω/meter, and a total heating capacity of 4.4 kW. The power was adjusted by a 0-220 V variable voltage transformer (variac). A type K thermocouple, connected to a thermostat, was mounted close to the heating cable at the refrigerant outlet of the heater to prevent overheating.

3.3.6 Refrigerant condensers

The refrigerant condensers (8) and (11) were tube-in-tube heat exchangers, with refrigerant flowing in the inner tube and water flowing in the annulus. The main circuit condenser (8) had an ID/OD 12/15 mm inner tube and an ID/OD 25/29 mm outer tube, while the tap-off circuit condenser (11) had an ID/OD 7/10 mm inner tube and an ID/OD 20/24 mm outer tube. A 4 mm wire was spun with 100 mm pitch on the inner tube in order to maintain a spacing in the annulus. The total length of the heat exchangers were 18 and 12 m, respectively. The tubes were coiled in units with a diameter of 500 mm.

3.3.7 Refrigerant pump

The flow in the loop was driven by a variable speed gear pump (MICROPUMP P220). The pump was powered by a motor, which was digitally controlled using an AC inverter. The number of revolutions could be varied between 500 and 2850 rpm. The maximum capacity of the pump was 5.0 litres per minute, at a differential pressure of 0.3 MPa. Unlike a compressor, the gear pump required no lubrication. Hence, the loop could be operated oil-free.

3.4 Instrumentation

To evaluate the two-phase distribution in the inlet manifold of the test rig, it was necessary to measure temperatures, pressures, mass flow rates and electrical power input. All data were logged and processed. This Section describes the instruments used and their uncertainties. Instrument uncertainties are based on calibration data or manufacturer data, and include uncertainty of the sensor, logger and reference. The uncertainties in Table 3.1 represents $\pm 2\sigma$ (with a confidence interval of 95%). Combined uncertainties in calculated values are discussed in Section 3.6.

3.4.1 Temperature

All temperature measurements in this study were measured with Thermocoax thermocouples type E (Chromel/Constantan). Crushed ice in thermos flasks was used as reference temperature for the measurements. In the refrigerant cycle the thermocoax elements had a diameter of 0.5 mm, and were placed in cannula tubes. In the water circuit, elements with a diameter of 1.0 mm were used. The elements were wetted along a length of about 10 cm, thus minimizing the effect of heat conduction from the environment. The thermocouples were shielded against electromagnetical interference.

3.4.2 Pressure

Absolute pressures in the refrigerant loop were measured with Honeywell type STG150C pressure transducers in the HFC-134a experiments. In the CO_2 experiments, pressure transducers of type DRUCK-PTX510 were utilized. The most

Table 3.1: Test rig instrumentation summary.

Location	Type of instrument	Fig 3.1	Uncertainty (2σ)
Electric power, preheater	Watt transducer, DEIF A/S TAP-210DG/3	$\dot{Q}_{ph}$	$\pm$14.1W
Refrigerant temperature, preheater inlet	Thermocouple type E, 0.5 mm	T_{phIn}	$\pm$0.1 K
Refrigerant temperature, tap-off condenser outlet	Thermocouple type E, 0.5 mm	T_{cOut}	$\pm$0.1 K
Water temperature, tap-off condenser inlet	Thermocouple type E, 1 mm	$T_{w,cIn}$	$\pm$0.1 K
Water temperature, tap-off condenser outlet	Thermocouple type E, 1 mm	$T_{w,cOut}$	$\pm$0.1 K
Water temperature, test section inlet	Thermocouple type E, 1 mm	$T_{w,tsIn}$	$\pm$0.1 K
Water temperature, test section outlet	Thermocouple type E, 1 mm	$T_{w,tsOut}$	$\pm$0.1 K
Refrigerant pressure, test section inlet, HFC-134a	Gauge pressure transmitter, Honeywell STG150C	P_{mIn}	$\pm$10.0 kPa
Refrigerant pressure, tap-off condenser inlet, HFC-134a	Gauge pressure transmitter, Honeywell STG150C	P_{cIn}	$\pm$10.0 kPa
Refrigerant pressure, test section inlet, CO_2	Gauge pressure transmitter, DRUCK-PTX510	P_{mIn}	$\pm$15.0 kPa
Refrigerant pressure, tap-off condenser inlet, CO_2	Gauge pressure transmitter, DRUCK-PTX510	P_{cIn}	$\pm$15.0 kPa
Manifold differential pressure	Differential pressure transducer, Siemens 7MF4432	dp_m	$\pm$0.15% of reading
Mass flow refrigerant, test section inlet	Coriolis type, Rheonik	$\dot{m}_{mIn}$	$\pm$0.2% of reading
Mass flow refrigerant, tap-off circuit	Coriolis type, Rheonik	$\dot{m}_{t,i}$	$\pm$0.2% of reading
Mass flow water, tap-off condenser	Coriolis type, Rheonik	$\dot{m}_{w,c}$	$\pm$0.2% of reading
Mass flow, water circuit	Coriolis type, Rheonik	$\dot{m}_{w,ts}$	$\pm$0.2% of reading

important pressure measurement was at the inlet of the test section. The primary purpose of this transducer was to verify agreement between the measured temperature and the saturation temperature based on the pressure measurement. During single-phase testing, this temperature sensor was also used to compute the refrigerant enthalpy from the equations of state. The pressure transducers were calibrated to the accuracy shown in Table 3.1. Uncertainty in the reference measurement and the logger was included in the total measurement uncertainty.

The pressure difference between the two outlet manifolds (dp_m) and the pressure difference between test section inlet and outlet (not shown in Figure 3.1) were measured with Siemens Smart transducers (7MF4432).

All pressure taps were mounted vertically on the test rig tubing. Tubing to the differential pressure cells was heated by an electrical heating cable to ensure single-phase vapour and hence avoid error in pressure measurements due to liquid columns.

3.4.3 Electric power

The electrical power input to the refrigerant preheater was measured using two TAP-210DG/3 watt transducers from DEIF A/S. The power input was regulated by a variable resistance (variac). The uncertainty in the power transducers was factory estimated at 0.5% of the range.

3.4.4 Mass flow

The refrigerant mass flow in the main circuit was measured with a coriolis mass flow meter Rheonik RHE 04, while the flow in the tap-off circuit was measured by Rheonik RHM 015 GET. The water circuit mass flow was measured using a Rheonik RHE 06, and a Rheonik RHE 04 was used on the tap-off circuit condenser. The mass flow meters were connected to Rheonik RHE 08 signal converters. The manufacturer specified the accuracy of the flow meters to $\pm$0.2% of reading (within the range 1:20).

3.4.5 Data logging and processing

The data were processed using a High Performance 6-1/2 digit multimeter with a forty channel multiplexer module. The Multiplexer changed between the differ-

ent input channels, while the multimeter measured the voltage, digitized it, and transferred the results to a Personal Computer. The precision of the multimeter measurements was $\pm 1 \mu V$.

The PC processed the data using the program Benchlink Data Logger v. 1.4 from Agilent Technologies, Inc. It converted the voltage and current signals to physical quantities. Dynamic time-charts and tables were used by the operator to monitor the experiments in real time. Data series were saved to text formatted files for further processing.

A dedicated program, written in Fortran90, was developed to analyse the data from the experiments. The data reduction procedures outlined in Section 3.5, mass and energy balance checks described in Section 3.7 and the reduction of the manifold flow data for the analysis described in Chapter 5 were all conducted in the program. Thermodynamic and transport properties of CO_2, HFC-134a and water were calculated using the inhouse thermodynamic property library RnLib. The thermodynamic properties of CO_2 were calculated based on the IUPAC-76 Equation of State presented by Angus et al. (1976) with the extensions by Pitzer and Schreiber (1988). Viscosity and thermal conductivity data for CO_2 were calculated based on Fenghour et al. (1998) and Vesovic et al. (1990), respectively. A detailed analysis of the accuracy of these sources are given by Skaugen (2002). Thermodynamic data for HFC-134a were calculated by the Martin-Hou equation of state with parameters given in product brochures from Genetron (Allied-Signal). Transport properties were calculated by correlations given in Reid et al. (1987).

3.5 Data reduction

Measured data from the experiments were logged and processed as explained in Section 3.4.5. Measurements were obtained at given nominal refrigerant mass flow rate and vapour fraction (fixed preheater power input), and fixed water circuit temperature at the inlet of the test section. Some simple calculations were necessary to provide the relevant variables to characterize the two-phase distribution in the manifold, which were the mass flow rate of each phase at the inlet of the test section and at the inlet of each branch. In addition to the measured mass flow rates, the vapour fractions are needed to calculate the flow rate of each phase. The measured values, which provided the basis for the data reduction can be summarized:

- Refrigerant total mass flow rate, $\dot{m}_{mIn}$
- Preheater power input, E_1
- Water circuit mass flow rate, $\dot{m}_{w,ts}$
- Water circuit test section inlet and outlet temperatures, $T_{w,tsIn}$ and $T_{w,tsOut}$
- Refrigerant temperature at inlet of preheater, T_{phIn}
- Refrigerant temperature at outlet of tap-off condenser, T_{cOut}
- Refrigerant tap-off circuit mass flow rate, $\dot{m}_{t,i}$
- Condenser water mass flow rate, $\dot{m}_{w,c}$, and inlet/outlet temperatures, $T_{w,cIn}/T_{w,cOut}$

3.5.1 Manifold inlet vapour fraction

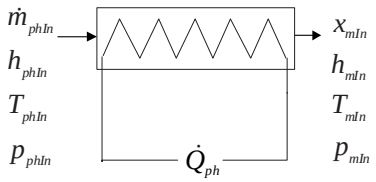

Figure 3.3: Notation for the refrigerant flow at preheater inlet and outlet. phIn: preheater inlet, mIn: manifold inlet.

The refrigerant always entered the preheater, shown in Figure 3.3, in a subcooled liquid state. Based on the available temperature and pressure measurements, the liquid enthalpy was calculated using the following expression from Moran and Shapiro (1993),

$$h_{phIn} = h_l^{sat}\left(T_{phIn}\right) + v_l^{sat}\left(T_{phIn}\right)\left(P_{phIn} - P^{sat}\left(T_{phIn}\right)\right) \tag{3.1}$$

A heat balance for the refrigerant side in the preheater provided the following:

$$\dot{Q}_{ph} = \dot{m}_{mIn}\left(h_{mIn} - h_{phIn}\right) \tag{3.2}$$

Heat leakage through the thermal insulation was not included for the preheater. The refrigerant saturation temperature in the preheater was close to the environment temperature, nominally 17°C for CO_2 and 27°C for HFC-134a, giving a

maximum estimated heat loss of 10 W (less than 0.3% of preheater power). Calibration tests with single-phase flow through the preheater supported the assumption of absence of heat loss. The refrigerant enthalpy at the inlet of the test section was calculated:

$$h_{mIn} = h_{phIn} + \frac{\dot{Q}_{ph}}{\dot{m}_{mIn}} \tag{3.3}$$

The vapour fraction at the test-section inlet could then computed:

$$x_{mIn} = \frac{h_{mIn} - h_l^{sat}(T_{mIn})}{h_{lg}(T_{mIn})} \tag{3.4}$$

3.5.2 Branch tube inlet vapour fraction

To calculate the vapour fraction at the inlet of the branch tube directed to the tap-off circuit, the following procedure was used:

- Calculate the refrigerant enthalpy at the inlet of the tap-off condenser, h_{cIn}, based on an energy balance between the water and the refrigerant side of the condenser.
- Calculate tap-off circuit refrigerant enthalpy at outlet of the test section, h_{tsOut}, based on h_{cIn} and estimated tubing heat leakage, $\dot{Q}_{leak,t}$.
- Calculate refrigerant vapour fraction at the inlet of the branch tube, $x_{t,i}$, based on an energy balance between the water and the refrigerant side of the evaporator tube.

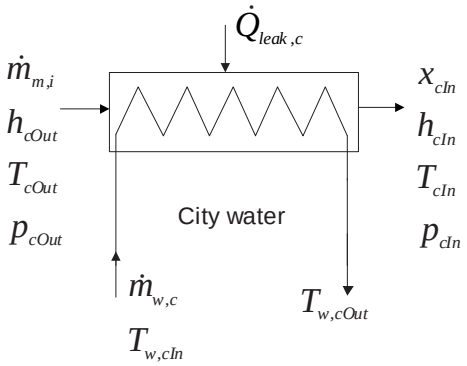

Figure 3.4: Notation for the refrigerant and water flows at inlet and outlet of tap-off circuit condenser.

The energy balance around the tap-off circuit condenser, shown in Figure 3.4, provided the following expression

$$\dot{m}_{w,c} c_{p,w} \left(T_{w,cOut} - T_{w,cIn}\right) = \dot{Q}_{leak,c} + \dot{m}_{t,i} \left(h_{cIn} - h_{cOut}\right) \tag{3.5}$$

where $\dot{Q}_{leak,c}$ is the heat leakage from the environment into the condenser. The water was flowing in the outside annulus of the double tube condenser and would always have a temperature below the environment temperature. The heat loss from the environment to the water was estimated based on single-phase refrigerant calibration measurements outlined in Appendix C. The water specific heat capacity was calculated by Equation 3.6. The use of an average value of $c_{w,p}$ is justified because of the linearity of the $c_{w,p}(T)$ function. The error in this approximation is clearly less than 0.1% of transferred heat to the water flow.

$$c_{p,w} = \left(c_{p,w}\left(T_{w,in}\right) + c_{p,w}\left(T_{w,out}\right)\right)/2 \tag{3.6}$$

To ensure single-phase liquid at the outlet of the condenser, the refrigerant was subcooled with a minimum of 5 K. Hence, the refrigerant enthalpy at the outlet of the condenser, h_{cOut}, could be determined using measured single-phase liquid properties (see Equation 3.1). The refrigerant enthalpy at the inlet of the condenser could then be calculated:

$$h_{cIn} = \frac{\dot{m}_{w,c} c_{p,w} \left(T_{w,cOut} - T_{w,cIn}\right) - \dot{Q}_{leak,c}}{\dot{m}_{t,i}} + h_{cOut} \tag{3.7}$$

In some experiments, the temperature of the refrigerant at the outlet of the test section could be up to 30 K above environment temperature. It was therefore necessary to take into account the heat leakage through the thermal insulated pipe connecting the test section and the tap-off circuit condenser, $\dot{Q}_{leak,t}$. As for the tap-off circuit, the heat leakage was estimated based on the single-phase calibration measurements outlined in Appendix C. The refrigerant enthalpy at the outlet of the test section, see Figure 3.5, could then be calculated:

$$h_{tsOut} = h_{cIn} + \frac{\dot{Q}_{leak,t}}{\dot{m}_{t,i}} \tag{3.8}$$

An energy balance for the single evaporator branch tube in the test section connected to the tap-off circuit gave

$$\dot{m}_{w,ts,i} c_{p,w} \left(T_{w,tsIn,i} - T_{w,tsOut,i}\right) = \dot{Q}_{leak,ts} + \dot{m}_{t,i} \left(h_{tsOut} - h_{t,i}\right) \tag{3.9}$$

where $h_{t,i}$ is the enthalpy at the inlet of branch tube *No i*. The water, flowing in the outside annulus of the evaporator tube, always had a temperature above

the environment temperature. The heat leakage to the environment was estimated based on single-phase refrigerant experiments outlined in Appendix C. The water flow rate in test section tube *No i* was calculated based on the measured total water mass flow rate, $\dot{m}_{w,ts}$, and calibration factors for the distribution of the total flow to the ten parallel evaporator circuits. The measurements that were used to obtain the calibration factors are outlined in Appendix C.

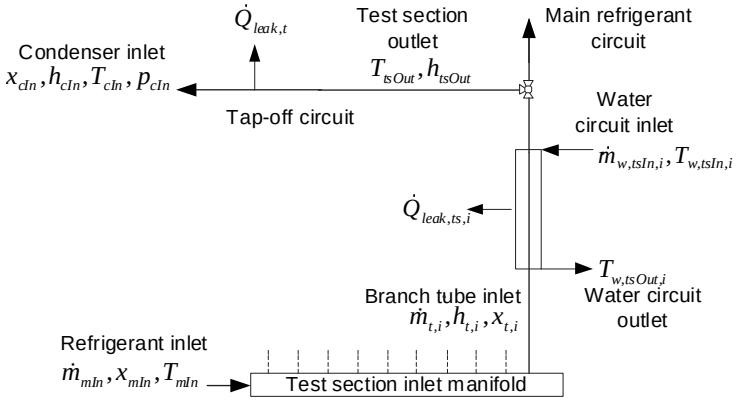

Figure 3.5: Notation for the refrigerant and water flows at inlet and outlet of test section branch tube *No i*.

Having obtained the enthalpy at the inlet of the branch tube, $h_{t,i}$, the corresponding vapour fraction, $x_{t,i}$ could be calculated similarly to Equation 3.4. Combined with Equations 3.7, 3.8 and 3.9, the branch tube inlet vapour fraction, $x_{t,i}$, could be expressed solely as a function of measured properties and properties calculated from calibration measurements ($\dot{m}_{w,ts,i}$, $\dot{Q}_{leak,c}$, $\dot{Q}_{leak,t}$ and $\dot{Q}_{leak,ts,i}$):

$$\begin{aligned} x_{t,i} &= \frac{\dot{m}_{w,c} c_{p,w} \Delta T_{w,c} - \dot{Q}_{leak,c} + h_{cOut} \dot{m}_{t,i} + \dot{Q}_{leak,t}}{h_{lv}(T_{mIn})\, \dot{m}_{t,i}} \\ &+ \frac{\dot{Q}_{leak,ts,i} - \dot{m}_{w,ts,i} c_{p,w} \Delta T_{w,ts,i} - h_l^{sat}(T_{mIn})\, \dot{m}_{t,i}}{h_{lv}(T_{mIn})\, \dot{m}_{t,i}} \end{aligned} \tag{3.10}$$

where,

$$\Delta T_{w,c} = (T_{w,cOut} - T_{w,cIn}) \tag{3.11}$$

and

$$\Delta T_{w,ts,i} = (T_{w,tsIn,i} - T_{w,tsOut,i}) \tag{3.12}$$

3.6 Uncertainty analysis

3.6.1 General

Uncertainties in the experimental data were calculated using the method described by Moffat (1988). A repeated reading with the same procedure and equipment does not provide a multi-sample result (ASHRAE, 1986). The results were therefore regarded as single-sample. The method estimated the uncertainty in a variable y that depended on N independent variables, x_i, with uncertainties δx_i. The equation for the uncertainty in y, δy, was then given by:

$$\delta y = \sqrt{\sum_{i=1}^{N} \left(\frac{\partial y}{\partial x_i} \partial x_i \right)^2} \tag{3.13}$$

The uncertainty of each measured quantity consisted of the uncertainty of the measurement device, the uncertainty of the data-acquisition system, interactions between the sensor and the experimental system and conceptual errors. Two uncertainties were of particular interest in the present study: (1) the uncertainty in the vapour fraction at the inlet of the manifold, and (2) the uncertainty of the vapour fraction in the inlet of the separate branch tubes. In addition, the uncertainty in the pressure regulation between the two outlet manifolds, in order to regulate the individual branch tube mass flow rates, is of importance and will be discussed in Section 3.7.

3.6.2 Uncertainty in manifold inlet vapour fraction

For the two-phase flow distribution measurements, the vapour fraction at the inlet of the manifold was calculated using the Equation 3.4. Factors that contribute to uncertainty in this calculation, ranked in approximate order of importance, are listed below:

- Preheater power measurement
- Refrigerant flow measurement
- Refrigerant saturation pressure measurement
- Refrigerant liquid temperature measurement

The root sum square method of combining the uncertainty components minimizes the effect of small uncertainties relative to larger contributions. Second-order effects was therefore neglected in the uncertainty calculations. Following Equation 3.13, the uncertainty in the preheater inlet single-phase liquid enthalpy was given by:

$$\delta h_{phIn} = \left[\left(\frac{\partial h_{phIn}}{\partial P_{phIn}} \delta P_{phIn} \right)^2 + \left(\frac{\partial h_{phIn}}{\partial T_{phIn}} \delta T_{phIn} \right)^2 \right]^{1/2} \tag{3.14}$$

The sensitivity coefficients ($\partial h/\partial P$ and $\partial h/\partial T$) were found by perturbing the input data to the thermodynamic property functions. Uncertainty in the specific liquid volume due to temperature measurement was omitted in the uncertainty calculation. Table 3.2 shows calculated uncertainty in enthalpy at the inlet of the preheater at typical temperature and pressure levels used in the reported experiments.

Table 3.2: Uncertainty in preheater inlet liquid enthalpy.

	HFC-134a	CO_2
δh_{phIn}	$\pm$ 135 J/kg	$\pm$ 254 J/kg

The uncertainty in CO_2 liquid enthalpy is larger than the uncertainty in the HFC-134a value because of the larger enthalpy differential ($\delta h/\delta T$) at the liquid saturation line, which gives larger deviation in calculated saturated liquid enthalpy for a constant temperature measurement error. The uncertainty in the enthalpy at the test section inlet, calculated by Equation 3.3, was then given by:

$$\delta h_{mIn} = \left[\delta h_{phIn}^2 + \left(\frac{\partial h_{mIn}}{\partial \dot{Q}_{ph}} \delta \dot{Q}_{ph} \right)^2 + \left(\frac{\partial h_{mIn}}{\partial \dot{m}_{mIn}} \delta \dot{m}_{mIn} \right)^2 \right]^{1/2} \tag{3.15}$$

The vapour fraction at the test section inlet, given by Equation 3.4, then had a corresponding uncertainty:

$$\delta x_{mIn} = \left[\left(\frac{\partial x_{mIn}}{\partial h_{mIn}} \delta h_{mIn} \right)^2 + \left(\frac{\partial x_{mIn}}{\partial T_{mIn}} \delta T_{mIn} \right)^2 \right]^{1/2} \tag{3.16}$$

The differential $\partial x/\partial T$ was found by perturbing the input data to the thermodynamic property functions. Tables 3.3 and 3.4 show calculated uncertainties in the manifold inlet vapour fraction at varying preheater heat load and refrigerant

mass flow rate (covering the range of measurements) for HFC-134a and CO_2, respectively. Uncertainties in the measurements of preheater heat load ($\pm$14.1 W), temperature ($\pm$0.1°C) and refrigerant mass flow rate($\pm$0.2%) were taken from Table 3.1.

Table 3.3: Uncertainty in test section inlet vapour fraction, HFC-134a.

$\dot{m}_{mIn}$, kg/s	0.025	0.033	0.0417
$\dot{Q}_{ph}$ =1.0 kW		$\pm$ 0.0028	
$\dot{Q}_{ph}$ =2.5 kW	$\pm$ 0.0036	$\pm$ 0.0028	$\pm$ 0.0023
$\dot{Q}_{ph}$ =4.0 kW		$\pm$ 0.0030	

Table 3.4: Uncertainty in test section inlet vapour fraction, CO_2.

$\dot{m}_{mIn}$, kg/s	0.025	0.033	0.0417
$\dot{Q}_{ph}$ =1.0 kW		$\pm$ 0.0038	
$\dot{Q}_{ph}$ =2.5 kW	$\pm$ 0.0041	$\pm$ 0.0034	$\pm$0.0031
$\dot{Q}_{ph}$ =4.0 kW		$\pm$ 0.0035	

3.6.3 Uncertainty in branch tube inlet vapour fraction

The uncertainty in the branch tube inlet vapour fraction $x_{t,i}$, computed using Equation 3.10, was given by:

$$\begin{aligned}\delta x_{t,i}^2 = &\left(\frac{\partial x_{t,i}}{\partial \dot{m}_{w,c}}\delta\dot{m}_{w,c}\right)^2 + \left(\frac{\partial x_{t,i}}{\partial \Delta T_{w,c}}\delta\Delta T_{w,c}\right)^2 + \left(\frac{\partial x_{t,i}}{\partial \dot{Q}_{leak,c}}\delta\dot{Q}_{leak,c}\right)^2 \\ &+ \left(\frac{\partial x_{t,i}}{\partial h_{cOut}}\delta h_{cOut}\right)^2 + \left(\frac{\partial x_{t,i}}{\partial \dot{m}_{t,i}}\delta\dot{m}_{t,i}\right)^2 + \left(\frac{\partial x_{t,i}}{\partial \dot{Q}_{leak,t}}\delta\dot{Q}_{leak,t}\right)^2 \\ &+ \left(\frac{\partial x_{t,i}}{\partial \dot{Q}_{leak,ts,i}}\delta\dot{Q}_{leak,ts,i}\right)^2 + \left(\frac{\partial x_{t,i}}{\partial \dot{m}_{w,ts,i}}\delta\dot{m}_{w,ts,i}\right)^2 \\ &+ \left(\frac{\partial x_{t,i}}{\partial \Delta T_{w,ts,i}}\delta\Delta T_{w,ts,i}\right)^2 + \left(\frac{\partial x_{t,i}}{\partial \Delta T_{mIn}}\delta\Delta T_{mIn}\right)^2\end{aligned} \tag{3.17}$$

where

$$\delta\Delta T = \sqrt{2}\delta T \tag{3.18}$$

The uncertainty in the calculation of the specific heat of water, $c_{p,w}$, was omitted due to infinitesimal impact on the overall calculation of $\partial x_{t,i}$. By evaluating the

partial derivatives in Equation 3.17 and by using the uncertainties in Table 3.1, the uncertainty in $x_{t,i}$ could be computed. The sensitivity coefficient with regard to the condenser water flow rate, $\partial x_{t,i}/\partial \dot{m}_{w,c}$ was dependent upon the water temperature difference as seen in:

$$\frac{\partial x_{t,i}}{\partial \dot{m}_{w,c}} = \frac{c_{p,w}\Delta T_{w,c}}{h_{lv}(T_{mIn})\,\dot{m}_{t,i}} \tag{3.19}$$

Likewise, the sensitivity coefficient with regard to the condenser water temperature difference, $\partial x_{t,i}/\partial \Delta T_{w,c}$ was dependent upon the water flow rate:

$$\frac{\partial x_{t,i}}{\partial \Delta T_{w,c}} = \frac{c_{p,w}\dot{m}_{w,c}}{h_{lv}(T_{mIn})\,\dot{m}_{t,i}} \tag{3.20}$$

As seen in Equation 3.20, there was a trade-off between the uncertainties in water flow rate and temperature difference measurements. Increasing the water flow rate through the condenser increased the uncertainty in $x_{t,i}$, due to the reduced water temperature difference. The same tradeoff applied also for the water flow through the evaporator test section.

Equation 3.17 showed clearly that the uncertainty in $x_{t,i}$ depended on the absolute value of $\dot{m}_{t,i}$, which appeared in the denominator of most of the sensitivity coefficients. At small values of refrigerant mass flow rate, small uncertainties in the measurements of temperatures and water mass flow rates would change the value of $x_{t,i}$ considerably.

The largest contribution to the uncertainty in $x_{t,i}$ was the 3.1% uncertainty in the measurement of the water flow rate through the test section (see Appendix C.2). The sensitivity coefficient with respect to test section water mass flow rate was given by:

$$\frac{\partial x_{t,i}}{\partial \dot{m}_{w,ts,i}} = \frac{c_{p,w}\Delta T_{w,ts,i}}{h_{lv}(T_{mIn})\,\dot{m}_{t,i}} \tag{3.21}$$

As shown in Equation 3.21, the sensitivity coefficient $(\delta x_{t,i}/\delta \dot{m}_{w,ts,i})$ was directly proportional to the measured temperature difference $\Delta T_{w,ts,i}$. Large values of $\Delta T_{w,ts,i}$ increased the uncertainty in $\delta x_{t,i}$. The computed uncertainty $\delta x_{t,i}$, is shown as function of refrigerant mass flow rate, $\dot{m}_{t,i}$, and test section water temperature differential in Figures 3.6 and 3.7 for HFC-134a and CO_2, respectively. Small differences are seen between the two fluids. The range of $\dot{m}_{t,i}$ (0.001 to 0.006 kg/s) covers the full range of the reported measurements. The uncertainties in the other properties involved in Equation 3.17 were calculated conservatively, which means

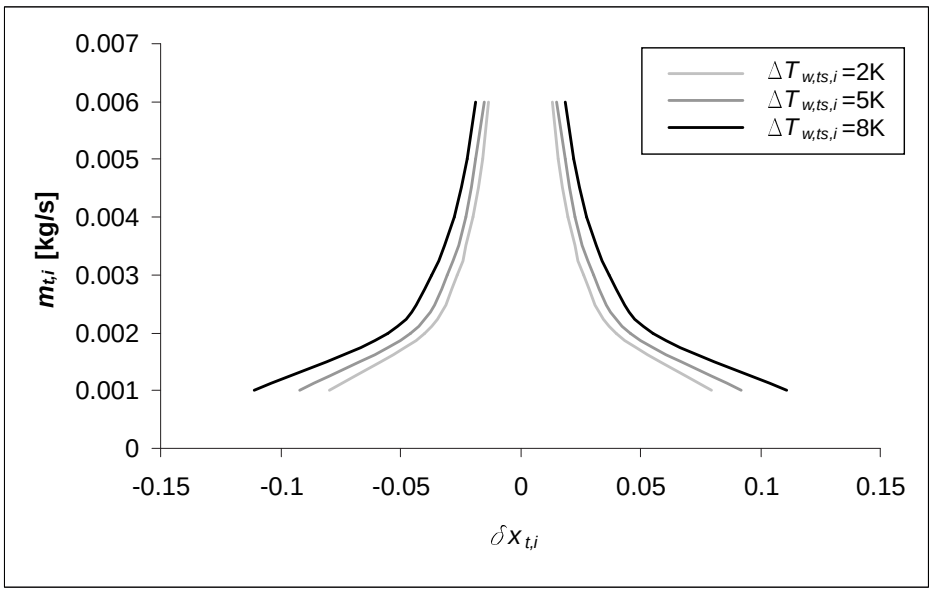

Figure 3.6: Uncertainty in branch tube inlet vapour fraction, $x_{t,i}$. Refrigerant: HFC-134a.

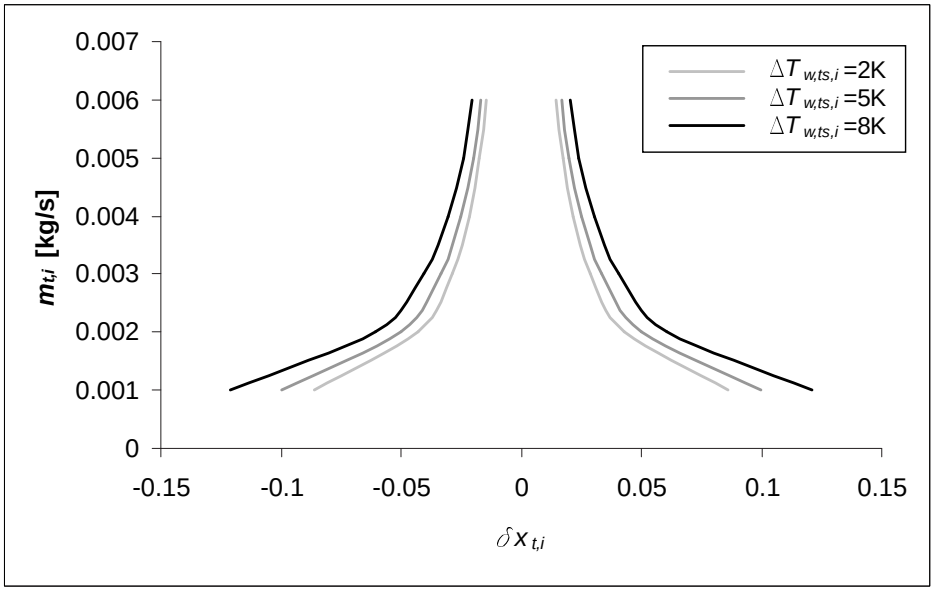

Figure 3.7: Uncertainty in branch tube inlet vapour fraction, $x_{t,i}$. Refrigerant: CO_2.

that the values presented in Figures 3.6 and 3.7 represent maximum uncertainties in the reported measurements of $x_{t,i}$ (within a confidence level of 95%).

In the presentation of the experimental results in Chapter 4, the temperature difference of the water over the test section is not given explicitly. However, by using the reported values of transferred heat per test section evaporator channel, $\dot{Q}_{ts,i}$, it is possible to calculate the water temperature difference:

$$\Delta T_{w,ts,i} = \frac{\dot{Q}_{ts,i}}{c_{p,w}\dot{m}_{w,ts,i}} \tag{3.22}$$

Nominally, the total mass flow rate in the water circuit was maintained at $m_{w,tsIn} = 0.15$ kg/s. The individual branch tube flow rates, $m_{w,tsIn,i}$, can be found by multiplying with the distribution factors given in Figure C.4.

In Chapter 4 the distribution of the liquid and the gas phase in the manifold is presented independently. The distribution of the liquid phase was calculated by the expression:

$$\dot{m}_{l,t,i} = (1 - x_{t,i})\,\dot{m}_{t,i} \tag{3.23}$$

Analogously for the gas mass flow rate:

$$\dot{m}_{g,t,i} = x_{t,i}\dot{m}_{t,i} \tag{3.24}$$

The uncertainty in the phase mass flow rates were then given by:

$$\delta\dot{m}_{g,t,i} = \delta\dot{m}_{l,t,i} = \left[\left(\frac{\partial\dot{m}_{l,t,i}}{\partial x_{t,i}}\delta x_{t,i}\right)^2 + \left(\frac{\partial\dot{m}_{l,t,i}}{\partial\dot{m}_{t,i}}\delta\dot{m}_{t,i}\right)^2\right]^{1/2} \tag{3.25}$$

The uncertainty in measured mass flow rate, $\dot{m}_{t,i}$, was infinitesimal compared to the uncertainty in $x_{t,i}$. Hence, the uncertainty in the phase mass flow rates could be computed by:

$$\delta\dot{m}_{g,t,i} = \delta\dot{m}_{l,t,i} \approx \dot{m}_{t,i}\delta x_{t,i} \tag{3.26}$$

3.7 Quality of measurements

The previous Section showed the uncertainties in the reported values of refrigerant mass flow rate and two-phase distribution in the manifold, which were caused by uncertainties in the instrumentation of the test rig. An additional uncertainty was caused by the measurement procedure of switching single channels to the separate outlet manifold, which affected the results of the two-phase distribution. The

procedure of regulating the pressure difference between the two outlet manifold to zero before running the experiments was described in Section 3.3.2. Ideally, the flow in the tap-off circuit, $\dot{m}_{t,i}$, should be equal to the flow in the corresponding evaporator tube *No i*, when all channels were connected to the main outlet manifold. To check the validity of this procedure, mass flow rate and vapour fraction balances were used. These results are presented in Sections 3.7.1 and 3.7.2.

3.7.1 Mass flow rate continuity

Figure 3.8 shows the relation between the measured total refrigerant flow at the inlet of the test section manifold and the sum of the mass flow rates in the ten branch tubes, as measured in the separate outlet manifold. The branch tube flow rates were obtained at ten consecutive measurement series with switching of each of the three-way valves in between. The collection of all measurement series reported in the current study is shown. 94.8% of the measurements were within $\pm$5% deviation. This indicates that the flow in the tap-off circuit was representative of the flow in the branch tube when all branches where connected to the same outlet manifold.

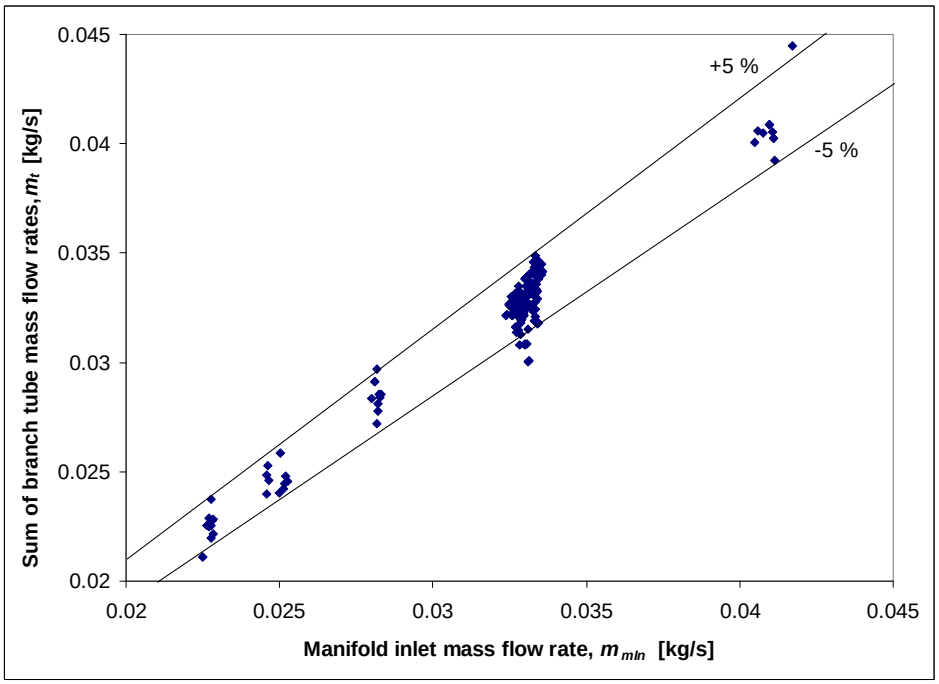

Figure 3.8: Mass flow rate continuity for all measurement series reported in the current study.

3.7.2 Vapour fraction continuity

Calculation of the vapour fraction at the inlet of the test section manifold and at the inlet of the single branch tubes was described in Section 3.5. Figure 3.9 contains a comparison of the calculated vapour fraction at the inlet of the manifold with the average vapour fraction at the inlet of the branch tubes. The average branch tube vapour fraction was obtained by a mass flow rate weighting:

$$\overline{x_t} = \frac{\sum_i (x_{t,i} \dot{m}_{t,i})}{\sum_i (\dot{m}_{t,i})} \tag{3.27}$$

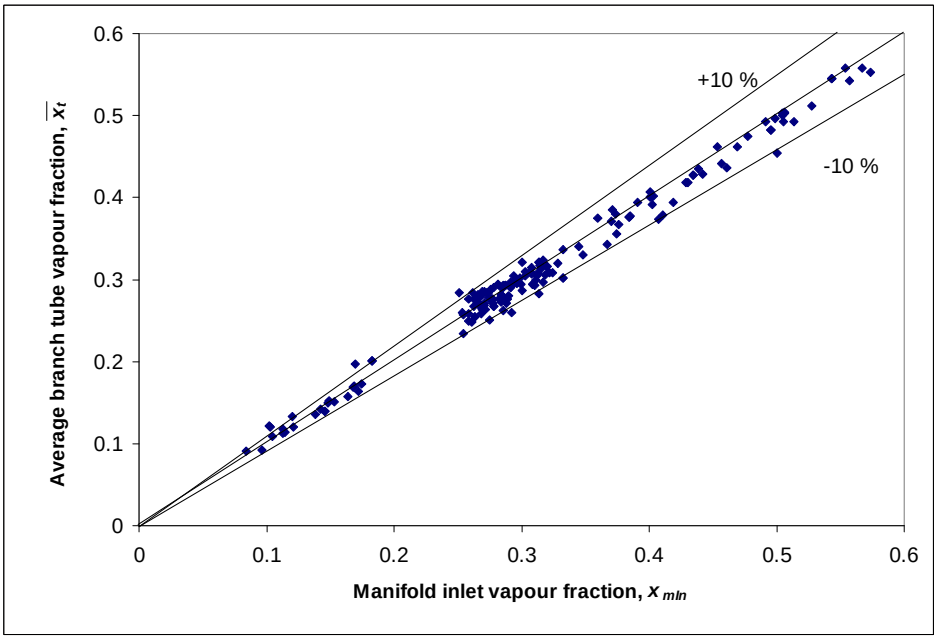

Figure 3.9: Vapour fraction continuity for all measurement series reported in the current study.

As shown in Section 3.6, the calculation of the vapour fraction at the inlet of the manifold, x_{mIn}, and at the inlet of the branch tubes, $x_{t,i}$, contained uncertainties in a number of temperature, mass flow, electric power and pressure measurements both in the refrigerant circuit and in the water circuits. The results in Figure 3.9 show that the vapour fraction continuity over the inlet manifold was fulfilled within $\pm$10% deviation in 96% of the measurement points.

3.7.3 Two-phase instability

Two-phase flow is by nature unstable. It is well known that two-phase flow in parallel channels can exhibit both so-called static and dynamic instabilities. Excellent introductions to the fundamentals of two-phase instabilities both in single channels and in parallel channel systems were provided by Yuncu and Kakac (1988) and Duffey et al. (1993). Kandlikar (2001) showed that pressure fluctuations in a multi-channel evaporator with six parallel 1mm $\times$ 1mm square micro-channels could cause instantaneous localized flow reversal in some of the channels under boiling conditions.

In the initial phase of running the test-rig, severe oscillations were seen in the differential pressure between the two outlet manifolds. This was explained by oscillatory instabilities due to friction and gravity between the vertical heat exchanger tubes. The test section was then rebuilt, as described in Section 3.3.2, such that the 0.9 m heat exchanger tubes were always in horizontal position. After this change in design, the instabilities in the pressure differential between the manifolds was significantly reduced and regulation of dp_m could be done by regulating the mass flow rate in the tap-off circuit by the needle valve (10).

Chapter 4

Experimental Results

The literature survey conducted in Chapter 2 demonstrated a lack of experimental research on two-phase distribution in manifolds and the need for relevant geometries in such experiments. The main objective of the experimental facility, described in Chapter 3, was to provide such experimental data under relevant operating conditions. The current Chapter contains a summary of the experimental results obtained. First, a listing of the tested manifold geometries is given in Section 4.1.1 and an outline of the experimental matrix of operating conditions is given in Section 4.1.2. Some introductory tests were performed using a glass manifold to allow for visual observation of the two-phase flow regime in the manifold. These results are presented in 4.2. Experimental results obtained with the ID 16 mm, ID 12 mm and ID 8 mm round tube manifolds are given in Sections 4.3, 4.4 and 4.5, respectively. Results from the base-case multiport extruded tube (MPE-tube) manifold are presented in Section 4.7 and results with various geometry modifications are given in Sections 4.8, 4.9, 4.10, 4.11 and 4.12. Results from the star type manifold are given in Section 4.13. Finally, a comparison between the different manifolds tested, with respect to two-phase distribution performance, is done in Section 4.14. Further analysis and discussion of the experimental data is given in Chapter 5.

An overview of the tested manifolds is given in Table 4.1.1.

4.1 Overview of the experimental measurements

4.1.1 Tested manifolds

The free flow area, A_c, is defined as the smallest cross-sectional area in the manifold. An example is shown in Figure 4.1, where a MPE branch tube is protruded into the manifold. The hydraulic diameter is calculated based on A_c and the perimeter, P:

$$D_H = \frac{4A_c}{P} \tag{4.1}$$

The tube insert ratio was defined as:

$$r = \frac{D - h_o}{D} \tag{4.2}$$

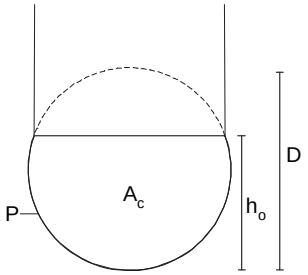

Figure 4.1: Definition of manifold cross-sectional area and perimeter. A flat MPE-tube protrudes into the circular manifold.

In Figure 4.2 a sketch of the ID 16 mm round tube manifold is shown. The manifolds M1, M2 and M3 have equal geometries, with exception of the variation in manifold diameter. Manifold M4 was equal to manifold M3, but the length of the manifold inlet tube was only 50 mm ,compared to 250 mm used for the other manifolds.

A drawing of the base-case MPE-tube manifold (M5) is shown in Figure 4.3 and geometrical details are given in Figure 4.4. The manifold was constructed in aluminum, such that the extruded aluminum MPE-tubes could be brazed to the manifold. The manifold had an upper part and a lower part, as shown in Figure 4.3, such that modifications to the geometry could easily be done. Also, this enabled the possibility of inspections of the MPE-tube port openings, to make sure that

Table 4.1: Tested manifolds

Manifold ID	Description	CO_2	HFC-134a	Hydraulic diameter D_H [mm]	Free flow area A_c [mm^2]	Tube insert ratio r	Tube pitch [mm]
M1	ID 16 mm round tube manifold	x	x	16.0	201.1	0	21
M2	ID 12 mm round tube manifold		x	12.0	113.1	0	21
M3	ID 8 mm round tube manifold	x	x	8.0	50.27	0	21
M4	M3 + short inlet tube		x	8.0	50.27	0	21
M5	MPE-tube manifold (base-case)	x	x	11.43	120.6	0.4	21
M6	M5 + tube insert ratio $r = 0.6$		x	7.996	75.1	0.6	21
M7	M5 + baffle insert		x	9.146	100.8	0.4	21
M8	M5 + 15 mm tube pitch		x	11.43	120.6	0.4	15
M9	M5 + spiral insert	x	x	11.43	120.6	0.4	21
M10	M5 + progressive insert		x	11.43 - 1.42	120.6 - 12.06	0.4	21
M11	Star manifold		x	12.0	113.1	0.1	-
M12	Glass manifold		x	16.0	120.6	0.4	21

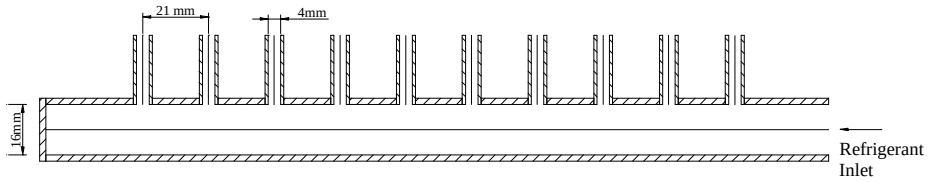

Figure 4.2: Manifold M1 (round tube manifold with inner diameter 16 mm). Tube pitch: 21 mm, branch tube inner diameter: 4 mm.

no brazing flux was blocking, which had been a major problem in prototype MPE heat exchanger tests (Song and Bullard, 2002). A steel plate with screw threads below the aluminum manifold was used to fasten the bolts, which kept the two manifold parts together. A total of 37 bolts were used. Refrigerant leakage was prevented with a rubber o-ring. Screw couplings with inside threads were used as connections between the MPE-tubes and the round tubes used in the heat exchanger part of the test section. More details of the base-case MPE-tube manifold are given in Figure 4.4 and in Appendix D.

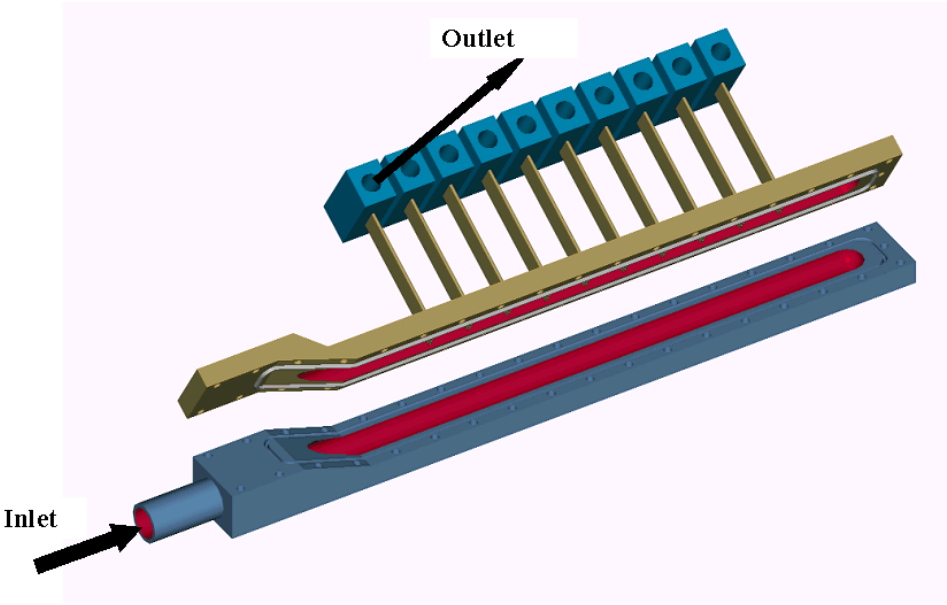

Figure 4.3: Manifold M5 (Base-case MPE-tube manifold). Round tube refrigerant inlet, MPE-tubes and screw couplings to the round heat exchanger branch tubes are shown.

Manifold M6 was identical to the base-case MPE-tube manifold with exception

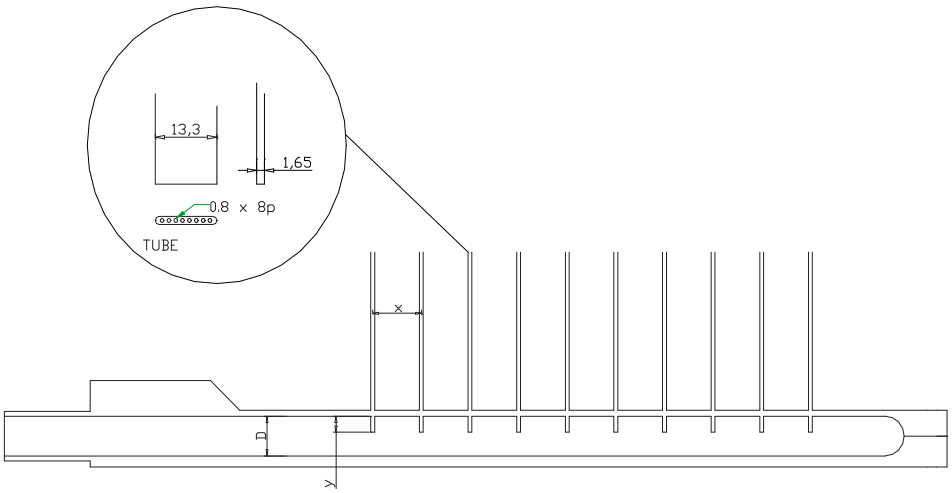

Figure 4.4: Manifold M5 (Base-case MPE-tube manifold). The MPE-tubes were inserted into the manifold with a length of $y = 0.4D$ (tube insert ratio $r = 0.4$) and the tube pitch was $x = 21$ mm. The MPE tubes had eight ports of 0.8 mm internal diameter.

that the MPE-tubes have a tube insert ratio $r = 0.6$. Hence, the free flow area in the manifold was reduced from 120.6 to 75.1 mm^2. Figure 4.5 shows the baffle insert used in manifold M7. The insert was glued to the bottom of the base-case MPE-manifold manifold, and the free flow area was reduced to 100.8 mm^2. Similar inserts were used by Butterworth (1980) to change two-phase flow distribution in T-junctions.

In figure 4.6, a drawing of manifold M8 is shown. The tube pitch was reduced from 21 mm in the base-case manifold to to 15 mm. By bending the flexible MPE-tubes, the M8 manifold was constructed with equal tube lengths, to avoid differences in frictional pressure losses. Results of the experiments with the manifold with 15 mm tube pitch are reported in Section 4.10.

To evaluate the effect of a mixed two-phase flow compared to a developed two-phase flow at the manifold inlet, a static mixer insert was used in manifold M9. The mixer, shown in Figure 4.7, was obtained from TAH Europe, Inc. (Product number: 121-510). Results obtained with the manifold with mixer insert is reported in Section 4.11.

In the patent of Burk, Salzer and Wolf (1994, DE 4,319,192), a decreasing manifold cross-sectional area was claimed to give improved two-phase distribution (see

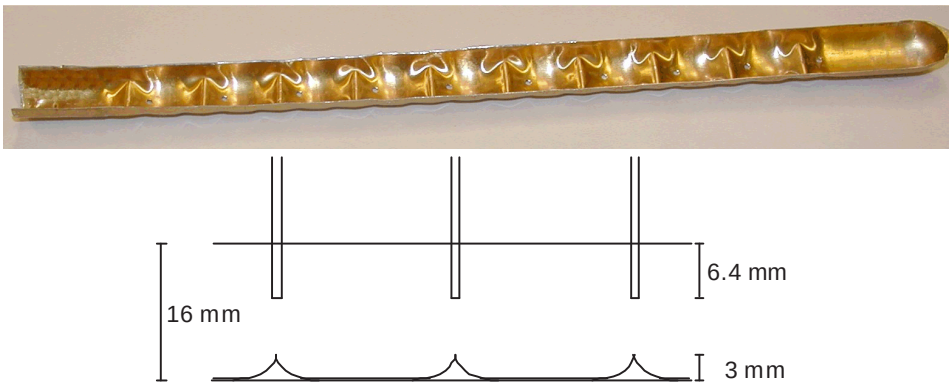

Figure 4.5: Baffle insert used in manifold M7.

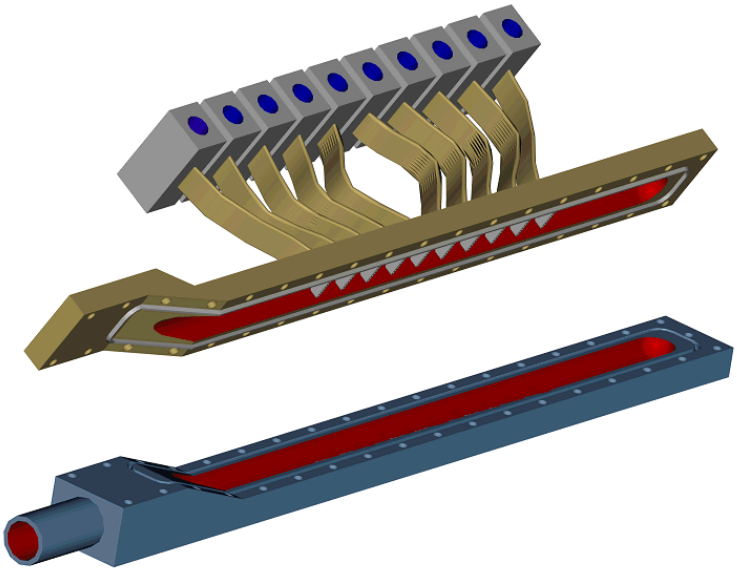

Figure 4.6: Manifold M8. The tube pitch between the MPE-tubes was reduced from 21 mm (base-case) to 15 mm.

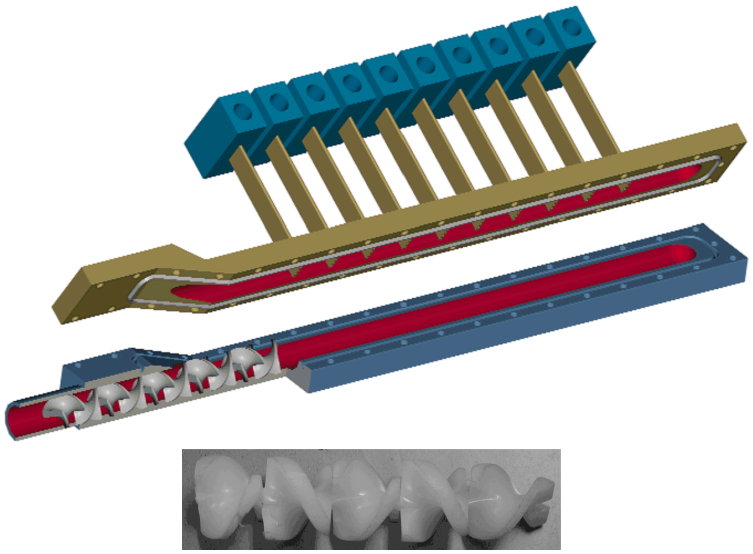

Figure 4.7: Manifold M9 with static mixer insert at the inlet.

Figure B.3). To investigate this, a manifold insert for progressively decreasing the manifold cross-sectional area was constructed. By machining a rod, producing a progressive insert, the cross-section of the manifold was reduced such that the mass flux (kg/(m^{2}s)) would be constant at the branch tube T-junctions throughout the manifold in the situation of equal two-phase flow distribution. The geometry of the rod used in manifold M10 is seen in Figure 4.8. Results of the experiments with the progressive insert manifold is reported in Section 4.12.

A novel manifold design, the ”star manifold”, was tested to check the hypothesis that a shorter manifold would give improved two-phase distribution. Hrnjak (2003) showed a prototype of the star manifold in a serpentine heat exchanger. The star manifold used in this study had eight MPE-tubes with equal dimensions as the tubes shown in Figure 4.4. The MPE-tubes all had equal length and were arranged in two layers around the circumference of the manifold as shown in Figure 4.9. The two remaining test section heat exchanger tubes were blocked during the experiments with the star manifold. The results of the star manifold are reported in Section 4.13.

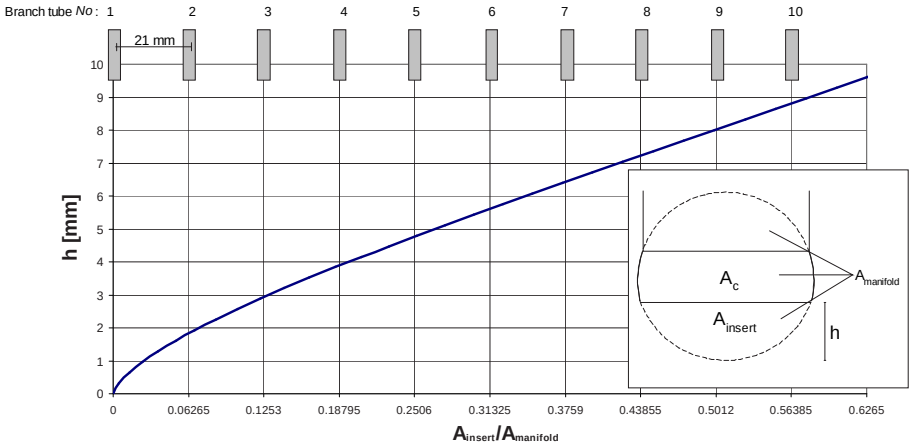

Figure 4.8: Dimensions of progressive insert used in manifold M10. The vertical height of the rod is seen as function of position in the manifold, with branch tube positions indicated at the top. The cross sectional area of the rod is shown as fraction of the total manifold cross sectional area. The free flow cross sectional area, without the progressive insert, was equal to $A_c/A_{manifold} = 0.6265$ ($A_{insert} = 0$).

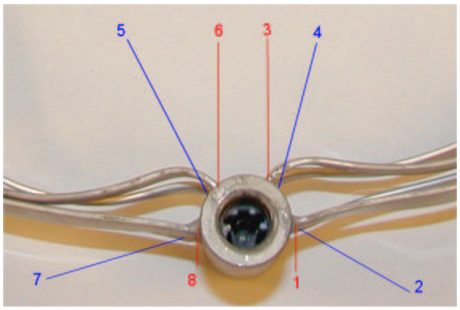

Figure 4.9: Star manifold, M11, with numbering of MPE-tubes used in the presentation of the results. Branch tubes *No* 1, 3, 6 and 8 constituted the first row closest to the inlet, while branch tubes *No* 2, 4, 5 and 7 constituted the second row.

4.1.2 Experimental matrix

The operating conditions for the experiments represented a sweep of the operating range of evaporators in car air-conditioning systems, within the limit of the possibilities of the test rig. The following parameters were varied in the experiments with indicated ranges:

- Refrigerant fluid (HFC-134a and CO_2).
- Manifold inlet vapour fraction (0.1 - 0.5).
- Manifold inlet mass flow rate (0.023 to 0.042 kg/s)
- Test rig water inlet temperature (40 to 60°C for HFC-134a and 30 to 50°C for CO_2). This corresponds to a total branch tube heat load of approximately (2.5 to 5.5 kW).
- Orientation of the manifold (horizontal manifold with upward or downward branch tubes).

Table 4.2 shows the mass flux at the manifold inlet, mass flux in the manifold at the first branch tube off-take and the average mass flux in the branch tubes.

Table 4.2: Mass flux in tested manifolds at $\dot{m}_{mIn}$= 0.033 kg/s. G_{mIn}: Total mass flux at manifold inlet. $G_{m,1}$: Total mass flux in manifold at first branch tube off-take. G_t: Average mass flux in branch tubes.

Manifold ID	Description	G_{mIn} [kg/(m^{2}s)]	$G_{m,1}$ [kg/(m^{2}s)]	G_t [kg/(m^{2}s)]
M1	ID 16 mm round tube manifold	164.1	164.1	262.6
M2	ID 12 mm round tube manifold	291.8	291.8	262.6
M3	ID 8 mm round tube manifold	656.5	656.5	262.6
M4	M3 + short inlet tube	656.5	656.5	262.6
M5	MPE-tube manifold (base-case)	164.1	273.6	820.7
M6	M5 + tube insert ratio $r = 0.6$	164.1	439.4	820.7
M7	M5 + baffle insert	164.1	327.4	820.7
M8	M5 + 15 mm tube pitch	164.1	273.6	820.7
M9	M5 + spiral insert	164.1	273.6	820.7
M10	M5 + progressive insert	164.1	273.6	820.7
M11	Star manifold	291.8	291.8	1025.8
M12	Glass manifold	164.1	273.6	262.6

4.1.3 Presentation of the experimental results

In the presentation of the results of the two-phase distribution measurements, the flow ratio, k, of the vapour and the liquid phase in tube $No\ i$ is presented in normalized form:

$$k_{p,i} = \frac{\dot{m}_{p,i}}{\sum_{j=1}^{N_t} \dot{m}_{p,j}/N_t} \tag{4.3}$$

where $p = l$ (liquid) and $p = g$ (gas). At homogenous distribution the flow ratio is equal to unity for both phases in all tubes. Tubes are numbered from the inlet.

In the discussion of the results, the Mean Vapour Flow Rate (MVFR) and the Mean Liquid Flow Rate (MLFR) are used. These numbers refer to the flow of vapour and liquid in a branch tube if the total flow was equally distributed in all ten branch tubes.

4.2 Visual observations in glass manifold

To gain visual experience of the two-phase flow structure in the manifold a glass model was constructed at SINTEF, Department of Chemistry, Figure 4.10.

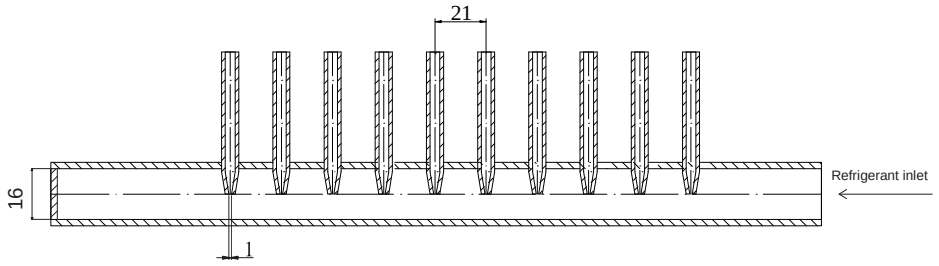

Figure 4.10: Glass manifold construction, M12.

The glass construction was hand-made, thus the openings to the heat exchanger tubes were not exactly equally sized. This geometrical effect affected the mass flow rate distribution. However, the visual observations of the flow development through the manifold were of great importance for the understanding of the flow distribution.

A digital video camera was used to document the two-phase flow at different mass flow rates and different inlet gas fractions. Some snapshots of the two-phase flow

in the manifold are shown in the Figures 4.11 to 4.15. The two-phase refrigerant was flowing into the manifold from the right and leaving through the ten parallel tubes upward out of the manifold.

Figure 4.11: Two-phase distribution in glass manifold M12. Refrigerant flows in from the right. HFC-134a, $\dot{m}_{mIn} = 0.042$ kg/s, $x_{mIn} = 0.05$.

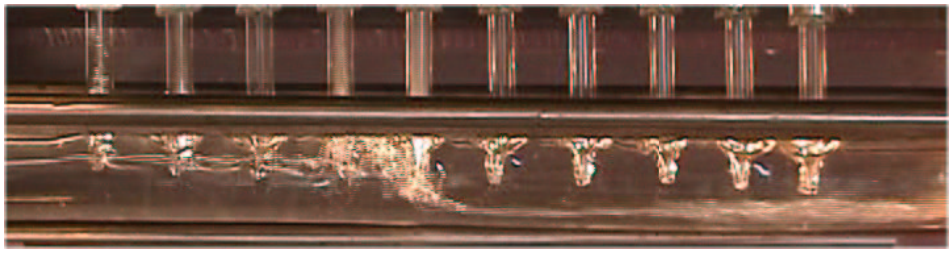

Figure 4.12: Two-phase distribution in glass manifold M12. Refrigerant flows in from the right. HFC-134a, $\dot{m}_{mIn} = 0.042$ kg/s, $x_{mIn} = 0.2$.

The pictures showed clearly the severe maldistribution of the two-phase flow. Phase separation lead to a pooling in the far end of the manifold. Even at an inlet vapour fraction of $x_{mIn} = 0.99$, a pool of liquid was seen feeding the last tubes of the manifold.

Figure 4.16 shows two-phase flow in downward branch tube configuration. The two-phase flow impinges at the first protruding branch pipe and a chaotic flow structure is seen downstream in the manifold.

Figure 4.13: Two-phase distribution in glass manifold M12. Refrigerant flows in from the right. HFC-134a, $\dot{m}_{mIn} = 0.042$ kg/s, $x_{mIn} = 0.36$.

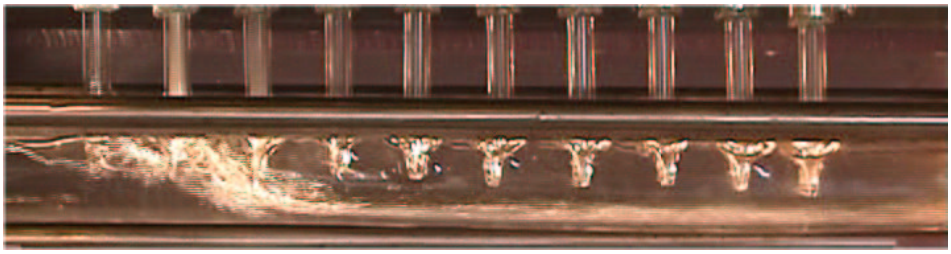

Figure 4.14: Two-phase distribution in glass manifold M12. Refrigerant flows in from the right. HFC-134a, $\dot{m}_{mIn} = 0.042$ kg/s, $x_{mIn} = 0.45$.

Figure 4.15: Two-phase distribution in glass manifold M12. Refrigerant flows in from the right. HFC-134a, $\dot{m}_{mIn} = 0.017$ kg/s, $x_{mIn} = 0.99$.

Figure 4.16: Two-phase distribution in glass manifold M12. Downward branch tubes. Refrigerant flows in from the left. HFC-134a, $\dot{m}_{mIn} = 0.042$ kg/s, $x_{mIn} = 0.36$.

4.3 Two-phase distribution in ID 16 mm round tube manifold (M1)

In the current Section, results of the experiments in the ID 16 mm round tube manifold, shown in Figure 4.2, are presented. First, results obtained in upward flow configuration is presented in Section 4.3.1. Next, results from the experiments in downward configuration is presented in Section 4.3.2.

4.3.1 Upward flow configuration

4.3.1.1 Two-phase distribution as a function of inlet vapour fraction

Figures 4.17 and 4.18 show two-phase distribution as a function of the manifold inlet vapour fraction, x_{mIn}, for HFC-134a and CO_2, respectively. The inlet mass flow rate was kept constant at $\dot{m}_{mIn} = 0.033$ kg/s, and the water inlet temperature of the test section was $T_{w,tsIn} = 50°C$.

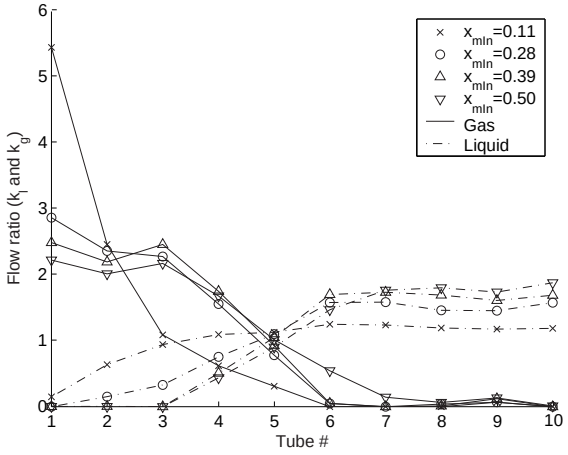

Figure 4.17: Measured two-phase distribution at varying x_{mIn}, ID 16 mm round tube manifold (M1), upward flow configuration, refrigerant: HFC-134a, $\dot{m}_{mIn} = 0.033$ kg/s, $T_{w,tsIn} = 50°C$ and $T_{mIn} = 29.5°C$.

It can be observed that both the vapour and the liquid phases are very unequally distributed to the different heat exchanger tubes. The vapour phase is distributed into the first tubes, and the liquid phase is distributed preferentially to the tubes *No* 6 to 10. The first tube gets 2.2 to 6.8 times the MVFR (Mean Vapour Flow

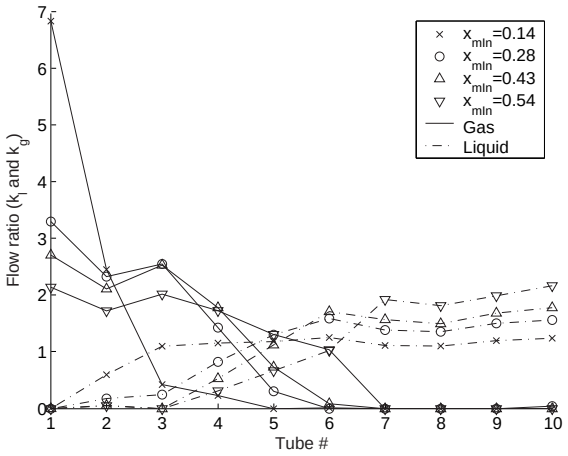

Figure 4.18: Measured two-phase distribution at varying x_{mIn}, ID 16 mm round tube manifold (M1), upward flow configuration, refrigerant: CO_2, $\dot{m}_{mIn} = 0.033$ kg/s, $T_{w,tsIn} = 40°C$ and $T_{mIn} = 18.7°C$.

Rate), and only 0 to 0.3 times the MLFR (Mean Liquid Flow Rate). Tubes *No* 6 to 10 receive 1.3 to 2.0 times the MLFR but almost no vapour.

Only small differences are seen between the measurements with CO_2 and HFC-134a.

At increasing vapour fraction in the manifold inlet stream, the liquid flow ratio in branch tubes *No* 6 to 10 increases, which means that the manifold liquid distribution performance is getting worse. However, the distribution of the vapour phase is more even at high manifold inlet vapour fractions.

To quantify the importance of two-phase distribution on the performance of the heat exchanger, the measured heat load on the ten evaporator tubes are shown in Figure 4.19 and 4.20 for HFC-134a and CO_2, respectively.

The measured heat load is a direct result of the two-phase distribution shown in Figures 4.17 and 4.18. Reduced heat load is seen for tubes having high inlet vapour fraction (less refrigerant latent heat cooling capacity available). It can be seen that for both the HFC-134a and the CO_2 series, the branch tube heat load varies considerably between the ten branch tubes. Only about 10 to 20% of the heat exchanged in branch tubes *No* 6 to 10 is exchanged in tube *No* 1.

For the low vapour fraction experiments ($x_{mIn} = 0.11$), more vapour is distributed to tubes *No* 1 and 2, and more liquid is distributed to tubes *No* 3 and 4. This is

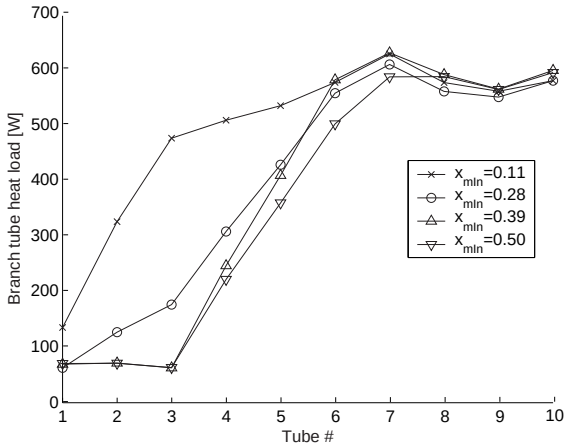

Figure 4.19: Measured branch tube heat load at varying x_{mIn}, ID 16 mm round tube manifold (M1), upward flow configuration, refrigerant: HFC-134a, $\dot{m}_{mIn} = 0.033$ kg/s, $T_{w,tsIn} = 50°$C and $T_{mIn} = 29.5°$C.

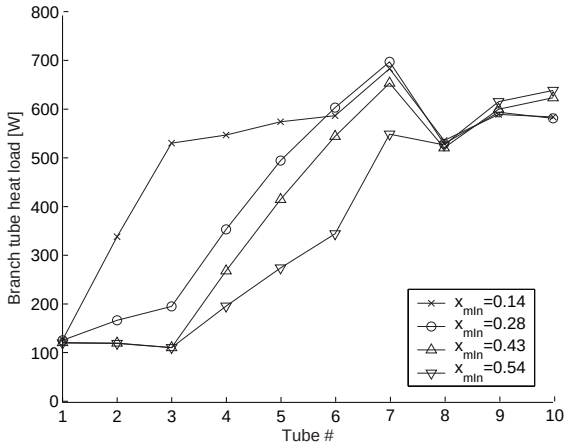

Figure 4.20: Measured branch tube heat load at varying x_{mIn}, ID 16 mm round tube manifold (M1), upward flow configuration, refrigerant: CO_2, $\dot{m}_{mIn} = 0.033$ kg/s, $T_{w,tsIn} = 40°$C and $T_{mIn} = 18.7°$C.

reflected in a considerably higher evaporator tube heat load in the fist four tubes compared to the experiments with higher inlet vapour fraction.

4.3.1.2 Two-phase distribution as a function of inlet mass flow rate

Figures 4.21 and 4.22 show results from experiments with varying mass flow rate at the manifold inlet, $\dot{m}_{mIn}$. The water temperature at the test section inlet was held constant. Also, the preheater power was adjusted, such that the vapour fraction at the manifold inlet was constant.

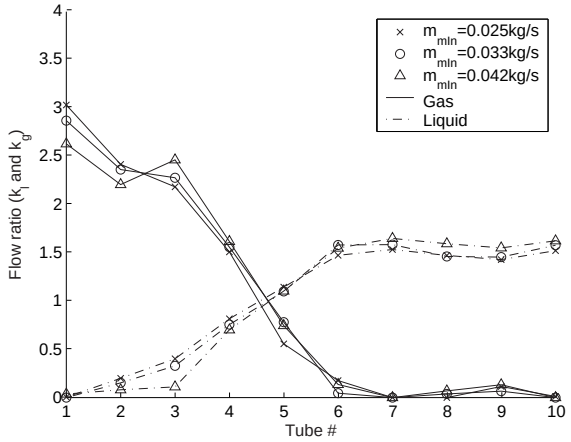

Figure 4.21: Measured two-phase distribution at varying $\dot{m}_{mIn}$, ID 16 mm round tube manifold (M1), upward flow configuration, refrigerant: HFC-134a, $x_{mIn} = 0.28$, $T_{w,tsIn} = 50°\text{C}$ and $T_{mIn} = 29.5°\text{C}$.

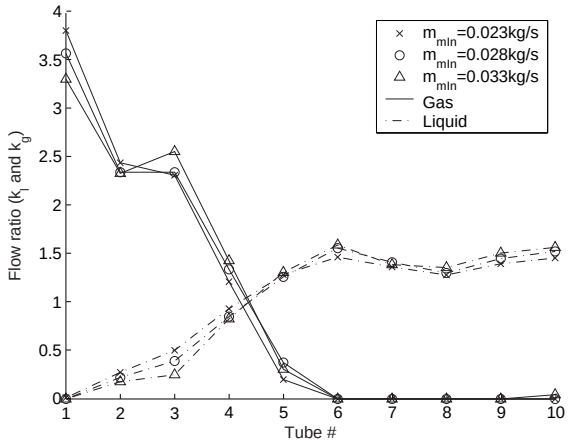

Figure 4.22: Measured two-phase distribution at varying $\dot{m}_{mIn}$, ID 16 mm round tube manifold (M1), upward flow configuration, refrigerant: CO_2, $x_{mIn} = 0.28$, $T_{w,tsIn} = 40°C$ and $T_{mIn} = 18.7°C$.

Figures 4.21 and 4.22 show that within the range of mass flow rates used in the measurements, very small changes in two-phase distribution occur.

4.3.1.3 Two-phase distribution as a function of evaporator load

To investigate the influence of varying evaporator tube heat load on the two-phase distribution in the manifold, the water inlet temperature to the evaporator test section ($T_{w,tsIn}$) was varied between 40, 50 and 60°C in the HFC-134a experiments ($T_{mIn} = 29.5°C$), and 30, 40 and 50°C in the CO_2 experiments ($T_{mIn} = 18.7°C$). Figures 4.23 and 4.24 show the two-phase distribution for HFC-134a and CO_2, respectively. The gross maldistribution of both the liquid and the vapour phase prevails, and is very little affected by the heat load on the heat exchanger tubes.

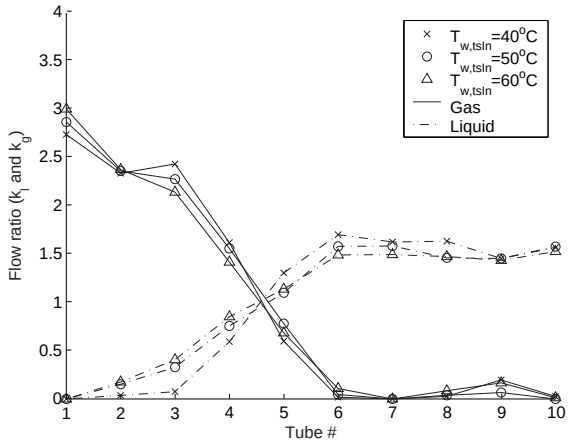

Figure 4.23: Measured two-phase distribution at varying $T_{w,tsIn}$, ID 16 mm round tube manifold (M1), upward flow configuration, refrigerant: HFC-134a, $x_{mIn} = 0.28$, $\dot{m}_{mIn} = 0.033$ kg/s and $T_{mIn} = 29.5°$C.

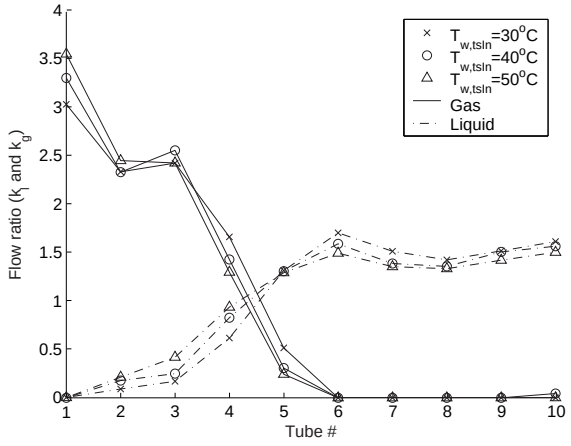

Figure 4.24: Measured two-phase distribution at varying $T_{w,tsIn}$, ID 16 mm round tube manifold (M1), upward flow configuration, refrigerant: CO_2, $x_{mIn} = 0.28$, $\dot{m}_{mIn} = 0.033$ kg/s and $T_{mIn} = 18.7°$C.

Figures 4.25 and 4.26 show the measured heat load for the measurements with varying water temperature, $T_{w,tsIn}$. The refrigerant is superheated out of the branch tubes at 50°C in the HFC-134a experiments and at 40°C for CO_2 experiments. This is the reason for the small change in branch tube heat load, when increasing the water temperature, $T_{w,tsIn}$, beyond these temperatures.

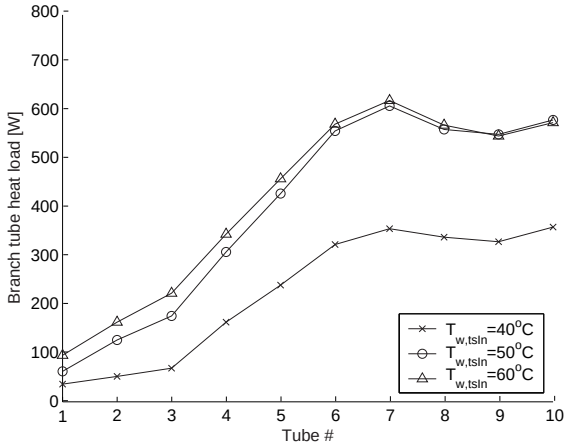

Figure 4.25: Measured branch tube heat load at varying $T_{w,tsIn}$, ID 16 mm round tube manifold (M1), upward flow configuration, refrigerant: HFC-134a, $x_{mIn} = 0.28$, $\dot{m}_{mIn} = 0.033$ kg/s and $T_{mIn} = 29.5°$C.

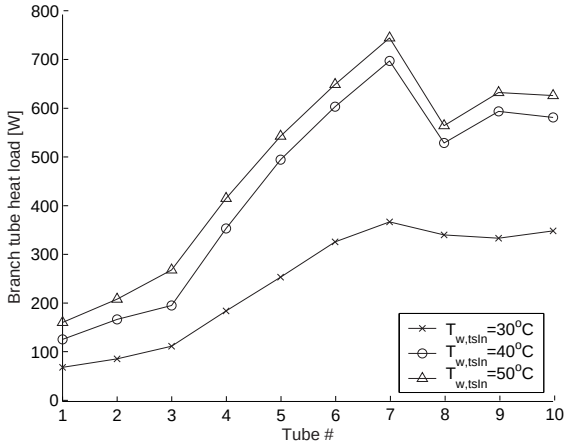

Figure 4.26: Measured branch tube heat load at varying $T_{w,tsIn}$, ID 16 mm round tube manifold (M1), upward flow configuration, refrigerant: CO_2, $x_{mIn} = 0.28$, $\dot{m}_{mIn} = 0.033$ kg/s and $T_{mIn} = 18.7°$C.

4.3.2 Downward flow configuration

In the current Section, experiments performed in the ID 16 mm manifold (M1) with vertical downward branch tubes are reported.

4.3.2.1 Two-phase distribution as a function of inlet vapour fraction

Figures 4.27 and 4.28 show the two-phase distribution for various vapour fractions, x_{mIn}, at the manifold inlet. Unlike for the upward flow configuration, the vapour now flows to the end of the manifold and is distributed in branch tubes No 4 to 10. As in upward flow configuration, increasing inlet vapour fraction evens out the vapour distribution while the distribution of liquid is best at low values of x_{mIn}.

Measured heat load is seen in Figures 4.29 and 4.30. At increasing vapour fraction the heat load is reduced (less refrigerant latent heat cooling capacity available). As in upward flow configuration, there is considerable difference between the branch tubes due to the maldistribution of the two-phase flow in the manifold.

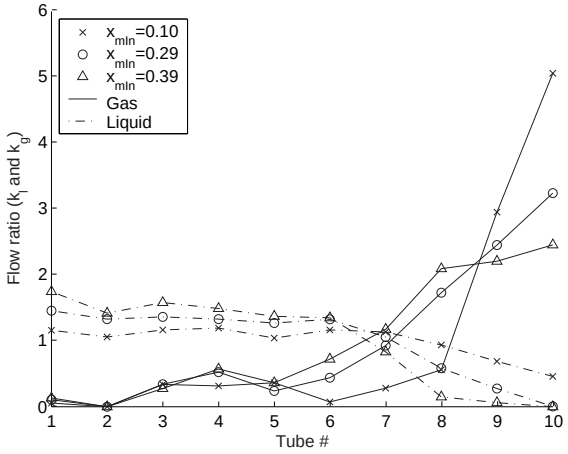

Figure 4.27: Measured two-phase distribution at varying x_{mIn}, ID 16 mm round tube manifold (M1), downward flow configuration, refrigerant: HFC-134a, $\dot{m}_{mIn} = 0.033$ kg/s, $T_{w,tsIn} = 50°$C and $T_{mIn} = 29.5°$C.

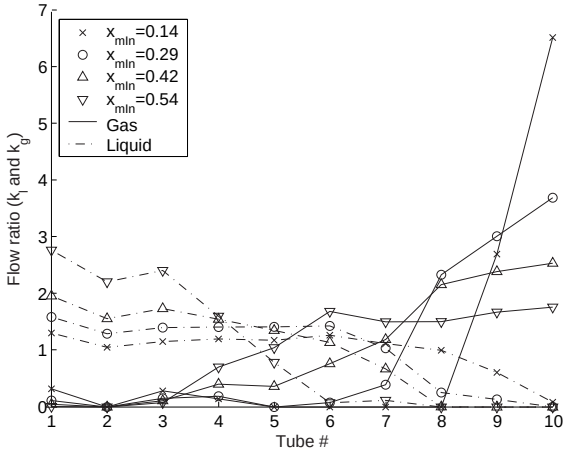

Figure 4.28: Measured two-phase distribution at varying x_{mIn}, ID 16 mm round tube manifold (M1), downward flow configuration, refrigerant: CO_2, $\dot{m}_{mIn} = 0.033$ kg/s, $T_{w,tsIn} = 40°$C and $T_{mIn} = 18.7°$C.

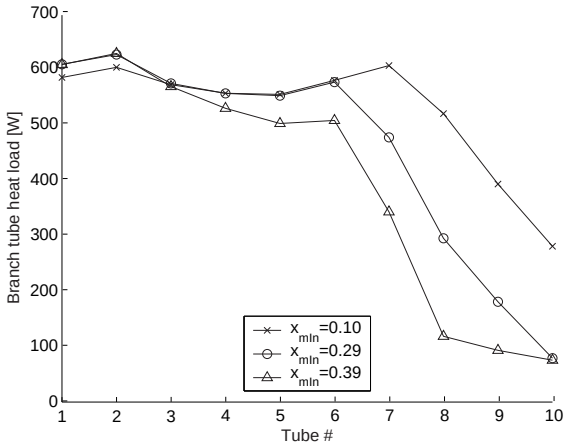

Figure 4.29: Measured branch tube heat load at varying x_{mIn}, ID 16 mm round tube manifold (M1), downward flow configuration, refrigerant: HFC-134a, $\dot{m}_{mIn} = 0.033$ kg/s, $T_{w,tsIn} = 50°$C and $T_{mIn} = 29.5°$C.

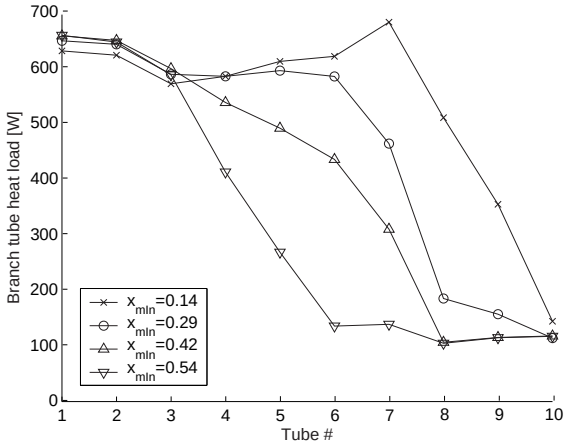

Figure 4.30: Measured branch tube heat load at varying x_{mIn}, ID 16 mm round tube manifold (M1), downward flow configuration, refrigerant: CO_2, $\dot{m}_{mIn} = 0.033$ kg/s, $T_{w,tsIn} = 40°$C and $T_{mIn} = 18.7°$C.

4.3.2.2 Two-phase distribution as a function of inlet mass flow rate

Figure 4.31 shows the two-phase CO_2 distribution at varying mass flow rate at the manifold inlet, $\dot{m}_{mIn}$. As in the upward flow configuration, very small changes in two-phase distribution are seen within the range of $\dot{m}_{mIn}$tested.

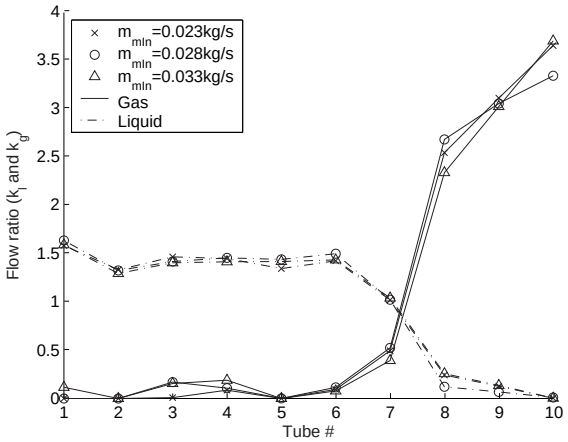

Figure 4.31: Measured two-phase distribution at varying $\dot{m}_{mIn}$, ID 16 mm round tube manifold (M1), downward flow configuration, refrigerant: CO_2, $x_{mIn} = 0.28$, $T_{w,tsIn} = 40^{\circ}$C and $T_{mIn} = 18.7^{\circ}$C.

4.3.2.3 Two-phase distribution as a function of evaporator load

The effect of varying evaporator load on the two-phase CO_2 distribution is seen in Figure 4.32. The two-phase distribution is very little changed when varying the heat load on the evaporator tubes.

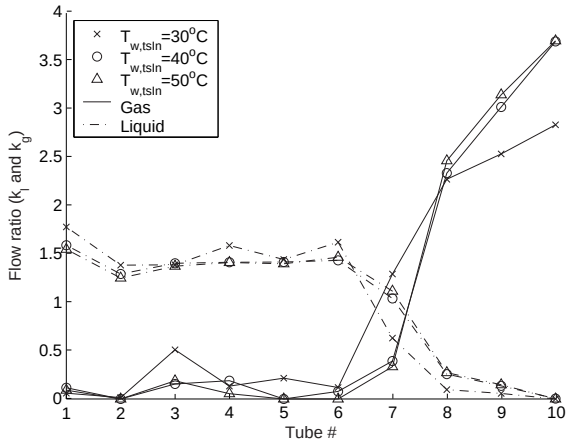

Figure 4.32: Measured two-phase distribution at varying $T_{w,tsIn}$, ID 16 mm round tube manifold (M1), downward flow configuration, refrigerant: CO_2, $x_{mIn} = 0.28$, $\dot{m}_{mIn} = 0.033$ kg/s and $T_{mIn} = 18.7°$C.

4.4 Two-phase distribution in ID 12 mm round tube manifold (M2)

A subset of the full experimental matrix was run with the ID 12 mm round tube manifold, M2. Refrigerant HFC-134a was used in upward flow configuration. Figure 4.33 shows the two-phase distribution at varying manifold inlet vapour fraction, x_{mIn}. The measured branch tube heat load is plotted in Figure 4.34.

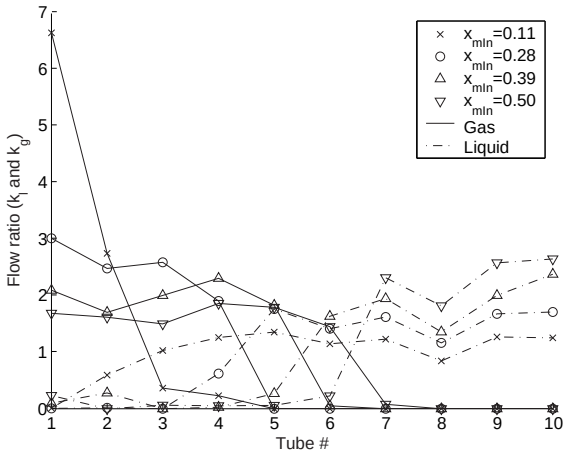

Figure 4.33: Measured two-phase distribution at varying x_{mIn}, ID 12 mm round tube manifold (M2), upward flow configuration, refrigerant: HFC-134a, $\dot{m}_{mIn} = 0.033$ kg/s, $T_{w,tsIn} = 50°$C and $T_{mIn} = 29.5°$C.

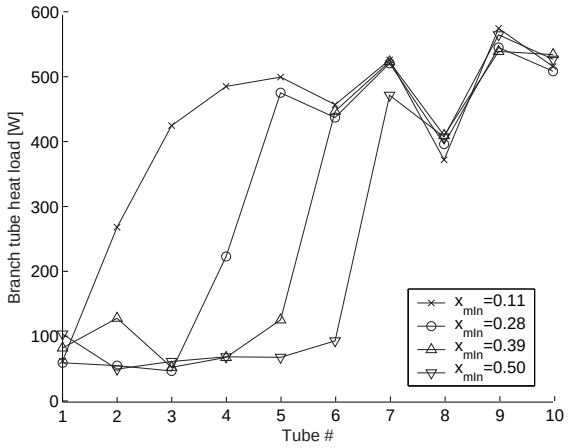

Figure 4.34: Measured branch tube heat load at varying x_{mIn}, ID 12 mm round tube manifold (M2), upward flow configuration, refrigerant: HFC-134a, $\dot{m}_{mIn} = 0.033$ kg/s, $T_{w,tsIn} = 50°$C and $T_{mIn} = 29.5°$C.

Only small changes in the two-phase distribution is seen in the ID 12 mm manifold (M2) compared to results from the ID 16 mm manifold (M1) (Figure 4.17).

4.5 Two-phase distribution in ID 8 mm round tube manifold (M3)

This Section contains the results obtained with the ID 8 mm round tube manifold (M3). Section 4.5.1 contains results obtained with upward flow configuration, while Section 4.5.2 contains results obtained with downward configuration.

4.5.1 Upward flow configuration

4.5.1.1 Two-phase distribution as a function of inlet vapour fraction

Figures 4.35 and 4.36 show the two-phase distribution in the ID 8 mm manifold (M3) at varying manifold inlet vapour fraction, x_{mIn}, for HFC-134a and CO_2, respectively. Corresponding values for the measured heat load on the evaporator tube branches are shown in Figures 4.37 and 4.38.

In the experiments with HFC-134a, more liquid was taken off in the first three branch tubes at manifold inlet vapour fractions above 0.2 compared to the experiments in manifold M1 and M2. This influenced the vapour flow rate, which was reduced in the first two tubes at the same manifold inlet vapour fractions. At low vapour fraction at the manifold inlet, $x_{mIn} = 0.11$, the two-phase distribution was almost equal in the three round tube manifolds (Figures 4.17, 4.33 and 4.35).

The CO_2 experiments, Figure 4.36, show larger differences compared to the results reported for the ID 16 mm manifold (M1) in Figure 4.18. At the lowest value of manifold inlet vapour fraction, $x_{mIn}= 0.15$, the distribution uniformity of both the vapour and the liquid is somewhat improved, but still quite equal to the distribution in the ID 16 mm manifold. At increasing manifold inlet vapour fractions, more liquid is distributed to the first branch tubes. Branch tubes *No* 3 to 6 get less than they would receive at homogenous distribution and branch tubes *No* 9 and 10 receive more. The vapour phase is preferentially distributed to tubes *No* 3 to 6 in these experiments.

Figures 4.37 and 4.38 show the corresponding measured heat load on the branch tubes for the measurements with varying vapour fraction at the manifold inlet.

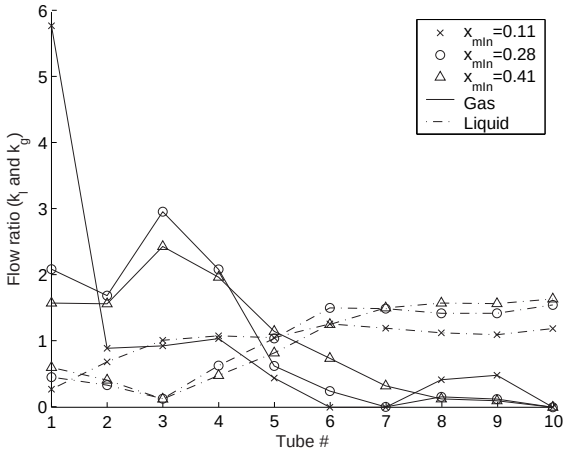

Figure 4.35: Measured two-phase distribution at varying x_{mIn}, ID 8 mm round tube manifold (M3), upward flow configuration, refrigerant: HFC-134a, $\dot{m}_{mIn} = 0.033$ kg/s, $T_{w,tsIn} = 50^{\circ}$C and $T_{mIn} = 29.5^{\circ}$C.

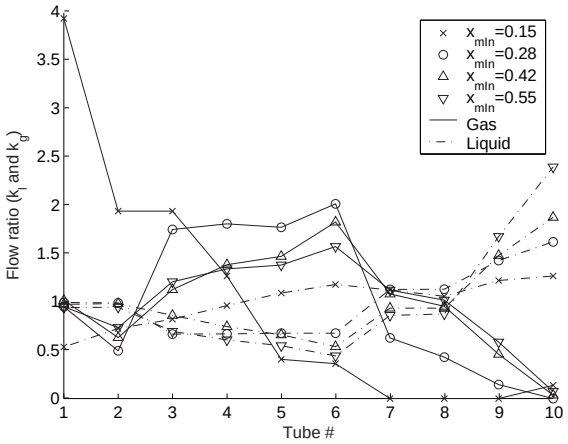

Figure 4.36: Measured two-phase distribution at varying x_{mIn}, ID 8 mm round tube manifold (M3), upward flow configuration, refrigerant: CO_2, $\dot{m}_{mIn} = 0.033$ kg/s, $T_{w,tsIn} = 40^{\circ}$C and $T_{mIn} = 18.7^{\circ}$C.

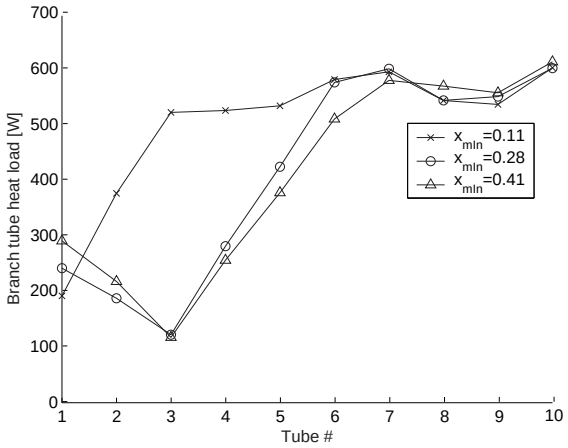

Figure 4.37: Measured branch tube heat load at varying x_{mIn}, ID 8 mm round tube manifold (M3), upward flow configuration, refrigerant: HFC-134a, $\dot{m}_{mIn} = 0.033$ kg/s, $T_{w,tsIn} = 50°$C and $T_{mIn} = 29.5°$C.

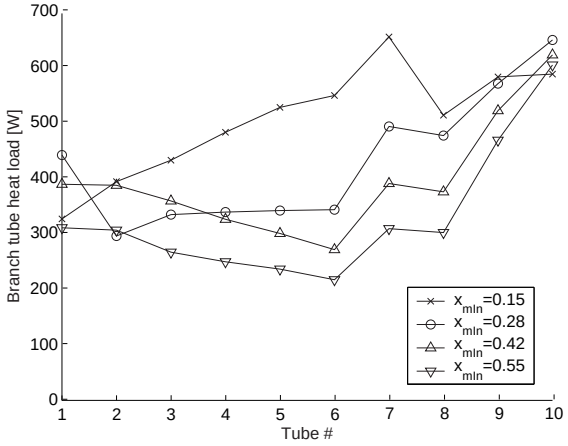

Figure 4.38: Measured branch tube heat load at varying x_{mIn}, ID 8 mm round tube manifold (M3), upward flow configuration, refrigerant: CO_2, $\dot{m}_{mIn} = 0.033$ kg/s, $T_{w,tsIn} = 40°$C and $T_{mIn} = 18.7°$C.

4.5.1.2 Two-phase distribution as a function of inlet mass flow rate

Figure 4.39 shows the two-phase distribution at three values of mass flow rate at the manifold inlet. Unlike for the experiments in the ID 16 mm manifold, Figure 4.22, the two-phase distribution is now affected by the mass flow rate at the manifold inlet. Increasing the mass flow rate at the manifold inlet evens out both the liquid and the vapour distribution.

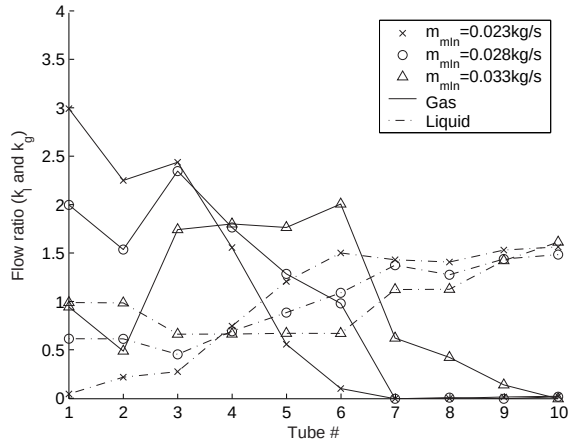

Figure 4.39: Measured two-phase distribution at varying $\dot{m}_{mIn}$, ID 8 mm round tube manifold (M3), upward flow configuration, refrigerant: CO_2, $x_{mIn} = 0.28$, $T_{w,tsIn} = 40^{\circ}$C and $T_{mIn} = 18.7^{\circ}$C.

4.5.1.3 Two-phase distribution as a function of evaporator load

In Figures 4.40 and 4.41, measurements with varying test section inlet water temperatures, $T_{w,tsIn}$, are shown for HFC-134a and CO_2, respectively. Only small changes in the two-phase distribution can be seen when changing the water temperature.

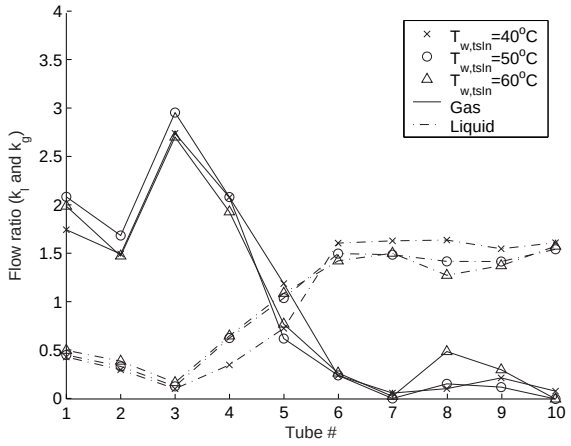

Figure 4.40: Measured two-phase distribution at varying $T_{w,tsIn}$, ID 8 mm round tube manifold (M3), upward flow configuration, refrigerant: HFC-134a, $x_{mIn} = 0.28$, $\dot{m}_{mIn} = 0.033$ kg/s and $T_{mIn} = 29.5°$C.

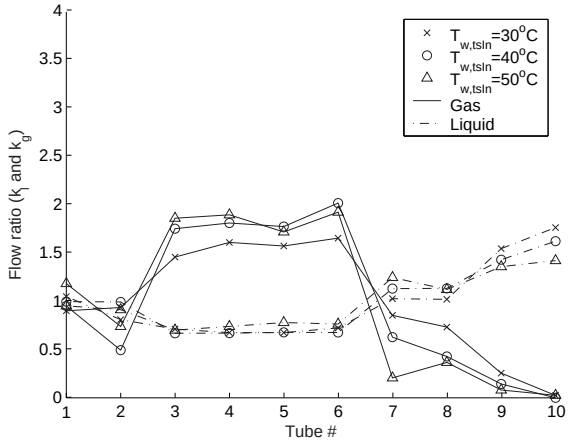

Figure 4.41: Measured two-phase distribution at varying $T_{w,tsIn}$, ID 8 mm round tube manifold (M3), upward flow configuration, refrigerant: CO_2, $x_{mIn} = 0.28$, $\dot{m}_{mIn} = 0.033$ kg/s and $T_{mIn} = 18.7°$C.

4.5.2 Downward flow configuration

4.5.2.1 Two-phase distribution as a function of inlet vapour fraction

Figures 4.42 and 4.43 show results from the ID 8 mm manifold (M3) in downward configuration for HFC-134a and CO_2, respectively. Compared to the results from the ID 16 mm manifold (Figures 4.27 and 4.28), both phases are somewhat more evenly distributed in the ID 8 mm manifold. The measured heat load on the evaporator branch tubes are shown in Figures 4.44 and 4.45.

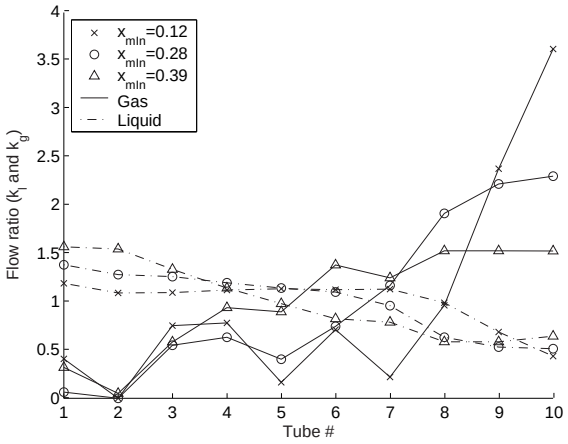

Figure 4.42: Measured two-phase distribution at varying x_{mIn}, ID 8 mm round tube manifold (M3), downward flow configuration, refrigerant: HFC-134a, $\dot{m}_{mIn} = 0.033$ kg/s, $T_{w,tsIn} = 50°$C and $T_{mIn} = 29.5°$C.

4.5.2.2 Two-phase distribution as a function of inlet mass flow rate

Figure 4.46 shows that the two-phase distribution is not changed very much due to a change in manifold inlet mass flow rate from 0.023 kg/s to 0.033 kg/s, when CO_2 was used as refrigerant in the ID 8 mm round tube manifold.

4.5.2.3 Two-phase distribution as a function of evaporator load

In Figure 4.47 the two-phase distribution is shown for three measurement series with varying water temperature at the test section inlet. The two-phase distribution was very little affected by the change in branch tube heat load.

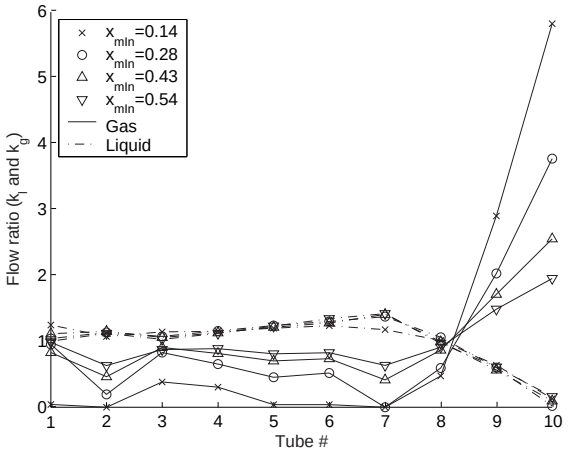

Figure 4.43: Measured two-phase distribution at varying x_{mIn}, ID 8 mm round tube manifold (M3), downward flow configuration, refrigerant: CO_2, $\dot{m}_{mIn} = 0.033$ kg/s, $T_{w,tsIn} = 40°$C and $T_{mIn} = 18.7°$C.

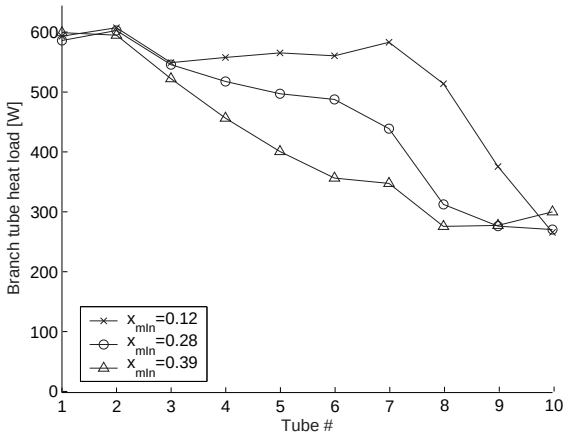

Figure 4.44: Measured branch tube heat load at varying x_{mIn}, ID 8 mm round tube manifold (M3), downward flow configuration, refrigerant: HFC-134a, $\dot{m}_{mIn} = 0.033$ kg/s, $T_{w,tsIn} = 50°$C and $T_{mIn} = 29.5°$C.

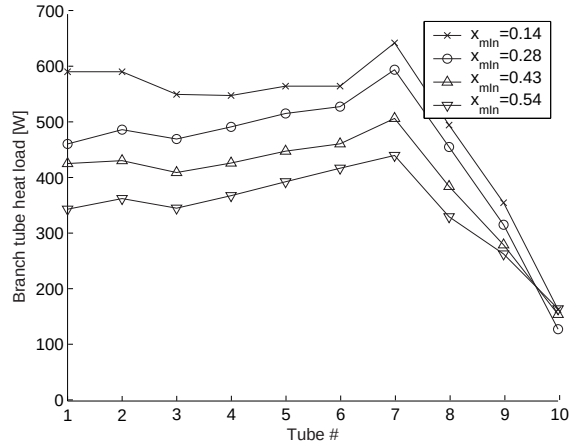

Figure 4.45: Measured branch tube heat load at varying x_{mIn}, ID 8 mm round tube manifold (M3), downward flow configuration, refrigerant: CO_2, $\dot{m}_{mIn} = 0.033$ kg/s, $T_{w,tsIn} = 40°$C and $T_{mIn} = 18.7°$C.

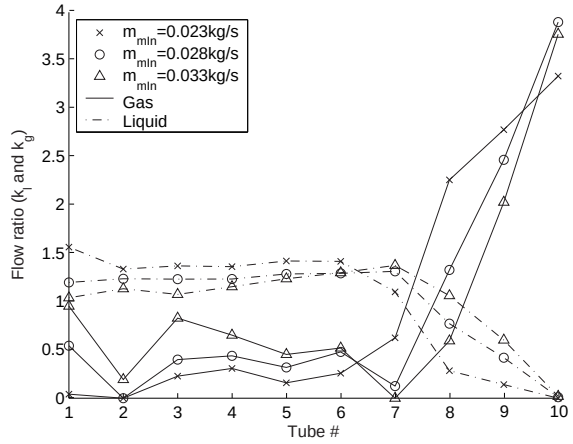

Figure 4.46: Measured two-phase distribution at varying $\dot{m}_{mIn}$, ID 8 mm round tube manifold (M3), downward flow configuration, refrigerant: CO_2, $x_{mIn} = 0.28$, $T_{w,tsIn} = 40°$C and $T_{mIn} = 18.7°$C.

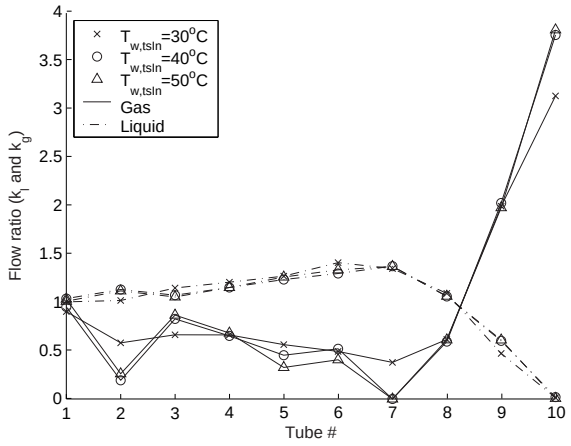

Figure 4.47: Measured two-phase distribution at varying $T_{w,tsIn}$, ID 8 mm round tube manifold (M3), downward flow configuration, refrigerant: CO_2, $x_{mIn} = 0.28$, $\dot{m}_{mIn} = 0.033$ kg/s and $T_{mIn} = 18.7°$C.

4.6 Two-phase distribution in ID 8 mm round tube manifold with short inlet tube, (M4)

To investigate the influence of the manifold inlet flow pattern on the two-phase flow distribution, a short inlet tube of 50 mm was used in some experiments (in contrast to the original inlet tube length of 250 mm from the horizontal 90° bend). Results are given in Section 4.6.1 for the upward configuration, and in Section 4.6.2 for downward configuration.

4.6.1 Upward flow configuration

Figure 4.48 shows two-phase HFC-134a distribution at varying manifold inlet vapour fraction, x_{mIn}, for the manifold ID 8 mm round tube manifold with short inlet tube (M4) in upward configuration.

The distribution pattern resembles the distribution in the CO_2 experiments with long inlet tube in Figure 4.36. Branch tubes *No* 3 to 6 is overfed with vapour, while branch tubes *No* 8 to 10 receive mostly liquid. As before, the liquid phase is more evenly distributed in experiments with low vapour fraction at the manifold inlet. The measured evaporator heat load is shown in Figure 4.49.

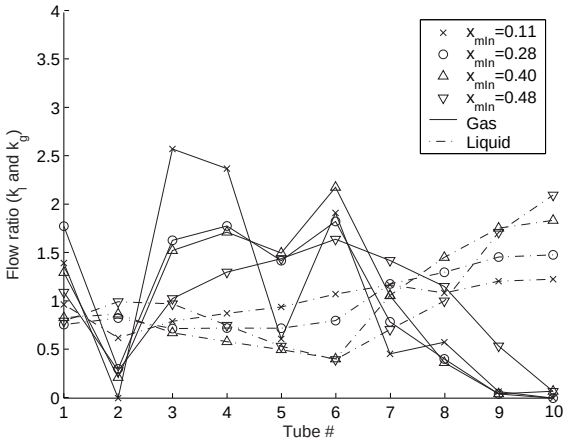

Figure 4.48: Measured two-phase distribution at varying x_{mIn}, ID 8 mm round tube manifold with short inlet tube (M4), upward flow configuration, refrigerant: HFC-134a, $\dot{m}_{mIn} = 0.033$ kg/s, $T_{w,tsIn} = 50°$C and $T_{mIn} = 29.5°$C.

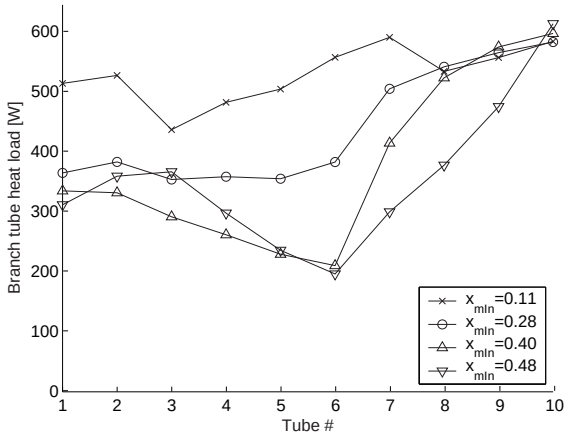

Figure 4.49: Measured branch tube heat load at varying x_{mIn}, ID 8 mm round tube manifold with short inlet tube, (M4), upward flow configuration, refrigerant: HFC-134a, $\dot{m}_{mIn} = 0.033$ kg/s, $T_{w,tsIn} = 50°$C and $T_{mIn} = 29.5°$C.

4.6.2 Downward flow configuration

As shown in Figure 4.50, the liquid phase in the M4 manifold in downward configuration is quite evenly distributed, with a liquid flow ratio varying from 0.5 to 1.5 of the MLFR. At high inlet vapour fractions, the vapour phase is also very evenly distributed. In the experiments with x_{mIn}= 0.10, most of the vapour is diverted to the last branch tube in the manifold. Corresponding heat load measurements are shown in Figure 4.51.

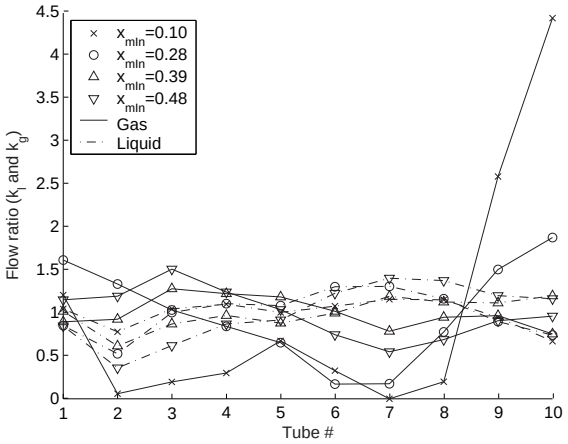

Figure 4.50: Measured two-phase distribution at varying x_{mIn}, ID 8 mm round tube manifold with short inlet tube (M4), downward flow configuration, refrigerant: HFC-134a, $\dot{m}_{mIn} = 0.033$ kg/s, $T_{w,tsIn} = 50°$C and $T_{mIn} = 29.5°$C.

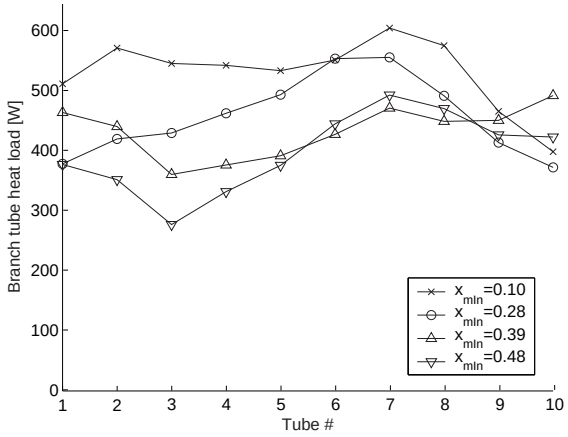

Figure 4.51: Measured branch tube heat load at varying x_{mIn}, ID 8 mm round tube manifold with short inlet tube, (M4), downward flow configuration, refrigerant: HFC-134a, $\dot{m}_{mIn} = 0.033$ kg/s, $T_{w,tsIn} = 50°$C and $T_{mIn} = 29.5°$C.

4.7 Two-phase distribution in MPE-tube manifold (M5)

In the current Section, experiments with the base-case MPE-manifold (M5) are reported. First, experiments in upward configuration are treated in Section 4.7.1, while results with downward configuration are shown in Section 4.7.2.

4.7.1 Upward flow configuration

4.7.1.1 Two-phase distribution as a function of inlet vapour fraction

Figure 4.52 and 4.53 show the two-phase distribution as a function of the manifold inlet vapour fraction for HFC-134a and CO_2, respectively.

At low vapour fraction at the manifold inlet, $x_{mIn} = 0.11$, the two-phase distribution was very similar to the distribution in the ID 16 mm manifold (M1). At increasing x_{mIn}, the liquid separated more than in the M1 manifold, with more liquid flowing into tubes *No* 9 and 10. The vapour distribution was improved, compared to the M1 manifold at high values of x_{mIn}.

Figures 4.54 and 4.55 show the measured heat load on the evaporator branch tubes. As seen in Figure 4.52, the first branch tube receives more liquid than the second tube for vapour fractions above $x_{mIn} = 0.11$. This results in a decrease in branch tube heat load, as seen in Figure 4.54. A further discussion of the manifold flow dynamics causing this effect will be given in Chapter 5.

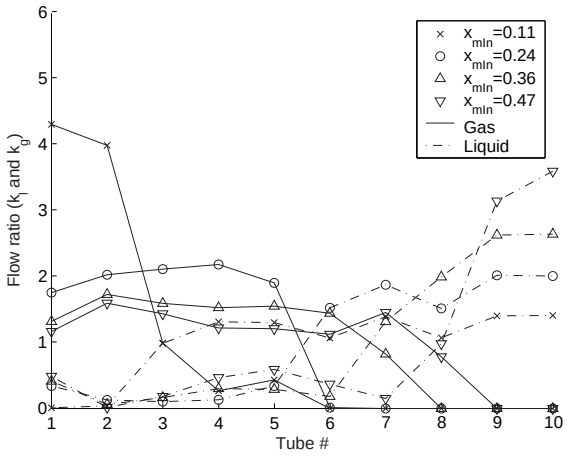

Figure 4.52: Measured two-phase distribution at varying x_{mIn}, MPE-tube manifold (M5), upward flow configuration, refrigerant: HFC-134a, $\dot{m}_{mIn} = 0.033$ kg/s, $T_{w,tsIn} = 50°$C and $T_{mIn} = 29.5°$C.

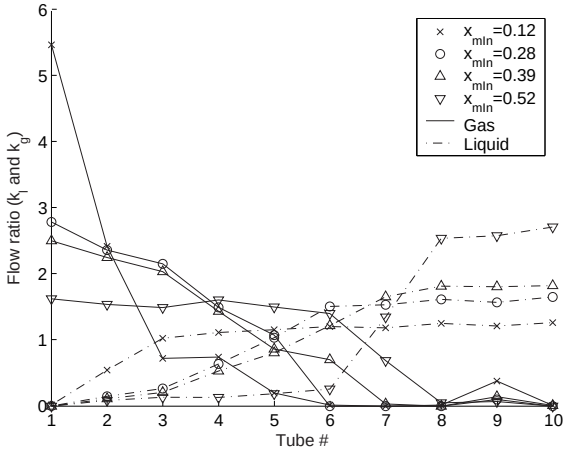

Figure 4.53: Measured two-phase distribution at varying x_{mIn}, MPE-tube manifold (M5), upward flow configuration, refrigerant: CO_2, $\dot{m}_{mIn} = 0.033$ kg/s, $T_{w,tsIn} = 40°$C and $T_{mIn} = 18.7°$C.

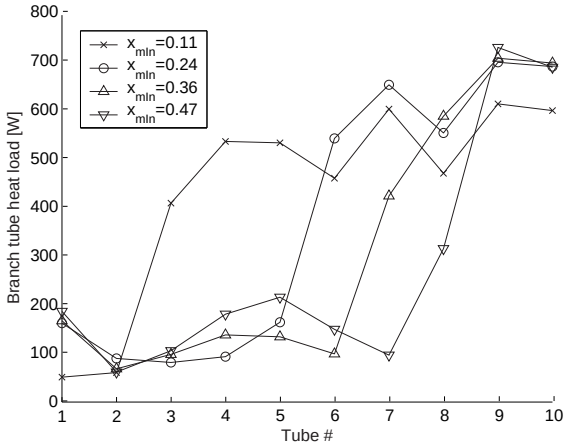

Figure 4.54: Measured branch tube heat load at varying x_{mIn}, MPE-tube manifold (M5), upward flow configuration, refrigerant: HFC-134a, $\dot{m}_{mIn} = 0.033$ kg/s, $T_{w,tsIn} = 50°$C and $T_{mIn} = 29.5°$C.

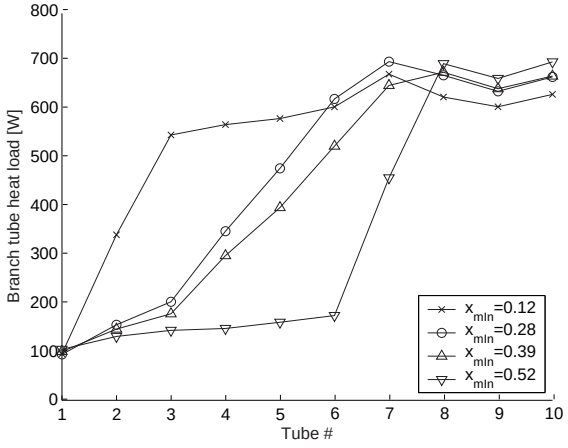

Figure 4.55: Measured branch tube heat load at varying x_{mIn}, MPE-tube manifold (M5), upward flow configuration, refrigerant: CO_2, $\dot{m}_{mIn} = 0.033$ kg/s, $T_{w,tsIn} = 40°$C and $T_{mIn} = 18.7°$C.

4.7.1.2 Two-phase distribution as a function of inlet mass flow rate

In Figures 4.56 and 4.57 the two-phase distribution is shown as function of mass flow rate at the manifold inlet, $\dot{m}_{mIn}$, for HFC-134a and CO_2, respectively. Es-

pecially for the CO_2 experiments, the two-phase distribution was unaffected by varying manifold inlet mass flow rate within the range of the measurements.

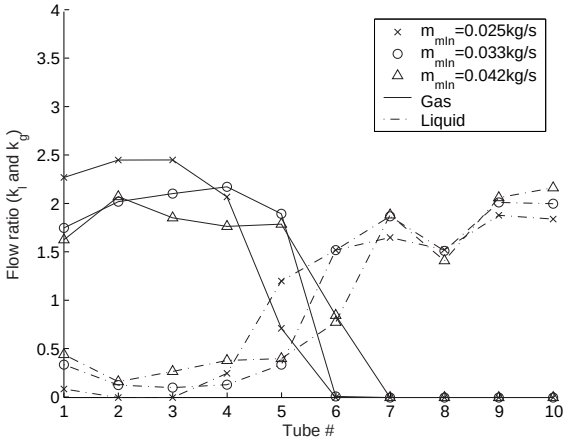

Figure 4.56: Measured two-phase distribution at varying $\dot{m}_{mIn}$, MPE-tube manifold (M5), upward flow configuration, refrigerant: HFC-134a, $x_{mIn} = 0.28$, $T_{w,tsIn} = 50°C$ and $T_{mIn} = 29.5°C$.

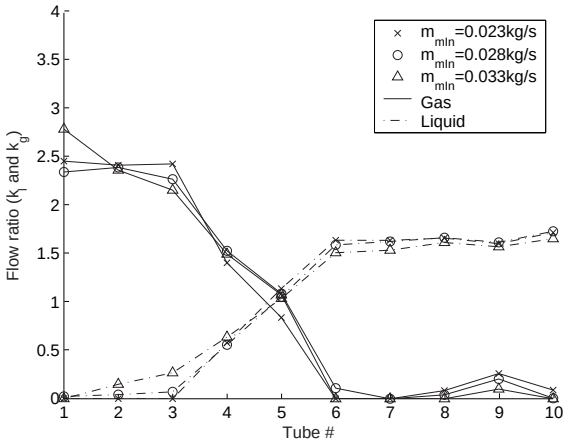

Figure 4.57: Measured two-phase distribution at varying $\dot{m}_{mIn}$, MPE-tube manifold (M5), upward flow configuration, refrigerant: CO_2, $x_{mIn} = 0.28$, $T_{w,tsIn} = 40°C$ and $T_{mIn} = 18.7°C$.

4.7.1.3 Two-phase distribution as a function of evaporator load

Figures 4.58 (HFC-134a) and 4.59 (CO_2) show the two-phase distribution as function of heat load on the evaporator. The distribution of both phases was very little affected by the heat load on the heat exchanger branch tubes.

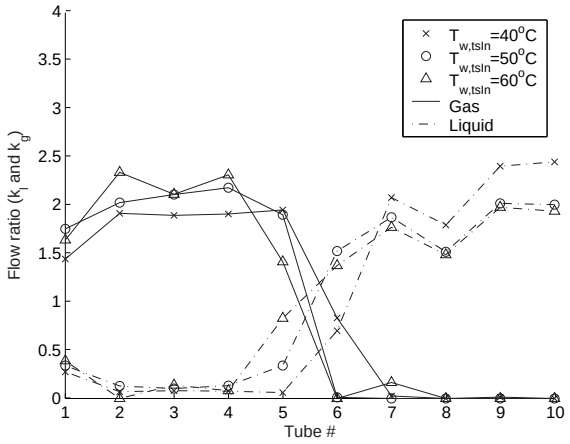

Figure 4.58: Measured two-phase distribution at varying $T_{w,tsIn}$, MPE-tube manifold (M5), upward flow configuration, refrigerant: HFC-134a, $x_{mIn} = 0.28$, $\dot{m}_{mIn} = 0.033$ kg/s and $T_{mIn} = 29.5°$C.

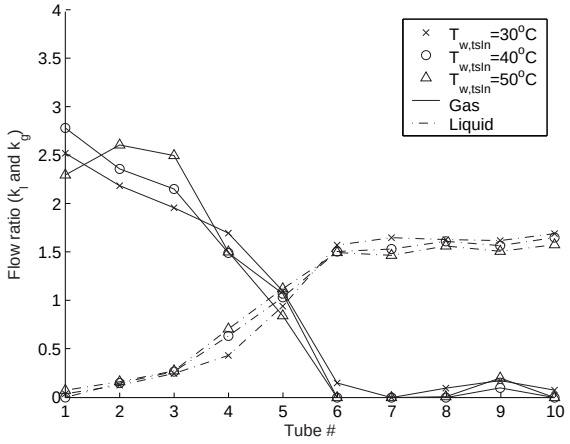

Figure 4.59: Measured two-phase distribution at varying $T_{w,tsIn}$, MPE-tube manifold (M5), upward flow configuration, refrigerant: CO_2, $x_{mIn} = 0.28$, $\dot{m}_{mIn} = 0.033$ kg/s and $T_{mIn} = 18.7°$C.

4.7.2 Downward flow configuration

4.7.2.1 Two-phase distribution as a function of inlet vapour fraction

Figure 4.60 and 4.61 show the two-phase distribution as a function of the manifold inlet vapour fraction in manifold M5 with downward configuration for HFC-134a and CO_2, respectively.

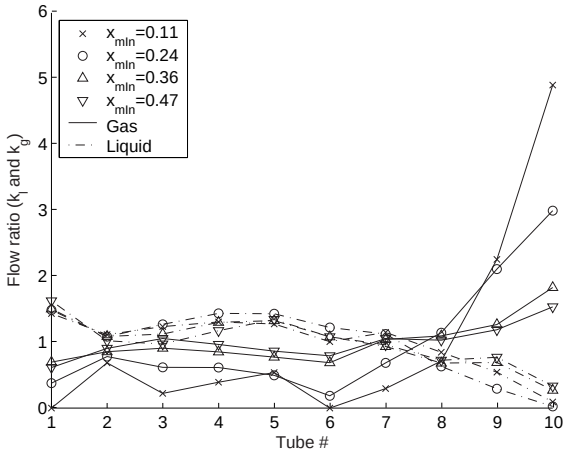

Figure 4.60: Measured two-phase distribution at varying x_{mIn}, MPE-tube manifold (M5), downward flow configuration, refrigerant: HFC-134a, $\dot{m}_{mIn} = 0.033$ kg/s, $T_{w,tsIn} = 50^{\circ}$C and $T_{mIn} = 29.5^{\circ}$C.

In the HFC-134a experiments, the liquid distribution was not much affected by change in vapour fraction at the inlet, while for the CO_2 experiments, the liquid distribution was more uniform at low values of x_{mIn}. For both fluids, the vapour distribution was best at the higher values of x_{mIn}. Measured heat load on the evaporator branch tubes is shown in Figures 4.62 and 4.63.

4.7.2.2 Two-phase distribution as a function of inlet mass flux

Two-phase distribution in the M5 manifold with downward configuration is shown as function of manifold inlet mass flow rate in Figures 4.64 and 4.65. The phase distribution dependents more on $\dot{m}_{mIn}$than what was the case in the ID 16 mm round tube manifold (Figure 4.31).

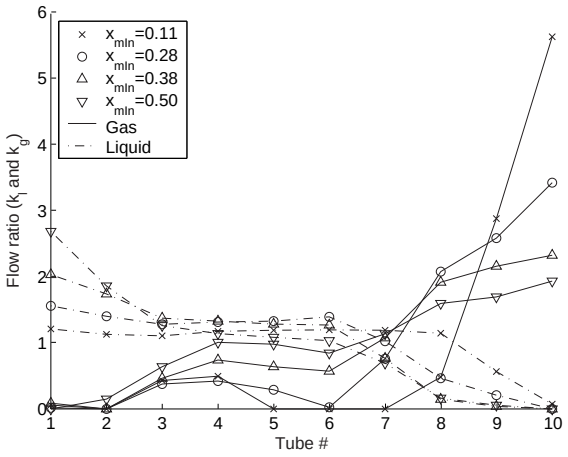

Figure 4.61: Measured two-phase distribution at varying x_{mIn}, MPE-tube manifold (M5), downward flow configuration, refrigerant: CO_2, $\dot{m}_{mIn} = 0.033$ kg/s, $T_{w,tsIn} = 40°$C and $T_{mIn} = 18.7°$C.

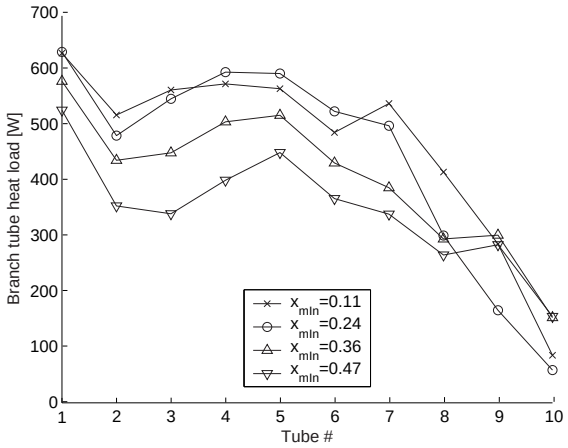

Figure 4.62: Measured branch tube heat load at varying x_{mIn}, MPE-tube manifold (M5), downward flow configuration, refrigerant: HFC-134a, $\dot{m}_{mIn} = 0.033$ kg/s, $T_{w,tsIn} = 50°$C and $T_{mIn} = 29.5°$C.

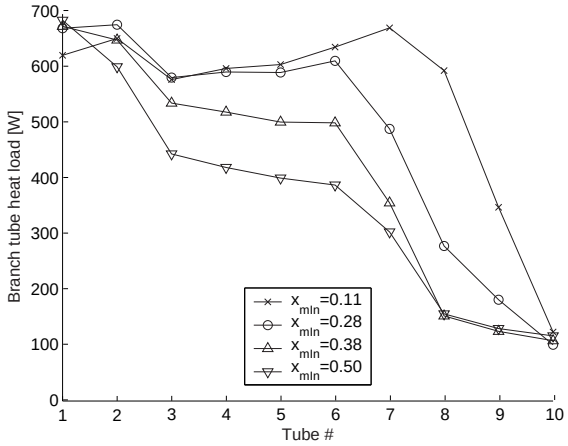

Figure 4.63: Measured branch tube heat load at varying x_{mIn}, MPE-tube manifold (M5), downward flow configuration, refrigerant: CO_2, $\dot{m}_{mIn} = 0.033$ kg/s, $T_{w,tsIn} = 40°C$ and $T_{mIn} = 18.7°C$.

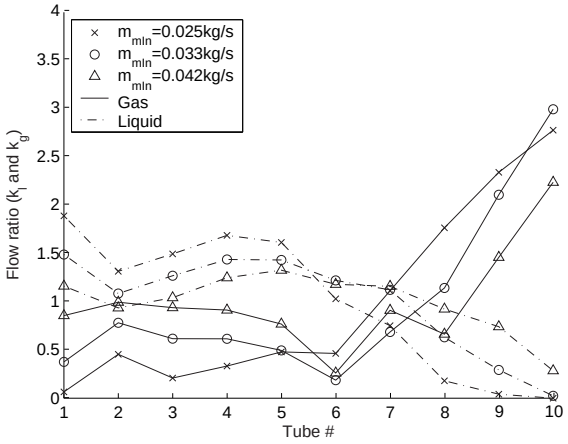

Figure 4.64: Measured two-phase distribution at varying $\dot{m}_{mIn}$, MPE-tube manifold (M5), downward flow configuration, refrigerant: HFC-134a, $x_{mIn} = 0.28$, $T_{w,tsIn} = 50°C$ and $T_{mIn} = 29.5°C$.

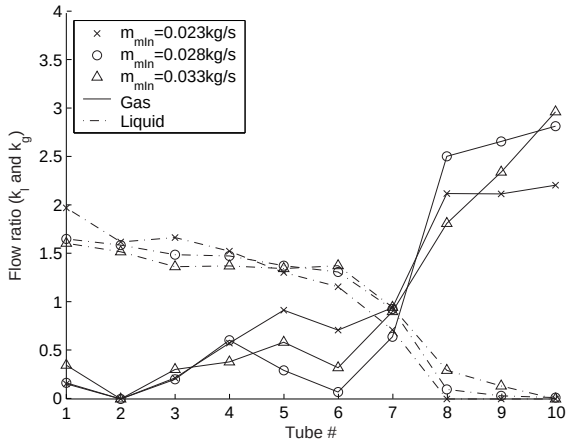

Figure 4.65: Measured two-phase distribution at varying $\dot{m}_{mIn}$, MPE-tube manifold (M5), downward flow configuration, refrigerant: CO_2, $x_{mIn} = 0.28$, $T_{w,tsIn} = 40°C$ and $T_{mIn} = 18.7°C$.

4.7.2.3 Two-phase distribution as a function of evaporator load

The effect of varying evaporator load on the two-phase distribution in the M5 manifold is seen in Figures 4.66 and 4.67. As for the round tube manifolds, the two-phase distribution was not much changed when varying the heat load on the evaporator branch tubes.

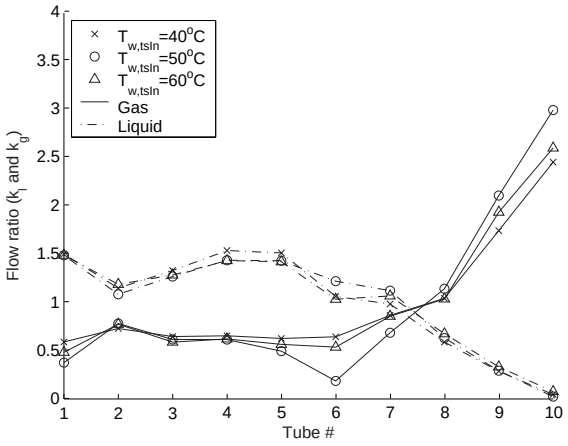

Figure 4.66: Measured two-phase distribution at varying $T_{w,tsIn}$, MPE-tube manifold (M5), downward flow configuration, refrigerant: HFC-134a, $x_{mIn} = 0.28$, $\dot{m}_{mIn} = 0.033$ kg/s and $T_{mIn} = 29.5°$C.

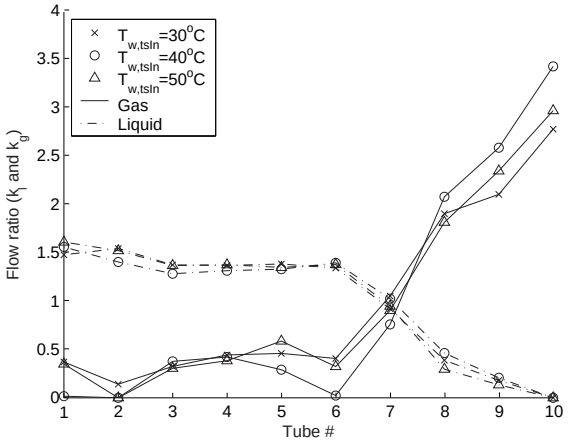

Figure 4.67: Measured two-phase distribution at varying $T_{w,tsIn}$, MPE-tube manifold (M5), downward flow configuration, refrigerant: CO_2, $x_{mIn} = 0.28$, $\dot{m}_{mIn} = 0.033$ kg/s and $T_{mIn} = 18.7°$C.

4.8 Two-phase distribution in MPE-tube manifold with tube insert ratio $r = 0.6$ (M6)

Figures 4.68 and 4.69 show the measured HFC-134a two-phase distribution in the MPE-manifold with tube insert ratio $r = 0.6$ (M6) in upward and downward configuration, respectively.

In upward configuration, the vapour phase was distributed somewhat more uniformly compared to the measurements in the base-case MPE-manifold shown in Figure 4.52. Small differences were seen for the liquid distribution.

The manifold M6 measurements in downward configuration showed a more irregular distribution pattern than what was the case for the base-case manifold (Figure 4.60). For manifold inlet vapour fractions above x_{mIn}= 0.13, the vapour phase was preferentially extracted to tubes No 3 to 6. For the measurements with manifold inlet vapour fraction x_{mIn}= 0.40 and x_{mIn}= 0.50, liquid was accumulated at the end of the manifold, and branch tubes No 7 to 10 received most liquid. At lower manifold inlet vapour fractions, the liquid take-off had a peak at branch tube No 7.

Corresponding measurements of heat load on the evaporator tubes are shown in Figures 4.70 and 4.71.

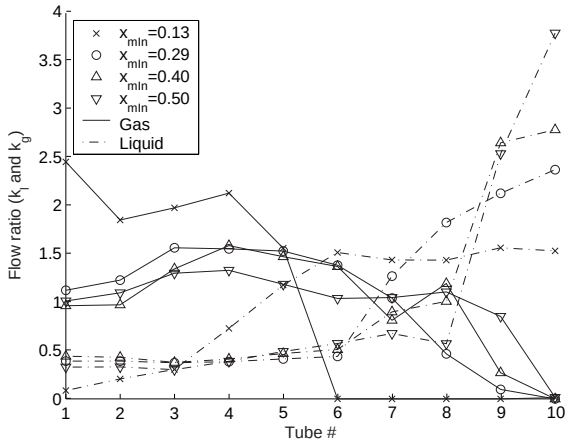

Figure 4.68: Measured two-phase distribution at varying x_{mIn}, MPE-tube manifold with tube insert ratio $r = 0.6$ (M6), upward flow configuration, refrigerant: HFC-134a, $\dot{m}_{mIn} = 0.033$ kg/s, $T_{w,tsIn} = 50°$C and $T_{mIn} = 29.5°$C.

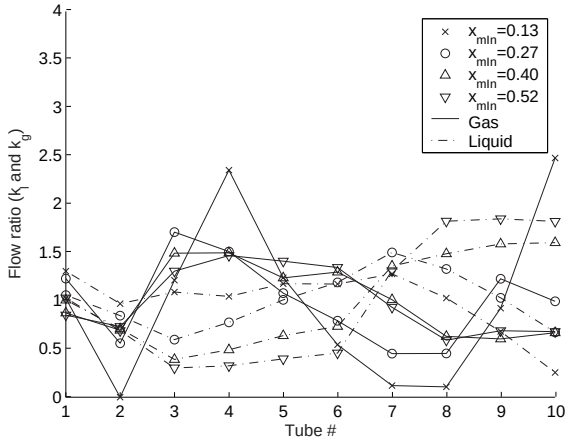

Figure 4.69: Measured two-phase distribution at varying x_{mIn}, MPE-tube manifold with tube insert ratio $r = 0.6$ (M6), downward flow configuration, refrigerant: HFC-134a, $\dot{m}_{mIn} = 0.033$ kg/s, $T_{w,tsIn} = 50°$C and $T_{mIn} = 29.5°$C.

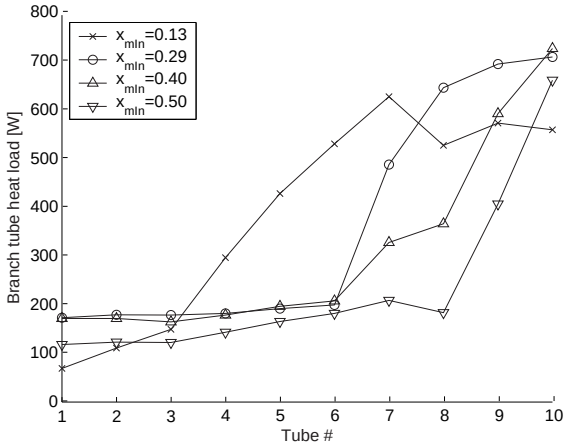

Figure 4.70: Measured branch tube heat load at varying x_{mIn}, MPE-tube manifold with tube insert ratio $r = 0.6$ (M6), upward flow configuration, refrigerant: HFC-134a, $\dot{m}_{mIn} = 0.033$ kg/s, $T_{w,tsIn} = 50°$C and $T_{mIn} = 29.5°$C.

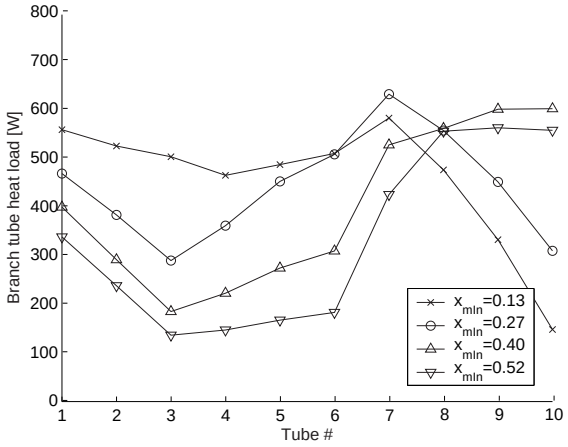

Figure 4.71: Measured branch tube heat load at varying x_{mIn}, MPE-tube manifold with tube insert ratio $r = 0.6$ (M6), downward flow configuration, refrigerant: HFC-134a, $\dot{m}_{mIn} = 0.033$ kg/s, $T_{w,tsIn} = 50°$C and $T_{mIn} = 29.5°$C.

4.9 Two-phase distribution in MPE-tube manifold with baffle insert (M7)

Two-phase distribution in both upward and downward configuration for the MPE-tube manifold with the baffle insert (M7) is shown in Figures 4.72 and 4.73.

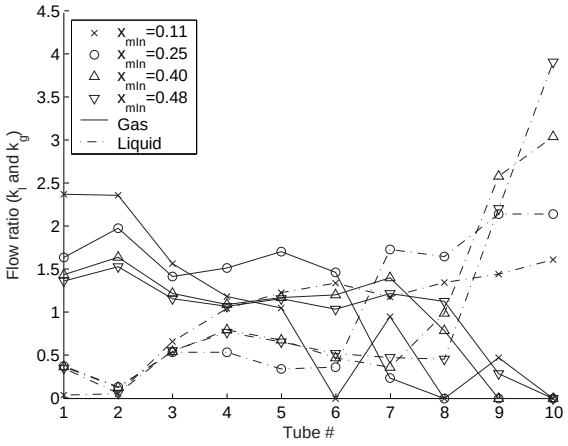

Figure 4.72: Measured two-phase distribution at varying x_{mIn}, MPE-tube manifold with baffle insert (M7), upward flow configuration, refrigerant: HFC-134a, $\dot{m}_{mIn} = 0.033$ kg/s, $T_{w,tsIn} = 50^{\circ}$C and $T_{mIn} = 29.5^{\circ}$C.

The liquid distribution was almost unchanged from the base-case manifold shown in Figure 4.52, while the vapour distribution was slightly improved.

In downward configuration, Figure 4.73, the liquid distribution was more affected by change in manifold inlet vapour fraction, than what was seen in the base-case manifold measurements, Figure 4.60. The vapour distribution was almost unchanged compared to the base-case manifold. Measured branch tube heat loads are shown in Figures 4.74 and 4.75.

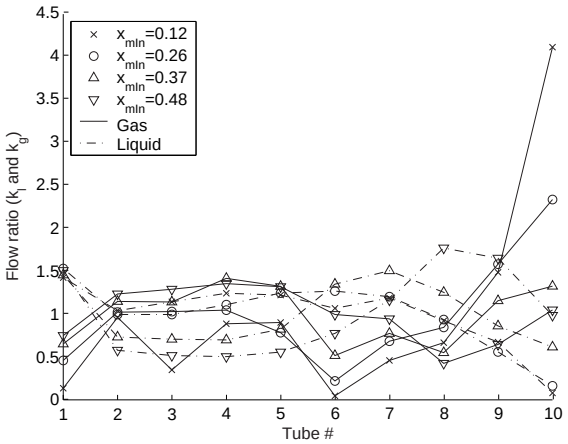

Figure 4.73: Measured two-phase distribution at varying x_{mIn}, MPE-tube manifold with baffle insert (M7), downward flow configuration, refrigerant: HFC-134a, $\dot{m}_{mIn} = 0.033$ kg/s, $T_{w,tsIn} = 50°$C and $T_{mIn} = 29.5°$C.

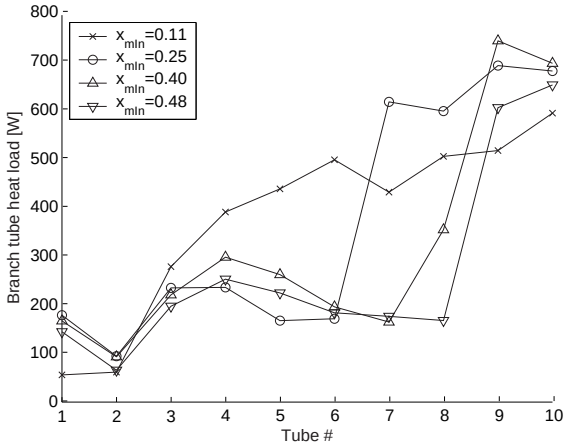

Figure 4.74: Measured branch tube heat load at varying x_{mIn}, MPE-tube manifold with baffle insert (M7), upward flow configuration, refrigerant: HFC-134a, $\dot{m}_{mIn} = 0.033$ kg/s, $T_{w,tsIn} = 50°$C and $T_{mIn} = 29.5°$C.

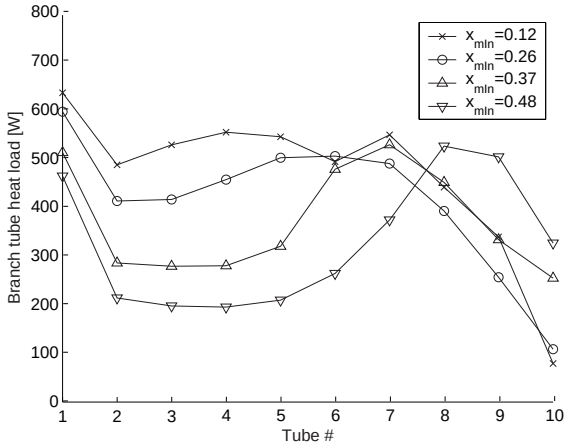

Figure 4.75: Measured branch tube heat load at varying x_{mIn}, MPE-tube manifold with baffle insert (M7), downward flow configuration, refrigerant: HFC-134a, $\dot{m}_{mIn} = 0.033$ kg/s, $T_{w,tsIn} = 50°$C and $T_{mIn} = 29.5°$C.

4.10 Two-phase distribution in MPE-tube manifold with 15 mm tube pitch (M8)

Figures 4.76 and 4.77 show the two-phase HFC-134a distribution in manifold M8 (MPE-manifold with tube pitch 15 mm). Both in upward and downward configuration, the two-phase distribution results were very similar to the results in the base-case MPE-manifold (M5) shown in Figure 4.52 and 4.60. Within the range of tested operating conditions it seemed that a reduction in tube pitch from 21 to 15 mm did not have significant influence on the two-phase flow distribution in the manifold.

Measured heat loads on the evaporator branch tubes are shown in Figures 4.78 and 4.79 for the measurements with manifold M8.

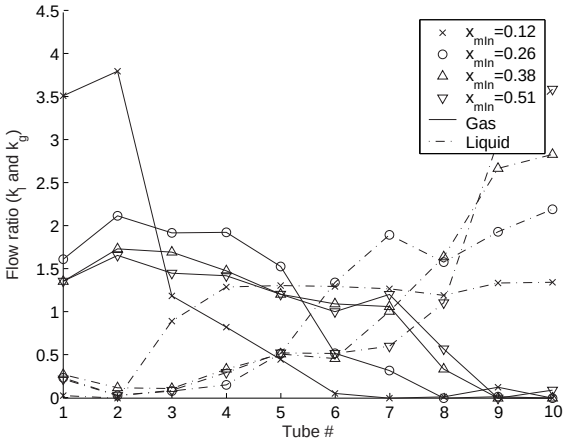

Figure 4.76: Measured two-phase distribution at varying x_{mIn}, MPE-tube manifold with 15 mm tube pitch (M8), upward flow configuration, refrigerant: HFC-134a, $\dot{m}_{mIn} = 0.033$ kg/s, $T_{w,tsIn} = 50°$C and $T_{mIn} = 29.5°$C.

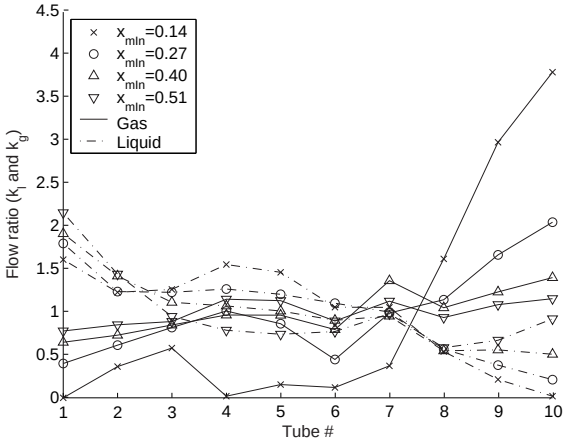

Figure 4.77: Measured two-phase distribution at varying x_{mIn}, MPE-tube manifold with 15 mm tube pitch (M8), downward flow configuration, refrigerant: HFC-134a, $\dot{m}_{mIn} = 0.033$ kg/s, $T_{w,tsIn} = 50°$C and $T_{mIn} = 29.5°$C.

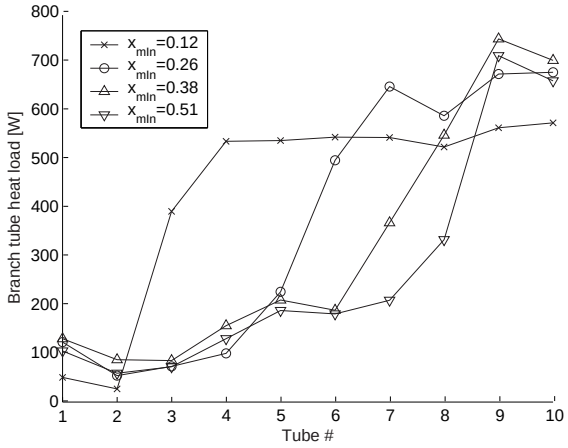

Figure 4.78: Measured branch tube heat load at varying x_{mIn}, MPE-tube manifold with 15 mm tube pitch (M8), upward flow configuration, refrigerant: HFC-134a, $\dot{m}_{mIn} = 0.033$ kg/s, $T_{w,tsIn} = 50°$C and $T_{mIn} = 29.5°$C.

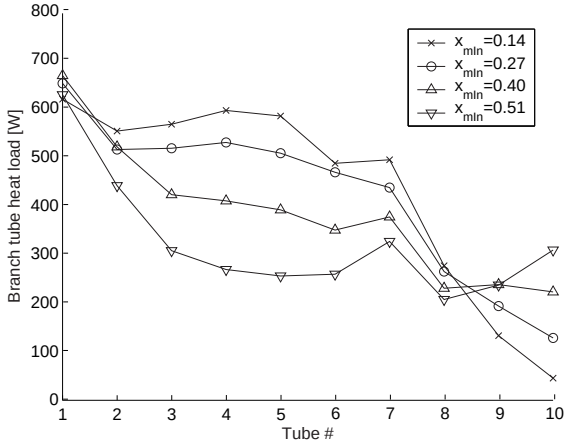

Figure 4.79: Measured branch tube heat load at varying x_{mIn}, MPE-tube manifold with 15mm tube pitch (M8), downward flow configuration, refrigerant: HFC-134a, $\dot{m}_{mIn} = 0.033$ kg/s, $T_{w,tsIn} = 50°$C and $T_{mIn} = 29.5°$C.

4.11 Two-phase distribution in MPE-tube manifold with spiral insert (M9)

4.11.1 Upward configuration

Two-phase distribution results with the static mixer at the inlet of the MPE-tube manifold (M9) are shown in Figures 4.80 and 4.81 for HFC-134a and CO_2, respectively.

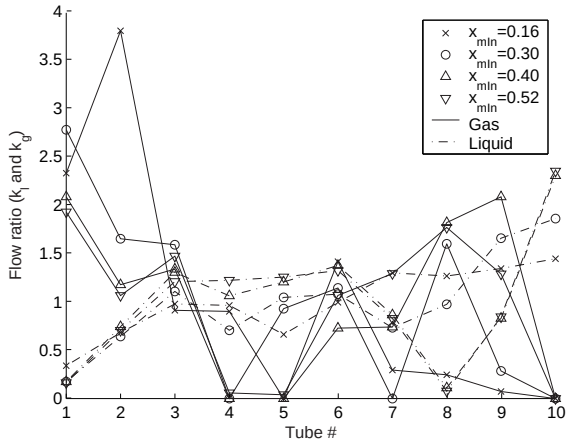

Figure 4.80: Measured two-phase distribution at varying x_{mIn}, MPE-tube manifold with spiral insert (M9), upward flow configuration, refrigerant: HFC-134a, $\dot{m}_{mIn} = 0.033$ kg/s, $T_{w,tsIn} = 50°$C and $T_{mIn} = 29.5°$C.

The two-phase distribution in upward configuration was more irregular than in the base-case MPE-tube manifold M5 in Figures 4.52 and 4.53, where the liquid was preferentially taken off in the last branch tubes, while the vapour was taken off in the first branch tubes of the manifold. The liquid phase distribution was quite similar for HFC-134a and CO_2 in Figures 4.80 and 4.81. More vapour was distributed to branch tubes *No* 1 to 3 in the HFC-134a measurements, while for the CO_2 measurements the gas was preferentially taken off in branch tubes *No* 4 to 6 at low manifold inlet vapour fraction and branch tubes *No* 8 and 9 in the high manifold inlet vapour fraction measurements. A detailed discussion of the flow dynamics causing the irregular distribution patterns is given in Chapter 5.

Measured heat load on the evaporator branch tubes are shown in Figures 4.82 and 4.83.

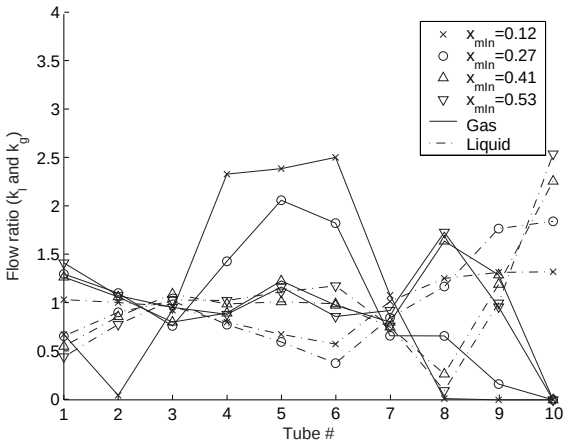

Figure 4.81: Measured two-phase distribution at varying x_{mIn}, MPE-tube manifold with spiral insert (M9), upward flow configuration, refrigerant: CO_2, $\dot{m}_{mIn} = 0.033$ kg/s, $T_{w,tsIn} = 40°C$ and $T_{mIn} = 18.7°C$.

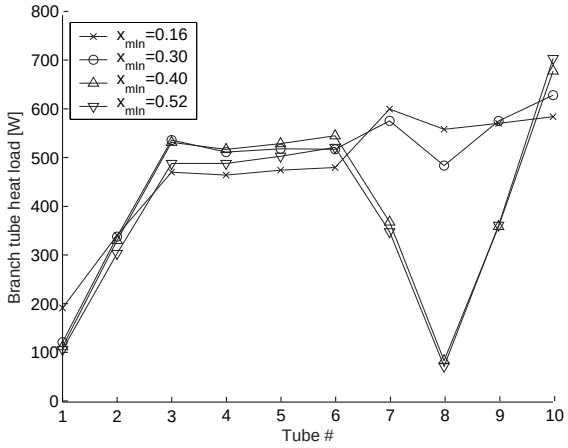

Figure 4.82: Measured branch tube heat load at varying x_{mIn}, MPE-tube manifold with spiral insert (M9), upward flow configuration, refrigerant: HFC-134a, $\dot{m}_{mIn} = 0.033$ kg/s, $T_{w,tsIn} = 50°C$ and $T_{mIn} = 29.5°C$.

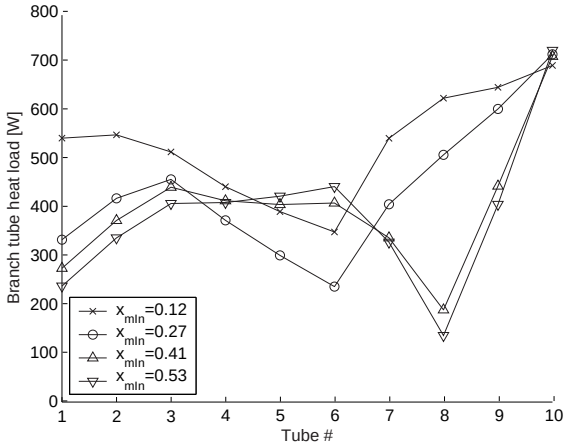

Figure 4.83: Measured branch tube heat load at varying x_{mIn}, MPE-tube manifold with spiral insert (M9), upward flow configuration, refrigerant: CO_2, $\dot{m}_{mIn} = 0.033$ kg/s, $T_{w,tsIn} = 40°C$ and $T_{mIn} = 18.7°C$.

4.11.2 Downward configuration

Results for manifold M9 in downward configuration are shown for HFC-134a and CO_2 in Figures 4.84 and 4.85.

Compared to the base-case MPE-tube manifold results in Figures 4.60 and 4.61, where the liquid preferentially was distributed to the first branch tubes and vapour was distributed to the last branch tubes of the manifold, the two-phase distribution pattern was changed radically. The liquid distribution pattern was quite similar for the measurements with HFC-134a and CO_2 in Figures 4.84 and 4.85. Small differences were seen for changes in vapour fraction at the inlet of the manifold, x_{mIn}. The liquid was preferentially distributed to branch tubes *No* 2 to 9, with an underfeeding of the first and last tube in the manifold, while the vapour phase was preferentially distributed to the branch tubes which was underfed with liquid.

Corresponding measurements of the heat load on the evaporator branch tubes are shown in Figures 4.86 and 4.87.

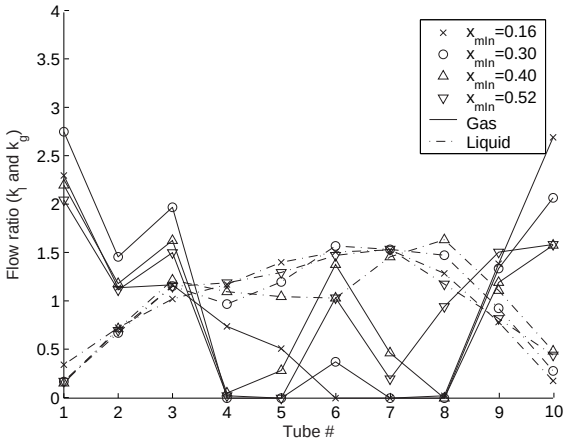

Figure 4.84: Measured two-phase distribution at varying x_{mIn}, MPE-tube manifold with spiral insert (M9), downward flow configuration, refrigerant: HFC-134a, $\dot{m}_{mIn} = 0.033$ kg/s, $T_{w,tsIn} = 50°$C and $T_{mIn} = 29.5°$C.

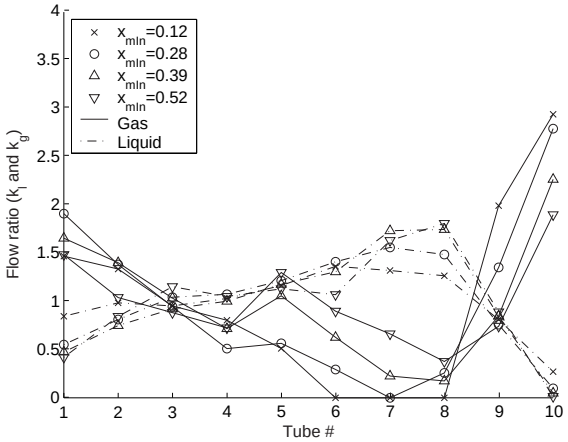

Figure 4.85: Measured two-phase distribution at varying x_{mIn}, MPE-tube manifold with spiral insert (M9), downward flow configuration, refrigerant: CO_2, $\dot{m}_{mIn} = 0.033$ kg/s, $T_{w,tsIn} = 40°$C and $T_{mIn} = 18.7°$C.

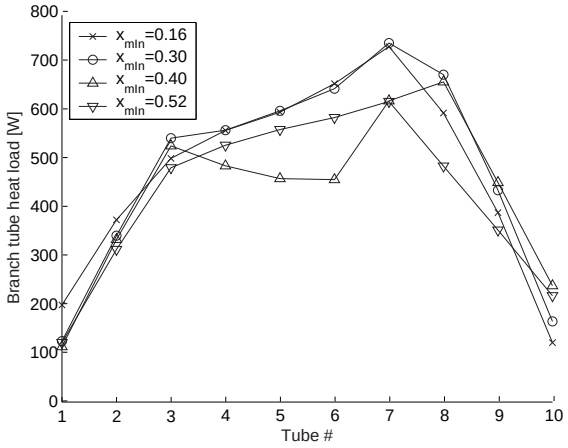

Figure 4.86: Measured branch tube heat load at varying x_{mIn}, MPE-tube manifold with spiral insert (M9), downward flow configuration, refrigerant: HFC-134a, $\dot{m}_{mIn} = 0.033$ kg/s, $T_{w,tsIn} = 50°$C and $T_{mIn} = 29.5°$C.

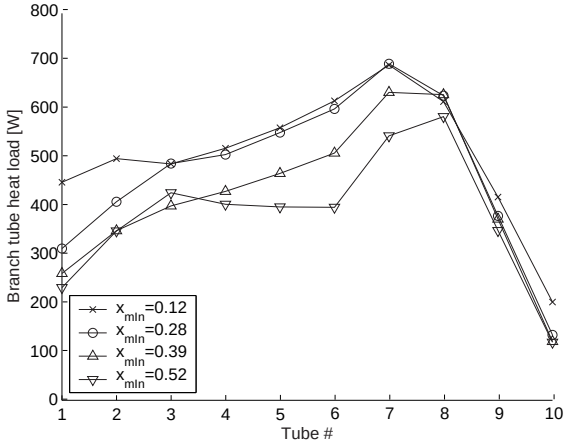

Figure 4.87: Measured branch tube heat load at varying x_{mIn}, MPE-tube manifold with spiral insert (M9), downward flow configuration, refrigerant: CO_2, $\dot{m}_{mIn} = 0.033$ kg/s, $T_{w,tsIn} = 40°$C and $T_{mIn} = 18.7°$C.

4.12 Two-phase distribution in MPE-tube manifold with progressive insert (M10)

Figures 4.88 and 4.89 contain results obtained with the MPE-manifold with progressive insert (M10), shown in Figure 4.8, for upward and downward configuration, respectively.

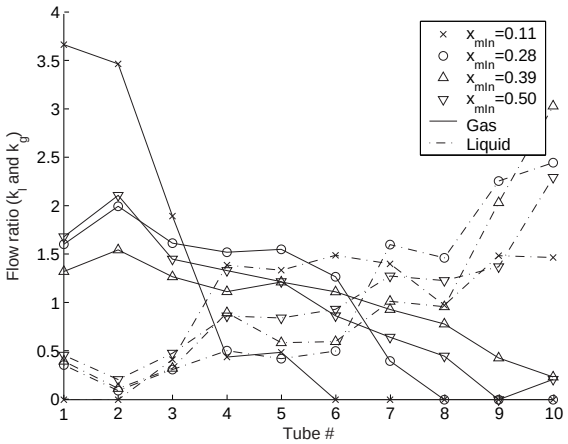

Figure 4.88: Measured two-phase distribution at varying x_{mIn}, MPE-tube manifold with progressive insert (M10), upward flow configuration, refrigerant: HFC-134a, $\dot{m}_{mIn} = 0.033$ kg/s, $T_{w,tsIn} = 50°$C and $T_{mIn} = 29.5°$C.

Comparing the results in upward configuration, Figure 4.88, with results from the base-case manifold, Figure 4.52, small differences in two-phase distribution are seen, except for some enhancement in the vapour distribution.

In downward configuration, Figure 4.89, there was a significant change in the distribution pattern compared to the base-case MPE-manifold (Figure 4.60). The liquid phase was now preferentially distributed to the last branch tube in the manifold, with a corresponding depression of the vapour feeding in that branch tube. Larger differences between the two-phase distributions at varying values of x_{mIn}were also seen, compared to the base-case MPE-tube manifold.

Measured heat lead on the evaporator branch tubes are shown in Figures 4.90 and 4.91 for upward and downward configuration in manifold M10, respectively.

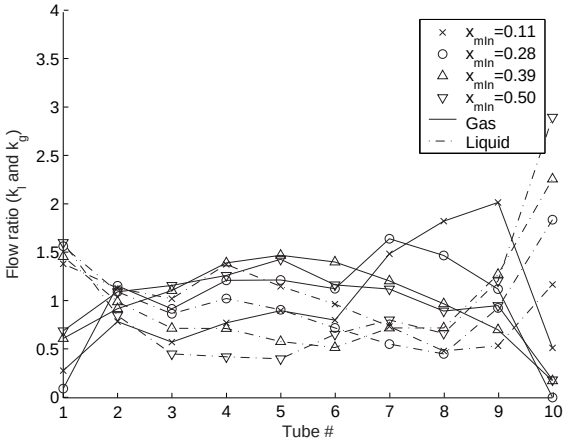

Figure 4.89: Measured two-phase distribution at varying x_{mIn}, MPE-tube manifold with progressive insert (M10), downward flow configuration, refrigerant: HFC-134a, $\dot{m}_{mIn} = 0.033$ kg/s, $T_{w,tsIn} = 50°$C and $T_{mIn} = 29.5°$C.

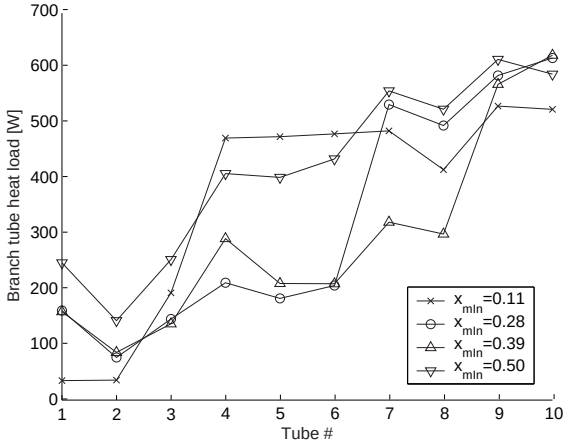

Figure 4.90: Measured branch tube heat load at varying x_{mIn}, MPE-tube manifold with progressive insert (M10), upward flow configuration, refrigerant: HFC-134a, $\dot{m}_{mIn} = 0.033$ kg/s, $T_{w,tsIn} = 50°$C and $T_{mIn} = 29.5°$C.

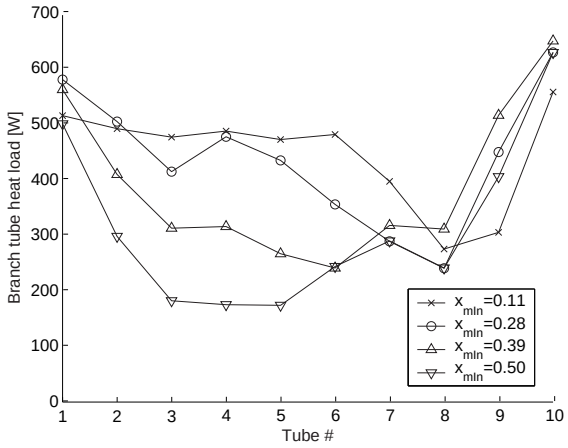

Figure 4.91: Measured branch tube heat load at varying x_{mIn}, MPE-tube manifold with progressive insert (M10), downward flow configuration, refrigerant: HFC-134a, $\dot{m}_{mIn} = 0.033$ kg/s, $T_{w,tsIn} = 50°$C and $T_{mIn} = 29.5°$C.

4.13 Two-phase distribution in star manifold (M11)

Two-phase distribution measurements with the star manifold (M11) at varying vapour fraction at the manifold inlet is shown in Figure 4.92. The manifold and the branch tube numbering were shown in Figure 4.9.

Gross maldistribution were seen both for the vapour and liquid phase. The geometrical symmetry of the manifold was reflected in the two-phase distribution. The second row of branch tubes at the bottom of the manifold, *No* 2 and 7, received most liquid, while the first row of branch tubes at the top of the manifold, *No* 3 and 6, received most vapour. Measured heat load on the evaporator branch tubes is shown in Figure 4.93.

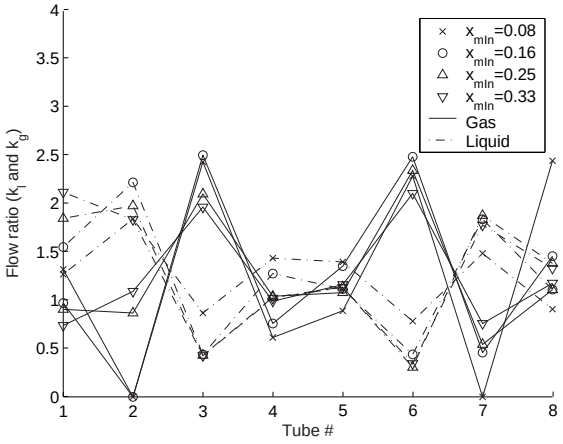

Figure 4.92: Measured two-phase distribution at varying x_{mIn}, Star manifold (M11), refrigerant: HFC-134a, $\dot{m}_{mIn} = 0.033$ kg/s, $T_{w,tsIn} = 50°$C and $T_{mIn} = 29.5°$C.

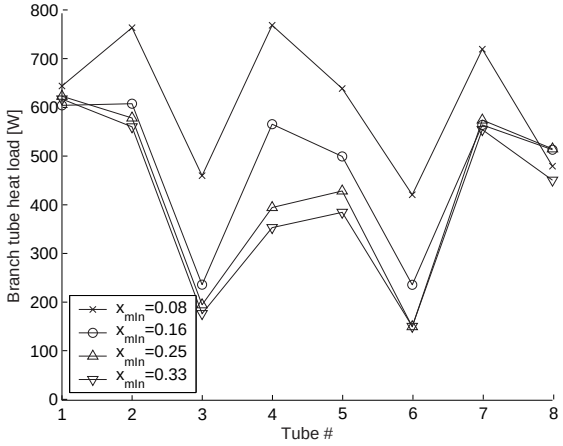

Figure 4.93: Measured branch tube heat load at varying x_{mIn}, star manifold (M11), refrigerant: HFC-134a, $\dot{m}_{mIn} = 0.033$ kg/s, $T_{w,tsIn} = 50°$C and $T_{mIn} = 29.5°$C.

4.14 Two-phase distribution performance - comparison of manifold geometries

4.14.1 Definitions to quantify manifold distribution performance

In order to characterize the performance of the manifold geometries in terms of two-phase distribution, a set of definitions was developed. These definitions quantified how well the two-phase flow was distributed to the branch tubes.

In the experimental results, the mass flow rate distribution was measured directly. The uniformity of the refrigerant mass flow distribution in the manifold is characterized by the deviation from the average branch tube mass flow rate, $\overline{\dot{m}_t}$:

$$STD_{\dot{m}_t} = \frac{\sqrt{VAR_{\dot{m}_t}}}{\dot{m}_t} = \frac{\sqrt{\frac{\sum_{i=1}^{N_t}\left(\dot{m}_{t,i}-\overline{\dot{m}_t}\right)^2}{N_t}}}{\overline{\dot{m}_t}} \tag{4.4}$$

The normalized standard deviation $STD_{\dot{m}_t}$ is a measure of the uniformity of the mass flow rate distribution in the branch tubes. The standard deviation is normalized with the average branch tube mass flow rate.

The uniformity of the mass flow distribution is an important measure, but even at uniform mass flow rate distribution, the distribution of the liquid and vapour phases can be highly nonuniform. Separate measures for the phase flow rate distributions are therefore necessary for analysis of the effects of two-phase flow distribution. Non-uniformities in the distributions of vapour and liquid flow rates can cancel out or amplify each other. It is therefore necessary to also analyse the total mass flow rate uniformity in addition to the uniformity in distribution of the vapour and liquid flow rates in order to quantify the manifold two-phase distribution.

The flow ratio, k, defined by Equation 4.3 is used to characterize the distribution of the liquid and vapour phases:

$$STD_{k_p} = \sqrt{VAR_{k_p}} = \sqrt{\frac{\sum_{i=1}^{N_t}\left(k_{p,i}-\overline{k}_p\right)^2}{N_t}} \tag{4.5}$$

where $p = l$ (liquid) and $p = g$ (gas). By definition, the average value of the flow ratio, $\overline{k}_p$ is equal to unity.

In the experimental facility, the uniformity of the measured heat transfer rate in the heat exchanger tubes were a indirect measurement of the distribution of the two-phase flow in the inlet manifold. The transferred heat in the branch tubes was affected both by the liquid and the vapour flow rate distributions in the manifold. In addition to the two-phase distribution, the uniformity in transferred heat in the heat exchanger branch tubes is also affected by the heat exchanger load. The variation in the branch tube heat transfer is defined by a normalized standard deviation:

$$STD_{\dot{Q}_{ts}} = \frac{\sqrt{\frac{\sum_{i=1}^{N_t}\left(\dot{Q}_{ts,i}-\overline{\dot{Q}}_{ts}\right)^2}{N_t}}}{\overline{\dot{Q}}_{ts}} \tag{4.6}$$

where $\overline{\dot{Q}}_{ts}$ is the average branch tube heat transfer.

4.14.2 Mass flow distribution

The standard deviation in branch tube mass flow rate distribution was calculated by Equation 4.4. Table 4.3 shows the calculated standard deviation values, expressed in per cent of the average branch tube mass flow rate values, based on all measurement series with two-phase flow at the inlet of the manifold.

Some conclusions can be drawn from the results shown in Table 4.3:

- The most uniform mass flow rate distribution was seen in the results of the ID 16 mm manifold (M1) with upward flow configuration and in the ID 8 mm manifold (M3) with downward configuration.
- The mass flow distribution was more uniform in downward configuration than in upward configuration (with exception of the ID 16 mm manifold, M1, results).
- The uniformity in mass flow rate distribution was better in the round tube manifolds compared to the MPE-tube manifolds.
- In upward flow configuration, the mass flow rate distribution was more uniform in the experiments with CO_2 than in the experiments with HFC-134a.
- In downward flow configuration the mass flow rate distribution was more uniform in the experiments with CO_2 than in the experiments with HFC-134a in the MPE-tube manifolds, but opposite in the round tube manifolds.

- In the HFC-134a experiments with upward configuration, the uniformity in mass flow rate distribution was almost equal for the MPE-tube manifolds, M5 to M10.
- The star manifold (M11) mass flow rate distribution was better than the MPE-tube manifold distributions in upward configuration, but in the same range as the MPE-tube manifolds in downward configuration.

Table 4.3: Standard deviation for branch tube mass flow distribution, $STD_{\dot{m}_t}$, expressed in per cent of average branch tube mass flow rate.

Manifold ID	Description	Upward configuration		Downward configuration	
		HFC-134a	CO_2	HFC-134a	CO_2
M1	ID 16 mm round tube manifold	5.81	6.75	6.79	11.29
M2	ID 12 mm round tube manifold	13.01			
M3	ID 8 mm round tube manifold	10.92	6.92	4.48	5.72
M4	M3 + short inlet tube	13.85		10.79	
M5	MPE-tube manifold	29.64	20.21	17.35	16.20
M6	M5 + 0.6D tube insert	33.62		18.05	
M7	M5 + baffle insert	29.22		12.89	
M8	M5 + 15mm tube pitch	29.80		22.76	
M9	M5 + spiral insert	29.70	15.17	24.24	13.35
M10	M5 + progressive insert	30.30		20.96	
M11	Star manifold	20.59			

4.14.3 Liquid phase distribution

The uniformity in branch tube liquid mass flow rates was calculated by Equation 4.5. Table 4.4 shows the calculated standard deviation values, in per cent of the liquid flow ratio, for all measurement series with two-phase flow at the inlet of the manifold.

Conclusions from the main results shown in Table 4.4 can be given:

- Most uniform liquid mass flow rate distribution was seen in the results of the ID 8 mm manifold with short inlet tube length, M4.
- The liquid mass flow distribution was most uniform in downward configuration (with exception of the CO_2 experiments in the ID 16 mm manifold, M1).
- The round tube manifolds had more uniform liquid mass flow distribution than the MPE-tube manifolds (with exception of the ID 12 mm manifold (M2)).
- In upward flow configuration, the liquid mass flow rate distribution was more uniform in the experiments with CO_2 than in the experiments with HFC-134a.
- In downward flow configuration the liquid mass flow rate distribution was more uniform in the experiments with HFC-134a than in the experiments with CO_2 (with exception of the experiments in M9).
- In the HFC-134a experiments with upward configuration, the uniformity in liquid mass flow rate distribution was almost equal for the MPE-tube manifolds, M5, M6, M7, M8 and M10. Manifold M9 with spiral insert showed an improved liquid distribution performance.
- The star manifold (M11) liquid mass flow rate distribution was more uniform than the base-case MPE-tube manifold (M5) in upward configuration, but less uniform than M5 in downward configuration.

Table 4.4: Uniformity of branch tube liquid mass flow rate distribution, given as standard deviation in per cent of the flow ratio.

Manifold ID	Description	Upward configuration		Downward configuration	
		HFC-134a	CO_2	HFC-134a	CO_2
M1	ID 16 mm round tube manifold	62.14	60.60	45.78	65.52
M2	ID 12 mm round tube manifold	81.81			
M3	ID 8 mm round tube manifold	49.70	38.24	30.08	40.55
M4	M3 + short inlet tube	37.09		21.97	
M5	MPE-tube manifold	85.43	69.79	43.64	61.35
M6	M5 + 0.6D tube insert	80.06		38.40	
M7	M5 + baffle insert	84.31		38.33	
M8	M5 + 15mm tube pitch	87.96		46.05	
M9	M5 + spiral insert	53.58	46.48	47.89	45.12
M10	M5 + progressive insert	81.46		45.97	
M11	Star manifold	53.57			

4.14.4 Vapour phase distribution

Equation 4.5 was used to calculate the uniformity in branch tube vapour mass flow rates. Table 4.5 shows the calculated standard deviation values, in per cent of the vapour phase flow ratio, for all measurement series with two-phase flow at the manifold inlet.

Some observations from the results shown in Table 4.5 can be given:

- Manifold M7 was seen to have most uniform vapour mass flow rate distribution in upward flow configuration, while manifold M6 and M10 had best performance in downward flow configuration.
- The vapour mass flow distribution was most uniform in downward configuration (Except for the experiments in M9 and the CO_2 experiments in M3).
- In upward flow configuration, the vapour mass flow rate distribution was

more uniform in the experiments with CO_2 than in the experiments with HFC-134a (with exception of M1).

- In downward flow configuration the vapour mass flow rate distribution was more uniform in the experiments with HFC-134a than in the experiments with CO_2 (Except for the experiments in M9).
- The star manifold (M11) vapour mass flow rate uniformity was comparable to the uniformity of the MPE-tube manifolds in upward configuration, but less uniform than the distribution in the MPE-tube manifolds in downward configuration (with exception of the experiments in M9).

Table 4.5: Uniformity of branch tube vapour mass flow rate distribution, given as standard deviation in per cent of the flow ratio.

Manifold ID	Description	Upward configuration		Downward configuration	
		HFC-134a	CO_2	HFC-134a	CO_2
M1	ID 16 mm round tube manifold	113.01	128.94	117.15	128.58
M2	ID 12 mm round tube manifold	105.26			
M3	ID 8 mm round tube manifold	107.23	77.45	80.17	102.28
M4	M3 + short inlet tube	72.63		59.18	
M5	MPE-tube manifold	96.11	105.14	68.80	101.44
M6	M5 + 0.6D tube insert	70.03		44.51	
M7	M5 + baffle insert	66.12		57.61	
M8	M5 + 15mm tube pitch	85.56		54.12	
M9	M5 + spiral insert	80.23	66.39	84.65	77.39
M10	M5 + progressive insert	75.33		42.81	
M11	Star manifold	72.18			

4.14.5 Branch tube heat transfer

To evaluate the influence of two-phase distribution on the performance of the heat exchanger, the uniformity of the branch tube heat transfer is useful. In this Section the uniformity in calculated branch tube heat transfer is calculated by Equation 4.6. Table 4.6 shows the calculated standard deviation values, in per cent of the average branch tube heat transfer, for all measurement series with two-phase flow at the inlet of the manifold.

Table 4.6: Uniformity in calculated branch tube heat transfer, given as standard deviation in per cent of the average branch tube heat transfer.

Manifold ID	Description	Upward configuration		Downward configuration	
		HFC-134a	CO_2	HFC-134a	CO_2
M1	ID 16 mm round tube manifold	50.52	44.12	37.73	47.68
M2	ID 12 mm round tube manifold	64.44			
M3	ID 8 mm round tube manifold	36.91	25.84	24.86	29.15
M4	M3 + short inlet tube	24.39		12.42	
M5	MPE-tube manifold	62.41	51.11	36.00	44.33
M6	M5 + 0.6D tube insert	55.25		29.36	
M7	M5 + baffle insert	61.83		32.41	
M8	M5 + 15mm tube pitch	69.23		38.52	
M9	M5 + spiral insert	36.40	31.09	38.89	33.16
M10	M5 + progressive insert	55.32		28.65	
M11	Star manifold	31.95			

Some conclusions from the results shown in Table 4.6 can be given:

- Large deviations in branch tube heat transfer rates were measured (ranging from 12.42% in manifold M4 with downward configuration to 69.23% in M8 with upward configuration).
- The ID 8 mm round tube manifold with short inlet tube length, M4, had the most uniform branch tube heat transfer rate both in upward and downward configuration.

- The branch tube heat transfer distribution was most uniform in downward configuration (with exception of the experiments in M9 and the CO_2 experiments in M1 and M3).
- In upward flow configuration, the branch tube heat transfer rate distribution was more uniform in the experiments with CO_2 than in the experiments with HFC-134a.
- In downward flow configuration the branch tube heat transfer rate distribution was more uniform in the experiments with HFC-134a than in the experiments with CO_2 (with exception of the experiments in M9).
- The only modification to the base-case MPE-tube manifold (M5) giving significant improvement in branch tube heat transfer distribution in upward flow configuration was the manifold with spiral insert at the inlet (M9).
- In downward flow configuration, geometry modifications to the base-case MPE-tube manifold (M5) gave small changes in branch tube heat transfer distribution.
- The star manifold (M11) branch tube heat transfer rate was more uniform than in the MPE-tube manifolds in upward configuration, but in the same range as in the MPE-tube manifolds in downward configuration.

Chapter 5

Analysis and Discussion of Experimental Results

5.1 Chapter overview

As discussed in Section 2.6, there has been a need for T-junction correlations in one-dimensional codes for calculation of two-phase flow phenomena in large thermo-hydraulic systems, e.g. nuclear reactors. Likewise, correlations for the phase split in manifolds are needed to be able to make computer simulations of the effects of two-phase flow maldistribution in compact heat exchangers. So far, there have been no reports on development of correlations for two-phase flow distribution which have been utilized in heat exchanger capacity simulations. The present Chapter outlines empirical correlations based on the experimental data presented in Chapter 4, which will be used in heat exchanger simulations in Chapter 6.

The Chapter starts by outlining the modelling concepts used in the correlation development and a discussion of the choices of selected correlations from literature, which the data are compared to. The experimental two-phase flow distribution data are reduced in order to be compared to the correlations.

Section 5.3 contains the analysis of the experimental data obtained in manifolds with vertical upward directed branch tubes. Starting with an analysis of the round tube ID 16 mm and ID 8 mm manifold data, the method is generalized by taking into account the measured phase split in the different geometries of the MPE-tube manifolds. A new correlation is presented in Section 5.3.5 and a discussion of

various factors affecting the two-phase flow distribution is given in Section 5.3.6.

Following the same methodology as for the analysis of the upward configuration data, the experimental results from the manifolds with vertical downward branch tubes are correlated and analysed in Section 5.4.

5.2 Basis for correlation development

5.2.1 Selection of correlation model concept

The concept used by Tompkins et al. (2002a) for two-phase manifold distribution, described in Section 2.7.2, and previously used by e.g. Bajura and Jones Jr (1976) and Chou and Cheng (2001) for single phase flow distribution, couples the two-phase distribution in all T-junctions of the manifold by a set of mass and momentum conservation equations. Tompkins et al. (2002a) claimed that an advantage with this approach was that boundary conditions only had to be set for the incoming flow to the manifold. This was a plausible approach for their setup, where all branches were vented to atmospheric pressure. However, in a real heat exchanger, the pressure drop in the individual heat exchanger channels and the pressure distribution in the outlet manifold have to be taken into account. The pressure drop in the heat exchanger channels will strongly affect the two-phase flow that will enter each separate channel. This pressure coupling between the T-junctions of the inlet manifold and the pressure drop in the heat exchanger tubes are important to take into account in heat exchanger analysis, and also in the present test rig setup. By using experimental measurements of the pressure distribution at the inlet of each branch tube, it would have been possible to adapt the model of Tompkins et al. (2002a), by including these in the model. However, because no local pressure measurements on the branch tubes are available, there is not enough information to utilize the modelling concept of Tompkins et al. (2002a). In addition, Tompkins et al. (2002a) used the empirical coefficients for pressure drop/gain in the manifold defined by Saba and Lahey (1984). These coefficients were developed for regular round tube T-junctions without branch protrusion into the main tube. Especially for the MPE-manifold geometries used in this study, the pressure drop coefficients of Saba and Lahey (1984) are probably not representative. Tompkins et al. (2002a) had to impose ”pressure reduction factors”, which were tuned to each measurement series, to be able to predict the mass flow rate distribution.

A second conceptual method which can be used when analysing two-phase distribution in manifolds is to regard the manifold as a series of sequential T-junctions.

This makes it possible to follow the methods used for single T-junctions, outlined in Section 2.5, to model the phase split in each separate manifold T-junction as a function of the inlet mass flow rate, inlet vapour fraction and branch tube mass flow rate. The remaining flow from one T-junction constitutes the incoming flow to the next T-junction in the manifold.

Moura (1990) stated that the use of T-junction analysis methods was not applicable for manifolds with short distance between the branch tubes. However, the results of Watanabe et al. (1995) showed that the phase split in the manifold only depended on the local flow properties upstream each T-junction in the manifold.

Based on the restrictions and shortcomings involved with the modelling concept of Tompkins et al. (2002a), the modelling concept used in the literature on T-junctions is followed in the present analysis. Hence, both the influence of the inlet stream to the local T-junction and the branch mass flow, which is strongly dependent on the downstream branch tube pressure losses, are taken into account in the correlation of the T-junction phase split. This makes it easy to compare the physics involved in the manifold two-phase distribution split with the large amounts of measurement data, which the T-junctions correlations are based upon. Because the manifold is conceptually divided in separate T-junctions the models also become relatively simple to incorporate in a heat exchanger analysis, which is necessary for the assessment of the consequences of two-phase maldistribution on the capacity of real heat exchangers (see Chapter 6). Figure 5.1 shows the flow properties involved in the correlation of the local manifold T-junction phase split.

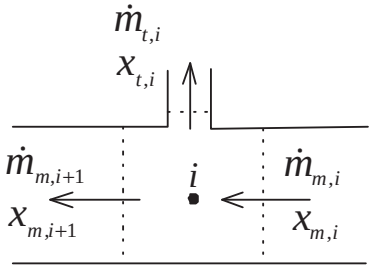

Figure 5.1: Flow properties involved in phase split correlations for the manifold T-junction *No i*.

Known properties: $\dot{m}_{m,i}$, $x_{m,i}$, $\dot{m}_{t,i}$

Property to be correlated: $x_{t,i}$

In the correlation development outlined in the current Chapter, the value of $\dot{m}_{t,i}$ is

given explicitly from the measurements. The values of $\dot{m}_{m,i}$ and $x_{m,i}$ are calculated based on a reduction of the experimental values as shown in Section 5.2.2. When the phase split correlations are used in a heat exchanger model the values of $\dot{m}_{t,i}$ will be provided by an overall system model that handles both the manifold split calculations and modelling of the heat exchanger tubes (see Chapter 6).

5.2.2 Reduction of experimental manifold data

For the development of the correlations discussed in Section 5.2.1, the local flow properties along the manifold are needed. As described in Section 3.3 the mass flow at the manifold inlet, $\dot{m}_{mIn}$, and the mass flow at the inlet of the branches, $\dot{m}_{t,i=1..10}$, are measured by coriolis flow meters. Notations are shown in Figure 5.2.

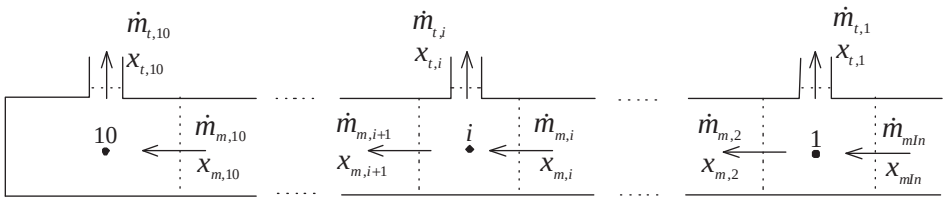

Figure 5.2: Discretization used in the model development.

From calorimetric calculations in the test rig, described in Section 3.5, the vapour fraction at the manifold inlet, x_{mIn}, and at the branch inlets, $x_{t,i=1..10}$, are known. Due to experimental uncertainties, a correction procedure is employed such that the sum of the branch mass flow rates becomes equal to the manifold inlet mass flow rate. A correction factor for the measured branch mass flow rate values is defined:

$$CF_{\dot{m}} = \frac{\dot{m}_{mIn}^{meas}}{\sum_{i=1}^{10} \dot{m}_{t,i}^{meas}} \tag{5.1}$$

The branch mass flow is then corrected such that the mass flow conservation is fulfilled,

$$\dot{m}_{t,i} = \dot{m}_{t,i}^{meas} CF_{\dot{m}} \tag{5.2}$$

Accordingly, the branch tube vapour fractions are adjusted such that the sum of the branch liquid mass flows are equal to the manifold inlet liquid mass flow (the result would be identical, using the vapour mass flow rates). A correction factor for the branch liquid mass flow is defined using the corrected total mass flow

values,

$$CF_l = \frac{\dot{m}_{mIn}^{meas}\left(1 - x_{mIn}^{meas}\right)}{\sum_{i=1}^{10}\left[\dot{m}_{t,i}\left(1 - x_{t,i}^{meas}\right)\right]} \tag{5.3}$$

The branch liquid mass flow is then calculated such that the liquid mass flow conservation is fulfilled:

$$\dot{m}_{l,t,i} = \left(1 - x_{t,i}^{meas}\right)\dot{m}_{t,i}CF_l \tag{5.4}$$

The corrected branch tube vapour fractions are then calculated:

$$x_{t,i} = \frac{\dot{m}_{t,i} - \dot{m}_{l,t,i}}{\dot{m}_{t,i}} \tag{5.5}$$

The mass flows along the manifold (positions $i = 1$ to $i = 9$) are calculated by employing the mass flow conservation equation:

$$\dot{m}_{m,i+1} = \dot{m}_{m,i} - \dot{m}_{t,i} \tag{5.6}$$

Finally, the vapour mass flow conservation equation yields the vapour fraction in the manifold:

$$x_{m,i+1} = \frac{1}{\dot{m}_{m,i+1}}\left(x_{m,i}\dot{m}_{m,i} - x_{t,i}\dot{m}_{t,i}\right) \tag{5.7}$$

Because of the correction procedure for fulfillment of total mass flow and liquid phase conservation described above the residual mass flow and vapour fraction for manifold position $i = 10$ are equal to the mass flow and vapour fraction in branch *No* 10.

5.3 Upward flow configuration

5.3.1 Selection of existing T-junction correlations for comparison

As shown in Section 2.7.1, Watanabe et al. (1995) developed an empirical model based on experiments in a round tube heat exchanger manifold with upward branch configuration. The current round tube ID 16 mm manifold data will be compared to the correlation of Watanabe et al. (1995) in Section 5.3.2.1. Four T-junction models developed for upward branch flow from a horizontal main pipe were outlined in Section 2.6.2: The models of Seeger et al. (1985), Smoglie et al. (1987), Maciaszek and Micaelli (1990), and Castiglia and Giardina (2002a) (Later referred to as the *Seeger*, *Smoglie*, *Maciaszek* and *Castiglia* models). These models

will be compared to the current experimental data and serve as a benchmark for the development of a new model.

In the models of Smoglie, Maciaszek and Castiglia the height h from the liquid surface to the top of the manifold at the inlet of a branch T-junction is needed (see Figure 5.3). Because no visual observations of the flow in the manifolds was possible during the experiments, the value of h had to be calculated based on geometrical formulations and an estimated void fraction in the manifold. With reference to Figure 5.3 the void fraction is defined by,

$$\alpha = \frac{A_g}{A_l + A_g} \tag{5.8}$$

Thome and El Hajal (2002) recommended the Rouhani and Axelsson (1970) void correlation for two-phase flow in horizontal pipes,

$$\alpha = \frac{x}{\rho_g}\left[1 + 0.12\,(1-x)\left(\frac{x}{\rho_g} + \frac{1-x}{\rho_l}\right) + \frac{1.18\,(1-x)\left[g\sigma\,(\rho_l - \rho_g)\right]^{\frac{1}{4}}}{G\rho_l^{0.5}}\right]^{-1} \tag{5.9}$$

The relation between h_l and the void fraction is given by the geometrical relation (see e.g. Bernoux (2000)),

$$\alpha = \frac{1}{\pi}\left[\arccos\left(2\frac{h_l}{D} - 1\right) - \left(2\frac{h_l}{D} - 1\right)\sqrt{1 - \left(2\frac{h_l}{D} - 1\right)^2}\right] \tag{5.10}$$

Using Equation 5.10 and the void fraction given by Equation 5.9, the value of h can be calculated numerically by e.g. an iterative Secant method.

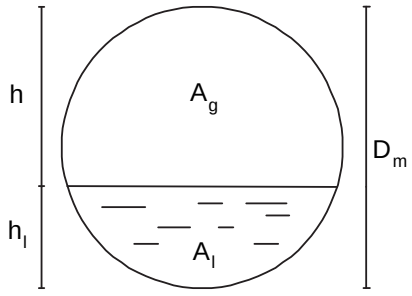

Figure 5.3: Geometrical relations for stratified horizontal flow in a circular manifold.

A comparison of the branch tube vapour fraction predictions of the Smoglie, Maciaszek and Castiglia models are shown in Figure 5.4 as a function of the non-dimensional height h/h_b. As illustrated in Figure 2.11, h_b is the critical height for liquid extraction into the branch. At $h > h_b$, no liquid is extracted in the branch tube, while at decreasing h an increasing amount of liquid is taken off. Predicted values are shown for both CO_2 and HFC-134a for the Smoglie and Maciaszek models, while the Castiglia model does not depend on fluid specific properties.

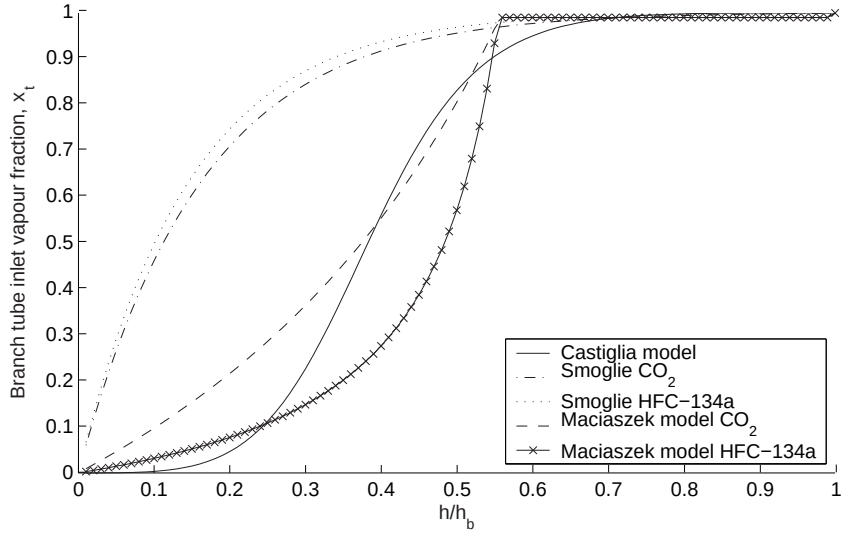

Figure 5.4: Simplified comparison of T-junction correlations. Predicted branch tube vapour fraction, x_t, as function of non-dimensional liquid height (see Figure 2.11). Example data: $T = 20°\text{C}$, $D_t = 4$ mm and $D_m = 16$ mm.

The Castiglia and Smoglie models are continuous, while the Maciaszek model is divided in two regions defined by the parameter h_{lim} (see Equation 2.17). h_{lim} defines the transition where the waves at the liquid interface reaches the branch entrance. For values of $h < h_{lim}$ the liquid take-off in the branch increases drastically. The value of h_{lim} strongly depends on the mass flow rate and vapour velocity in the main pipe. The curves in Figure 5.4 are based on the fixed values $G_t = 200$ kg/m^{2}s and $\rho_{tp,t} = 200$ kg/m^3. When the models are used in comparison to the experimental data, the values of $u_{g,m}$ and G_t are based on measured flow properties and the two-phase density is calculated from the momentum density model (Coleman and Krause, 2002):

$$\rho_{tp} = \frac{x^2}{\rho_g \alpha} + \frac{(1-x)^2}{\rho_l (1-\alpha)} \tag{5.11}$$

It should be noted that the Smoglie model was developed solely based on data with high branch tube vapour fraction, $x_t > 0.95$. As shown in Figure 5.4 the Smoglie model predicts a larger vapour fraction in the high liquid extraction domain ($h = 0 - 0.5h_b$). The difference in density ratio between HFC-134a and CO_2 yields a higher branch tube vapour fraction for HFC-134a in the Smoglie model, while the Maciaszek model predicts highest branch tube vapour fraction for CO_2.

5.3.2 Phase split in ID 16 mm round tube manifold

5.3.2.1 Comparison to the model of Watanabe et al. (1995)

Watanabe et al. (1995) predicted the branch tube vapour fraction $(x_{t,i})$ by separate correlations for the vapour and the liquid take-off fractions of the manifold flow. In the current Section, the Watanabe model is compared to the experimental data obtained with the ID 16 mm round tube manifold (M1). The experimental gas mass flux $(G_{g,m,i} = x_{m,i}G_{m,i})$, gas Reynolds number $(Re_{g,m,i} = x_{m,i}\dot{m}_{m,i}D_m/(A_c\mu_g))$ and liquid mass flow rate $(\dot{m}_{l,m,i})$ at the inlet of the manifold T-junction *No* i, are calculated based on the values of $\dot{m}_{m,i}$ and $x_{m,i}$ derived by the procedure outlined in Section 5.2.2. Figures 5.5 and 5.6 show the measured branch gas mass flux, $G_{g,t,i}$, as function $G_{g,m,i}$ for measurements with HFC-134a and CO_2, respectively. Data points having the highest manifold gas mass flux represents the first branch T-junctions in the manifold, while successive T-junctions are represented by data points with decreasing manifold gas mass flux values. The indicated line represents the prediction of the Watanabe model.

The Watanabe model fails to predict the behaviour of the measured data. The trend in the relationship between the measured branch and manifold gas mass flux seems to fall off at high manifold gas mass flux compared to the linear relation predicted by the Watanabe model. In the experiments of Watanabe et al. (1995) the maximum value of the branch gas mass flux, $G_{g,t}$, was approximately 200 kg/(m^{2}s), which may indicate that their data range was not wide enough to catch the nonlinear behaviour observed in the present data. However, when inspecting of the measurement data in Figure 5 in the paper of Watanabe et al. (1995), it seems clear that the measured data very well could be described by a nonlinear curve similar to a fit of the current data instead of the linear relationship that was chosen.

Watanabe et al. (1995) found that the liquid take-off fraction could be correlated by the gas Reynolds number at the inlet of the local manifold T-junction, $Re_{g,m,i}$. Figures 5.7 and 5.8 show the measured liquid take-off fraction, $\dot{m}_{l,t,i}/\dot{m}_{l,m,i}$, as

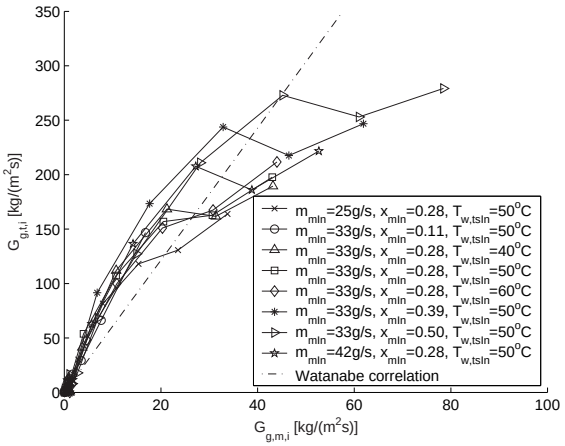

Figure 5.5: Branch gas mass flux, $G_{g,t,i}$, as function of gas mass flux at the inlet of the manifold T-junction, $G_{g,m,i}$. Refrigerant: HFC-134a, $T_{mIn} = 29.5°C$. All measurement series and the prediction of the Watanabe model are shown.

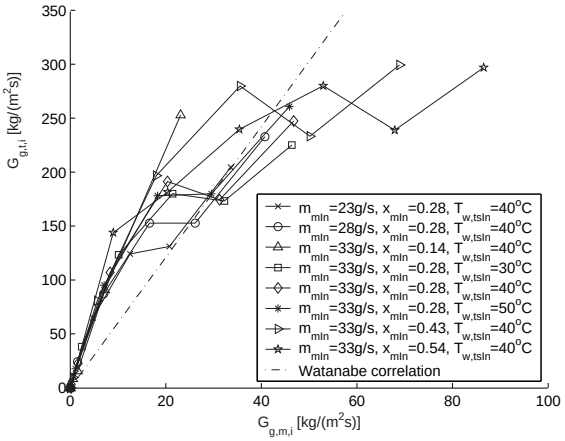

Figure 5.6: Branch gas mass flux as function of gas mass flux at the inlet of the manifold T-junction. Refrigerant: CO_2, $T_{mIn} = 18.7°C$. All measurement series and the prediction of the Watanabe model are shown.

function of $Re_{g,m,i}$, for measurements with HFC-134a and CO_2 respectively.

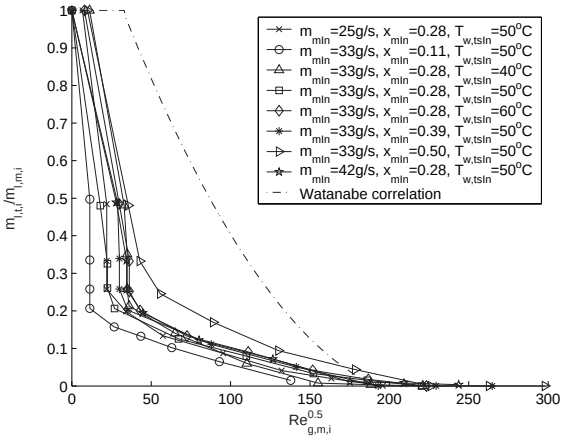

Figure 5.7: Branch liquid fraction take-off, $\dot{m}_{l,t,i}/\dot{m}_{l,m,i}$, as function of gas Reynolds number at the inlet of the manifold T-junction. Refrigerant: HFC-134a, $T_{mIn} = 29.5°C$. All measurement series and the prediction of the Watanabe model are shown.

Large deviations between current data and the prediction by the Watanabe model are seen in Figures 5.7 and 5.8. The model predicts a much higher liquid fraction take-off than what is seen in the measurement data. This is linked to the geometrical difference in that Watanabe et al. (1995) used a manifold with four branches compared to the current setup with ten branches. A larger fraction of the liquid flow in the manifold must be taken off in each branch when the total number of branches are smaller. Hence, the prediction of the gas mass flux in the branch is highly dependent on the specific geometry used by the authors. It is therefore concluded that the Watanabe model is not generally applicable for manifold two-phase flow analysis.

5.3.2.2 Comparison to existing T-junction models

Figure 5.9 shows a comparison between the branch tube vapour fraction, x_t, of a representative data series with CO_2 ($\dot{m}_{mIn} = 0.033$ kg/s, $x_{mIn} = 0.28$, $T_{w,tsIn} = 40°C$) and the calculated values from the Seeger, Smoglie, Maciaszek and Castiglia models. The correlations are able to reproduce the measured phase split with mainly gas take-off in the first branches and liquid take-off in the last branches of the manifold.

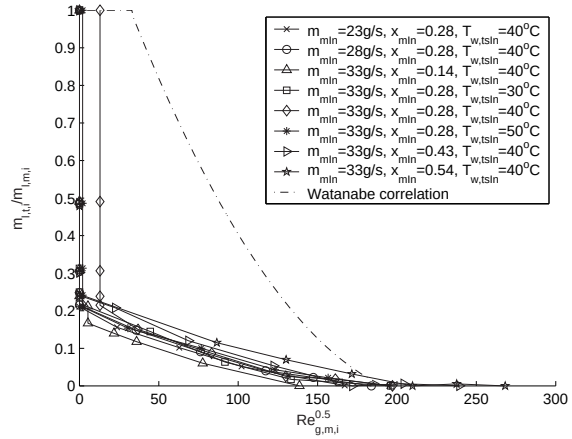

Figure 5.8: Branch liquid fraction take-off as function of gas Reynolds number at the inlet of the manifold T-junction. Refrigerant: CO_2, $T_{mIn} = 18.7°C$. All measurement series and the prediction of the Watanabe model are shown.

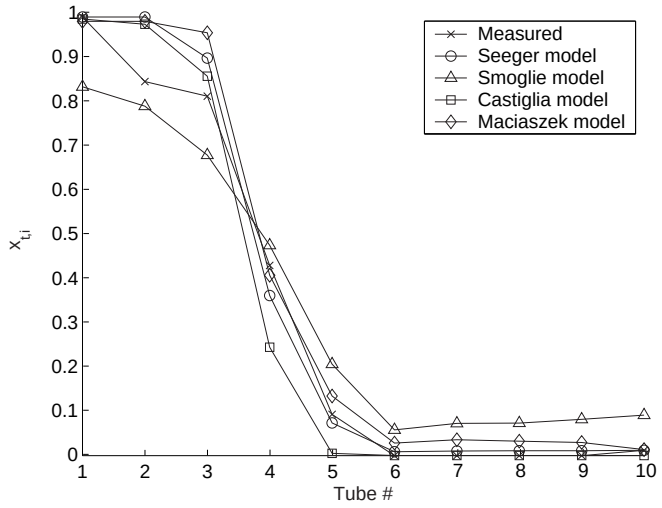

Figure 5.9: Measured branch tube vapour fraction, $x_{t,i}$, compared to the Seeger, Smoglie, Castiglia and Maciaszek T-junction models. ID 16 mm manifold. Refrigerant: CO_2, $\dot{m}_{mIn} = 0.033$ kg/s, $x_{mIn} = 0.28$, $T_{mIn} = 18.7°C$, $T_{w,tsIn} = 40.0°C$.

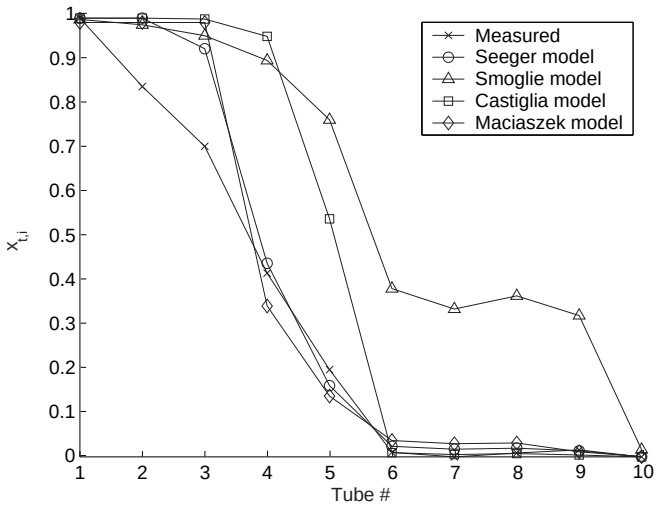

Figure 5.10: Measured branch tube vapour fraction, $x_{t,i}$, compared to the Seeger, Smoglie, Castiglia and Maciaszek T-junction models. ID 16 mm manifold. Refrigerant: HFC-134a, $\dot{m}_{mIn} = 0.033$ kg/s, $x_{mIn} = 0.28$, $T_{mIn} = 29.5°$C, $T_{w,tsIn} = 50.0°$C.

In Figure 5.10 a representative measurement series with HFC-134a in the ID 16 mm manifold is compared with the correlations. The Seeger and Maciaszek models overpredict the vapour fraction in branch *No* 2 and 3 while the Castiglia model overpredicts the vapour fraction in branch *No* 2 to 5. The Smoglie model is unable to predict the measured branch tube vapour fraction with reasonable accuracy for both the CO_2 and the HFC-134a experimental series. By comparing the results in Figure 5.9 (CO_2) and Figure 5.10 (HFC-134a) the measured vapour fractions and the predictions by the Seeger model are quite similar. The Castiglia model predicts a larger vapour fraction for branch *No* 3 to 5 for HFC-134a. The reason for this difference is the void fraction model, which predicts higher values for HFC-134a than for CO_2 due to the larger density ratio of HFC-134a. At 20°C and $x = 0.3$, the Rouhani and Axelsson (1970) void correlation predicts $\alpha_{CO_2} = 0.48$ and $\alpha_{HFC-134a} = 0.83$. The large HFC-134a void fraction yields a higher value of h in Equation 2.20 and therefore less liquid take-off in the branch.

Due to the poor performance of the Smoglie model in the prediction of branch tube vapour fraction the model will not be used in the following Sections.

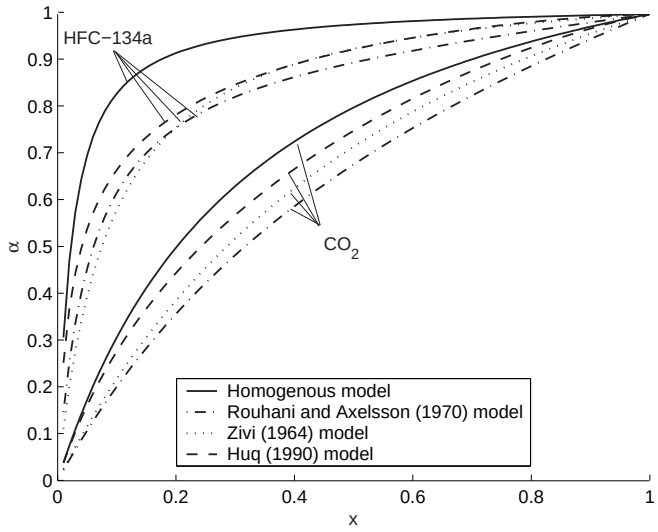

Figure 5.11: Void fraction, α, plotted as function of vapour fraction, x, for CO_2 and HFC-134a. The homogeneous void fraction model (see e.g. Whalley (1996)) is shown together with the commonly used void correlations given by Zivi (1964), Rouhani and Axelsson (1970) and Huq (1990).

5.3.2.3 Data reduction and model development

Several alternatives were tested in order to correlate the phase-split in the measurement data. Following the T-junction methodology, the branch tube vapour fraction could be correlated to the properties of the flow at the T-junction inlet. Although their model was not generally applicable, Watanabe et al. (1995) found that both the liquid and the gas take-off could be correlated to the gas flow properties in the manifold. Following the same reasoning, the measured branch tube vapour fraction, $x_{t,i}$, is plotted as a function of the gas mass flux, $G_{g,m,i}$, at the inlet of the local T-junction in the manifold in Figures 5.12 and 5.13. All measurement series with CO_2 and HFC-134a in the ID 16 mm manifold are shown. The data clearly shows a correlation between $x_{t,i}$ and $G_{g,m,i}$. At $G_{g,m,i} > 40$ kg/(m^{2}s), only gas enters the branch. The Watanabe and the T-junction models used in the previous Section also had limits for liquid take-off in the branch based on the flow properties at the inlet of the T-junction.

The measurement series show that the phase split in the ID 16 mm manifold is more dependent on the local gas mass flux in the manifold, than it is on position in the manifold. This observation indicates that a T-junction approach is justified

for analysis of phase split in the ID 16 mm manifold.

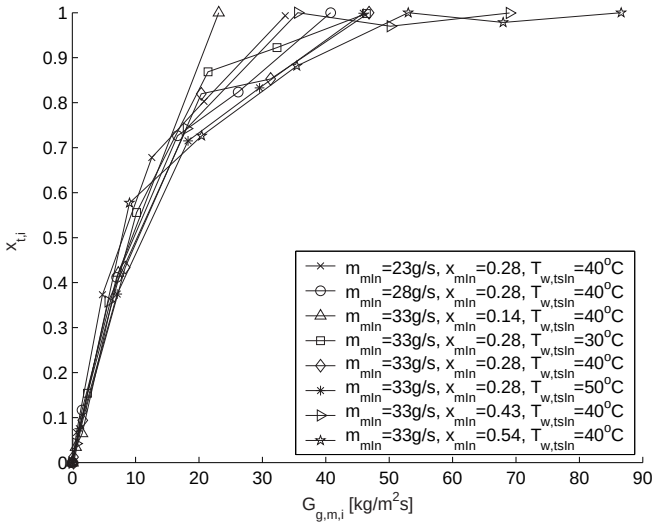

Figure 5.12: Measured branch tube vapour fraction, $x_{t,i}$, as function of gas mass flux, $G_{g,m,i}$, at inlet of manifold T-junctions. Series with branch *No* 1 to 10 are shown from the right to the left (decreasing $G_{g,m,i}$). ID 16 mm manifold. Refrigerant: CO_2, $T_{mIn} = 18.7^{\circ}$C.

The main difference between the results with HFC-134a compared to CO_2 is a small shift to lower branch tube vapour fraction values for HFC-134a in the region $G_{g,m,i} = 0 - 40$ kg/(m^{2}s). As proposed in many studies of T-junction phase split (e.g. Azzopardi (2000)), the density ratio between liquid and vapour affects the phase split. The phase having the lowest momentum, (ρu^2), can more easily make the turn into the branch, while the phase having the highest momentum continues along the axial direction of the main pipe. Based on this, a simple model to predict the vapour fraction in branches of the ID 16 mm manifold is suggested:

$$x_{t,i} = \frac{1}{1 + \frac{1-\gamma}{\gamma}\left(\frac{\rho_l}{\rho_g} b_1\right)^{b_2}} \tag{5.12}$$

where,

$$\gamma = \frac{G_{g,m,i}}{G_{g,m,lim}} \tag{5.13}$$

$G_{g,m,lim}$ is the mass flux giving a transition from two-phase flow to single-phase vapour flow in the branch. Hence, Equation 5.12 is valid for $\gamma < 1.0$. By inspection

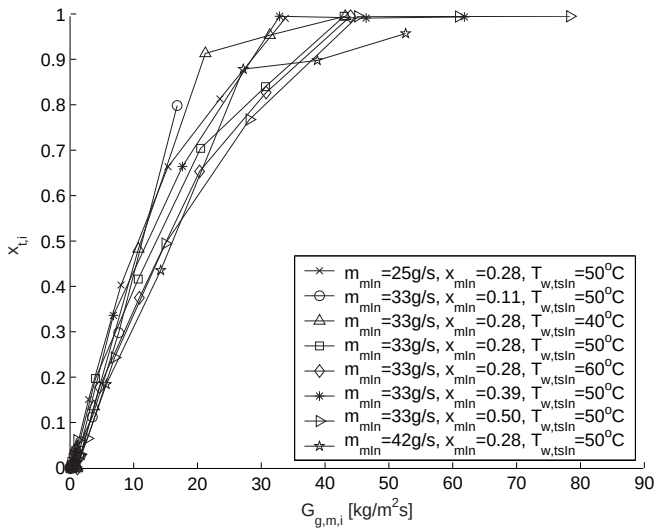

Figure 5.13: Measured branch tube vapour fraction, $x_{t,i}$, as function of gas mass flux, $G_{g,m,i}$, at inlet of manifold T-junctions. Series with branch *No* 1 to 10 are shown from the right to the left (decreasing $G_{g,m,i}$). ID 16 mm manifold. Refrigerant: HFC-134a, $T_{mIn} = 29.5°$C.

of Figures 5.12 and 5.13 the value of the transition parameter was found to be $G_{g,m,lim} = 40$ kg/(m^{2}s) for the ID 16 mm manifold.

The form of Equation 5.12 is equal to the form of the homogeneous void correlation ($b_1 = b_2 = 1$). A non-linear least-squares data fitting algorithm, nlinfit in Matlab, was used to fit the parameters b_1 and b_2 to the experimental data. The algorithm applies the Gauss-Newton method with Levenberg-Marquardt modifications for global convergence. A good description of the Levenberg-Marquardt method is given in Press et al. (1999). The obtained values for the regression parameters were $b_1 = 2.536 \times 10^{-4}$ and $b_2 = 0.1987$.

Figure 5.14 shows the measured data and the developed model for CO_2 and HFC-134a. In Figures 5.15 and 5.16 two of the data series are shown with the new model and the Seeger, Castiglia and Maciaszek models.

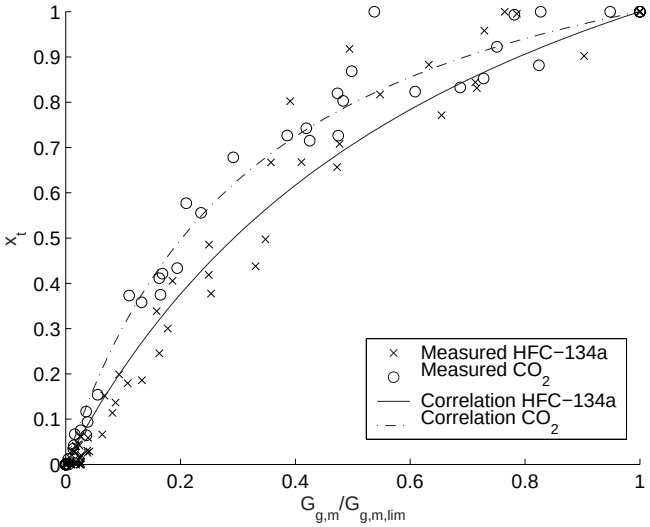

Figure 5.14: Comparison of measured branch tube vapour fraction and the new correlation based on the ID 16 mm manifold data.

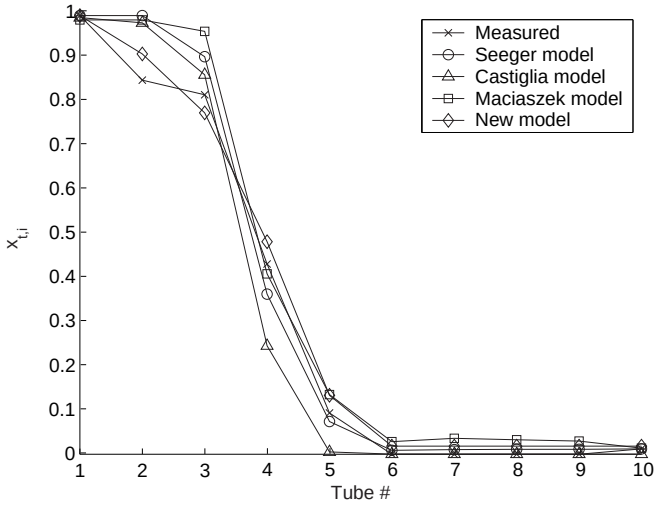

Figure 5.15: Measured branch tube vapour fraction, $x_{t,i}$, compared to predictions using the Seeger, Castiglia, Maciaszek and the new model. ID 16 mm manifold. Refrigerant: CO_2, $\dot{m}_{mIn} = 0.033$ kg/s, $x_{mIn} = 0.28$, $T_{mIn} = 18.7°$C, $T_{w,tsIn} = 40.0°$C.

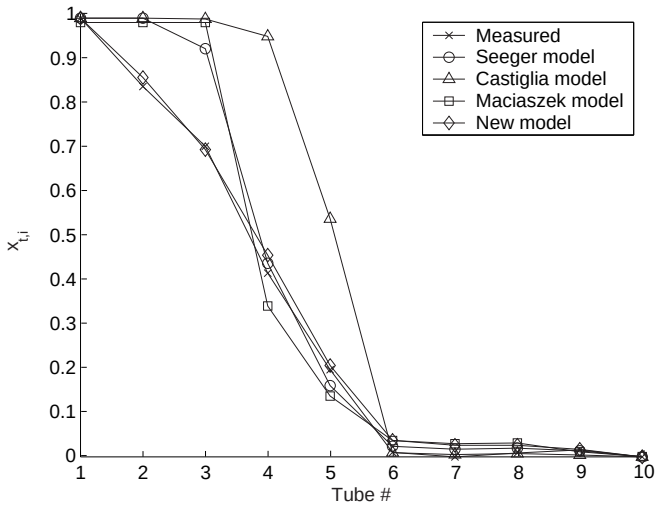

Figure 5.16: Measured branch tube vapour fraction, $x_{t,i}$, compared to predictions using the Seeger, Castiglia, Maciaszek and the new model. ID 16 mm manifold. Refrigerant: HFC-134a, $\dot{m}_{mIn} = 0.033$ kg/s, $x_{mIn} = 0.28$, $T_{mIn} = 29.5°$C, $T_{w,tsIn} = 50.0°$C.

Figures 5.17 and 5.18 show the deviation between measured vapour fraction, $x_{t,i}$, and the predicted vapour fraction, $x_{t,i}^{pred}$, for all measurement series for CO_2 and HFC-134a, respectively. The new empirical model reduces the deviation from experimental data compared to existing T-junction models. However, the three T-junction models are also able to predict most of the measurement data remarkably well, with a maximum deviation of $\mid x_{t,i} - x_{t,i}^{pred} \mid \approx 0.22$. The Castiglia and Maciaszek models are physically based on the assumption of stratified flow in the main pipe. In Figures 5.19 and 5.20, calculated flow properties at the T-junction inlets in the manifold are plotted in the flow map of Kattan et al. (1998). All measurement values obtained in the ID 16 mm manifold are in the stratified or stratified-wavy regions of the flow map. A discussion on the relevance of using flow maps intended for prediction of flow regimes in developed two-phase flows, in the analysis of the manifold flow is given in Section 5.3.3.2. When moving to smaller manifold diameters in the following sections, the manifold mass flux increases, and the predicted flow regime changes into the intermittent region of the flow map. The performance of the T-junction models will be reduced accordingly.

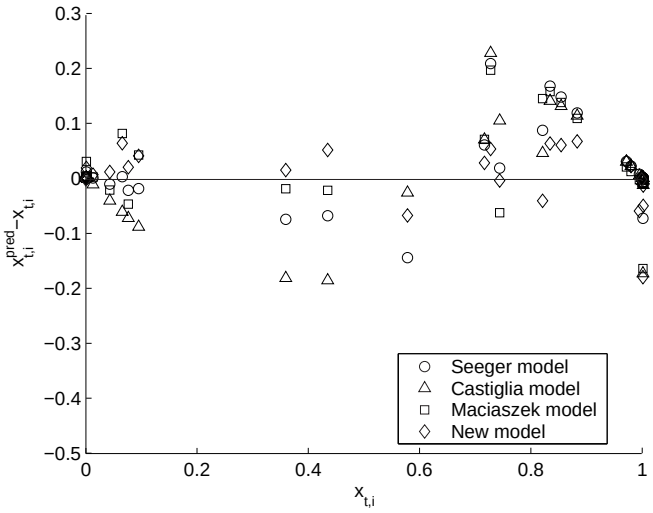

Figure 5.17: Absolute deviation between predicted and measured branch tube vapour fraction. All measurement series using CO_2 in the ID 16 mm manifold are shown.

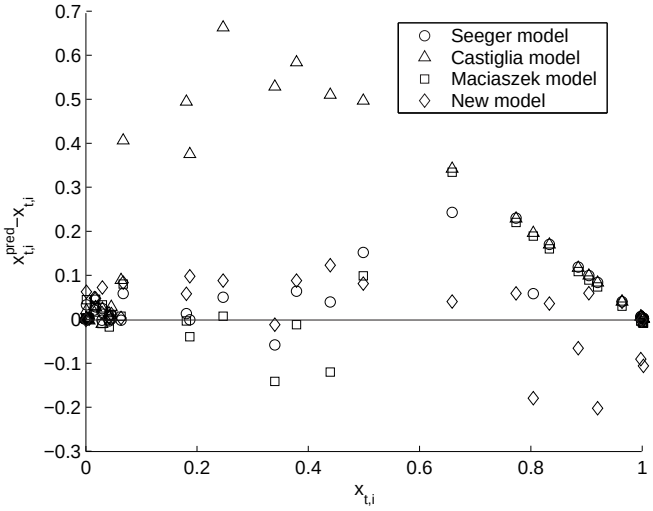

Figure 5.18: Absolute deviation between predicted and measured branch tube vapour fraction. All measurement series using HFC-134a in the ID 16 mm manifold are shown.

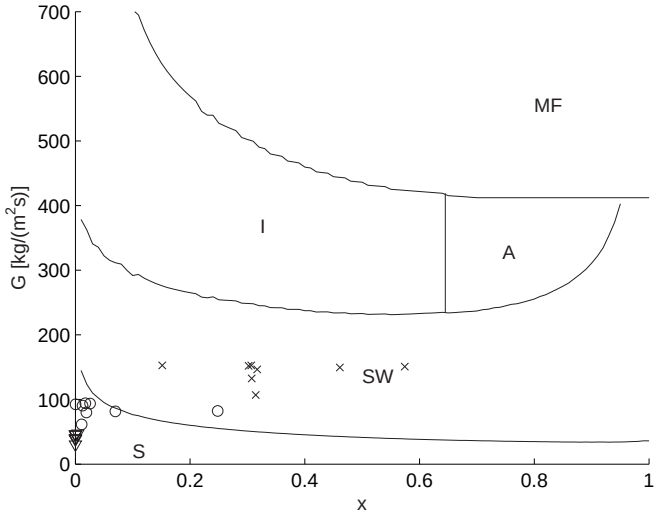

Figure 5.19: Flow map based on Kattan et al. (1998), with extensions of Zürcher et al. (1999). X: manifold inlet, O: position 5 in manifold, $\bigtriangledown$: position 8 in manifold (See Figure 5.2). All measurement series with CO_2 in the ID 16 mm manifold. Abbreviations are explained in Figure 2.3.

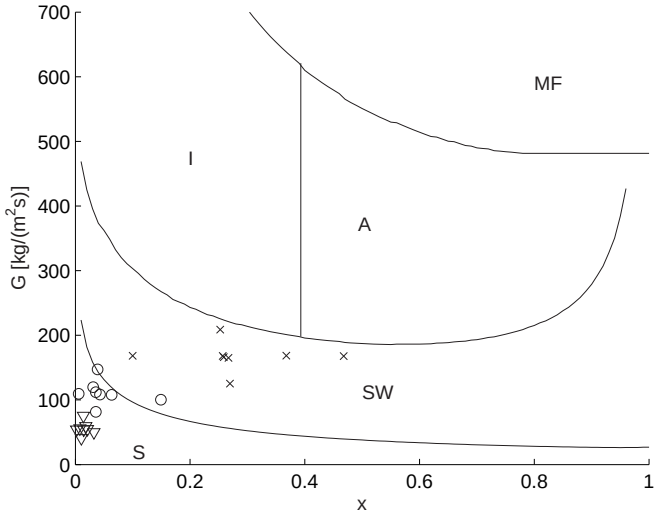

Figure 5.20: Flow map based on Kattan et al. (1998), with extensions of Zürcher et al. (1999). X: manifold inlet, O: position 5 in manifold, $\bigtriangledown$: position 8 in manifold (See Figure 5.2). All measurement series with HFC-134a in the ID 16 mm manifold. Abbreviations are explained in Figure 2.3.

5.3.3 Phase split in ID 8 mm round tube manifold

5.3.3.1 Comparison to existing T-junction models

As shown in Section 5.3.2.1, the model of Watanabe et al. (1995) could not be applied to other geometries than used by the authors. Therefore, the measurement results of the ID 8 mm round tube manifold are compared to the existing T-junction models only.

Figures 5.21 and 5.22 show measurement series and T-junction model predictions for the ID 8 mm manifold with CO_2 and HFC-134a, respectively. The Seeger and Maciaszek models seem to predict $x_{t,i}$ in branch No 6 to 10 quite well, while they severely overpredict the vapour fraction in the first five branches for the CO_2 experiments. The same pattern is seen in the HFC-134a experiments where the Seeger model overpredicts the vapour fraction in branches No 1 to 3, and the Maciaszek model overpredicts the vapour fraction in branches No 1 and 2. The Castiglia model predicts some liquid entrainment in the first branches in the CO_2 experiments, but overpredicts the vapour fraction in the first four branches and underpredicts in branches No 6 to 9. Like the Seeger correlation, the Castiglia model predicts $x_{t,i}$ in branches No 4 to 10 in the HFC-134a experiments remarkably well.

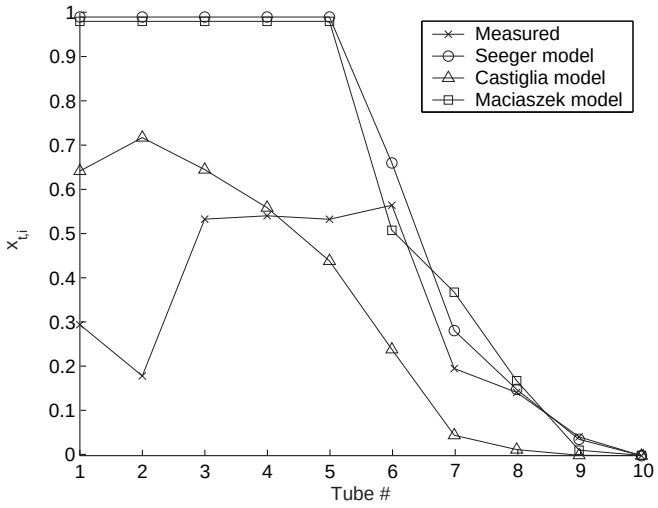

Figure 5.21: Measured branch tube vapour fraction, $x_{t,i}$, compared to the Seeger, Castiglia and Maciaszek T-junction models. ID 8 mm manifold. Refrigerant: CO_2, $\dot{m}_{mIn} = 0.033$ kg/s, $x_{mIn} = 0.28$, $T_{mIn} = 18.7°$C, $T_{w,tsIn} = 40.0°$C.

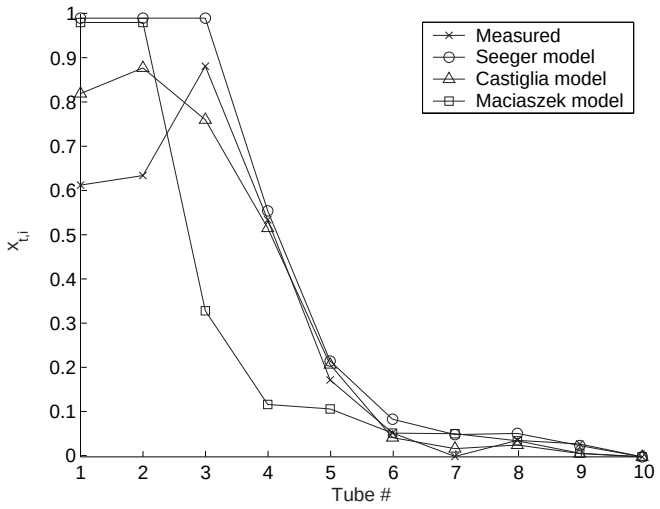

Figure 5.22: Measured branch tube vapour fraction, $x_{t,i}$, compared to the Seeger, Castiglia and Maciaszek T-junction models. ID 8 mm manifold. Refrigerant: HFC-134a, $\dot{m}_{mIn} = 0.033$ kg/s, $x_{mIn} = 0.28$, $T_{mIn} = 29.5°$C, $T_{w,tsIn} = 50.0°$C.

5.3.3.2 Data reduction and model development

Following the same procedure as for the ID 16 mm manifold, the measured branch tube vapour fractions are plotted as a function of gas mass flux at the inlet of the manifold T-junction, $G_{g,m,i}$. Figures 5.23 and 5.24 contain all measurement series with CO_2 and HFC-134a in the ID 8 mm manifold, respectively. The data series show a similar behaviour as in the ID 16 mm manifold data in Figure 5.12 and 5.13 at values of manifold gas mass flux below approximately 50 kg/(m^{2}s). Then a sudden transition appears and the branch tube vapour fraction does not approach unity as shown for the ID 16 mm manifold and also predicted by the Watanabe and the T-junction models.

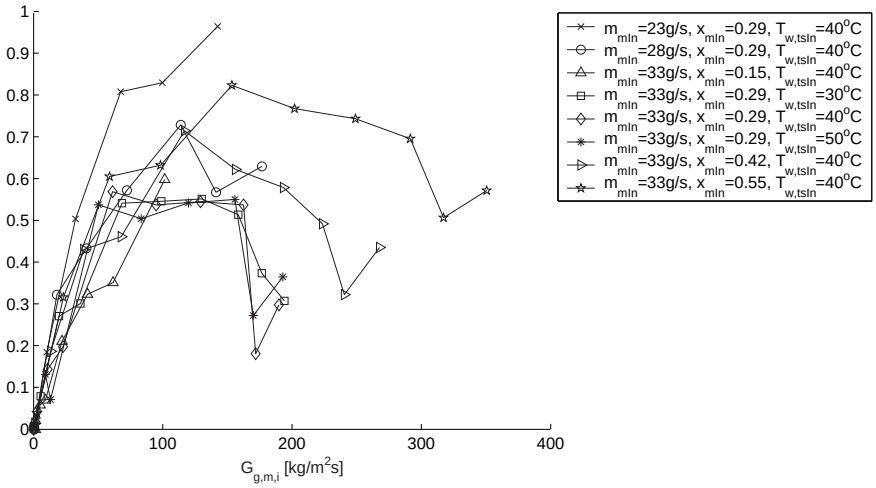

Figure 5.23: Measured branch tube vapour fraction, $x_{t,i}$, as function of gas mass flux, $G_{g,m,i}$, at inlet of manifold T-junctions. Series with branch *No* 1 to 10 are shown from the right to the left (decreasing $G_{g,m,i}$). ID 8 mm manifold. Refrigerant: CO_2, $T_{mIn} = 18.7°C$.

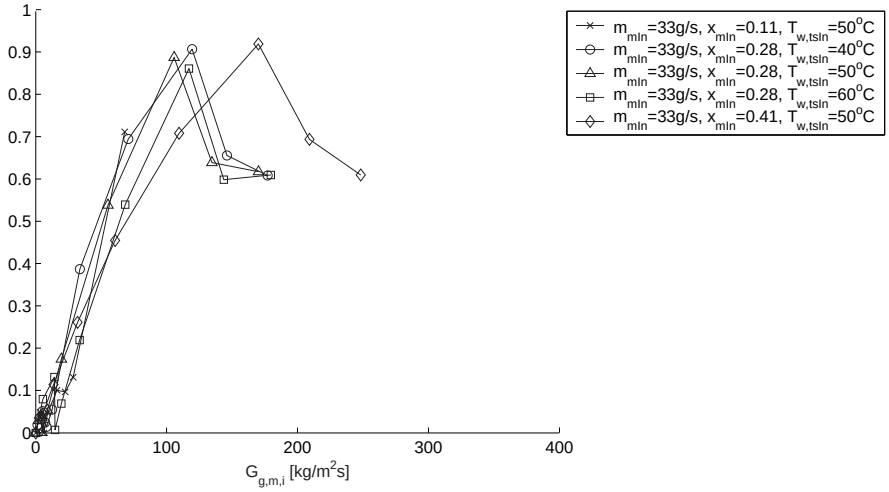

Figure 5.24: Measured branch tube vapour fraction, $x_{t,i}$, as function of gas mass flux, $G_{g,m,i}$, at inlet of manifold T-junctions. Series with branch *No* 1 to 10 are shown from the right to the left (decreasing $G_{g,m,i}$). ID 8 mm manifold. Refrigerant: HFC-134a, $T_{mIn} = 29.5°C$.

At equal flow rates, the mass flux in the ID 8 mm manifold is four times higher than in the ID 16 mm manifold. A transition in flow regime in the manifold is one possible explanation for the sudden transition seen in Figures 5.23 and 5.24, where the continuous increase in branch tube vapour fraction as function of $G_{g,m}$ is changed to a fluctuating shape of the vapour fraction curves.

Figures 5.25 and 5.26 show the flow maps of Kattan et al. (1998) including the flow properties at the inlet of T-junctions *No* 1, 5 and 8 in the ID 8 mm manifold for all measurement series with CO_2 and HFC-134a, respectively. Most of the manifold T-junctions experience intermittent flow (slug or plug flow), but as the mass flux and vapour fraction are reduced along the length of the manifold, the predicted flow regime changes to stratified-wavy and stratified flow.

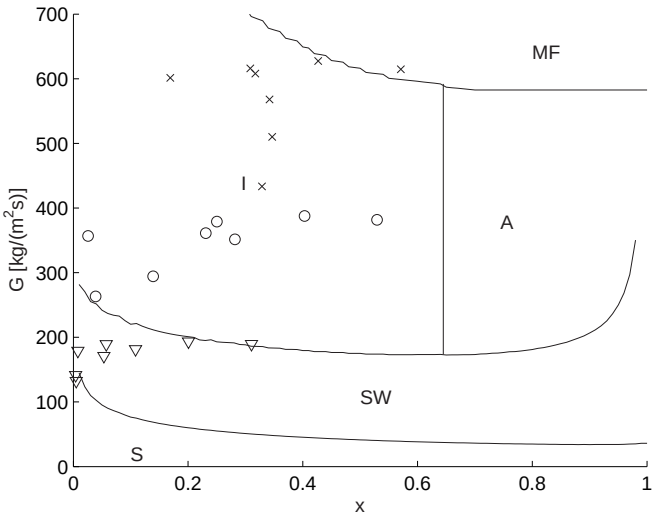

Figure 5.25: Flow map based on Kattan et al. (1998), with extensions of Zürcher et al. (1999). X: manifold inlet, O: position 5 in manifold, $\bigtriangledown$: position 8 in manifold (See Figure 5.2). All measurement series with CO_2 in the ID 8 mm manifold. Abbreviations are explained in Figure 2.3.

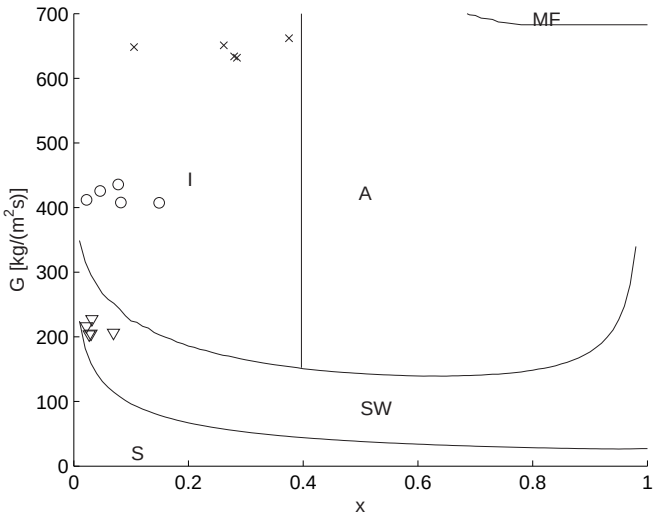

Figure 5.26: Flow map based on Kattan et al. (1998), with extensions of Zürcher et al. (1999). X: manifold inlet, O: position 5 in manifold, $\bigtriangledown$: position 8 in manifold (See Figure 5.2). All measurement series with HFC-134a in the ID 8 mm manifold. Abbreviations are explained in Figure 2.3.

When using flow maps for two-phase flow in a manifold, one has to remember that the flow transition criteria are based on fully developed two-phase flow, which is not the case in a manifold. At the end of the manifold, downstream effects such as liquid pooling will give a higher liquid level than what would be predicted by the transition criteria for fully developed two-phase flow. Also, disturbances due to radial flow in the manifold caused by the branch tubes will probably affect the two-phase flow pattern. However, the transition criterion between stratified-wavy and intermittent or annular flow, which is based on the relation between inertia and gravitational forces, is assumed to give a quantitative indication of important forces affecting the two-phase flow pattern in the manifold. The two-phase flow at the inlet of the manifold is considered to be almost fully developed, passing through a straight pipe section of $15D_m$ before entering the ID 16 mm manifold ($30D_m$ for the ID 8 mm manifold).

Based on the work by Kattan et al. (1998), Zürcher et al. (1999) defined a revised version of the transition curve between stratified-wavy and intermittent or annular flow:

$$G_{wavy} = \left(\frac{16A_{gd}^3 g D_m \rho_l \rho_g}{x^2\pi^2\left(1-(2h_{ld}-1)^2\right)^{0.5}} \left[\frac{\pi^2}{25h_{ld}^2}(1-x)^{F_1(q)} \left(\frac{We}{Fr}\right)_l^{F_2(q)} + 1 \right] \right)^{0.5} + 50 - 75e^{-\left(\frac{\left(x^2-0.97\right)^2}{x(1-x)}\right)} \quad (5.14)$$

A_{gd} is the dimensionless vapour cross-sectional area ($A_{gd} = A_g/D_m^2$) and h_{ld} is the dimensionless liquid height in stratified flow. The ratio of the liquid Weber number to the liquid Froude number is given by:

$$\left(\frac{We}{Fr}\right) = \frac{gD_m^2\rho_l}{\sigma} \quad (5.15)$$

The non-dimensional empirical exponents $F_1(q)$ and $F_2(q)$ include the effect of heat flux on the onset of dryout of the annular film. In the case of adiabatic flow the values become, $F_1(q) = 1.0$ and $F_2(q) = 1.023$.

To bring the effect of flow regime change into the analysis of phase split in the manifold, a transition criterion between the inertia dominated intermittent flow regime and the gravity dominated stratified-wavy regime is used. Several paths were tried to find a method of correlating the two-phase flow split in the manifold T-junctions to the flow properties in the manifold. In Figure 5.27 the fraction of liquid taken off in the branch, $\dot{m}_{l,t,i}/\dot{m}_{l,m,i}$, is plotted against a dimensionless manifold mass flux, $G_m/G_{m,wavy}$. $G_{m,wavy}$ is the mass flux at the transition between stratified-wavy and intermittent flow regimes, defined in Equation 5.14, calculated using the two-phase properties at the inlet of each T-junction. Above a value of approximately $G_m/G_{m,wavy} = 2.0$, defined as the transition criterion $MMFTC$ (Manifold Mass Flux Transition Criterion, see Figure 5.29), the liquid take-off is approximately constant. This effect was not taken into account in the correlations outlined in the previous Section, where the liquid take-off was zero above a certain value of gas mass flux in the manifold.

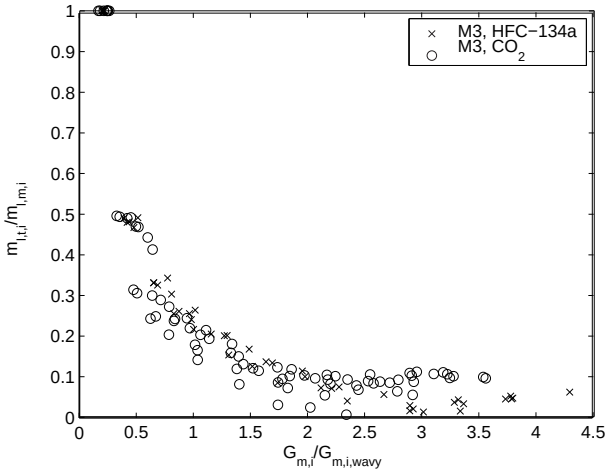

Figure 5.27: Liquid take-off fraction, $\dot{m}_{l,t,i}/\dot{m}_{l,m,i}$, as function of dimensionless manifold mass flux. Values from all measurement series in the ID 8 mm manifold are plotted.

The effect of using the dimensionless manifold mass flux, $G_m/G_{m,wavy}$, is seen in Figure 5.28 where the liquid take-off fraction is plotted as a function of G_m directly. The use of G_{wavy} in Figure 5.27 collects the data points for both HFC-134a and CO_2 on a curve with a clear trend between ($\dot{m}_{l,t,i}/\dot{m}_{l,m,i}$) and $G_m/G_{m,wavy}$ compared to Figure 5.28 where the data points are more scattered. The reason for this behaviour is the change in G_{wavy} at increasing vapour fraction (examples of transition lines are seen in Figures 5.25 and 5.26). Also, the effect of the fluid properties e.g. surface tension, liquid and vapour densities on the two-phase flow regime is taken into account in the calculation of G_{wavy}. The difference between the CO_2 and the HFC-134a liquid fraction take-off in Figure 5.28 is almost eliminated by using the dimensionless mass flux $G_m/G_{m,wavy}$ in Figure 5.27. This indicates that the effect of fluid properties on the two-phase flow split is taken into account in the calculation of G_{wavy}.

The correlation between liquid fraction take-off and the parameter $G_m/G_{m,wavy}$ makes it possible to find the dependence between the branch tube vapour fraction and the flow properties at the inlet of the manifold T-junction. As can be seen in Figure 5.23 and 5.24, the branch inlet vapour fraction varies considerably in the region of high mass flux in the manifold. When the liquid take-off fraction, $\dot{m}_{l,t,i}/\dot{m}_{l,m,i}$, is taken as constant and the total mass flow in the branch tube, $\dot{m}_t$, is known from the experiments, the branch tube vapour fraction is calculated by Equation 5.16.

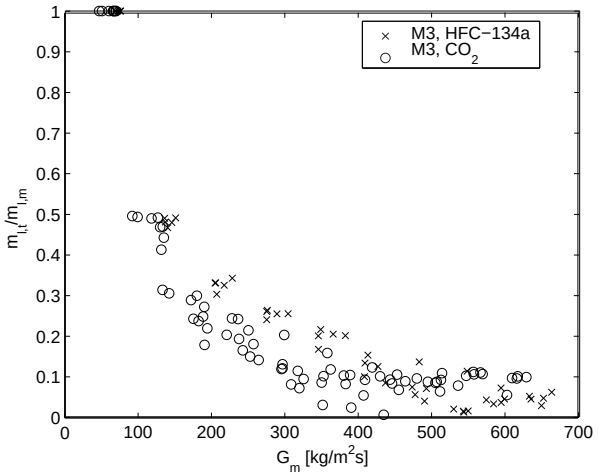

Figure 5.28: Liquid take-off fraction, $\dot{m}_{l,t,i}/\dot{m}_{l,m,i}$, as function of total manifold mass flux. Values from all measurement series in the ID 8 mm manifold are plotted.

$$x_{t,i} = \frac{\dot{m}_{g,t,i}}{\dot{m}_{t,i}} = \frac{\dot{m}_{t,i} - \dot{m}_{l,t,i}}{\dot{m}_{t,i}} = \frac{\dot{m}_{t,i} - CLTF\dot{m}_{l,m,i}}{\dot{m}_{t,i}} \tag{5.16}$$

where $CLTF$ is the Constant Liquid Take-off Fraction in the region above the transition criterion, $MMFTC$, see Figure 5.29. The values of $CLTF$ are obtained by calculating the mean of the experimental data points above the transition criterion. The resulting values are $CLTF = 0.08$ for CO_2 and $CLTF = 0.04$ for HFC-134a. The higher value of $CLTF$ for CO_2 results in a better two-phase distribution for CO_2 than for HFC-134a when the mass flux at the inlet of the manifold is as high as in the ID 8 mm manifold experiments. As described in the T-junction literature review in Section 2.5, a likely reason for this observation is the small density ratio of CO_2 ($\rho_l/\rho_g = 4.3$ at 18.7°C) compared to HFC-134a ($\rho_l/\rho_g = 32.0$ at 29.5°C), which allows more liquid to divert into the branch.

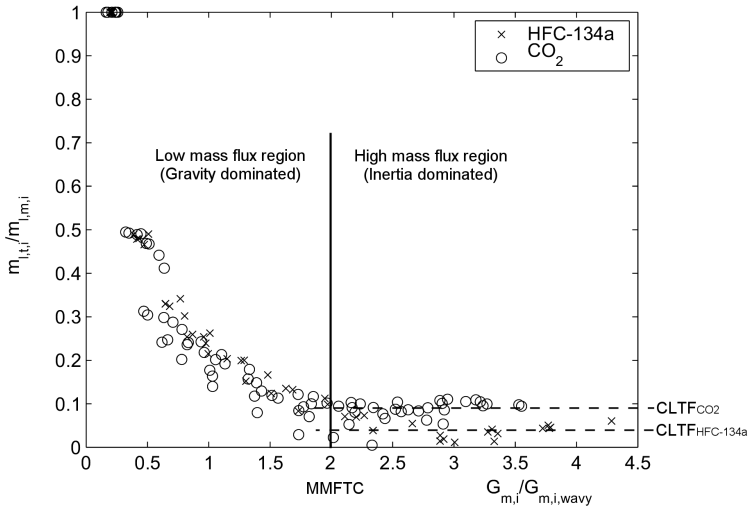

Figure 5.29: Visualization of the definitions of *MMFTC* (Manifold Mass Flux Transition Criterion) and *CLTF* (Constant Liquid Take-off Fraction).

5.3.3.3 Phase split in ID 8 mm round tube manifold with short inlet tube (M4)

In Figure 5.30 the branch tube vapour fraction, $x_{t,i}$, is plotted as a function of the gas mass flux at the inlet of the manifold T-junction, $G_{g,m,i}$, for the experiments with short inlet tube (50 mm) in the ID 8 mm manifold (M4). As for results with long inlet tube reported in the previous section, the measured vapour fraction breaks off from the continuous increasing curve which was used to fit the ID 16 mm manifold results in Section 5.3.2.3.

The liquid take-off fraction for the HFC-134a experiments in the ID 8 mm manifold with both long and short inlet tube is shown in Figure 5.31. As noted in Chapter 4, the two-phase flow distribution is more even when using a short inlet tube. This is due to the higher liquid take-off fraction $CLTF = 0.1$ in the high mass flux regime. In the low mass flux regime, the results of the two measurement series are very close to identical. As will be discussed in Section 5.3.6 the difference in liquid take-off fraction in the high mass flux regime can be explained by better mixing of the liquid and vapour phase at the inlet of the manifold when using a short inlet tube length.

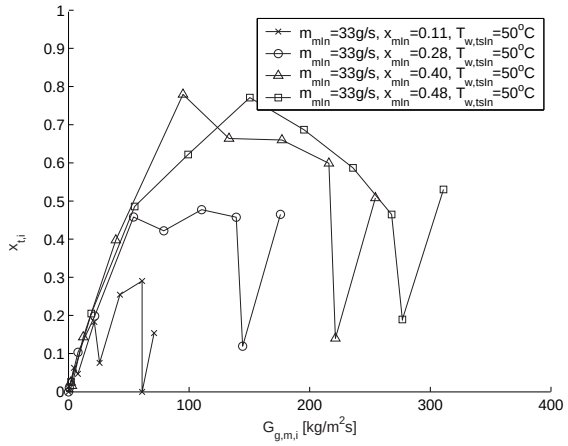

Figure 5.30: Measured branch tube vapour fraction, $x_{t,i}$, as function of gas mass flux, $G_{g,m,i}$, at inlet of manifold T-junctions. Series with branch *No* 1 to 10 are shown from the right to the left (decreasing $G_{g,m,i}$). ID 8 mm manifold with short inlet tube (50mm). Refrigerant: HFC-134a, $T_{mIn} = 29.5°$C.

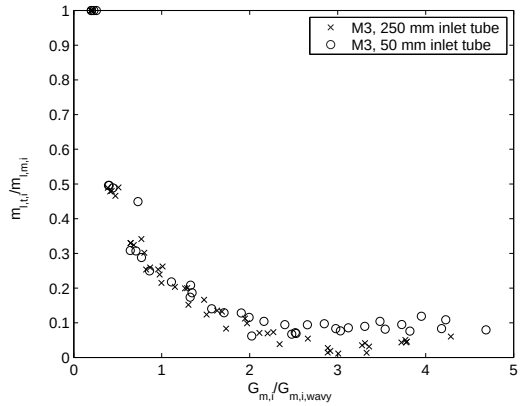

Figure 5.31: Liquid take-off fraction, $\dot{m}_{l,t,i}/\dot{m}_{l,m,i}$, as function of dimensionless manifold mass flux. Values from all measurement series both with short and long inlet tube length in the ID 8 mm manifold are plotted. Refrigerant: HFC-134a.

5.3.3.4 Concluding remarks

Based on the analysis of the ID 16 mm and ID 8 mm round tube manifold results, it seems clear that flow regime transitions in the manifold have to be taken into

account in the construction of a general correlation for the two-phase flow distribution. At manifold mass flux below a transition criterion based on the Zürcher et al. (1999) correlation, MMFTC, the branch tube vapour fraction can be correlated against the gas mass flux in the manifold. At mass flux above MMFTC, a constant liquid take-off fraction, CLTF, can be assumed. In this case, the amount of gas take-off is related to down-stream pressure losses. Hence, the vapour fraction can obtain an irregular pattern dependent on the amount of gas take-off, for instance as shown in Figure 5.30.

In the following Section the full set of manifold geometries that were used in the experimental program is analysed in order to understand the relationships between the parameters used to describe the two-phase flow distribution and the manifold geometry. In Section 5.3.5 the generalized correlation, taking into account the manifold free geometry, is outlined and a comparison to the measurement data and the T-junction correlations is done.

5.3.4 Phase split in additional manifold geometries

The experimental data obtained using the ID 12 mm and ID 16 mm round tube manifolds and the MPE-tube manifold with various geometry modifications are presented in the same way as the ID 8 mm manifold results. The treatment of the experimental data will constitute the basis for the correlation development in Section 5.3.5. Reference is made to Table 4.1.1 for a description of the geometry details of the specific manifolds. In the calculation of mass fluxes and void fractions in the manifold, the hydraulic diameter, D_h, and the free flow cross-sectional area, A_c, of the narrowest passage, reported in Table 4.1.1, are utilized.

Figure 5.32 shows the liquid take-off fraction for the measurements in the ID 16 mm manifold. The trend in the data resembles the data reported for the ID 8 mm manifold in Figure 5.32. However, there seems to be no liquid extraction above a certain value of the dimensionless mass flux. Following the concept of the previous section, the manifold mass flux transition criterion is set to $MMFTC = 0.5$ and the constant liquid take-off in the region above the $MMFTC$ is set to $CLTF = 0.0$, for both HFC-134a and CO_2.

The experimental results obtained in the round tube ID 12 mm and ID 16 mm manifold experiments are shown in Figure 5.33. The liquid take-off in the ID 12 mm manifold is higher than in the ID 16 mm manifold for a given dimensionless mass flux. The value of the manifold mass flux transition criterion was set to $MMFTC = 0.9$, and the constant liquid take-off fraction was set to $CLTF = 0.15$.

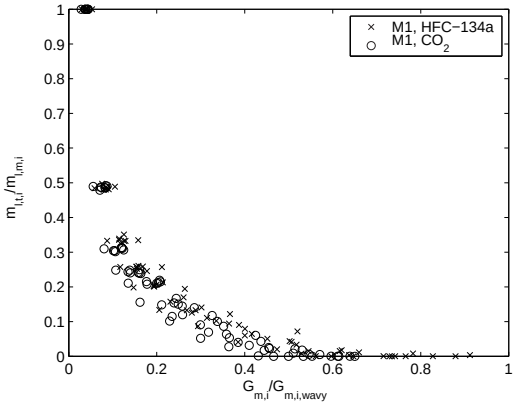

Figure 5.32: Liquid take-off fraction, $\dot{m}_{l,t,i}/\dot{m}_{l,m,i}$, as function of dimensionless manifold mass flux. Values from all measurement series in the round tube ID 16 mm manifold with CO_2 and HFC-134a are plotted.

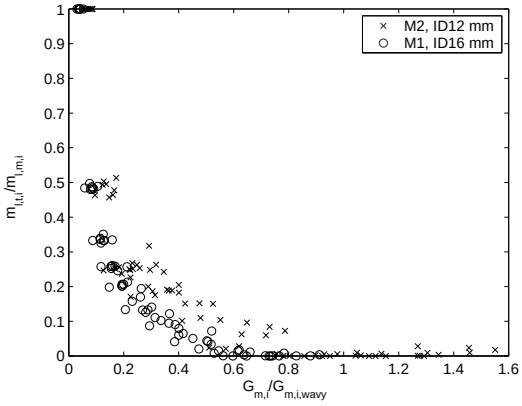

Figure 5.33: Liquid take-off fraction, $\dot{m}_{l,t,i}/\dot{m}_{l,m,i}$, as function of dimensionless manifold mass flux. Values from all measurement series in the round tube ID 12 mm and ID 16 mm manifolds are plotted.

Figure 5.34 contains the liquid take-off fraction from all measurements with CO_2 and HFC-134a in the manifold M5 (base-case MPE-tube manifold). Similar patterns as in the results from the ID 8 mm manifold are seen, with an approach to constant liquid take-off at high manifold mass flux rates. Contrary to the results in the ID 8 mm manifold, the liquid take-off is larger for HFC-134a compared to CO_2 in the region of high mass flux. By inspection of Figure 5.34 the transition criterion between the low and high mass flux region is set to $MMFTC = 0.7$ for HFC-134a and $MMFTC = 0.9$ for CO_2. Averaging the mass flux in the high mass flux area yields constant liquid take-off fractions, $CLTF_{HFC-134a} = 0.023$ and $CLTF_{CO_2} = 0.011$.

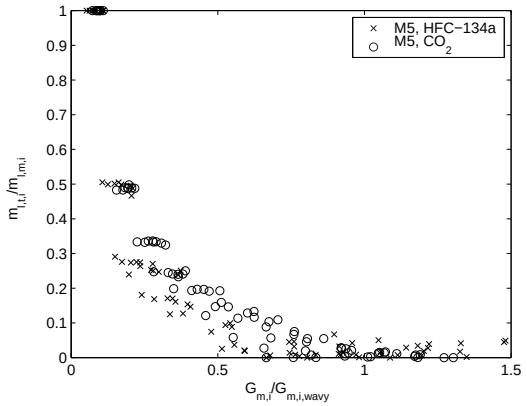

Figure 5.34: Liquid take-off fraction, $\dot{m}_{l,t,i}/\dot{m}_{l,m,i}$, as function of dimensionless manifold mass flux. Values from all measurement series in the base-case MPE-tube manifold (M5) are plotted.

Figure 5.35 compares the liquid take-off fraction in manifold M5 and M6 (variation in branch tube insert ratio). Due to the reduced cross-sectional area, the mass flux is 60.6% higher in manifold M6 for the same total mass flow rate. Inspection of Figure 5.35 yields a transition criterion of $MMFTC = 1.3$ and $CLTF = 0.040$ for the HFC-134a measurements in manifold M6.

The results obtained with manifold M8 (15 mm branch tube pitch) are shown in Figure 5.36 together with the base-case manifold M5. For M8 the values of the transition criterion and the liquid take-off fraction in the high mass flux regime are found to be $MMFTC = 0.75$ and $CLTF = 0.02$. Very small differences in liquid take-off fraction can be seen from the variation in branch tube pitch.

Inserting baffles in the manifold (M7) yields a 19.6% increase in mass flux, at the same total mass flow rate, due to reduced cross-sectional area. The transition

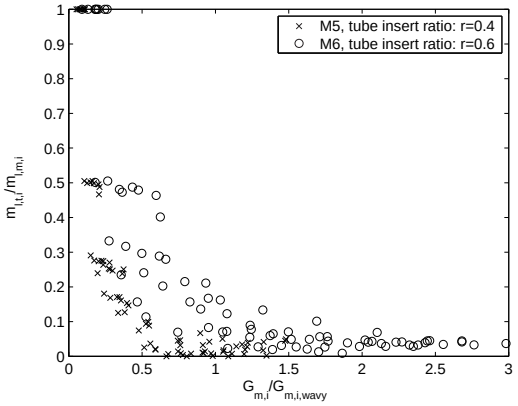

Figure 5.35: Liquid take-off fraction, $\dot{m}_{l,t,i}/\dot{m}_{l,m,i}$, as function of dimensionless manifold mass flux. Values from all measurement series in the manifold M5 and M6 (variation in branch insert ratio) with HFC-134a are plotted.

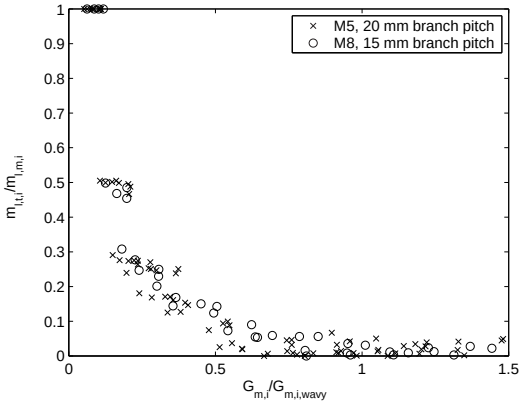

Figure 5.36: Liquid take-off fraction, $\dot{m}_{l,t,i}/\dot{m}_{l,m,i}$, as function of dimensionless manifold mass flux. Values from all measurement series in the manifold M5 and M8 (variation in branch tube pitch) with HFC-134a are plotted.

criterion for the M7 manifold, Figure 5.37, is approximately $MMFTC = 0.9$ and the liquid take-off in the high mass flux area is $CLTF = 0.048$. The baffle insert provides a slight increase in $CLTF$ compared to the base-case MPE-manifold.

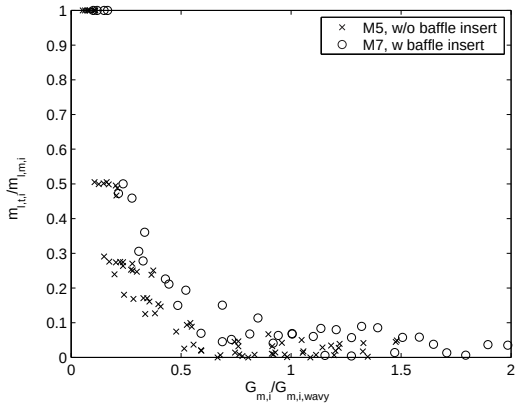

Figure 5.37: Liquid take-off fraction, $\dot{m}_{l,t,i}/\dot{m}_{l,m,i}$, as function of dimensionless manifold mass flux. Values from all measurement series in the manifold M5 and M7 (baffle inserts) with HFC-134a are plotted.

Figure 5.37 shows the liquid take-off fraction from the experiments with both CO_2 and HFC-134a in the MPE-tube manifold with spiral mixer insert at the manifold inlet, M9. More scatter in the experimental data are seen compared to the base-case manifold, M5, in Figure 5.34. However, the data follow the same trend as seen before and a transition criterion between low and high mass flux regimes is defined, $MMFTC = 0.5$ for both CO_2 and HFC-134a. The liquid fraction in the high mass flux region, $CLTF = 0.11$, is calculated by averaging the experimental data values.

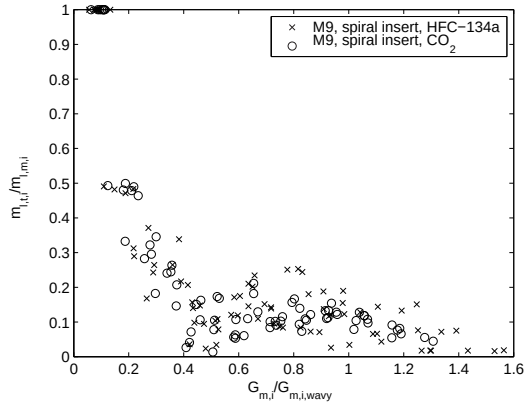

Figure 5.38: Liquid take-off fraction, $\dot{m}_{l,t,i}/\dot{m}_{l,m,i}$, as function of dimensionless manifold mass flux. Values from all measurement series in the manifold M9 (spiral mixer inserts) are plotted.

5.3.5 Unified model for phase split in manifolds with upward flow configuration

5.3.5.1 Outline of the model

Based on the data reduction of the experimental results in the previous sections and the methodology to split the correlation for two-phase flow distribution in the manifold T-junctions in two parts depending on the flow regime, a unified model for the whole set of manifold geometries is outlined. The split in a high and a low mass flux region is done by a transition criterion, $MMFTC$, as shown in Figure 5.29. To bring the dependency of manifold geometry into the correlation, the transition criterion is plotted as a function of the manifold free-flow cross-sectional area, A_c, in Figure 5.39.

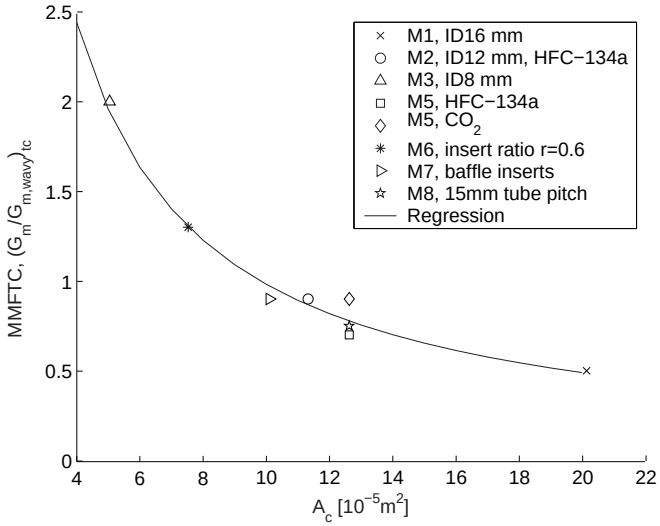

Figure 5.39: Transition criterion $MMFTC$ plotted as function of manifold free flow cross sectional area, A_c, for all manifold geometries together with regression curve.

The data are fitted by a best fit regression equation obtained by the commercial software package *Datafit* v. 8.0 by *Oakdale Engineering*,

$$\left(\frac{G_m}{G_{m,wavy}}\right)_{tc} = \frac{b_1}{1+b_2 A_c \times 10^5} \tag{5.17}$$

where $b_1 = 148.7$ and $b_2 = 14.89$.

As seen in Figure 5.29, the correlation is split in two regions dependent on the mass flux at the inlet of the manifold T-junction:

- High mass flux region
- Low mass flux region

High mass flux region: At mass flux above the transition criterion, the constant liquid take-off fraction, $CLTF$, is modelled independently of the two-phase flow properties, because no general trend was found for the differences between CO_2 and HFC-134a. In the ID 8 mm round tube manifold, the $CLTF$ was largest in the CO_2 experiments, while the opposite results were seen for the base-case MPE-tube manifold (M5). As seen in the previous sections, the value of $CLTF$

varied between manifold geometries. In Figure 5.40 the values of $CLTF$ are plotted as a function of manifold cross-sectional area. $CLTF$ is reduced for increasing cross-sectional area, and the best fit regression curve from *Datafit* is given by:

$$CLTF = (\dot{m}_{l,t}/\dot{m}_{l,m})_{const} = b_1 + e^{\frac{b_2}{A_c \times 10^5 + b_3}} \tag{5.18}$$

where $b_1 = -1.055$, $b_2 = 1.450$ and $b_3 = 7.248$. Given $CLTF$, Equation 5.16 is used to calculate the branch tube vapour fraction, x_t.

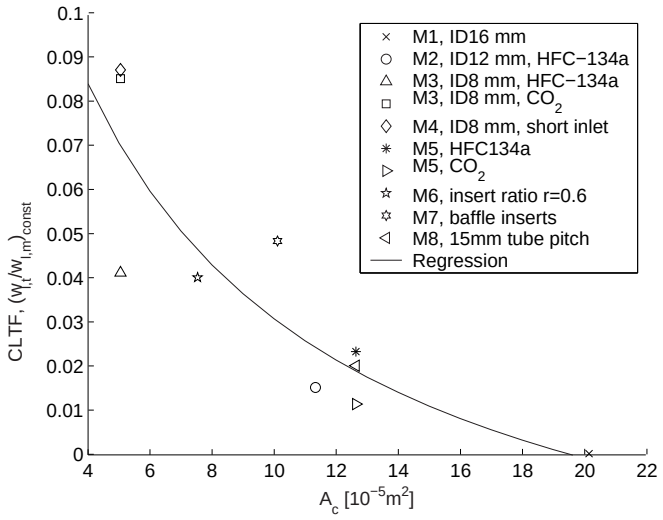

Figure 5.40: Values of the constant liquid take-off fraction, $CLTF$, for all tested manifolds.

In Figures 5.39 and 5.40 the results of all manifolds, with exception of the manifold with spiral insert at the inlet (M9), are included. Manifold M9 had $MMFTC = 0.5$ and $CLTF = 0.11$, which is well below and above, respectively, the regression curves for the rest of the manifolds. The reason for the deviation using the spiral insert manifold is discussed in Section 5.3.6.

Low mass flux region: At manifold mass flux below $MMFTC$ a simplified version of the correlation developed specifically for the ID 16 mm manifold in Section 5.3.2 is suggested. Instead of the nonlinear curve from $x_t = 0$ at $G_{g,m} = 0$ to $x_t = 1$ at $G_{g,m} = G_{g,m,lim}$ a linear curve is used. Based on the plots of x_t as function of $G_{g,m}$ the threshold value $G_{g,m,lim}$ was registered for all manifolds. Figures 5.12 and 5.13 contain the ID 16 mm measurements and Figures 5.23 and 5.24 shows

the results of the ID 8 mm measurements. Corresponding plots for the additional manifolds are provided in Appendix E.1. A linear regression curve is adapted to the $G_{g,m}$ data in the low mass flux region. The value of $G_{g,m,lim}$ is then obtained at the intersection of the regression curve and x_t =1. Figure 5.41 contains the $G_{g,m,lim}$ values for all manifolds plotted against the manifold cross-sectional area, A_c.

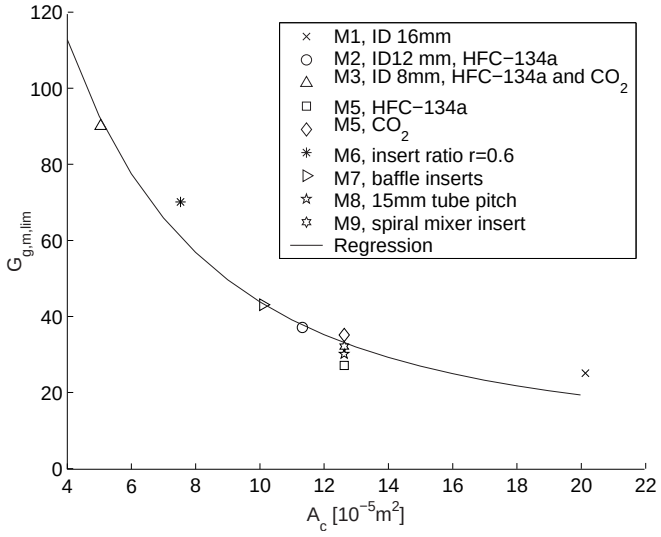

Figure 5.41: Threshold value, $G_{g,m,lim}$, for the low mass flux region.

The best fit regression equation, provided by *Datafit*, to fit the data in Figure 5.41 is:

$$G_{g,m,lim} = b_1 + e^{\frac{b_2}{A_c \times 10^5 + b_3}} \tag{5.19}$$

where $b_1 = 4.471$, b_2 =103.4 and b_3 =18.07. The branch tube vapour fraction in the low mass flux region is then calculated by:

$$\begin{aligned} G_{g,m} < G_{g,m,lim}: &\quad x_t = \frac{G_{g,m}}{G_{g,m,lim}} \\ G_{g,m} \geq G_{g,m,lim}: &\quad x_t = 1 \end{aligned} \tag{5.20}$$

A complete model for the calculation of two-phase distribution in manifold T-junctions is now obtained. The principles of the correlation procedure is given in

Figure 5.42.

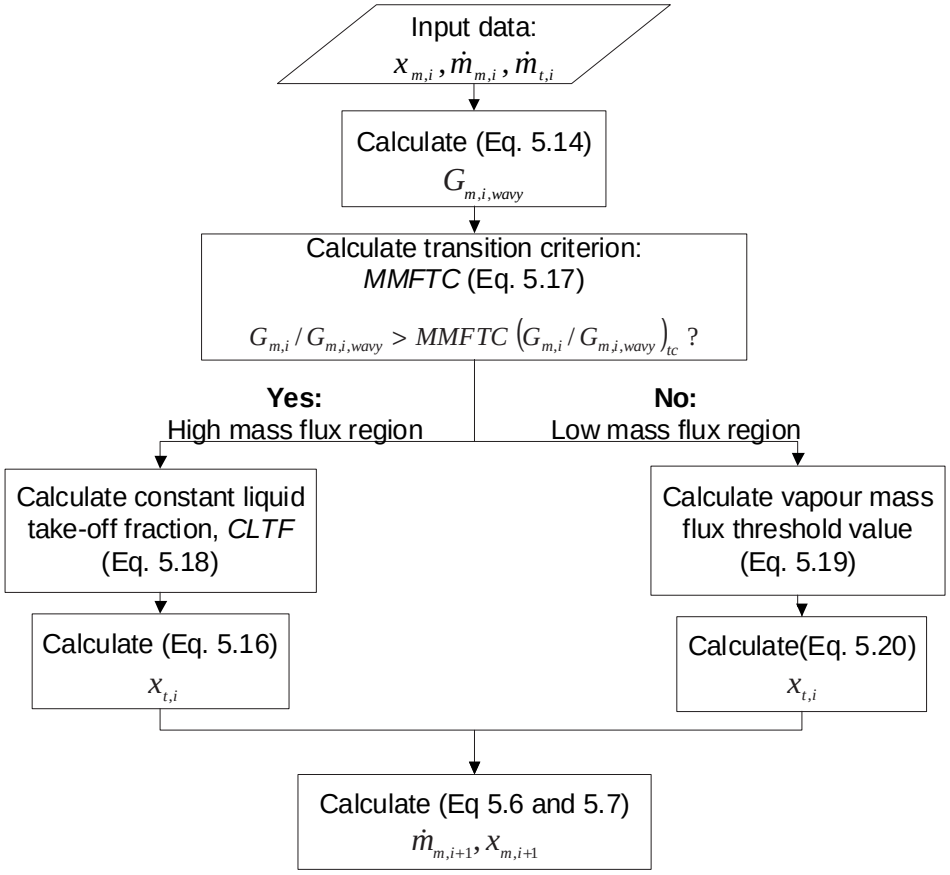

Figure 5.42: Correlation procedure for manifolds with upward flow in branch tubes.

5.3.5.2 Comparison of the new model to experimental results and T-junction models

In this Section the developed model is compared to the experimental data and to the T-junction models of Seeger et al. (1985), Maciaszek and Micaelli (1990) and Castiglia and Giardina (2002a) (the *Seeger*, *Maciaszek* and *Castiglia* models). The calculation procedure in Figure 5.42 is followed for all manifold models. Results are shown for single data series in Appendix E.2.1 and the absolute deviations are shown for all manifold data series in Appendix E.2.2.

In Figures E.9 and E.10 representative data series for the ID 16 mm manifold with HFC-134a and CO_2 are shown. The deviation to the experimental data is almost the same for the new model and the models of Seeger and Maciaszek, while the Castiglia model overpredicts the vapour fraction in branches *No* 2 to 5 for HFC-134a. The coarser linearized model, Equation 5.20, for the branch tube vapour fraction calculation gives larger deviation to the experimental data than what was obtained with the specially made non-linear model for the ID 16 mm manifold outlined in Section 5.3.2. Figures E.22 and E.23 contain the deviation between predicted and measured branch tube vapour fraction for all measurement points obtained in the ID 16 mm manifold (M1).

Figures E.12 and E.13 show representative data series for the ID 8 mm manifold with refrigerant HFC-134a and CO_2 , respectively, and the deviation between measured and predicted values are given in Figures E.25 and E.26 for the whole sets of data series. The new model is seen to underpredict x_t in the first branches of the HFC-134a experiments. This is due to the large deviation from the regression curve in Figure 5.40 for the ID 8 mm manifold experiments with HFC-134a (A physical interpretation of these observations is given in Section 5.4.4.3). For the CO_2 experiments in Figures E.13 and E.26 as well as for the ID 8 mm round tube manifold experiments with short manifold inlet tube, Figures E.14 and E.27, the new model has better predictability than the T-junction models.

Figures E.15 and E.17 contain representative data series for the base-case MPE-tube manifold (M5) with HFC-134a and CO_2 , respectively. Figures E.28 and E.29 present deviations between measured and predicted values for the full set of experimental data series. Likewise, results are presented for manifold M6 (branch insert ratio, $r = 0.6$) in Figures E.16 and E.30, manifold M8 (15 mm branch tube pitch) in Figures E.18 and E.32 and manifold M7 (baffle inserts) in Figures E.19 and E.31. A tabular comparison of the deviation from the experimental data is given for all models in the next section.

In Figures E.20 and E.21 two representative data series for the manifold M9 (MPE-tube manifold with spiral mixer insert) are shown, while E.33 and E.34 contain the deviation between predicted and measured values for all data series. As discussed in the previous Section the liquid take-off fraction in the high mass flux region is higher for M9 than for all other manifolds tested. A constant liquid take-off fraction $CLTF = 0.11$ is therefore employed for both the CO_2 and HFC-134a data sets.

5.3.5.3 Summary of correlation results

A new empirical model for the prediction of branch tube vapour fraction has been developed. The model takes into account the change in flow regime in the manifold due to reduction of mass flow and vapour fraction along the manifold length. Different manifold geometries have been used to analyse how changes in manifold free flow cross-sectional area changes the two-phase distribution.

In Figure 5.43 results of the new correlation are compared to the models of Seeger et al. (1985), Castiglia and Giardina (2002a) and Maciaszek and Memponteil (1986). Average values of the absolute deviation between predicted branch tube vapour fraction, x_t^{pred}, and measured branch tube vapour fraction, x_t, are used to compare the models. The calculation is based on the total set of experimental data series.

$$\overline{\Delta x_t} = \sum_{i=1}^{n} \frac{\mid x_t^{pred}(i) - x_t(i) \mid}{n} \tag{5.21}$$

where n is the number of measurements in the experimental data set.

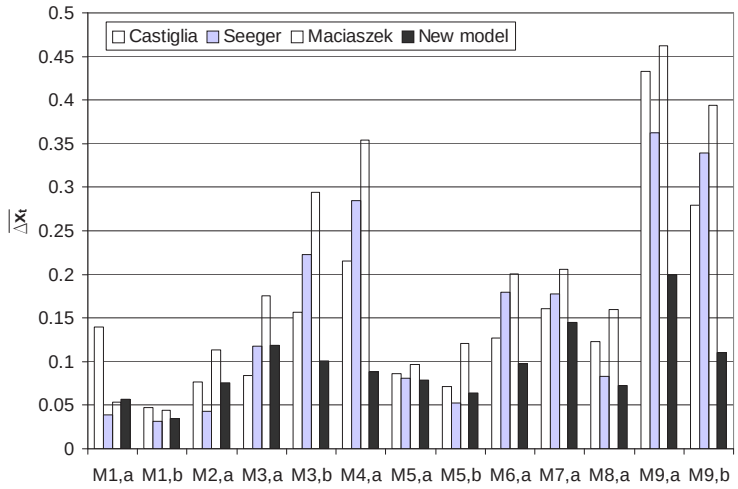

Figure 5.43: Average deviation between measured branch tube vapour fraction and predictions of Seeger et al. (1985), Castiglia and Giardina (2002a), Maciaszek and Memponteil (1986) and the new model. a = HFC-134a, b = CO_2 .

The single T-junction models all predict that the vapour fraction approaches single-phase vapour flow at high mass flow values in the main pipe. The new model takes

into account observed behaviour that at increasing the mass flow there is a transition to a regime where the liquid take-off fraction can be regarded as constant.

The results in Figure 5.43 show that the new model is able to predict the phase distribution within a mean absolute deviation between predicted and measured vapour fraction of 0.04 in the ID 16 mm manifold to 0.20 in manifold M9. Based on these results it seems that a T-junction analysis approach is applicable for the prediction of phase distribution in the manifolds investigated in this study.

5.3.6 Analysis of factors influencing two-phase flow distribution in upward configuration

By analysing the manifold two-phase flow distribution using a local T-junction approach, it was possible to evaluate the effects of manifold flow properties and manifold geometry on the gas and liquid take-off in the branch tubes. Based on the experimental results in Chapter 4 and the results from the correlation work in the previous sections, there are a number of trends.

5.3.6.1 Manifold mass flux

The effects of gravity and momentum flux ratio between the liquid and gas phase, $(\rho u^2)_l / (\rho u^2)_g$, favoured gas off-take in the upward configuration. The gravity made the liquid gather at the bottom of the manifold, providing a non-homogeneous void distribution in the manifold, while the momentum-flux difference favoured low momentum flux gas take-off due to the adverse pressure field in the longitudinal direction of the manifold.

The two-phase distribution data in the different manifolds tested showed a behaviour that made it plausible to divide the correlation into two separate regions depending on the total mass flux at the inlet of the local T-junctions in the manifold. Therefore a high mass flux and a low mass flux region was defined, with different dominating physical phenomena affecting the two-phase flow distribution.

The manifold with the smallest cross sectional area, A_c, and hence the largest inlet mass flux, was the ID 8 mm round tube manifold (M3). The first branch tubes in M3 had almost constant liquid take-off fraction (LTF), independent of branch tube position and vapour fraction at the manifold inlet (Figure 5.27). A transition to a low mass flux region occured along the manifold, where the phase separation

in the T-junctions could be correlated using the same methodology as in the ID 16 mm manifold. The transition between the regions of high and low mass flux was defined as the $MMFTC$ (Manifold Mass Flux Transition Criterion).

High mass flux region

In the high mass flux region, inertia was strong compared to the gravity acting on the fluid. This could explain the poor predictability of the T-junction correlations in this region, which were developed for stratified flow in the main pipe. As was seen in the correlation development in Section 5.3.5, the liquid mass flow rate in the branch tube was proportional to the manifold liquid mass flow rate at the inlet of the local T-junction for a given manifold geometry. Hence, the liquid take-off fraction in the branch tube was found to be constant ($CLTF$ - Constant Liquid Take-off Fraction). In contrast, the gas take-off could vary much between the individual branch tubes (see e.g. Figures 4.35 and 4.36). The variation in gas flow rate in the branch tubes could be caused by the static pressure distribution both in the inlet and the outlet manifold, and the pressure losses in the branch heat exchanger tubes. It therefore seemed that in the high mass flux region, the liquid distribution was mostly affected by the local two-phase split in the manifold, while the gas take-off was much more affected by the pressure distribution in the total heat exchanger system.

The constant liquid take-off fraction ($CLTF$) was seen to vary with the free-flow cross-sectional area, A_c of the manifold (Figure 5.40). The $CLTF$ was reduced at increasing manifold cross-sectional area. This was in accordance with the T-junction results reported by e.g. Reimann et al. (1988), who argued that the vertical height that the liquid had to be elevated, to overcome the gravitational forces, was important for the fraction of liquid take-off. Stacey et al. (2000) found similar results, where a $D_1 = 0.005$ m T-junction gave higher liquid take-off than equivalent data of Buell et al. (1994) ($D_1 = 0.038$ m). The authors explained the difference with the greater distance the liquid had to traverse to enter the branch tube at large pipe diameters. Also, (Azzopardi, 2000) found a diameter effect on the void distribution in horizontal tubes, where the asymmetry increased for increasing pipe diameters. Hence, the region of the manifold cross-section where flow was diverted into the branch tube would have a higher void fraction in T-junctions with larger diameter main tubes.

Transition between the high and the low mass flux region

The transition between the regions of high and low mass flux was defined as the Manifold Mass Flux Transition Transition Criterion, $MMFTC$, Figure 5.29. A close correlation was found between the $MMFTC = G_m/G_{m,wavy}$ and the cross-

sectional area, A_c, of the manifold (Figure 5.39). The $MMFTC$ decreases with increasing A_c. As defined by Kattan et al. (1998), a two-phase flow having mass flux below G_{wavy} was stratified and gravitationally dominated. At mass flux greater than G_{wavy}, the flow was intermittent and dominated by inertia forces. A reason for the strong relation between $MMFTC$ and A_c could be that there is a diameter effect on the mechanism of flow split in the T-junctions, that was not fully taken into account when using the transition criterion from stratified to intermittent flow developed for horizontal pipes. Especially in upward branch configuration, the work that had to be exerted to overcome the gravitational forces and raise the liquid phase into the branch tube was probably larger than the gravitational force necessary to create intermittent flow in a straight pipe, which was accounted for in the flow regime map of Kattan et al. (1998).

Low mass flux region

In the low mass flux region, the branch tube vapour fraction was found to be linearly dependent on the manifold gas mass flux (Equation 5.20). Corresponding results were shown by Watanabe et al. (1995), who correlated the branch tube liquid and vapour take-off fractions by the manifold gas mass flux. In T-junction experiments with upward branch tubes, Ballyk and Shoukri (1990) found that, especially with stratified flow in the main pipe, the gas flow could turn into the branch without interacting with the liquid. As a result, interfacial drag of liquid on the vapour could be neglected. However, the interfacial drag effects of vapour on the liquid could be significant. As seen in the results from the ID 16 mm manifold, liquid entrainment increased along the manifold as a function of the reduction in manifold gas mass flux (see Figures 5.12 and 5.13). At gas mass flux values below $G_{g,m,lim} = 43$ kg/(m^{2}s) liquid was extracted into the branch tube. Similar criterions based on the stratified liquid height in the main tube were used in the phenomenological T-junction models to define a boundary value for pure gas take-off in the branch tube. In the manifolds with smaller A_c, liquid take-off was seen at considerably larger manifold gas mass flux. The reduced distance necessary for elevating the liquid into the branch tube, reduced the effect of gravity and increased the liquid take-off. The T-junction correlations of Seeger et al. (1985), Maciaszek and Micaelli (1990) and Castiglia and Giardina (2002a) showed remarkably good agreement to the current results in the low mass flux region.

Varying manifold cross sectional area - progressive insert

The results with the progressive insert in the manifold (Section 4.12) showed that a constant total mass flux along the length of the manifold did not alter the two-phase distribution significantly compared to the measurements in the base-case manifold (M5). The area reduction at the first tube outlets did not affect the liquid

take-off in these tubes. Hence, the first tubes received less liquid than what would be necessary for an equal distribution and the surplus liquid was transported to the last tubes of the manifold as in the base-case manifold. This showed a weakness of the correlation concept, where the phase distribution is correlated to the manifold mass flux. There is probably a boundary effect coming into account at the end of the manifold, which implied that all surplus liquid, not extracted in the first tubes of the manifold, has to be taken off in the last tubes of the manifold, irrespective of the manifold mass flux. The definition of the $MMFTC$ should therefore only be used for manifolds with constant cross-sectional area. As seen in the pictures of two-phase flow in the glass manifold, the liquid was pooling at the end of the manifold (Figures 4.11 to 4.15). Azzopardi and Smith (1992) found that downstream geometry could affect the two-phase distribution in stratified flow. At downstream flow restrictions, the liquid level was raised at the T-junction and more liquid was taken off in the branch tube. The finite length of the manifold acted as a flow restriction in the longitudinal flow direction, because no flow was allowed to go beyond the last branch tube outlet.

5.3.6.2 Two-phase flow properties at the manifold inlet

The manifold with spiral mixer at the inlet (M9) was an attempt to increase the liquid take-off in the first tubes of the manifold by making the two-phase flow more homogeneous before entering the branch tube T-junctions. As seen in Figure 5.38, there was no clear constant liquid take-off fraction in the high mass flux region. However, taking an average of the liquid take-off fractions above $G_{m,i}/G_{m,i,wavy} = 0.5$ yielded a value of $CLTF = 0.11$, which was well above the value for the base-case MPE-manifold ($CLTF = 0.02 - 0.025$). This implied that more liquid was taken off in the first branch tubes in manifold M9 (also seen in Figures 4.80 and 4.81). A more irregular distribution pattern was seen compared to the manifolds with developed two-phase flow at the inlet. Even if the void distribution was more homogenized due to the spiral mixer, and more liquid was transported as droplets in the upper part of the manifold, the liquid still had much higher momentum flux than the gas phase. This was probably the reason why the gas take-off in tubes No 1 and 2 was large, especially in the HFC-134a experiments (Figure 4.80). The density ratio between liquid and gas was $\rho_l/\rho_g = 4.3$ for CO_2 and $\rho_l/\rho_g = 32.0$ for HFC-134a at the experimental test conditions. The larger momentum flux ratio between the liquid and the gas phase of HFC-134a could therefore explain the larger gas take-off in the first tubes. However, as seen in Section 4.14, no general conclusion could be drawn regarding manifold performance and distribution of HFC-134a and CO_2. Because of better mixing of the

phases and reduced gas momentum due to large mass flow take-off in Tubes *No* 1 to 3, the liquid was more easily taken off in tubes *No* 3 to 6 in the HFC-134a experiments. Combined effects of fluid mixing, gravity and momentum fluxes influenced the two-phase distribution in the spiral mixer manifold results.

Effects of mixing of the two-phase flow at the manifold inlet were also seen in the results reported for the ID 8 mm manifold with short inlet tube, M4, in Figure 4.48. More liquid was allowed to enter the first tubes, indicating a more homogeneous void fraction distribution at the inlet of the manifold, compared to the results obtained with the long manifold inlet tube (Figure 4.35).

5.3.6.3 Manifold geometry

Because of the large number of variables affecting the two-phase distribution in the manifold, the developed empirical model had to be simplified with regard to geometrical parameters. The free flow cross-sectional area, A_c, and the manifold diameter, were taken into the analysis.

In the MPE-tube manifolds (M5 to M10), the tubes were protruding into the manifold. The protrusion of the MPE tubes into the header created a series of obstacles creating turbulence in the two-phase flow. More droplets were probably entrained in the gas phase. Thus, the branch tube T-junctions were likely to be exposed to a more homogeneous flow. However, the correlation analysis showed that the MPE-tube manifold data could be predicted using the same correlation as the round tube manifolds taking into account the reduction in A_c, which was calculated as the free flow cross-sectional area of the manifold below the branch tube inserts. Figure 5.40 showed that the constant liquid take-off fraction, $CLTF$, in the high mass flux region coincided with the line drawn through the round tube manifold data. Minor deviations were seen due to changes in geometry, other than the reduction in A_c. The use of the baffle inserts in manifold M7 gave a small increase in $CLTF$ compared to the correlation prediction. Also, the manifold M6 with tube insert ratio $r = 0.6$ was predicted well by the correlation based on the reduced A_c. Almost no change in two-phase distribution could be seen when changing the pitch between the branch tubes from 21 mm to 15 mm in manifold M8 (See Figures 4.52 and 4.76). Also in the prediction of the manifold mass flux transition criterion, $MMFTC$, in Figure 5.39 and in the prediction of the threshold value $G_{g,m,lim}$ for the low mass flux region in Figure 5.41, the same conclusion could be drawn that the main geometric factor influencing the two-phase flow distribution was the manifold free flow cross-sectional area.

A novel star-manifold geometry, M11, was tested in order to investigate the effect of a shorter longitudinal manifold length on the two-phase distribution. It was initially thought that the short length would provide a smaller pressure gradient along the manifold, and therefore improve the two-phase distribution. The results in Figure 4.92 showed, however, that both the liquid and vapour phase were severely maldistributed also in this manifold design (see Tables 4.4 and 4.5). It was seen that the vapour phase was preferentially taken off in the MPE-tubes in the upper part of the manifold and that the liquid was taken off in the tubes situated in the lower part of the manifold. The problem of maldistribution between the ports of the MPE-tubes could also be expected to be larger in this design because of the longitudinal mounting of the tubes as shown in Figure 4.9. However, no measurements of maldistribution between the ports could be done in the current test rig setup.

5.4 Downward flow configuration

5.4.1 Comparison to existing T-junction models

Four different T-junction models developed for downward branch flow from a horizontal main pipe were outlined in Section 2.6.2: the models of Seeger et al. (1985), Smoglie et al. (1987), Maciaszek and Micaelli (1990) and Castiglia and Giardina (2002a) (Later referred to as the *Seeger, Smoglie, Maciaszek* and *Castiglia* models). As for the analysis of the upward configuration in Section 5.3, these models will be compared to the current experimental data and serve as a benchmark for the development of a new empirical model.

In the current Section the T-junction models are compared to representative data series from the ID 16 mm manifold (M1), ID 8 mm manifold (M3), the base-case MPE-tube manifold (M5) and the MPE-tube manifold with spiral mixer insert (M9). Comparisons to results obtained in the remaining manifolds are shown in Appendix F.2, including also the new correlation model that will be outlined in Section 5.4.2. A thorough analysis of the physical factors affecting two-phase flow distribution is provided in Section 5.4.4.

The procedure for reduction of the experimental data outlined in Section 5.2.2 was used to obtain the mass flow rates and the vapour fractions at the inlet of the successive manifold T-junctions. The void fraction definition, Equation 5.8, and the void fraction model of Rouhani and Axelsson (1970), given in Equation 5.9, was also used in the data analysis for the downward configuration. The liquid

height, h_l, was calculated assuming stratified flow, using Equation 5.10.

Figure 5.44 shows a comparison between the branch tube vapour fraction, x_t, of a representative data series ($\dot{m}_{mIn} = 0.033$ kg/s, $x_{mIn} = 0.28$, $T_{w,tsIn} = 50°$C) and the calculated values from the Seeger, Smoglie, Maciaszek and Castiglia models. The correlations are able to reproduce the main trend in the measured phase split with mainly liquid take-off in the first branches and gas take-off in the last branches of the manifold.

In Figure 5.45 measurement data are shown together with correlation predictions for a measurement series in the ID 8 mm manifold. The models are less able to predict experimental data than for the ID 16 mm manifold. The trend in measured vapour fraction is quite equal to the ID 16 mm results in Figure 5.44, with the exception that some of the liquid is transported to the end of the manifold. The T-junction model predictions are unable to reproduce the increasing trend in the measured branch tube vapour fraction.

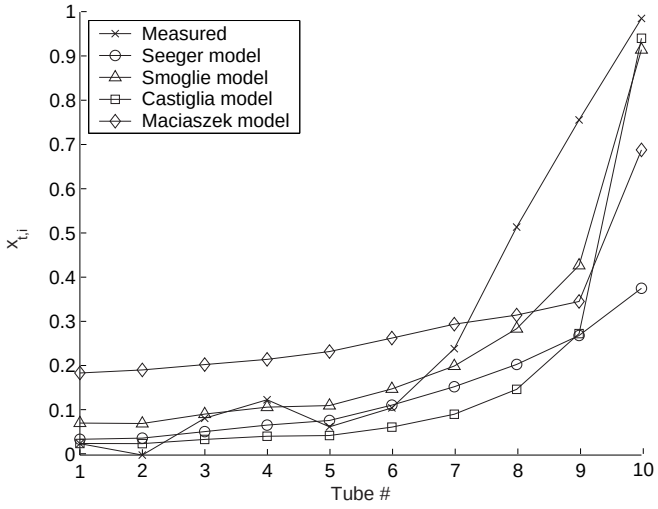

Figure 5.44: Measured branch tube vapour fraction, $x_{t,i}$, compared to the Seeger, Smoglie, Castiglia and Maciaszek T-junction models. ID 16 mm manifold (M1). Refrigerant: HFC-134a, $\dot{m}_{mIn} = 0.033$ kg/s, $x_{mIn} = 0.28$, $T_{mIn} = 29.5°$C, $T_{w,tsIn} = 50.0°$C.

Figure 5.46 shows measured data in the base-case MPE-tube manifold. The models, with exception of the Maciaszek model, are able to predict the main trend in the measured data. In Figure 5.47, measurements from the MPE-tube manifold with spiral mixer insert are shown together with the T-junction model predictions. Here, the models fail to predict the trend in the measurement data with gas take-off

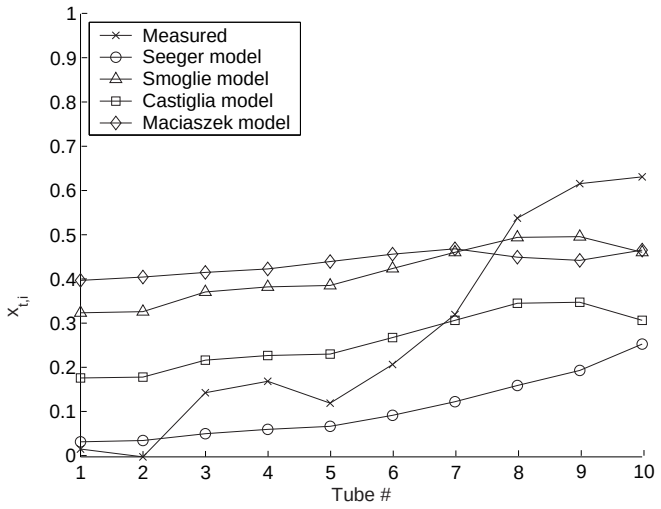

Figure 5.45: Measured branch tube vapour fraction, $x_{t,i}$, compared to the Seeger, Smoglie, Castiglia and Maciaszek T-junction models. ID 8 mm manifold (M3). Refrigerant: HFC-134a, $\dot{m}_{mIn} = 0.033$ kg/s, $x_{mIn} = 0.28$, $T_{mIn} = 29.5°$C, $T_{w,tsIn} = 50.0°$C.

mainly in the three first and the last two branch tubes.

5.4.2 Data reduction and model development

The Seeger, Smoglie and Castiglia models predicted the trends in the measured branch tube vapour fractions quite well in the ID 16 mm manifold and the base-case MPE-tube manifold, while larger deviations were seen for the rest of the manifolds. The Smoglie, Castiglia and the Maciaszek models were developed for stratified flow in the main pipe and for regular T-junctions, without branch tube protrusions into the main tube. As seen in Section 5.3, the flow regime at the inlet of the ID 8 mm manifold was in the intermittent region for the mass flow rates and vapour fractions utilized in the current study. Also, the protrusion of the MPE-tubes in the manifolds M5 to M10 are expected to provide substantial mixing of the two-phase flow in downward configuration, as visualized in the glass tube manifold in Figure 4.16.

In order to correlate phase-split in the measurement data, the T-junction approach outlined in Section 5.2.1 was used. Several alternatives were tested to find general relations depending on properties of the manifold flow and the manifold geome-

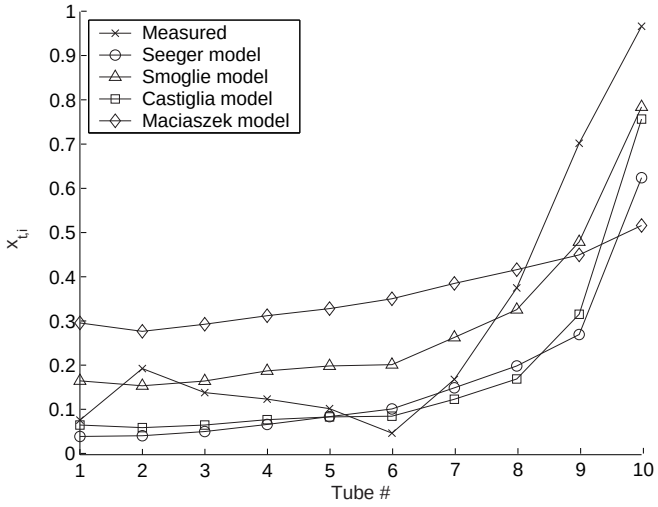

Figure 5.46: Measured branch tube vapour fraction, $x_{t,i}$, compared to the Seeger, Smoglie, Castiglia and Maciaszek T-junction models. Base-case MPE-tube manifold (M5). Refrigerant: HFC-134a, $\dot{m}_{mIn} = 0.033$ kg/s, $x_{mIn} = 0.28$, $T_{mIn} = 29.5°$C, $T_{w,tsIn} = 50.0°$C.

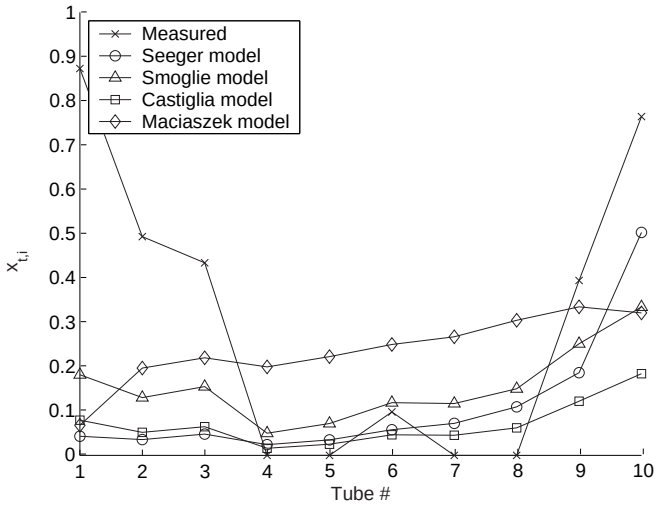

Figure 5.47: Measured branch tube vapour fraction, $x_{t,i}$, compared to the Seeger, Smoglie, Castiglia and Maciaszek T-junction models. Manifold M9 (MPE-tube manifold with spiral mixer insert). Refrigerant: HFC-134a, $\dot{m}_{mIn} = 0.033$ kg/s, $x_{mIn} = 0.28$, $T_{mIn} = 29.5°$C, $T_{w,tsIn} = 50.0°$C.

try. Figures 5.48 and 5.49 show measurement data from the ID 8 mm manifold and the base-case MPE-tube manifold presented as liquid take-off fraction (LTF), $\dot{m}_{l,t,i}/\dot{m}_{l,m,i}$, as function of dimensionless manifold mass flux, $G_m/G_{m,wavy}$, following the same procedure as for upward flow described in Section 5.3.3.2. The transition between the stratified-wavy and intermittent flow regime, G_{wavy}, was defined in Equation 5.14. Again, it must be stressed that the flow regime transition defined by Zürcher et al. (1999) was intended for use only in fully developed two-phase flow in horizontal tubes. However, it was used in the current context under the assumption that it would provide a measure for the relative strength of the gravitational and inertia forces in the developing manifold flow. $G_{m,i,wavy}$ is the mass flux at the transition between stratified-wavy and intermittent flow regimes calculated using the two-phase properties at the inlet of manifold T-junction *No i*.

As in the analysis of measurement data in upward flow, a clear correlation between LTF and $G_m/G_{m,wavy}$ is seen in Figures 5.48 and 5.49. Similar results from the remaining manifolds are shown in Appendix F.2. It was concluded in the analysis of upward configuration data that the effects of fluid properties e.g. surface tension, liquid and vapour densities on the two-phase flow regime were taken into account in the calculation of G_{wavy}. The same appears to be valid also in downward configuration, considering the small scattering of the reduced measurement data in Figures 5.48 and 5.49. It seems clear that a feasible procedure is to correlate LTF against the dimensionless manifold mass flux in order to estimate the phase split in manifold T-junctions.

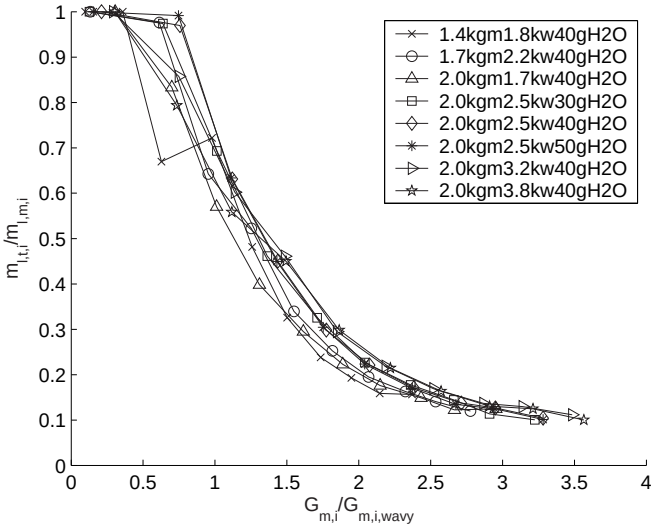

Figure 5.48: Liquid take-off fraction (LTF), $\dot{m}_{l,t,i}/\dot{m}_{l,m,i}$, as function of dimensionless manifold mass flux. Values from all measurement series in the ID 8 mm manifold with CO_2 are plotted.

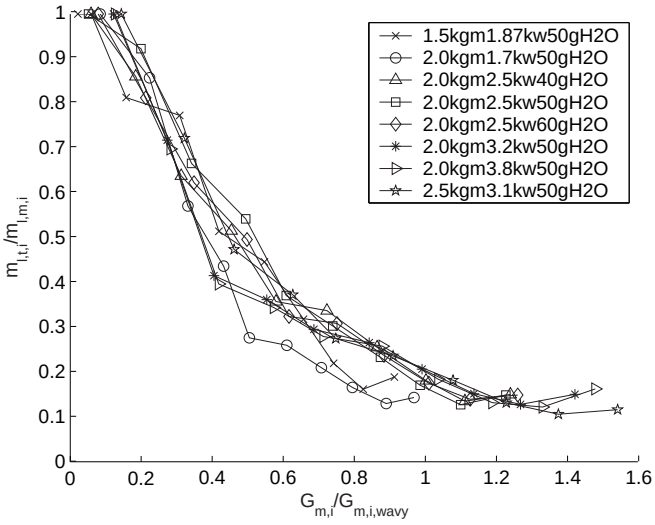

Figure 5.49: Liquid take-off fraction (LTF), $\dot{m}_{l,t,i}/\dot{m}_{l,m,i}$, as function of dimensionless manifold mass flux. Values from all measurement series in the base-case MPE-tube manifold (M5) with HFC-134a are plotted.

The slope of the LTF data is different for the two manifolds shown in Figures 5.48 and 5.49. The manifold with the smallest cross-sectional area (ID 8 mm) gives higher LTF for a given value of $G_m/G_{m,wavy}$. Therefore, a multi-variable regression was performed using the *Datafit* software, fitting the LTF data to $G_m/G_{m,wavy}$ and manifold cross sectional area, A_c. Based on the data set, *Datafit* found the function that gave the least regression error from a large set of predefined functions. The algorithm applied a Gauss-Newton method with Levenberg-Marquardt modifications for global convergence (Press et al., 1999). The two-dimensional best fit regression is given in Equation 5.22 and shown in Figure 5.50.

$$LTF = \frac{\dot{m}_{l,t,i}}{\dot{m}_{l,m,i}} = a + bx_1 + cx_1^2 + dx_1^3 + ex_1^4 + fx_1^5 + g/A_c + h/A_c^2 \tag{5.22}$$

where,

$$x_1 = \log(G_{m,i}/G_{m,i,wavy}) \tag{5.23}$$

The fitted parameters are given in Table 5.1. The ID 16 mm manifold experimental data, shown in Figures F.1 and F.2, gave large disturbances in the data regression and were therefore left out. However, the developed model was compared also to the ID 16 mm data.

Table 5.1: Regression parameters, provided by *Datafit*, for the empirical model defined by Equation 5.22.

$a = -0.093718$	$e = -0.021347$
$b = -0.37993$	$f = -0.0042291$
$c = 0.087394$	$g = 2.8725$
$d = 0.013578$	$h = 0.38019$

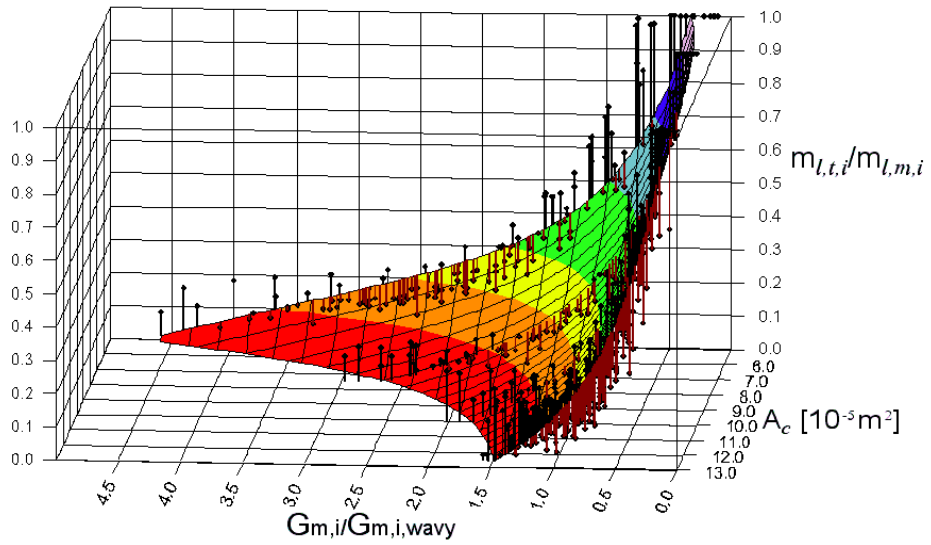

Figure 5.50: Results of the multi-variable regression (Equation 5.22). The 3D-regression surface is shown as well as the deviation in the measurement data.

As seen in Figures 5.48 and 5.49, the liquid take-off fraction, LTF, is equal to unity at small mass flux values in the manifold. It was beneficial to correlate the transition between the region of $LTF = 1$ and $LTF < 1$, because the regression in Equation 5.22 could provide non-physical values, $LTF > 1$, at manifold mass fluxes approaching zero. By inspection of the measurement data in Figures 5.48 and 5.49 and in Appendix F.2, the transition curve was fitted as shown in Figure 5.51.

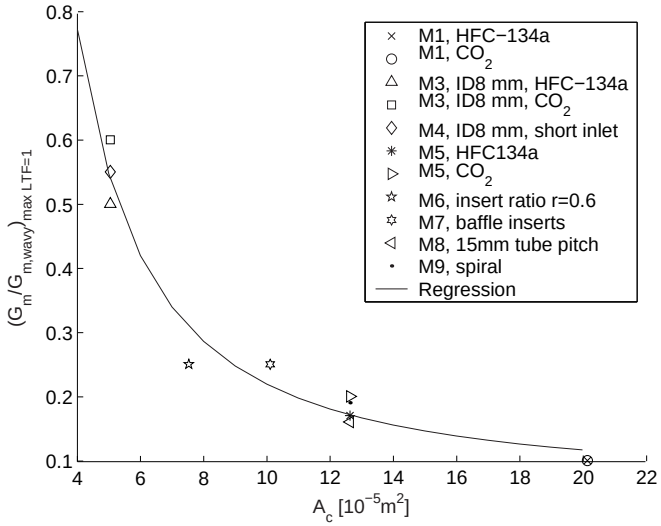

Figure 5.51: Dimensionless mass flux at transition between $LTF = 1.0$ and $LTF < 1$ for all manifolds.

The best fit regression curve shown in Figure 5.51 was found by *Datafit*:

$$\left(\frac{G_m}{G_{m,wavy}}\right)_{max,LTF=1} = a + \frac{b}{A_c} + \frac{c}{A_c^2}; \tag{5.24}$$

The following regression parameters were found: $a = 0.056508$, $b = 0.82231$ and $c = 8.2167$. Also, by inspection of the measurement data in Figures 5.48 and 5.49 and in Appendix F.2, it was found that a lower bound on the correlation should be defined. A value of $LTF_{min} = 0.1$ was therefore utilized.

Results of the new model are shown for the ID 8 mm manifold and the base-case MPE-tube manifold (with the same data sources as Figures 5.48 and 5.49) in Figures 5.52 and 5.53. Corresponding results are shown for the remaining manifolds in Appendix F.2.

The empirical correlation for the liquid take-off fraction (LTF), $\dot{m}_{l,t,i}/\dot{m}_{l,m,i}$, found by Equations 5.22 and 5.24 can now be used to predict the branch tube vapour fraction based on measured branch tube mass flow rates, following the same procedure as outlined in the upward flow configuration in Equation 5.16:

$$x_{t,i} = \frac{\dot{m}_{g,t,i}}{\dot{m}_{t,i}} = \frac{\dot{m}_{t,i} - \dot{m}_{l,t,i}}{\dot{m}_{t,i}} = \frac{\dot{m}_{t,i} - LTF\dot{m}_{l,m,i}}{\dot{m}_{t,i}} \tag{5.25}$$

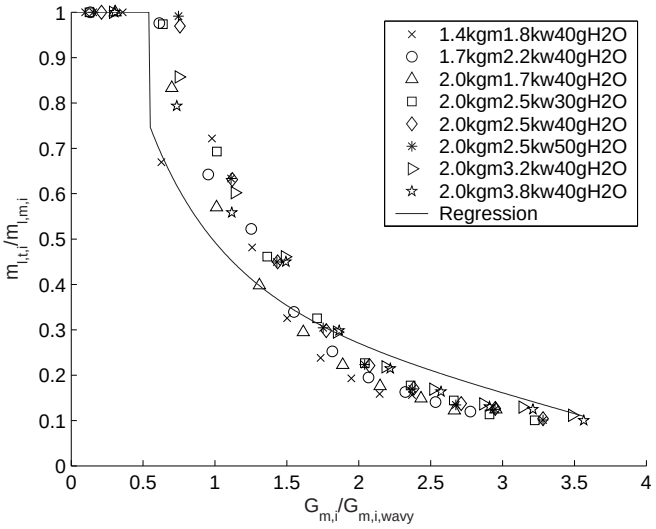

Figure 5.52: Liquid take-off fraction, $\dot{m}_{l,t,i}/\dot{m}_{l,m,i}$, as function of dimensionless manifold mass flux. Values from all measurement series in the ID 8 mm manifold (M3) with CO_2 are plotted together with the general manifold regression (Equation 5.22).

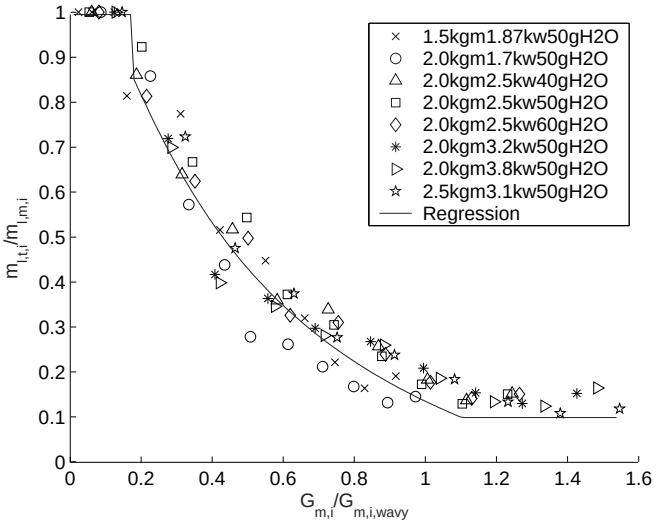

Figure 5.53: Liquid take-off fraction, $\dot{m}_{l,t,i}/\dot{m}_{l,m,i}$, as function of dimensionless manifold mass flux. Values from all measurement series in the base-case MPE-tube manifold (M5) with HFC-134a are plotted together with the general manifold regression (Equation 5.22).

5.4.3 Summary of correlation results

In order to analyze the performance of the correlation procedure developed in the previous section, simulations were performed using Equation 5.25 to calculate x_t. Results are shown for single data series in Appendix F.2.1 and the absolute deviations are shown for all manifold data series in Appendix F.2.2. A summary of the results is shown in Figure 5.54, containing the average deviation between model predictions and experimental measurements for all manifolds. Equation 5.21 was used to calculated the average deviation between the predicted branch tube vapour fraction and the measurement values.

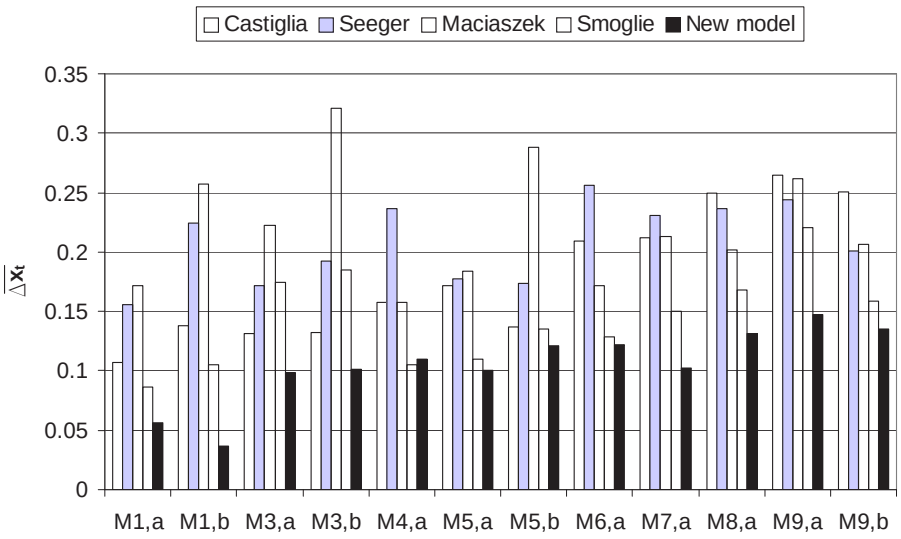

Figure 5.54: Average deviation between measured branch tube vapour fraction and predictions of Seeger et al. (1985), Castiglia and Giardina (2002a), Maciaszek and Memponteil (1986), Smoglie et al. (1987) and the new model. a = HFC-134a, b = CO_2 .

Figure 5.54 shows that the new empirical model was able to predict the branch tube vapour fraction within an average deviation of $\pm 15\%$ in all manifolds.

5.4.4 Analysis of factors influencing two-phase flow distribution in downward configuration

Several effects of manifold flow properties and manifold geometry on the gas and liquid take-off in downward configuration can be analysed based on the T-junction correlation approach developed in the Section 5.4.2. The current Section contains a qualitative discussion on the factors influencing two-phase flow distribution in horizontal manifolds with vertically downward directed branch tubes.

5.4.4.1 Manifold mass flux

In downward configuration, the effects of gravity and momentum flux ratio between the phases, $\left(\rho u^2\right)_l / \left(\rho u^2\right)_g$, acts in opposite directions with regard to two-phase flow distribution. The gravity favours liquid take-off in the downward directed branch tubes, while the momentum difference between the phases favours low momentum gas take-off in the branch tubes, due to the adverse pressure field in the longitudinal direction of the T-junction. As described in Section 2.5.2, the pressure gain caused by retardation of flow in the manifold favours a take-off of gas in the branch tubes, while the liquid, generally having higher momentum due to the larger density, is not deflected into the T-junction. As shown in Figures 2.8 and 2.9, Seeger et al. (1985) measured that liquid was preferentially taken off in a regular T-junction under most test conditions. However, when the influence of the momentum flux ratio exceeded the influence of gravity, the branch tube vapour fraction could be higher than the T-junction inlet vapour fraction. At increasing mass flow take-off values, $\dot{m}_3/\dot{m}_1$, Seeger et al. (1985) observed increasing vapour take-off. Also, the vapour take-off was increased for increasing vapour fraction at the inlet of the T-junction (Figure 2.8).

The two-phase distribution results in the ID 16 mm manifold, shown in Figures 4.27 and 4.28, revealed that tubes *No* 1 to 6 received more liquid and less gas than they would do at homogeneous distribution. The experiments at lowest inlet vapour fraction showed the most severe maldistribution of the gas phase, with almost all of the gas going to the two last tubes of the manifold. According to the Kattan et al. (1998) flow map, the two-phase flow pattern at the inlet of the ID 16 mm manifold was expected to be in the stratified region (see Figures 5.19 and 5.20). These results were in accordance with the observations of Shoukri et al. (2002), who showed that a decreasing vapour flow rate in the main tube, producing a thicker liquid layer, resulted in onset of vapour extraction at higher flow split ratios.

Change in the mass flow in the ID 16 mm manifold did not change the two-phase distribution much. Keeping the vapour fraction constant at the manifold inlet, the void fraction and hence the height of the liquid layer at the bottom of the manifold would be almost unchanged, as long as the mass flows were within the range of the stratified flow regime.

Reducing the manifold cross-sectional area, A_c, from the ID 16 mm manifold to the ID 8 mm manifold increased the mass flux by a factor of four. As shown in Section 5.3.3, this led to a transition from stratified to intermittent flow at the inlet of the manifold. In the ID 8 mm manifold, more gas was taken off in the branch tubes *No* 3 to 7, and more liquid was transported to the tubes at the end of the manifold (Figures 4.42 and 4.43). The increase in mass flux in the manifold would increase the effect of the phase momentum flux ratio compared to the effect of gravity. Also, the height of a possible liquid layer at the bottom of the manifold would be lower due to the reduced manifold diameter. However, especially the results with HFC-134a in Figure 4.42 showed that almost only liquid was taken off in the two first branch tubes. This could be explained by the effect observed in annular flow by Azzopardi (2000) that a low momentum liquid film at the wall was preferentially extracted at low mass flow extraction ratios. The T-junction correlations, developed based on stratified flow in the main pipe, thus showed poor predictability in the ID 8 mm manifold.

The correlation development in the previous section showed that the liquid mass flow rate in the branch tube was proportional to the manifold liquid mass flow rate at the inlet of the local T-junction, for a given manifold geometry. The variation in gas flow rate in the branch tubes could be caused by the static pressure distribution both in the inlet and the outlet manifold, and the pressure losses in the branch heat exchanger tubes. It therefore seemed that the liquid distribution was given mainly by the local two-phase split in the manifold, while the gas take-off was also influenced by the pressure distribution in the total heat exchanger system.

5.4.4.2 Manifold geometry

Visual observations of the glass manifold, Figure 4.16, revealed that the flow in the manifold at downward configuration was much more disturbed due to the protrusion of the branch tubes than what was the case in upward configuration. The liquid layer at the bottom of the manifold was mixed into the gas flow at the first branch tube protrusion. In the MPE-tube manifolds (M5 to M10), the tubes protruded into the manifold, creating turbulence in the two-phase flow. As seen in the results of the base-case MPE-tube manifold in Figure 5.46, more gas was ex-

tracted in tubes *No* 1 to 5 than what was observed in the round tube manifolds. This could be due to the increased effect of phase momentum ratio compared to gravity, since the gas could be taken off into the branch tube without being sucked through a liquid film travelling along the bottom of the manifold. In addition, the low momentum liquid film at the bottom of the manifold inlet tube was mixed and accelerated into the gas flow, thus increasing gas take-off due to the tube protrusions.

5.4.4.3 Two-phase flow properties at the manifold inlet

The short inlet tube to the ID 8 mm manifold, Figure 4.50, provided a more uniform distribution compared to the results with long inlet tube. Also the gas distribution was more uniform with exception of the experiment at lowest vapour fraction at the manifold inlet ($x_{mIn} = 0.10$), where most of the gas was transported to the two last branch tubes of the manifold. It could be anticipated that the flow disturbance, caused by the 90° bend close to the manifold inlet would be more pronounced at the higher vapour fractions because of the higher velocities. The large difference between the long and short inlet tube of the ID 8 mm manifold indicated that phase mixing at the inlet of the manifold was important for distribution in the manifold also in downward flow. Mixing of the two-phase flow reduced the height of the liquid layer at the bottom of the manifold favouring gas take-off in the first branch tubes. Also, mixing provided a more homogeneous flow with less slip between the phases. At reduced slip, the velocity difference between the phases was reduced. This would imply an increase in the liquid momentum and a reduction in the gas momentum, favouring gas take-off in the first branch tubes of the manifold.

The spiral mixer at the inlet of manifold M9 was an attempt to homogenize the two-phase flow before entering the branch tube T-junctions. In upward flow configuration this yielded improved distribution due to higher liquid take-off in the first branch tubes. Results from the downward configuration experiments with the spiral mixer, Figures 4.84 and 4.85, showed that the first tubes of the manifold extracted more gas than they would do at equal two-phase distribution. The effect of mixing was greater than what was measured for the ID 8 mm manifold with the short inlet tube. The momentum of the liquid phase in the mixed flow was now too large to provide an equal liquid take-off in branch tubes *No* 1 and 2. As seen in Figures 4.84 and 4.85, the tubes *No* 3 to 8 received much liquid because of the reduced momentum of the flow due to flow take-off in the first branch tubes. Most of the remaining gas, not taken off in the first three tubes, was transported to the last two tubes of the manifold. A conclusion based on this discussion would be

that a moderate mixing at the inlet provided the most uniform flow distribution in downward configuration.

When comparing the results of the experiments with HFC-134a and CO_2 in Figures 4.60 and 4.61 for the base-case MPE-tube manifold, a difference was seen in the vapour take-off in the first two branch tubes of the manifold. The larger momentum flux ratio in the HFC-134a experiments, due to the higher liquid to gas density ratio, favoured the take-off of gas compared to the CO_2 experiments. Thus, the two-phase distribution with HFC-134a was more homogeneous than with CO_2 in downward flow in the base-case MPE-tube manifold. The same effect was seen in the experiments with the spiral mixer insert. However, the large gas take-off in the first branch tubes due to the mixed two-phase flow was amplified in the HFC-134a experiments, providing even higher gas take-off and reduced uniformity, as seen in Tables 4.4 and 4.5.

Smaller differences were seen between HFC-134a and CO_2 in the ID 16 mm manifold. Due to stratified flow conditions at the inlet, and no tube protrusions disturbing the stratified flow regime, it could be argued that the gravity effect was greater than the effect of phase momentum ratio, resulting in smaller differences between HFC-134a and CO_2 in this manifold. The effect of momentum flux ratio was more pronounced because of the increased mass flux in the ID 8 mm manifold. The same pattern as in the base-case MPE-tube manifold was seen with improved gas extraction in the first tubes, resulting in more uniform two-phase distribution in the HFC-134 experiments.

Chapter 6

Heat Exchanger Simulations

The current Chapter outlines a simulation model which was developed in order to elucidate the consequences of refrigeration maldistribution in heat exchangers with parallel flow circuits.

In Section 6.1, the heat exchanger model is described. The overall network structure of the model and a detailed review of the component models are outlined. Three different models for two-phase distribution in the inlet manifold are implemented. First, uniform distribution is modelled with equal vapour fraction entering all the parallel heat exchanger tubes. Second, a model is developed based on full separation of the liquid and the gas in the inlet manifold. The gas enters the first tubes of the manifold, and the liquid is distributed to the last tubes. Total separation of liquid and gas represents the 'worst case'-scenario of manifold maldistribution. Third, the two-phase distribution correlations developed in Chapter 5 are implemented.

Section 6.2 contains a single-tube heat exchanger analysis, comparing the heat transfer calculations to the measured heat transfer in the experiments. An analysis of the dependency between mass flow, pressure drop and inlet vapour fraction in a single heat exchanger tube is also given.

Heat exchanger simulations are performed in Section 6.3, where the three models for two-phase flow distribution in the inlet manifold are compared and consequences of maldistribution are investigated.

6.1 Outline of the heat exchanger model

As seen in Chapters 4 and 5, the two-phase flow was generally unevenly distributed to the heat exchanger tubes. Yet, in heat exchanger models it has been common practice to ignore manifold maldistribution and assume a homogenous mixture of liquid and vapour entering parallel tubes of a heat exchanger pass[1]. In heat exchanger design, the capacity reduction due to maldistribution has normally been compensated for by adding extra heat exchanger surface area, compared to simulation results.

In order to analyse the relations between two-phase distribution in the manifolds and heat transfer capacity of the heat exchanger tubes, the computational model must handle the strongly coupled system of several heat exchanger tubes in parallel. Especially, the nonlinearity in the momentum equations in this system place constraints on the solution procedure. Also, in order to use the correlations developed in Chapter 5, a flexible model had to be developed that could take into account the T-junction flow splits. Network solvers have previously been utilized for centralized numerical integration of stiff pressure-flow couplings of large and complex thermal/hydraulic systems, see e.g. Endrestøl et al. (1989) and Malik et al. (1998).

Because of the distributed structure of the network modelling concept, the model is well suited for an object-oriented programming structure. The Fortran90 programming language was selected because of its semi object-oriented features and its outstanding computational strength.

6.1.1 Hydraulic network model

6.1.1.1 Network topological properties

An example of a simple network model is shown in Figure 6.1, where pipe sections, denoted *units*, are connected in *nodes*. The units can contain pipe sections, fittings, bends, valves, pumps, compressors or any other component whose differential pressure versus mass flow rate is known. A node is a point where two or more units join. As seen in the next section, the network flow problem is solved by defining continuity equations for mass and energy in the nodes. Feed and sink units are used to define boundary conditions in the model, where mass flow rates,

[1] A heat exchanger pass consists of several tubes in parallel connected to common inlet and outlet manifolds. A heat exchanger can contain several passes in series.

pressures and enthalpies can be specified.

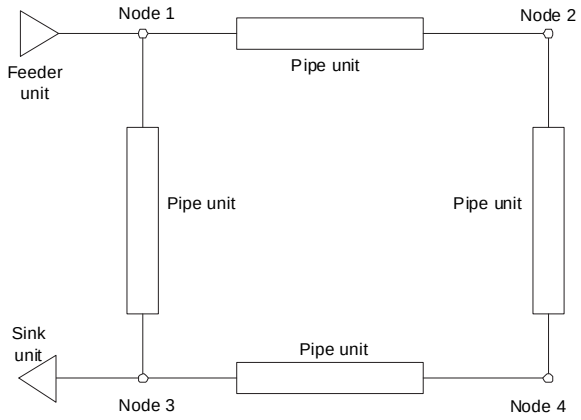

Figure 6.1: Simple network model with nodes and units.

Because of the modular concept of the network model, there are no limitation on the complexity of the unit models. To simulate the experimental test rig described in Chapter 3, special purpose models were developed for the countercurrent refrigerant/water tubes (outlined in Section 6.1.2) as well as unit models representing the straight tube sections in the inlet and outlet manifolds between the branch tube T-junctions. These tube sections take into account frictional pressure drop, as well as sudden pressure changes related to the flow splits in the manifold (see Sections 6.1.3.3 and 6.1.3.4). Special nodes are used to model different two-phase flow distributions in the inlet manifold. These are described in Section 6.1.4.

The network model is easily configured, such that different types of heat exchanger designs can efficiently be investigated. The model is made up of manifolds and tubes which can be arranged to imitate different heat exchangers, both evaporators and condensers. The network structure with n nodes and u units is defined in a node-unit connection matrix, which is an n by u matrix that has a row for every node and a column for every unit. For each column the nonzero entries $+1$ and -1 indicate the node at the inlet and outlet of the unit, respectively.

6.1.1.2 Network conservation equations

Regardless of the topological configuration of the network, the flow of a fluid in the system is governed by conservation of mass and energy. A dynamic formulation of the conservation equations is used in the overall network model. At

this time, the dynamic equations are used only to find the solution of the steady state-problem. However, the dynamic formulations would make it easier to extend the model to a dynamic heat exchanger simulator at a later stage. The mass and energy conservation equations for the nodes are given by:

$$\frac{\partial(\rho V)}{\partial t} = \sum_{in} \dot{m}_{in} - \sum_{out} \dot{m}_{out} \tag{6.1}$$

$$\frac{\partial(\rho u V)}{\partial t} = \sum_{in} \dot{m}_{in} h_{in} - \sum_{out} \dot{m}_{out} h_{out} \tag{6.2}$$

The equation of state is used to express the density time derivative in terms of pressure and enthalpy,

$$\frac{\partial \rho}{\partial t} = \frac{\partial \rho}{\partial p}\frac{\partial p}{\partial t} + \frac{\partial \rho}{\partial h}\frac{\partial h}{\partial t} \tag{6.3}$$

In case of two-phase flow, the homogeneous model is used to calculate the density in the nodes.

6.1.1.3 Solution procedure for the network flow problem

In the solution algorithm, the pressure and enthalpy are chosen as state variables for the nodes. By assuming constant node volume and decoupling pressure and enthalpy, the enthalpy derivative in the mass conservation equation (6.1) can be discarded, thus giving:

$$V\left(\frac{\partial \rho}{\partial p}\frac{\partial p}{\partial t}\right) = \sum_{in} \dot{m}_{in} - \sum_{out} \dot{m}_{out} \tag{6.4}$$

A simplified case of one inlet and one outlet stream to/from node *No i* is shown in Figure 6.2.

The mass conservation equation for node *No i* in Figure 6.2 is given by:

$$\frac{\partial p_i}{\partial t} = \frac{1}{V_i\left(\frac{\partial \rho}{\partial p}\right)_i}\left(\dot{m}_{j-1} - \dot{m}_j\right) \tag{6.5}$$

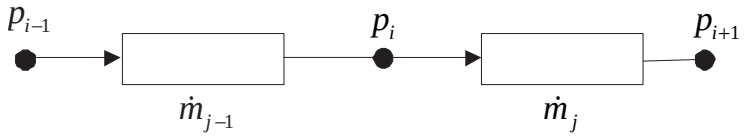

Figure 6.2: Node and unit notations.

Linearization of the pressure differential from timestep n to timestep $n+1$ and using implicit expressions for the unit mass flow rate values yield:

$$p_i^{n+1} = p_i^n + \Delta t \frac{1}{\tau}\left(\dot{m}_{j-1}^{n+1} - \dot{m}_j^{n+1}\right) \tag{6.6}$$

where Δt is the time step length. The time constant τ is defined as:

$$\tau = V_i \left(\frac{\partial \rho}{\partial p}\right)_i^n \tag{6.7}$$

The implicit mass flow rate terms in Equation 6.6 are linearized to be expressed in pressure p^{n+1} and known properties at timestep n:

$$\begin{aligned} \dot{m}_j^{n+1} = \quad & \dot{m}_j^n\left(p_i^n, p_{i+1}^n, h_i^n\right) + \left(\tfrac{\partial \dot{m}_j}{\partial p_i}\right)^n \left(p_i^{n+1} - p_i^n\right) \\ & + \left(\tfrac{\partial \dot{m}_j}{\partial p_{i+1}}\right)^n \left(p_{i+1}^{n+1} - p_{i+1}^n\right) \end{aligned} \tag{6.8}$$

$$\begin{aligned} \dot{m}_{j-1}^{n+1} = \quad & \dot{m}_{j-1}^n\left(p_{i-1}^n, p_i^n, h_{i-1}^n\right) \\ & + \left(\tfrac{\partial \dot{m}_{j-1}}{\partial p_{i-1}}\right)^n \left(p_{i-1}^{n+1} - p_{i-1}^n\right) + \left(\tfrac{\partial \dot{m}_{j-1}}{\partial p_i}\right)^n \left(p_i^{n+1} - p_i^n\right) \end{aligned} \tag{6.9}$$

Equations 6.8 and 6.9 are substituted into Equation 6.6. This gives an implicit equation in p_{i-1}, p_i and p_{i+1}.

The linear equation system generated at each timestep couples the pressures in the network nodes. This equation system is basically tridiagonal in 1-D flow regions, but off-diagonal coefficients are added by the presence of T-junctions in the network structure. The resulting equation system was solved by a lower-upper triangular matrix factorization (LU-decomposition), using the *IMSL* library from Visual Numerics Inc. In larger network models, it would be beneficial to use a sparse matrix solver, e.g. the SuperLU direct sparse matrix solver outlined by Xiaoye (1996).

To solve the equation system we need to compute the terms: $\dot{m}_j^n$, $(\partial \dot{m}_j/\partial p_i)^n$ and $(\partial \dot{m}_j/\partial p_{i+1})^n$ for all units in the network model. The mass flow rate through a unit is a function of the differential pressure. When using literature correlations for frictional pressure drop, which are commonly given explicit in Δp, an iterative method must by used to calculate $\dot{m}$ as function of Δp. Alternatively, the correlations can be reformulated. A perturbation in pressure was used to calculate the differentials $(\partial \dot{m}_j/\partial p_i)^n$ and $(\partial \dot{m}_j/\partial p_{i+1})^n$, for the unit models being to complicated to be differentiated analytically (e.g. the counterflow heat exchanger tube model described in Section 6.1.2). The following procedure defines the calculation sequence in each time step of the network model:

1. Transfer h from nodes to downstream units and transfer p from nodes to both upstream and downstream units.
2. Calculate all unit operations at fixed inlet and outlet p and inlet h.
3. Calculate new node h, based on new unit $\dot{m}$ and unit outlet h values (use old p values).
4. Calculate node $\partial \rho/\partial p$ at constant h for all nodes.
5. Solve network equation system to calculate new node pressures.
6. Check for convergence in node p and h. If no convergence, start from return to 1.

In the search for the steady state solution, the dynamic equations are run until convergence is obtained both for enthalpy and pressure in the node network.

6.1.2 Counterflow heat exchanger tube model

In order to compare the simulation model to the experimental results from the test rig, a counterflow heat transfer unit model was developed, comprising a single refrigerant tube with water flowing in opposite direction in an outside annulus. For the purpose of the current simulations, a steady-state model was developed with the governing conservation equations for mass, momentum and energy given by:

$$\frac{d}{dz}(\dot{m}) = 0 \tag{6.10}$$

$$\frac{dp}{dz} = \frac{dp}{dz}_{fric} + \frac{dp}{dz}_{grav} + \frac{dp}{dz}_{acc} \tag{6.11}$$

$$\frac{d}{dz}\left[\dot{m}\left(h + \frac{u^2}{2}\right)\right] = \frac{\dot{Q}}{dz} \tag{6.12}$$

The counterflow heat exchanger tube model was discretized as shown in Figure 6.3. Here, a refrigerant control volume together with its neighbouring water control volume is denoted a *cell*. Each cell is itself a counterflow heat exchanger with the outlet of one cell forming the inlet of the neighbouring cell. The equations for each cell were combined to solve for the variables of interest. The state variables that were used to describe the physical parameters in each cell were: (i) the pressure and the enthalpy for the refrigerant side and (ii) the enthalpy for the water side. Enthalpy was used instead of temperature on the refrigerant side because two-phase conditions were modelled. The pressure effect on the heat capacity of water was neglected.

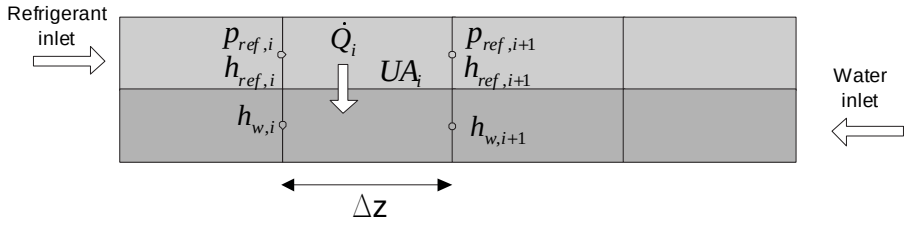

Figure 6.3: Discretization of the refrigerant tube.

The momentum equation yields:

$$p_{ref,i+1} = p_{ref,i} - \frac{dp}{dz}_{fric,i}\Delta z + \frac{dp}{dz}_{grav,i}\Delta z + \frac{dp}{dz}_{acc,i}\Delta z \tag{6.13}$$

The calculation of the friction, gravitation and acceleration part of the pressure drop momentum balance is outlined in Section 6.1.3. Neglecting the kinetic energy $\left(\frac{u^2}{2}\right)$ in the energy conservation equation, finite volume discretization gives:

$$h_{ref,i+1} = h_{ref,i} + \frac{\dot{Q}_i}{\dot{m}_{ref}} \tag{6.14}$$

$$h_{w,i+1} = h_{w,i} + \frac{\dot{Q}_i}{\dot{m}_w} \tag{6.15}$$

where the heat transfer rate $\dot{Q}_i$ was assumed to be driven by the arithmetic mean temperatures difference:

$$\dot{Q}_i = UA\left(\frac{T_{w,i+1}+T_{w,i}}{2} - \frac{T_{ref,i+1}+T_{ref,i}}{2}\right) \tag{6.16}$$

The overall heat transfer coefficient based on refrigerant-side area, U, was determined from:

$$\frac{1}{U} = \frac{A_i}{h_w A_o} + \frac{D_i}{\lambda_t} ln\left(\frac{D_o}{D_i}\right) + \frac{1}{h_{ref}} \tag{6.17}$$

Notations used in Equation 6.17 are shown in Figure 6.4. Heat transfer coefficients for water (h_w) and refrigerant (h_{ref}) were calculated from empirical correlations described in Section 6.1.3.

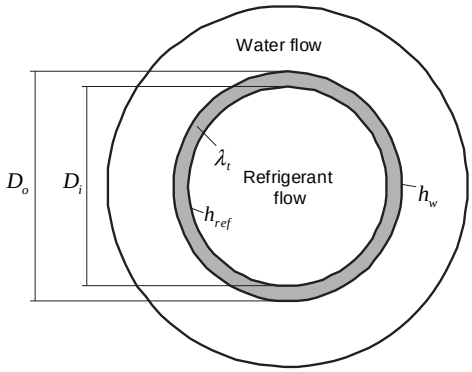

Figure 6.4: Geometry of heat exchanger tubes, with countercurrent water flowing in outside jacket.

The above formulations yield three equations for each cell, one pressure equation and two enthalpy equations. For N cells, there were $3N$ equations and $N+1$ nodes with three variables at each node. Three boundary values were therefore required for solving the equations. In the model the refrigerant inlet pressure, refrigerant inlet enthalpy and water inlet enthalpy were used as boundary conditions.

The enthalpy equations for each cell were combined to form a set of linear equation that was solved simultaneously to get the updated values for the enthalpy. A band matrix solver was used to solve the equation system, which had a total bandwidth of 5.

For each iteration of the enthalpy equation system, the following strategy for solving for the variables was used:

1. March from inlet of the refrigerant stream and update the pressure at all nodes using equation 6.13.
2. Solve the linear equation system of enthalpies using the new pressures.
3. Check convergence in the pressure and enthalpy values. If convergence is not achieved go to step 1.

6.1.3 Pressure loss and heat transfer correlations

6.1.3.1 Heat transfer correlations

The water side and the refrigerant side single-phase heat transfer coefficients were calculated using the correlation developed by Gnielinski (1976). The Gnielinski (1976) correlation was developed based on the heat transfer - pressure drop analogy.

For calculation of the two-phase evaporation heat transfer coefficients, the correlation of Gungor and Winterton (1986), which was based on a large data bank of different fluids and operating ranges, was chosen. Corberan and Melon (1998) compared literature correlations for two-phase heat transfer under evaporation of HFC-134a and concluded that the correlation of Gungor and Winterton (1986) fitted their data best.

6.1.3.2 Refrigerant tube pressure drop correlations

The Selander (1978) explicit Colebrook-White equation was used for calculation of the frictional pressure gradient in the straight tube sections. For the two-phase frictional pressure gradient, the CESNEF-2 correlation of Lombardi and Carsana (1992), recommended by Tengblad (1996), was chosen. Pettersen (2002) found good agreement with the CESNEF-2 correlation for CO_2 measurements in microchannel tubes.

For the inclined tube sections and for the upward/downward inclined bends, the gravitational pressure gradient was calculated using the Rouhani and Axelsson (1970) void correlation. For the calculation of the two-phase frictional pressure gradient in bends, Collier and Thome (1994) recommended the correlation of Chisholm and Sutherland (1969).

The acceleration pressure drop in the evaporation section of the heat exchanger was calculated by the separated flow model given by Hambræus (1993).

6.1.3.3 Inlet manifold pressure loss models

To model the pressure distribution in the inlet manifold, the manifold was divided in a series of dividing nodes, representing a series of T-junctions. The discrete pressure losses associated with the T-junctions were added to the downstream manifold tubes as shown in Figure 6.5. The T-junction pressure loss terms were modelled according the Saba and Lahey (1984) model, outlined in Appendix A. Frictional pressure loss in the manifold was calculated in the manifold tube units between the T-junction nodes (e.g. unit U2 in Figure 6.5).

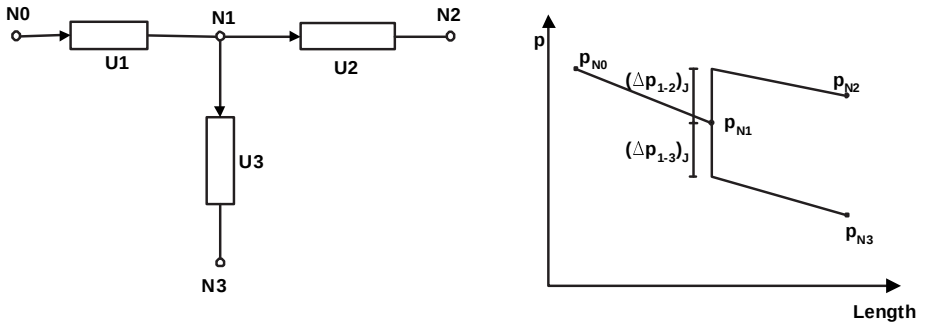

Figure 6.5: Inlet manifold T-junction pressure loss terms.

The pressure gain due to retardation of the flow in the manifold, $(\Delta p_{1-2})_J$ was added to the downstream unit (U2) and modelled using a momentum correction factor, or a pressure recovery coefficient, as shown in Equation A.16. Likewise, the pressure loss due to turning of the flow into the branch, $(\Delta p_{1-3})_J$, was modelled using a reversible and an irreversible component as shown in Equation A.8. The reversible term was due to the Bernoulli effect, while the irreversible term consisted of a pressure loss coefficient, K_{1-3}, and a two-phase multiplier.

6.1.3.4 Outlet manifold pressure loss models

The outlet manifold of the heat exchanger was modelled in a similar way as the inlet manifold. Frictional pressure losses were modelled in the manifold tube units (e.g. unit U2 in Figure 6.6), while the pressure losses associated with the com-

bining T-junctions were added to the upstream units (Unit U1 and U3 in Figure 6.6).

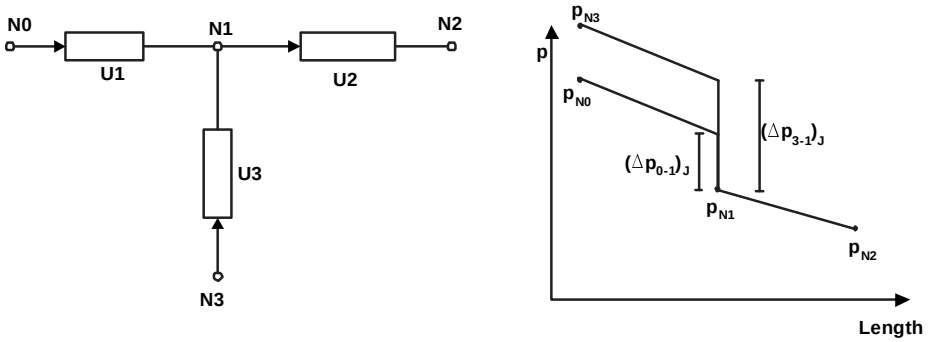

Figure 6.6: Outlet manifold T-junction pressure loss terms.

The reversible and irreversible T-junction pressure changes were modelled using the homogeneous forms of the correlations reported by Schmidt and Loth (1994).

6.1.4 Inlet manifold two-phase distribution models

Three different options were implemented such that the consequences of maldistribution in the inlet manifold could be analysed. These options are outlined in the current Section.

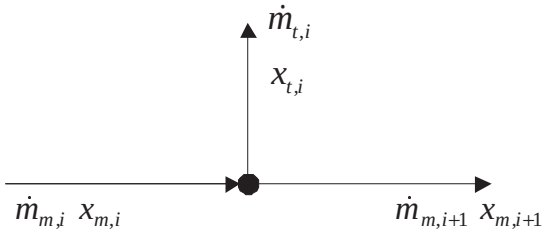

Figure 6.7: Inlet manifold junction node.

6.1.4.1 Uniform two-phase distribution

With uniform distribution, all branch tubes in a heat exchanger pass receive equal vapour fraction:

$$x_{t,i} = x_{m,i} \tag{6.18}$$

However, due to pressure changes along both the inlet and the outlet manifold, the mass flow rate can vary among the tubes. At equal branch tube mass flow rates, this option corresponds to the traditional way of modelling heat exchangers.

6.1.4.2 Separated two-phase distribution

To analyse the 'worst-case' maldistribution scenario, a separated two-phase distribution model was implemented. In this case only gas flows into the first tubes and liquid only into the last branch tubes of the manifold. By traversing the manifold from the first to the last junction node, the branch tube vapour fractions were calculated:

$$\begin{aligned} \dot{m}_{t,i} \leq \dot{m}_{m,i} x_{m,i} \Rightarrow & \begin{cases} x_{t,i} = 1.0 \\ x_{m,i+1} = \frac{m_{m,i} x_{m,i} - m_{t,i}}{m_{m,i+1}} \end{cases} \\ \dot{m}_{t,i} > \dot{m}_{m,i} x_{m,i} \Rightarrow & \begin{cases} x_{t,i} = 1 - \left(\frac{m_{m,i}(1-x_{m,i}) - m_{m,i+1}}{m_{t,i}} \right) \\ x_{m,i+1} = 0.0 \end{cases} \end{aligned} \tag{6.19}$$

6.1.4.3 Two-phase distribution correlation

The correlations developed in Chapter 5 was implemented to model the phase split in the inlet manifold junction nodes based on the experimental results. The branch tube vapour fraction was then given as a function of the node inlet vapour fraction, node inlet mass flow rate, and the branch tube mass flow rate:

$$x_{t,i} = x_{t,i}\left(x_{m,i}, \dot{m}_{m,i}, \dot{m}_{t,i}\right) \tag{6.20}$$

6.2 Single heat exchanger tube analysis

The counterflow heat exchanger tube model described in Section 6.1.2, was used to visualize the dependency between refrigerant mass flow rate, inlet vapour fraction and pressure drop in a single heat exchanger tube. The measured variables shown in Figure 6.8 were used as input values to the simulations. The outlet parameters $T_{t,out}$, $p_{t,out}$, $x_{t,out}$, $T_{w,out}$ and the heat transfer rate, $\dot{Q}$, were calculated.

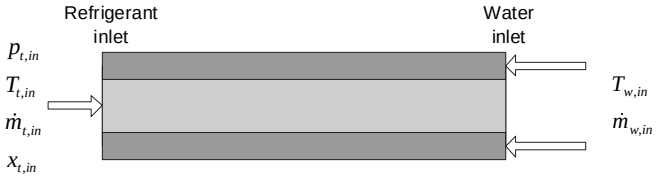

Figure 6.8: Input variables to the single heat exchanger tube analysis.

The following geometrical data for the single heat exchanger tube analysis were used:

- Length: 0.9 m
- Refrigerant tube inner diameter: 0.004 m
- Refrigerant tube outer diameter: 0.006 m
- Water jacket tube inner diameter: 0.008 m

6.2.1 Heat exchanger tube capacity prediction

Single tube simulations of all measurement data series reported in Chapter 4 were run in order to compare the heat transfer correlation predictions to the measured data. The variables shown in Figure 6.8 were used as input, and the heat transfer rates were calculated by the single tube simulation model. Figure 6.9 shows the predicted and measured heat transfer rates for all measurements. The RMS (root mean square) error for the predicted heat transfer rates was 4.4%.

6.2.2 Pressure drop as function of inlet vapour fraction

In the two-phase distribution experiments reported in Chapter 4, the vapour fraction at the inlet of the branch tubes varied from $x_{t,in} = 0.0$ to $x_{t,in} = 1.0$. A set of

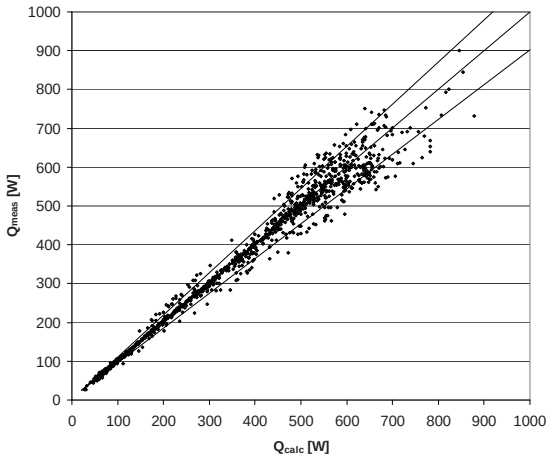

Figure 6.9: Comparison of single tube measured and predicted heat transfer rates.

simulations on the single tube model were run to analyse the tube pressure drop as function of the inlet vapour fraction. Figure 6.10 shows the two-phase pressure drop correlation of Lombardi and Carsana (1992) as function of vapour fraction for HFC-134a and CO_2 at relevant operating conditions. A curve for HFC-134a at 18.7°C is shown to illustrate the difference between the refrigerants at equal temperature.

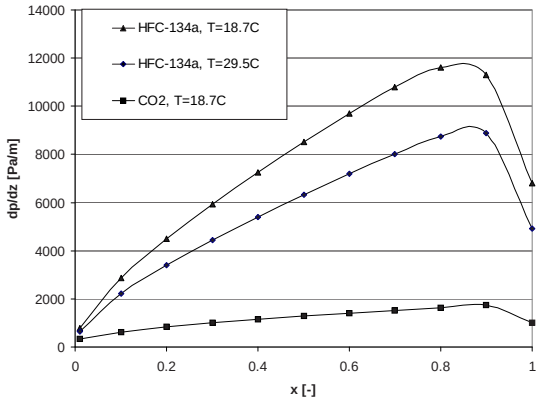

Figure 6.10: Refrigerant pressure gradient, given by the correlation of Lombardi and Carsana (1992), as function of vapour fraction. $\dot{m} = 0.0033$ kg/s, $D_i = 0.004$ m.

Especially for HFC-134a, the pressure gradient is a strong function of vapour fraction. Therefore, the refrigerant pressure drop dependents quite significantly on the vapour fraction at the inlet of the branch tube. Five simulations were run at constant water flow rate, water inlet temperature, refrigerant mass flow rate and refrigerant inlet pressure. The inlet vapour fraction was varied from $x_{t,in} = 0.0$ to $x_{t,in} = 1.0$. In figure 6.11, the calculated vapour fraction development along the refrigerant tube length is shown for the five cases.

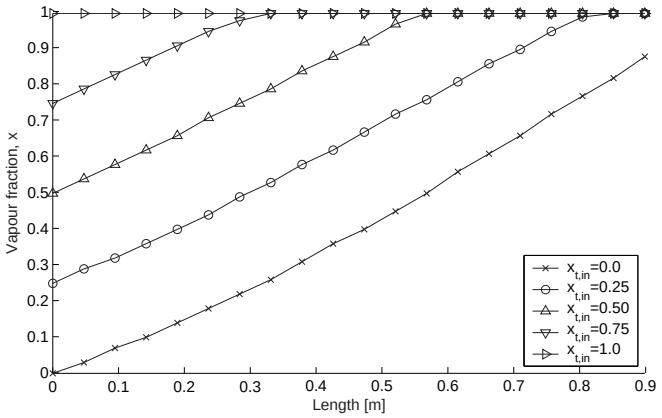

Figure 6.11: Vapour fraction along the refrigerant tube length, as a function of the inlet vapour fraction, $x_{t,in}$. Refrigerant HFC-134a, $\dot{m}_{t,in} = 0.0033$ kg/s and $T_{t,in} = 29.5°$C.

Corresponding temperature curves for refrigerant and water are shown in Figure 6.12 and refrigerant pressure along the length of the refrigerant tube is shown in Figure 6.13.

As seen in Figure 6.13, the tube pressure loss varies depending on the vapour inlet fraction, from $\Delta p = 5.5$ kPa at $x_{t,in} = 1.0$ to $\Delta p = 7.0$ kPa at $x_{t,in} = 0.5$. In Figures 6.14 and 6.15, the refrigerant tube pressure drop is plotted as a function of mass flow rate for different inlet vapour fractions for HFC-134a and CO_2, respectively. At a given refrigerant tube pressure drop, the variation in mass flow rate is greater for HFC-134a than it is for CO_2. This is due to the greater variation in two-phase pressure drop as function of vapour fraction for HFC-134a seen in Figure 6.10.

Assuming a fixed pressure drop between the inlet and the outlet manifold of a heat exchanger, several simulations were run to visualize the variation of mass flow rate caused by two-phase maldistribution in the inlet manifold. The experimental reference mass flow rate of $\dot{m}_{t,in} = 0.0033$ kg/s and vapour inlet vapour fraction of $x_{t,in} = 0.25$ corresponds to a pressure drop of approximately 6.0 kPa for HFC-

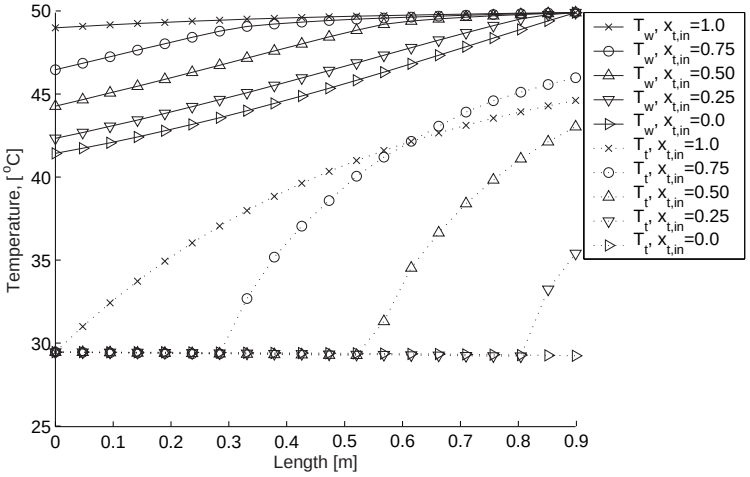

Figure 6.12: Refrigerant and water temperatures along the tube length, as a function of the inlet vapour fraction, $x_{t,in}$. Refrigerant HFC-134a, $\dot{m}_{t,in} = 0.0033$ kg/s and $T_{t,in} = 29.5°$C.

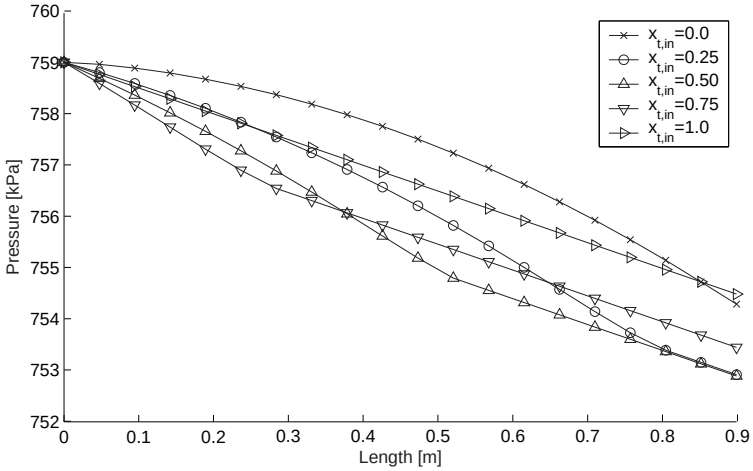

Figure 6.13: Refrigerant pressure along tube length, as a function of the inlet vapour fraction, $x_{t,in}$. Refrigerant HFC-134a, $\dot{m}_{t,in} = 0.0033$ kg/s and $T_{t,in} = 29.5°$C.

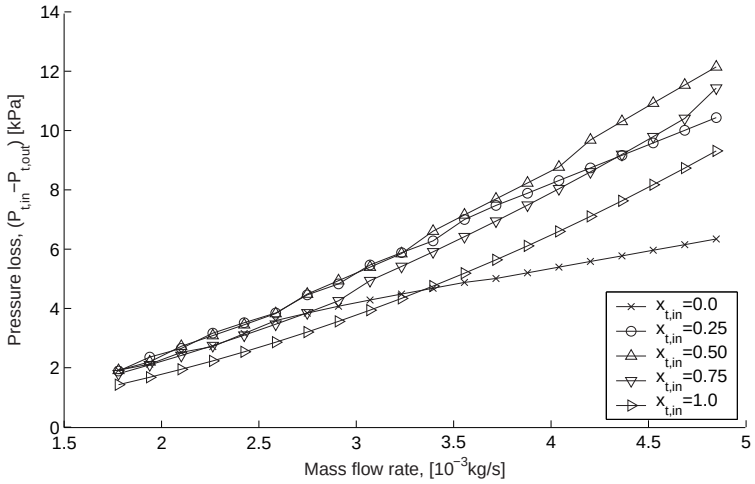

Figure 6.14: Single pipe pressure loss as function of mass flow rate at different values of $x_{t,in}$. Refrigerant: HFC-134a, $T_{t,in}$ =29.5°C.

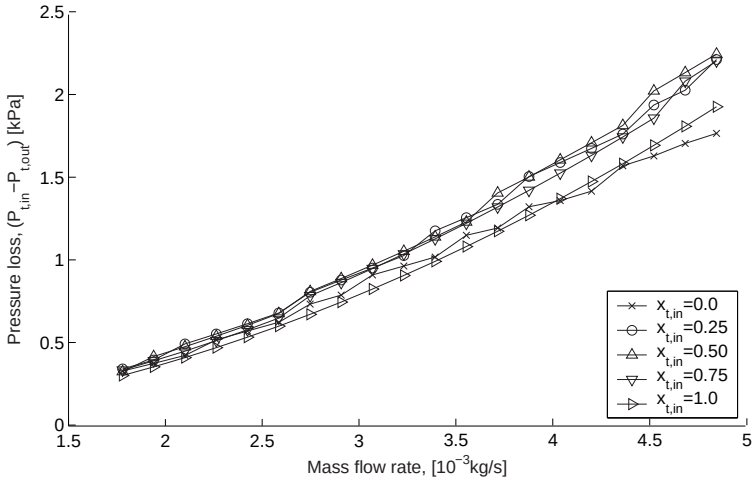

Figure 6.15: Single pipe pressure loss as function of mass flow rate at different values of $x_{t,in}$. Refrigerant: CO_2, $T_{t,in}$ =18.7°C.

134a and 1.0 kPa for CO_2, as seen in Figures 6.14 and 6.15. In Figures 6.16 and 6.17 the mass flow rate at fixed pressure drop is plotted as a function of inlet vapour fraction, $x_{t,in}$, for CO_2 and HFC-134a, respectively. Curves are shown for the three different water inlet temperatures used in the experiments.

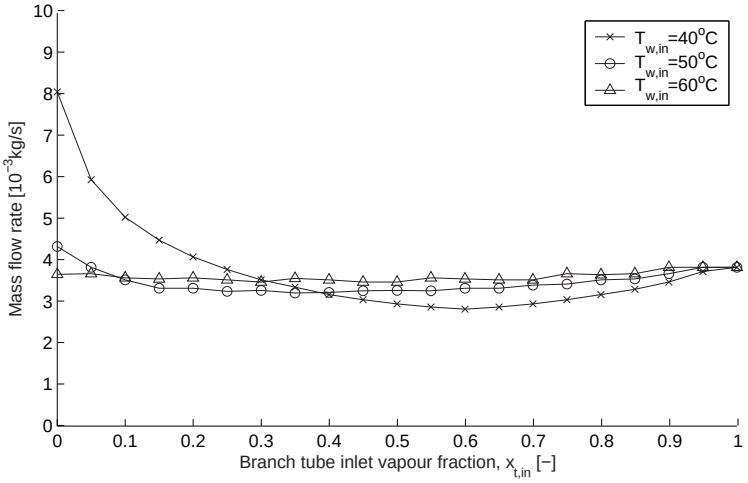

Figure 6.16: Single pipe mass flow rate at a tube pressure loss of $\Delta p = 6.0$ kPa, at different values of $x_{t,in}$. Curves are shown for three different water inlet temperatures. Refrigerant: HFC-134a, $T_{t,in} = 29.5°$C.

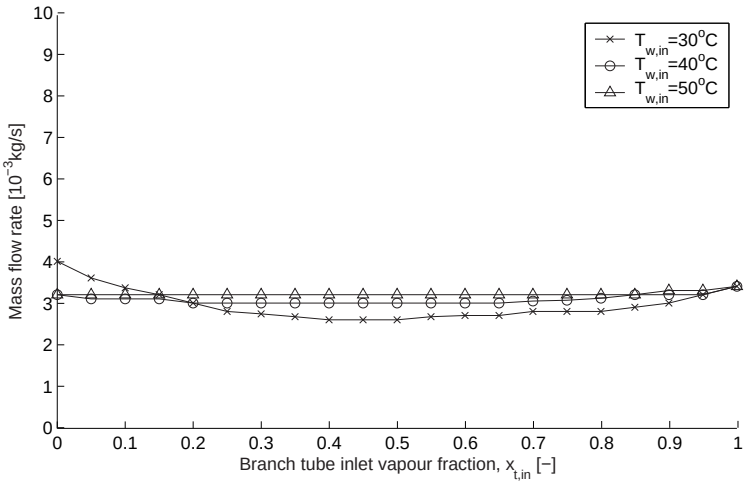

Figure 6.17: Single pipe mass flow rate at a tube pressure loss of $\Delta p = 1.0$ kPa different values of $x_{t,in}$. Curves are shown for three different water inlet temperatures. Refrigerant: CO_2, $T_{mIn} = 18.7°$C.

As shown in Figures 6.16 and 6.17, the mass flow rate in the refrigerant branch tubes varies significantly with the inlet vapour fraction at low water temperatures. At increasing water temperature, more of the refrigerant liquid is evaporated, and the difference in mass flow rate is evened out between tubes receiving different vapour fraction at the inlet. As shown in the next section, the differences in mass flow rate between the refrigerant tubes will affect the total capacity of the heat exchanger.

6.3 Heat exchanger simulation results and analyses

6.3.1 Network heat exchanger model results

The network heat exchanger model outlined in Section 6.1 was utilized to estimate the consequences of maldistribution on heat exchanger capacity. The geometry of the experimental test rig was implemented as a network model, in order to verify the computational model with the experimental results. In Figure 6.18 the distributed network model with the inlet and outlet manifolds and the ten parallel counterflow heat exchanger tubes is shown.

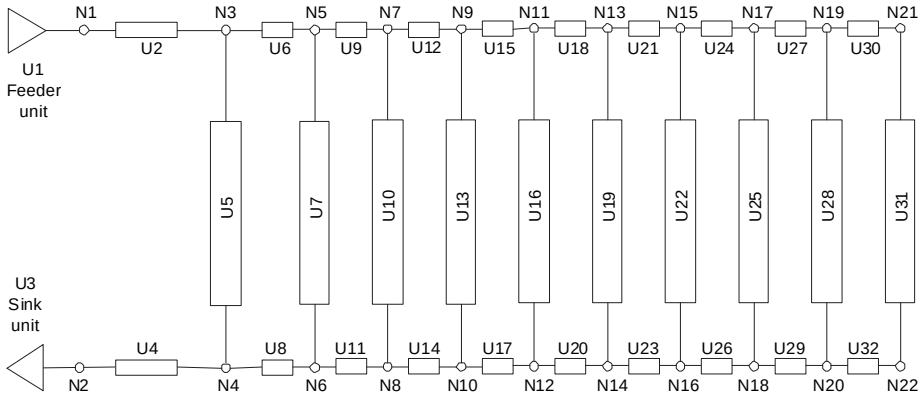

Figure 6.18: Test rig heat exchanger represented as a network model with nodes and units.

The inlet manifold was divided into ten nodes with interconnected manifold units. The three different models for two-phase split, outlined in Section 6.1.4, were used for the nodes in the inlet manifold, such that the consequences of maldistribution could be analysed:

- Distribution model 1: Uniform phase distribution, calculated by Equation 6.18.
- Distribution model 2: Total separation in the inlet manifold, with gas feeding of the first tubes and liquid feeding of the last tubes of the inlet manifold, calculated by Equation 6.19.
- Distribution model 3: Two-phase flow distribution based on the correlations developed in Chapter 5, calculated by Equation 6.20.

In Figures 6.19, 6.20, 6.21 and 6.22, model results are shown together with experimental measurements for the round tube ID 16 mm manifold (M1) with the following boundary conditions applied in the model calculations:

- Manifold inlet mass flow rate: $\dot{m}_{mIn} = 0.033$ kg/s.
- Manifold inlet vapour fraction: $x_{mIn} = 0.28$.
- Manifold inlet temperature: $T_{mIn} = 29.5°$C.
- Water inlet temperature to the test section: $T_{w,tsIn} = 50°$C.
- Branch tube water mass flow rates were set equal to the measured values, with distribution calibration coefficients calculated in Appendix C.2.

The abscissa of these plots represent the physical layout of the heat exchanger, with branch *No* 1 being the first branch that the inlet flow encounters as it moves from left to right in the inlet manifold.

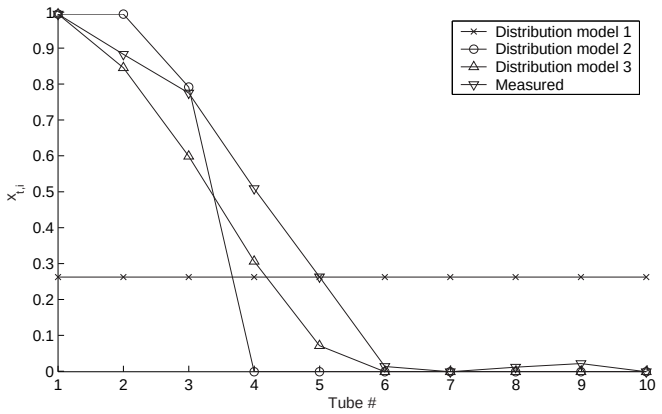

Figure 6.19: Vapour fraction at the inlet of the heat exchanger branch tubes. Model simulations and experimental measurements. Refrigerant: HFC-134a, ID 16 mm round tube inlet manifold (M1).

Figure 6.19 shows the calculated and measured inlet manifold two-phase distribution. The uniform distribution model provided equal vapour fraction at the inlet of the ten branch tubes. This is in accordance with the traditional way of modelling heat exchangers, lumping all branch tubes in a pass into one calculation unit. The total separation model, distribution model 2, was feeding single-phase gas in branch tubes *No* 1 and 2, and single-phase liquid in tubes *No* 4 to 10. The intermediate tube *No* 3 received two-phase flow with a vapour fraction of $x_t = 0.79$. The correlation-based distribution model 3 was seen to give a satisfactory prediction of the experimentally measured vapour fraction distribution.

In Figure 6.20 the modelled pressure distribution in the inlet and outlet manifold is shown. There was a slight pressure recovery along the inlet manifold due to the retardation of the two-phase flow. The frictional pressure loss almost cancelled out the retardation pressure gain, providing a total pressure recovery from the inlet to the end of the manifold of only 49 Pa. The pressure drop along the outlet manifold was increasing due to the acceleration of the flow combined with the junction pressure losses and increasing frictional pressure drop. As a result, there was a slight, yet noticeable, decrease in available pressure drop over the branch tubes from tube *No* 1 to tube *No* 10.

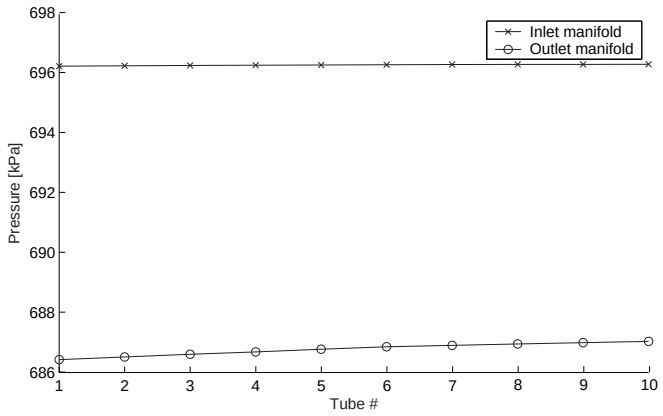

Figure 6.20: Modelled pressure distribution along the inlet and outlet manifolds using distribution model 3. Refrigerant: HFC-134a, ID 16 mm round tube inlet manifold (M1).

Pressure gradients along the manifolds yield difference in pressure drop over the parallel heat exchanger tubes. Manifold pressure induced maldistribution have been analysed in single-phase flow heat exchangers by e.g. Yin et al. (2002). Because the frictional pressure gradient partially cancels out the pressure gradient due to retardation in the inlet manifold, the pressure change in the outlet manifold is more important for the design of the heat exchanger to avoid manifold pressure gradient induced maldistribution. This yields the opportunity to use small diameter inlet manifolds, to keep the two-phase flow in the ”high mass flux” in order to avoid gravitationally induced phase stratification, which was shown to have detrimental effects on the two-phase distribution in Chapter 5.

The modelled mass flow rate distribution among the ten branch tubes is shown in Figure 6.21, together with experimental measurements. The maldistribution was caused partly by the difference in pressure drop between the inlet and outlet manifold (Figure 6.20), but it was also caused by the phase maldistribution and the difference in mass flow rate depending on the branch inlet vapour fraction, as shown in Figure 6.16. At uniform phase distribution in the manifold, distribution model 1, the mass flow rate was almost constant among the tubes (decreasing with 0.5% from tube *No* 1 to tube *No* 10). This indicated that the pressure difference between the inlet and the outlet manifold was less important than the difference in branch tube inlet vapour fraction for the mass flow rate maldistribution. It also supports the assumption made in the experimental concept developed in Chapter 3, that the pressure distribution in the outlet manifold did not have significant contribution to the mass flow rate and vapour fraction distribution among the branch

tubes. The trend with lower mass flow rate in branch tubes receiving two-phase flow is seen both in the measurements, having two-phase flow inlet at branch tubes *No* 2 to 5, and in the modelling results using the distribution models 2 and 3.

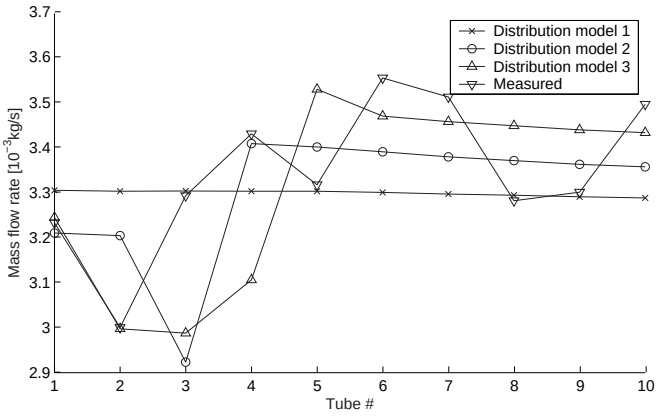

Figure 6.21: Branch tube mass flow rate distribution. Modelled results using the three different distribution models are shown together with experimental measurements. Refrigerant: HFC-134a, ID 16 mm round tube inlet manifold (M1).

Figure 6.22 shows the branch tube heat load measurements, together with the model results. Due to the equal vapour fraction distribution and the almost equal mass flow rate distribution, the heat load was almost constant using the uniform distribution model 1. At separated distribution, the heat load was a strong function of the branch tube inlet vapour fraction. More latent heat available in the tubes overfed with liquid provided higher branch tube heat load, while the liquid-starved tubes had less capacity. A comparison between the total heat exchanger capacity using the three distribution models is given in the next Section.

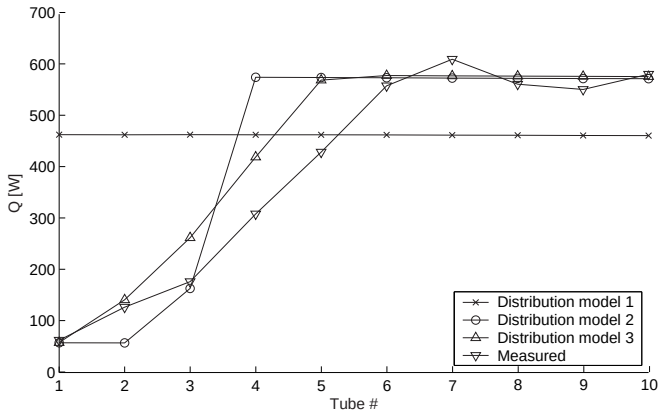

Figure 6.22: Branch tube heat load. Modelled results using the three different distribution models are shown together with experimental measurements. Refrigerant: HFC-134a, ID 16 mm round tube inlet manifold (M1).

6.3.2 Consequences of manifold maldistribution

In order to analyse the consequences of two-phase maldistribution in the inlet manifold, the total heat exchanger capacity, defined as the sum of the branch tube heat loads, were compared for simulations using the three different distribution models. Figures 6.23 and 6.24 show the reduction in heat exchanger capacity for the distribution models 2 and 3 compared to simulations using the uniform distribution model 1 for HFC-134a and CO_2, respectively. Simulations were conducted at different water temperatures to visualize the importance of refrigerant outlet conditions on the results. In the HFC-134a simulations using the uniform distribution model, the branch tube outlet vapour fraction at $T_{w,in} = 35°C$ and $T_{w,in} = 40°C$ was 0.58 and 0.80, respectively. Increasing the water temperature to $T_{w,in} = 50°C$ gave a superheat of 8.0°C, which increased to 13°C at an inlet water temperature of $T_{w,in} = 60°C$. Refrigerant maldistribution causes some tubes to have excessive superheat while others remain in two-phase flow at the branch tube exits. In such situations, some branch tubes are inefficiently using heat exchanger area by transferring heat to superheated vapour instead of two-phase refrigerant, and the total heat exchanger capacity is reduced.

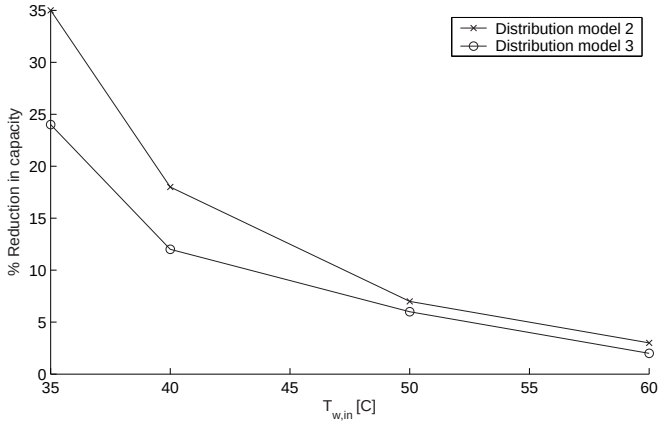

Figure 6.23: Heat exchanger simulation, reduction in capacity due to manifold maldistribution as function of water temperature. Refrigerant HFC-134a, $T_{t,in} = 29.5°$C, ID 16 mm round tube inlet manifold (M1).

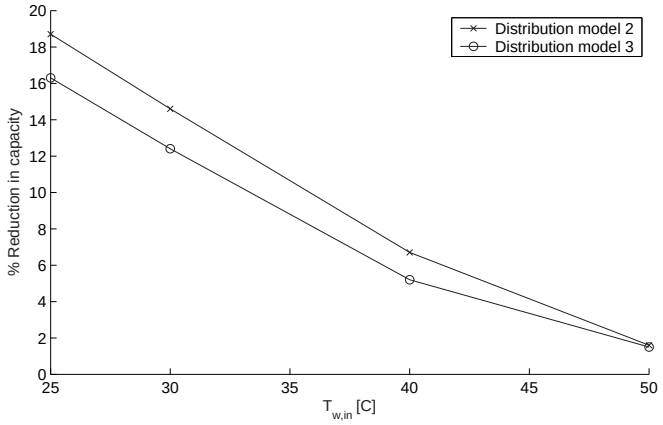

Figure 6.24: Heat exchanger simulation, reduction in capacity due to manifold maldistribution as function of water temperature. Refrigerant CO_2, $T_{t,in} = 18.7°$C.

The largest reduction in heat exchanger capacity is, as expected, seen for distribution model 2, providing full separation in the inlet manifold. At high water temperatures, the loss in heat load in the liquid-starved branch tubes is partially regained in the liquid fed tubes, because the temperature difference to the water is large enough to fully evaporate the excess liquid. When reducing the water temperature, liquid is approaching the outlet manifold, and the difference in heat exchanger capacity compared to uniform distribution increases. In evaporators

with several passes and intermediate manifolds, most often only the last pass will have superheated gas at the outlet at design conditions. Then, the first passes will be susceptible to potential large reductions in capacity due to two-phase maldistribution.

The simulation results with CO_2 in Figure 6.24 show a smaller reduction in heat exchanger capacity caused by two-phase maldistribution than what was seen for HFC-134a in Figure 6.23. While HFC-134a gave a reduction in heat transfer capacity, using distribution model 2, of 35% at $T_{w,in} = 35°C$ ($T_{w,in} - T_{t,in} = 5.5°C$), CO_2 gave a reduction of only 18.7% at $T_{w,in} = 25°C$ ($T_{w,in} - T_{t,in} = 6.3°C$). This difference between HFC-134a and CO_2 is due to the smaller difference in pressure gradient through the two-phase region for CO_2, as shown in Figure 6.10, providing less difference in mass flow rate between branch tubes fed with different vapour fractions as shown in Figure 6.17.

Within the operating range used in the current experimental work , the correlation distribution model showed a potential increase in heat exchanger capacity of 12%, both for HFC-134a ($T_{w,in} = 40°C$) and CO_2 ($T_{w,in} = 30°C$), if uniform two-phase distribution could be obtained in the ID 16 mm round tube manifold (M1).

References

Anderson, J. L., Benedetti, R. L., 1986. Critical flow through small pipe breaks. Tech. rep., EPRI NP-4532.

Angus, S., Armstrong, B., DeReuck, K. M., 1976. Carbon Dioxide - International thermodynamic Tables of The Fluid State. Pergamon Press.

ASHRAE, 1986. Guide for engineering analysis of experimental data ANSI/ASHRAE Guideline 2-1986. American Society of Heating, Refrigerating and Air-Conditioning Engineers, Inc.

Asoh, M., Hirao, Y., Watanabe, Y., Fukano, T., 1991. Phase separation of refrigerant two-phase mixture flowing downward into three thin branches from a horizontal manifold pipe. In: ASME/JSME Thermal Eng. Proc. ASME, pp. 159–164.

Azzopardi, B. J., 1999. The effect of branch tube diameter on phase split at T-junctions. In: SPE Annual Technical Conference and Exhibition, Houston, October.

Azzopardi, B. J., 2000. Phase separation at T junctions. Multiphase Science and Technology 11, 223–329.

Azzopardi, B. J., Hervieu, E., 1994. Phase separation at T junctions. Multiphase Science and Technology 8, 645–714.

Azzopardi, B. J., Memory, S. B., 1989. The split of two-phase flow at a horizontal T - annular and stratified flow. In: 4th Int. Conf. on Multiphase Flow, Nice, France, 19-21 June.

Azzopardi, B. J., Smith, P. A., 1992. Flow split at a T-junction: effect of branch tube orientation and downstream geometry. Int. J. Multiphase Flow 18, 861–875.

Azzopardi, B. J., Whalley, P. B., 1982. The effect of flow pattern on two phase flow in a T junction. Int. J. Multiphase Flow 8, 481–507.

Bajura, R. A., 1971. A model for flow distribution in manifolds. In: J. of Engineering for Power. pp. 7–12.

Bajura, R. A., Jones Jr, E. H., 1976. Flow distribution manifolds. In: Trans. of the ASME. Gas Turbine and Fluids Engineering Conference. Paper No. 76-FE-7.

Baker, J. R., 1991. Motionless mixers stir up new uses. Chemical Eng. Progress , 32–38.

Baker, O., 1954. Design of pipe lines for simultaneous flow of oil and gas. Oil and Gas J. 26.

Ballyk, J. D., Shoukri, M., 1990. On the development of a model for predicting phase separation phenomena in dividing two-phase flow. Nuclear Engineering and Design 123, 67–75.

Ballyk, J. D., Shoukri, M., Chan, A. M. C., 1988. Steam-water annular flow in a horizontal dividing T-junction. Int. J. Multiphase Flow 14, 265–285.

Ballyk, J. D., Shoukri, M., Peng, F., 1991. The effect of branch size and orientation on two-phase flow in T-junction with horizontal inlet. In: Int. Conf. Multiphase Flows, September 24-27, Tsukuba, Japan, 13-16.

Beaver, A. C., Hrnjak, P. S., Yin, J. M., Bullard, C. W., 2000. Effects of distribution in headers of microchannel evaporators on transcritical CO_2 heat pump performance. In: Proceedings of the ASME Advanced Energy Systems Division. Vol. 40.

Bernoux, P., Septembre 2000. Etude de la distribution d'un melange liquide-vapeur a l'entree des echangeurs de chaleur. Ph.D. thesis, Universite Henri Poincare - Nancy I.

Buell, J. R., Soliman, H. M., Sims, G. E., 1994. Two-phase pressure drop and phase distribution at a horizontal tee junction. Int. J. Multiphase Flow 20, 819–836.

Butterworth, D., 1980. Unresolved problems in heat exchanger design. In: Interflow 80 - The fluid handling conference, Harrogate, U.K.

Castiglia, F., Giardina, M., 2002a. Mass discharge through branches in horizontal two-phase flow. In: Twelfth Int. Heat Transfer Conf., Grenoble, France, August 18-23, 2002.

Castiglia, F., Giardina, M., 2002b. Modelling two-phase flow discharge through lateral branches in large horizontal pipes with stratified flow. In: Eight Int. Conf. Multiphase flow in Industrial Plants, Alba (Cueno), Italy September 18-20, 2002.

Chisholm, D., 1967. Pressure losses in bends and tees during steam-water flow. Tech. Rep. 318, NEL.

Chisholm, D., 1972. An equation for velocity ratio in two-phase flow. Tech. Rep. 535, NEL.

Chisholm, D., Sutherland, L. A., 1969. Prediction of pressure gradients in pipeline systems during two-phase flow. In: Symposium on Fluid Mechanics and Measurements in Two-phase Flow Systems, Leeds.

Cho, H., Cho, K., Youn, B., Kim, Y. S., 2002. Flow mal-distribution in microchannel evaporator. In: Ninth Int. Refrigeration and Air Conditioning Conf., Purdue.

Choi, J. M., Payne, V., Domanski, P. A., 2003. Effects of non-uniform refrigerant and air flow distribution on finned-tube evaporator performance. In: Int. Congress of Refrigeration, Washington, D.C.

Chou, H. T., Cheng, R. Y., 2001. Outflow distribution along multiple-port diffusers. In: Proc. of the Natl. Sci. Council. ROC(A). Vol. 25. pp. 94–101.

Coleman, J. W., Krause, P. E., 2002. Two phase pressure losses of R134a in microchannel tube headers with large free flow area ratios. In: Compact Heat Exchanger Symposium, A Festschrift on the 60th Birthday of R.K. Shah, August 24, Grenoble, France.

Collier, J. G., 1976. Single-phase and two-phase behaviour in primary circuit components. In: Proc. N.A.T.O. Advanced Study Institute on Two-phase Flow and Heat Transfer. Hemisphere, Washington D.C., pp. 322–333.

Collier, J. G., Thome, J. R., 1994. Convective boiling and condensation, 3rd Edition. Oxford University Press, Oxford Engineering Science Series.

Corberan, J. M., Melon, M. G., 1998. Modelling of plate finned tube evaporators and condensers working with R134A. Int. J. Refrigeration 21, 273–284.

Duffey, R. B., Hughes, E. D., Rohatgi, U. S., 1993. Two-phase flow stability and dryout in parallel channels in natural circulation. In: AIChE Symposium Series, Heat Transfer - Atlanta. Vol. 89.

Endrestøl, G. O., Sira, T., Østenstad, M., Meeg, M., Thrane, J., 1989. Simultaneous computation within a sequential process simulation tool. Modeling, Identification and Control 10, 203–211.

Fei, P., Chandrak, D., Hrnjak, P., 2002. Refrigerant distribution in the inlet header of plate evaporators. In: SAE World Congress, Paper 2002-01-0948.

Fenghour, A., Wakeman, W. A., Vesovic, V., 1998. The viscosity of carbon dioxide. J. Phys. Chem. Ref. Data 27 (1), 31–44.

Fouda, A. E., Rhodes, E., 1974. Two-phase annular flow stream division in a simple tee. Trans. Inst. Chem. Engrs. 52, 354–360.

Franchello, G., Stadtke, H., Worth, B., 1993. A system code for thermal - hydraulic networks. Tech. rep., EUR 15141EN, Ispra Site Institute for Safety Technology, Joint Research Centre.

Giot, M., 1981. Singular pressure drops. In: Thermohydraulics of two-phase flow systems for industrial design and nuclear engineering. pp. 247–254.

Gnielinski, V., 1976. New equations for heat and mass transfer in turbulent pipe and channel flow. Int. Chem. Eng. 16, 359–368.

Gungor, K. E., Winterton, R. H. S., 1986. A general correlation for flow boiling in tubes and annuli. Int. J. Heat and Mass Transfer 29, 351–358.

Hafner, A., 2003. Compact interior heat exchangers for CO_2 mobile heat pumping systems. Dr. ing. thesis, NTNU.

Hambræus, K., 1993. Flow boiling of pure and oil contaminated refrigerants - heat transfer and pressure drop in a horizontal tube. Ph.D. thesis, Department of Energy Technology, The Royal Institute of Technology, Sweden.

Hart, J., Hamersma, P. J., Fortuin, J. M. H., 1991a. A model for predicting liquid route preference during gas-liquid flow through horizontal branched pipelines. Chem. Eng. Sci. 46, 1609–1622.

Hart, J., Hamersma, P. J., Fortuin, J. M. H., 1991b. Phase distribution during gas-liquid flow through horizontal dividing junctions. Nuclear Engineering and Design 126, 293–312.

Heggs, P. J., Scheidat, H. J., 1992. Thermal performance of plate heat exchangers with flow maldistribution. In: Compact heat exchangers for power and process industries. Vol. HDT-Vol. 201. ASME, pp. 87–93.

Hench, J. E., Johnston, J. P., 1968. Two-dimensional diffuser performance with subsonic two-phase air/water flow. Tech. rep., APED-5477.

Henry, J. A. R., 1981. Two-phase flow splitting in a pipe tee. Int. J. Multiphase Flow 7, 343–355.

Holm, M., Nilsson, I., Wilhelmsson, B., 2001. Reduction of maldistribution in large rising film plate evaporators. In: Third Int. Conf. on Compact Heat Exchangers and Enhancement Technology for the Process Industries, Davos, Switzerland.

Hong, K. C., 1978. Two-phase flow splitting in a pipe tee. J. of Petroleum Technology , 290–296.

Horiki, S., Osakabe, M., 1999. Water flow distribution in horizontal protruding-type header contaminated with bubbles. In: Proceedings of the ASME Heat Transfer Division, HDT-Vol. 364-2.

Hrnjak, P., 2003. Two phase flow distribution in headers of parallel flow heat exchangers and its effect on performance. In: 2nd Int. Conf. on Heat Transfer, Fluid Mechanics and Thermodynamics, 23-26 June 2003, Victoria Falls, Zambia.

Huq, R., 1990. An analytical two-phase flow void prediction method. In: AIAA/ASME 5th Joint Thermophysics and Heat Transfer Conf.

Hwang, S. T., Lahey, R. T., 1988. A study on single- and two-phase pressure drop in branching conduits. Experimental Thermal and Fluid Science 1, 111–125.

Jacobi, A. M., 2001. High performance heat exchangers for air conditioning and refrigeration applications (non-circular tubes). Tech. rep., ARTI 21-CR Project 20020-Phase 2.

Kandlikar, S. G., 2001. Two-phase flow patterns, pressure drop and heat transfer during boiling in minichannel and microchannel flow passages of compact evaporators. In: Third Int. Conf. on Compact Heat Exchangers and Enhancement Technology for the Process Industries, Davos, Switzerland.

Katsaounis, A., 1987. Flow pattern and pressure drop in tees. Chem. Eng. Communications 54, 119–138.

Kattan, N., Thome, J. R., Favrat, D., 1998. Flow boiling in horizontal tubes : Part 1 - development of a diabatic two-phase flow map. Trans. ASME, J. Heat Transfer 120, 140–147.

Lahey, R. T., 1986. Current understanding of phase separation mechanisms in branching conduits. Nuclear Engineering and Design 95, 145–161.

Lahey, R. T., Azzopardi, B. J., Cox, M., 1985. Modelling two-phase flow division at T-junctions. In: 2nd. Int. Conf. Multi-Phase Flow, London, U.K. 19-21 June, pub., BHRA.

Lahey, R. T. J., Moody, F. J., 1977. The thermal-hydraulics of a boiling water nuclear reactor. Tech. rep., ANS Monograph.

Lalot, S., Florent, P., Lang, S. K., Bergles, A. E., 1999. Flow maldistribution in heat exchangers. Applied Thermal Eng. 19 (8), 847–863.

Lee, J. K., Lee, S. Y., 2002. Distribution of two-phase annular flow at header-channel junctions. In: Compact Heat Exchanger Symposium, A Festschrift on the 60th Birthday of R.K. Shah, August 24, Grenoble, France.

Li, G., Braun, J. E., Groll, E. A., Frankel, S., Wang, Z., 2002. Evaluating the performance of refrigerant flow distributors. In: Ninth Int. Refrigeration and Air Conditioning Conf., Purdue.

Lombardi, C., Carsana, C. G., 1992. A dimensionless pressure drop correlation for two-phase mixtures flowing upflow in vertical ducts covering wide parameter range. Int. J. Heat and Technology 10, 125–141.

Maciaszek, T., Memponteil, A., 1986. Experimental study on phase separation in tee junction for steam-water stratified inlet flow. In: European two-phase flow working group meeting, Munich, FRG, June, 10-13, paper C2.

Maciaszek, T., Micaelli, J. C., 1990. CATHARE phase separation modeling for small breaks in horizontal pipes with stratified flow. Nuclear Engineering and Design 124, 247–256.

Malik, M. N., Afzal, M., Tariq, G. F., 1998. Mathematical modeling and computer simulation of transient flow in centrifuge cascade pipe network with optimizing techniques. Computers Math. Applic. 36, 63–76.

Marti, S., Shoham, O., 1997. A unified model for stratified-wavy two-phase flow splitting at a reduced T-junction with an inclined arm. Int. J. Multiphase Flow 23, 725–748.

McCreery, G. E., 1984. A correlation for phase separation in a tee. In: Multi-phase Flow and Heat Transfer III Part B: Applications. Elsevier Science Pub. B.V., Amsterdam, pp. 165–178.

Moffat, R. J., 1988. Describing the uncertainties in experimental results. Experimental Thermal and Fluid Science 1, 3–17.

Moran, M. J., Shapiro, H. N., 1993. Fundamentals of engineering thermodynamics. John Wiley & Sons, Inc.

Moura, L. F. M., 1990. Experimental and numerical study on the two-phase flow distribution between two passes of a heat exchanger. In: Winter Annual Meeting of the ASME.

Mudde, R. F., Groen, J. S., van den Akker, H. E. A., 1993. Two-phase flow redistribution phenomena in large T-junctions. Int. J. Multiphase Flow 19, 563–573.

Mueller, A. C., 1987. Effects of some types of maldistribution on the performance of heat exchangers. Heat Transfer Engineering 8, 75–86.

Mueller, A. C., Chiou, J. P., 1988. Review of various types of flow maldistribution in heat exchangers. Heat Transfer Eng. 9, 36–50.

Müller, U., Reimann, J., 1991. Redistribution of two-phase flow in branching conduits: A survey. In: Proc. Int. Conf. Multiphase Flows, Tsukuba, Japan. pp. 85–107.

Oranje, L., 1973. Condensate behaviour in gas pipelines is predictable. Oil and Gas J. 71, 39–44.

Osakabe, M., Hamada, T., Horiki, S., 1999. Water flow distribution in horizontal header contamined with bubbles. Int. J. Multiphase Flow 25, 827–840.

Ottens, M., Hoefsloot, H. C. J., Hammersma, P. J., 1999. Effect of small branch orientation on gas-liquid flow separation in T-junctions. AIChE J. 45, 465–474.

Payne, W. V., Domanski, P. A., September 2002. Potential benefits of smart refrigerant distributors. Tech. rep., ARTI-21CR/605-200-50-1.

Peng, F., Shoukri, M., Ballyk, J. D., 1998. An experimental investigation of stratified steam-water flow in T-junctions. In: 3rd Int. Conf. On Multiphase Flow, Lyon, France, June 8-12.

Peng, F., Shoukri, M., Chan, A. M. C., 1996. The effect of branch orientation on annular two-phase flow. Trans. ASME, J. Fluid Eng. 118, 166–171.

Penmatcha, R., Ashton, P. J. N., Shoham, O., 1996. Two-phase flow splitting at a tee-junction with inclined arm. Int. J. Multiphase Flow 22, 1105–1122.

Pettersen, J., 2002. Flow vaporization of CO_2 in microchannel tubes. Dr. techn. thesis, NTNU.

Pettersen, J., Aflekt, K., Skaugen, G., 2000. Optimization of extruded-tube evaporator for R134a: Circuiting and effect of liquid distribution. Tech. rep., SINTEF Energy Research, Trondheim, Norway, confidential Report.

Pitzer, K. S., Schreiber, D. R., 1988. Improving equations-of-state accuracy in the critical region; equations for carbon dioxide and neopentane as examples. Fluid Phase Equilibria 41, 1–17.

Press, W. H., Teukolsky, S. A., Vetterling, W. T., Flannery, B. P., 1999. Numerical receipes in C. Cambridge University Press.

Rea, S. Azzopardi, B. J., 2001. The split of horizontal stratified flow at a large diameter T-junction. Chem. Eng. Research and Design 79, 470–476.

Reid, R. C., Prausnitz, J. N., Poling, B. E., 1987. The properties of gases and liquids. McGraw-Hill Book Company, New York.

Reimann, J., Brinkmann, H. J., Domanski, R., 1988. Gas-liquid flow in dividing tee-junctions with a horizontal inlet and different branch orientations and diameters. Tech. Rep. KFK 4399, Kernforschungszentrum Karlsruhe.

Reimann, J., Kahn, M., 1984. Flow through a small break at the bottom of a large pipe with stratified flow. Nuclear Science and Engineering 88, 297–310.

Reimann, J., Seeger, W., 1986. Two-phase flow in a T-junction with a horizontal inlet - Part ii: pressure differences. Int. J. Multiphase Flow 12, 587–608.

Roberts, P. A., Azzopardi, B. J., Hibbert, S., 1995. The split of horizontal semi-annular flow in a large diameter T-junction. Int. J. Multiphase Flow 21, 455–466.

Rong, X., Kawaji, M., Burgers, J. G., 1995. Two-phase header flow distribution in a stacked plate heat exchanger. In: ASME/JSME Fluid Engineering and Laser Anemometry Conference and Exhibition.

Rong, X., Kawaji, M., Burgers, J. G., 1996. Gas-liquid and flow rate distributions in single end tank evaporator plates. In: SAE Technical Paper Series, Paper no. 960375.

Rouhani, Z., Axelsson, E., 1970. Calculation of void volume fraction in the subcooled and quality boiling regions. Int. J. Heat Mass Transfer 13, 383–393.

Rubel, M. T., Timmerman, B. D., Soliman, H. M., Sims, G. E., Ebadian, M. A., 1988. Phase distribution of high-pressure steam-water flow at a large diameter tee junction. Trans. ASME, J. Fluid. Eng. 54, 119–138.

Saba, N., Lahey, R. T., 1984. The analysis of phase separation phenomena in branching conduits. Int. J. Multiphase Flow 10, 1–20.

Samson, E. B., Stark, J. A., Grote, M. G., 1988. Two-phase flow manifold tests. In: Publication of McDonnel Douglas Astronautics Co. 871440, ASME. pp. 6484–6500.

Schmidt, H., Loth, R., 1994. Predictive methods for two-phase flow pressure loss in tee junctions with combining conduits. Int. J. Multiphase Flow 20, 703–720.

Schrock, V. E., Revankar, S. T., Mannheiner, C. H., Wang, C. H., December 1986. Small break critical discharge - the role of vapor and liquid entrainment in a stratified two-phase region upstream of the break. Tech. rep., NUREG/CR4761.

Seeger, W., Reimann, J., Muller, U., 1985. Phase separation in a T-junction with horizontal inlet. The 2nd Int. Conf. Multi-phase Flow, London, England , 13–26.

Seeger, W., Reimann, J., Muller, U., 1986. Two-phase flow in a T-junction with a horizontal inlet - Part i: phase separation. Int. J. Multiphase Flow 12, 575–586.

Selander, W. N., 1978. Explicit formulas for computation of friction factors in turbulent pipe flow. Tech. rep., Chalk River, Ontario Canada, Chalk River Nuclear Laboratories.

Shoham, O., Arirachakaran, S., Brill, J. P., 1989. Two-phase flow splitting in a horizontal reduced pipe tee. Chem. Eng. Sci. 44, 2388–2391.

Shoham, O., Brill, J. P., 1987. Two-phase splitting in a Tee junction - experiment and modelling. Chem. Eng. Sci. 42, 2667–2676.

Shoukri, M., Hassan, I., Peng, F., 2002. Steam-water stratified flow in T-junctions - experiments and modelling. Trans. of the CSME 26 (2), 241–259.

Skaugen, G., 2002. Investigation of transcritical CO_2 vapour compression systems by simulation and laboratory experiments. Dr. ing. thesis, NTNU.

Skorek, T., 1995. Modelling of two-phase flow in dividing T-junctions with horizontal inlet pipe. In: First Int. Symp. on Two-phase Flow Modelling and Experimentation, Rome, Italy, 9-11 October.

Smoglie, C., 1984. Two-phase flow through small branches in a horizontal pipe with stratified flow. Tech. Rep. KFK 3861, Kernforschungszentrum Karlsruhe.

Smoglie, C., Reimann, J., 1986. Two-phase flow through small branches in a horizontal pipe with stratified flow. Int. J. Multiphase Flow 12, 609–626.

Smoglie, C., Reimann, J., Muller, U., 1987. Two-phase flow through small breaks in a horizontal pipe with stratified flow. Nuclear Engineering and Design 99, 117–130.

Song, S., Bullard, C. W., 2002. Experimental and simulation analysis of microchannel evaporators. Tech. Rep. CR-47, ACRC, University of Illinois.

Stacey, T., Azzopardi, B. J., Conte, G., 2000. The split of annular two-phase flow at a small diameter T-junction. Int. J. Multiphase Flow 26, 845–856.

Steiner, D., 1993. Heat transfer to boiling saturated liquids. In: VDI-W*ä*rmeatlas, 6. auflage. VDI-Verlag, Ch. Hbb.

Stott, S. L., Bullard, C. W., Duun, W. E., 2002. Experimental analysis of a minimum-TEWI air conditioner prototype. Tech. Rep. CR-47, ACRC, University of Illinois.

Tae, S. J., Cho, K., 2003. Effect of geometric and dynamic parameters on the two-phase flow distribution of R-22 in branch tubes. In: Int. Congress of Refrigeration, Washington, D.C.

Taitel, Y., 1990. Flow pattern transition in two-phase flow. In: 9th Int. Heat Transfer Conference, Jerusalem.

Taitel, Y., Dukler, A. E., 1976. A model for predicting flow regime transitions in horizontal and near-horizontal gas-liquid flow. AIChE J. 22, 47–55.

Tengblad, N., 1996. Cooling of electronic components with closed loop two-phase thermosiphons. Ph.D. thesis, Department of Energy Technology, The Royal Institute of Technology, Sweden.

Thome, J. R., El Hajal, J., 2002. Two-phase flow pattern map for evaporation in horizontal tubes: Latest version. In: 1st Int. Conf. on Heat Transfer, Fluid Mechanics and Thermodynamics, South Africa.

Tompkins, D. M., Newell, T. A., Hrnjak, P. S., 2002a. Single phase, two-phase modeling; X-ray visualization for a microchannel manifold distribution system. Tech. Rep. TR-206, ACRC, University of Illinois.

Tompkins, D. M., Yoo, T., Hrnjak, P., Newell, T., Cho, K., 2002b. Flow distribution and pressure drop in micro-channel manifolds. In: Ninth Int. Refrigeration and Air Conditioning Conf., Purdue.

Vesovic, V., Wakeham, W. A., Olchowy, G. A., Sengers, J. V., Watson, J. T. R., Millat, J., 1990. The transport properties of carbon dioxide. J. Phys. Chem. Ref. Data 19 (3), 763–808.

Vist, S., Pettersen, J., 2002. Two-phase flow distribution in compact heat exchanger manifolds. In: Compact Heat Exchanger Symposium, A Festschrift on the 60th Birthday of R.K. Shah, August 24, Grenoble, France.

Vist, S., Pettersen, J., 2003. Two-phase CO_2 distribution in a compact heat exchanger manifold. In: 2nd Int. Conf. on Heat Transfer, Fluid Mechanics and Thermodynamics, 23-26 June 2003, Victoria Falls, Zambia.

Vist, S., Pettersen, J., 2004. Two-phase flow distribution in compact heat exchanger manifolds. Experimental Thermal and Fluid Science 28, 209–215.

Wallis, G. B., 1969. One-dimensional two-phase flow. McGraw Hill, New York.

Walters, L. C., Soliman, H. M., Sims, G. E., 1998. Two-phase pressure drop and phase distribution at reduced T-junctions. Int. J. Multiphase Flow 24, 775–792.

Watanabe, M., Katsuta, M., Nagata, K., 1995. Two-phase flow distribution in multi-pass tube modeling serpentine type evaporator. In: Proceedings of the ASME/JSME Thermal Engineering Conference. Vol. 2. pp. 35–42.

Whalley, P. B., 1996. Two-phase flow and heat transfer, 3rd Edition. Oxford University Press, Oxford Science Publications.

Wren, E., Azzopardi, B. J., Rea, S., 1999. Geometric effects on phase split in a large diameter T-junction. In: 2nd Int. Symp. Two-Phase Flow Modelling and Experimentation, Pisa, 23-26 May. pp. 811–818.

Wu, X. M., Webb, R. L., 2002. Thermal and hydraulic analysis of brazed aluminum evaporator. Applied Thermal Eng. 22, 1369–1390.

Xiaoye, S. L., 1996. Sparse gaussian elimination on high performance computers. Ph.D. thesis, Tech Report CSD-96-919, Computer Science, UC Berkeley.

Yin, J. M., Bullard, C. W., Hrnjak, P. S., 2002. Single-phase pressure drop measurements in a microchannel heat exchanger. Heat Transfer Eng. 23, 3–12.

Yoo, T., Hrnjak, P., Newell, T. A., 2002. An experimental investigation of two-phase flow distribution in microchannel manifolds. Tech. Rep. TR-207, ACRC, University of Illinois.

Yuncu, H., Kakac, S., 1988. Fundamentals of two-phase flow instabilities. In: Two-phase flow heat exchangers. Kluwer Academic Publishers, pp. 375–406.

Zetzmann, K., 1982. Phasenseparation and druckfall in zweiphasen durchstromten vertikalen rohrabzwigungen. Ph.D. thesis, University of Hannover, FRG.

Zietlow, D. C., Campagna, M., Dias, J. F., 2002. Innovative experimental apparatus to measure liquid flow distribution in two-phase flow occuring in the manifolds of compact heat exchangers. ASHRAE Trans .

Zivi, S. M., 1964. Estimation of steady-state steam void fraction by means of the principle of minimum entropy production. Trans. ASME (J. Heat Transfer) 86, 247–252.

Zürcher, O., Favrat, D., Thome, J. R., 1999. Evaporation of ammonia in a smooth horizontal tube: heat transfer measurements and predictions. J. Heat Transfer 121 (1), 89–101.

Zürcher, O., Favrat, D., Thome, J. R., 2002. Development of a diabatic two-phase flow pattern map for horizontal flow boiling. Int. J. Heat and Mass Transfer 45 (2), 291–301.

Appendices

Appendix A

The Saba and Lahey (1984) T-junction model

The current Appendix contains an outline of the model for prediction of phase separation in T-junctions developed by Saba and Lahey (1984) and Lahey et al. (1985). The framework of the model, and the applicability of it, is commented in Section 2.6.1. Nomenclature used in the model is shown in Figure A.1.

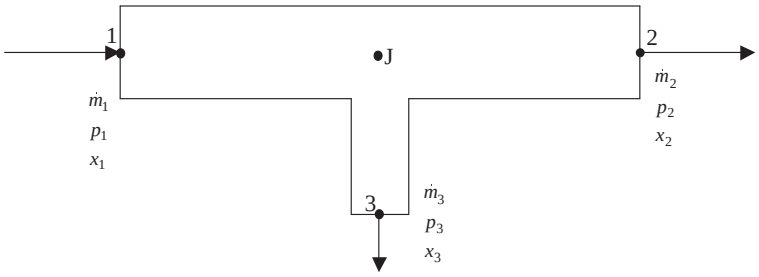

Figure A.1: Variables and notation used in the manifold phase separation model.

Mixture continuity equation

The mixture continuity equation was given by:

$$\dot{m}_1 = \dot{m}_2 + \dot{m}_3 \tag{A.1}$$

Vapour phase continuity equation

Assuming no phase change in the junction, the vapour phase continuity equation

became:

$$\dot{m}_1 x_1 = \dot{m}_2 x_2 + \dot{m}_3 x_3 \tag{A.2}$$

The branch tube linear momentum equation

The branch tube linear momentum equation contained the pressure loss terms related to the redirection of the fluid and frictional and gravitational pressure drops in the sections before and after the T-junction (see Figure A.2):

$$\Delta p_{1-3} \equiv p_1 - p_3 = (p_1 - p_{1J}) + (\Delta p_{1-3})_J + (p_{3J} - p_3) \tag{A.3}$$

where the pressure change before and after the T-junction, respectively, were due to friction and gravity:

$$p_1 - p_{1J} = \frac{1}{2}\frac{f_1 L_1}{D_{H_1}}\frac{G_1^2}{\rho_l}\phi_{Lo_1}^2 + \bar{\rho}_1 g L_1 \sin\gamma_1 \tag{A.4}$$

$$p_3 - p_{3J} = \frac{1}{2}\frac{f_3 L_3}{D_{H_3}}\frac{G_3^2}{\rho_l}\phi_{Lo_3}^2 + \bar{\rho}_3 g L_3 \sin\gamma_3 \tag{A.5}$$

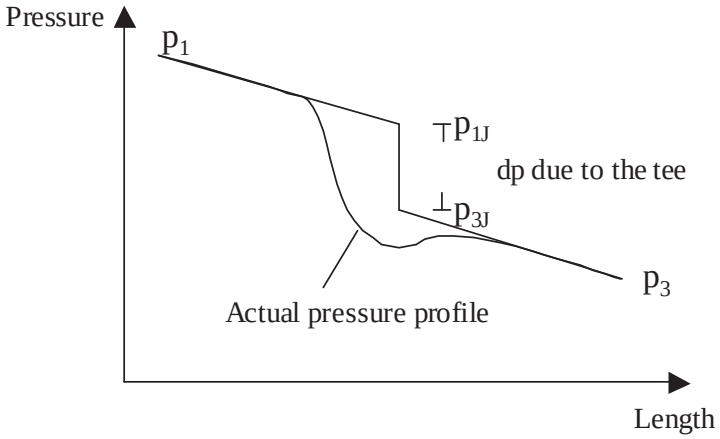

Figure A.2: Flow split pressure loss from main pipe to side branch.

Saba and Lahey (1984) utilized a homogeneous two-phase friction loss multiplier,

$$\phi_{Lo_i}^2 = \left(1 + \frac{v_{lg}}{v_l} x_i\right) \tag{A.6}$$

where,

$$v_{lg} = \left(\frac{1}{\rho_g} - \frac{1}{\rho_l}\right) = \frac{\rho_l - \rho_g}{\rho_l \rho_g} \tag{A.7}$$

The pressure loss related to the T-junction was partitioned into a reversible and an irreversible part,

$$(\Delta p_{1-3})_J = (\Delta p_{1-3})_{rev} + (\Delta p_{1-3})_{irrev} = \frac{1}{2}\rho_{h3}\left[\frac{G_3^2}{\rho_{e3}^2} - \frac{G_1^2}{\rho_{e1}^2}\right] + \frac{1}{2}K_{13}\frac{G_1^2}{\rho_l}\Phi_{13} \quad \text{(A.8)}$$

For the reversible part Saba and Lahey (1984) recommended to use the so-called energy density. The energy and homogeneous densities were defined by,

$$\frac{1}{\rho_e^2} \equiv \left[\frac{(1-x)^3}{\rho_l^2(1-\alpha)^2} + \frac{x^3}{\rho_g^2\alpha^2}\right] \quad \text{(A.9)}$$

and,

$$\frac{1}{\rho_h} \equiv \frac{x}{\rho_g} + \frac{1-x}{\rho_l} \quad \text{(A.10)}$$

Saba and Lahey (1984) used a correlation for the single phase pressure loss coefficient given by,

$$K_{13} = \left[1.18 + \left(\frac{G_3A_3}{G_1A_1}\right)^2 - 0.8\left(\frac{G_3A_3}{G_1A_1}\right)\right]\left(\frac{A_1}{A_3}\right) \quad \text{(A.11)}$$

The local loss two-phase multiplier was given by (Chisholm, 1967),

$$\Phi_{13} = (1-x_1)^2\left[1 + \frac{C_{13}}{X_{tt}} + \frac{1}{X_{tt}^2}\right] \quad \text{(A.12)}$$

where,

$$C_{13} = \left[1 + (C_3 - 1)\left(\frac{\rho_l - \rho_g}{\rho_l}\right)^{1/2}\right]\left[\left(\frac{\rho_l}{\rho_g}\right)^{1/2} + \left(\frac{\rho_g}{\rho_l}\right)^{1/2}\right] \quad \text{(A.13)}$$

For separated flow conditions, the suggested value of C_3 was 1.75, while in homogeneous flow conditions the suggested value of C_3 was 1.0. The Lockhart-Martinelli parameter was defined as:

$$\frac{1}{X_{tt}} \equiv \left(\frac{x_1}{1-x_1}\right)\left(\frac{\rho_l}{\rho_g}\right)^{0.5} \quad \text{(A.14)}$$

The main pipe mixture linear momentum equation

The main pipe mixture linear momentum equation consisted of components related to pressure change in the inlet section, the pressure change in the T-junction and the pressure change in the downstream section (as shown in Figure A.3):

$$\Delta p_{1-2} \equiv p_1 - p_2 = (p_1 - p_{1J}) + (\Delta p_{1-2})_J + (p_{2J} - p_2) \tag{A.15}$$

The pressure change before and after the T-junction was due to friction and momentum as shown in equations A.4 and A.5.

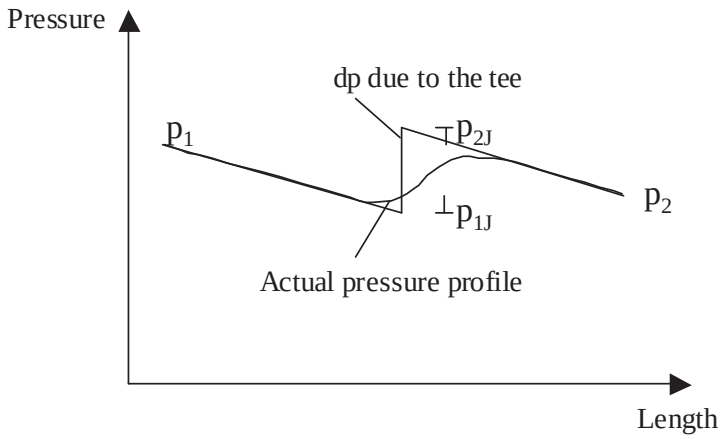

Figure A.3: Pressure loss in main pipe across T-junction.

Pressure recovery due to the T-junction, was given by:

$$(\Delta p_{1-2})_J = p_{1J} - p_{2J} = \frac{K_{1-2}}{2}\left[\frac{G_2^2}{\rho_2'} - \frac{G_1^2}{\rho_1'}\right] \tag{A.16}$$

Empirical pressure recovery coefficient K_{1-2} was fitted to single-phase data:

$$K_{1-2} = 0.11 + \frac{5.0}{\left[\frac{G_1 D_{H1}}{\mu_{l1}}\right]^{0.17}} \tag{A.17}$$

The momentum density was given by:

$$\frac{1}{\rho_i'} \equiv \left[\frac{(1-x_i)^2}{\rho_l\,(1-\alpha_i)} + \frac{x_i^2}{\rho_g \alpha_i}\right] \tag{A.18}$$

Vapour phase momentum equation for the branch tube

The first four equations were straight forward conservation equations for the two-phase flow split. The fifth equation provided the closure and could be formulated in a number ways, e.g. like the phase split equations described in Section 2.6.2. In the original model of Saba and Lahey (1984) the closure equation of the problem was chosen to be formulated as a vapour phase momentum equation for the branch tube. Saba and Lahey (1984) argued that the dominant factor affecting the phase distribution in the T-junction was the ability of the vapour phase to make the turn into the branch tube, thus it was considered to be the most important effect to be modelled. The steady state formulation of the equation, assuming no phase change, was given by,

$$\alpha\rho_g u_g \frac{du_g}{dz} = -\alpha\frac{dp}{dz} - \alpha F_d - \alpha F_w - g\rho_g \alpha \sin\gamma_{13} \tag{A.19}$$

where u_g was the vapour phase velocity, F_d was the volumetric interfacial drag force on the vapour and F_w was the volumetric wall drag force on the vapour in the T-junction. Integrating Equation A.19 along the vapour streamlines through the T-junction gave,

$$\begin{aligned}(\Delta p_{13})_J &= \frac{3}{4}\rho_l \frac{C_D}{D_B} V_{rJ}^2 L_J + \frac{1}{2}\rho_{g3}\left[\left(\frac{\dot{m}_3 x_3}{\rho_{g3}\alpha_3}\right)^2 - \left(\frac{\dot{m}_1 x_1}{\rho_{g1}\alpha_1}\right)^2\right] \\ &+ \frac{1}{2}K_{13}\left(\frac{\dot{m}_1 x_1}{\rho_{g1}\alpha_1}\right)^2 + \rho_{g3} g L_J \sin\gamma_{13}\end{aligned} \tag{A.20}$$

The parameter C_D/D_B was the cross sectionally averaged one-dimensional drag coefficient, which was a function of the cross-sectionally averaged void fraction, α. Saba and Lahey (1984) used the Hench's (churn turbulent) drag model (Hench and Johnston, 1968),

$$\frac{C_D}{D_B} = 54.9\left[\frac{\rho_g}{\rho_l}\alpha(1-\alpha)^2 - (1-\alpha)^3\right] \tag{A.21}$$

The equivalent path length for the mean vapour streamline was correlated to experimental data by the authors (Saba and Lahey, 1984),

$$L_J = 2.81 D_{H3}(1-x_3)^3 \exp\left[-0.12\left(\frac{1-x_1}{x_1}\right)^{0.15}\left(\frac{\rho_{g1}}{\rho_{l1}}\right)^{0.5}\right]\left(\frac{\dot{m}_3}{\dot{m}_1}\right)^{(1-x_1)^3} \tag{A.22}$$

A standard Zuber-Findlay drift flux relation (Lahey and Moody, 1977) was used to determine the void fraction and the relative velocity of the phases,

$$\alpha_i = \frac{x_i}{C_0\left[x_i + \frac{\rho_{gi}}{\rho_{li}}(1-x_i)\right] + \frac{\rho_{gi} V_{gji}}{G_i}} \tag{A.23}$$

$$U_{ri} \equiv u_{gi} - u_{li} = \frac{j_i\,(C_0 - 1) + V_{gji}}{(1-\alpha_i)} \tag{A.24}$$

where the volumetric flux was given by,

$$j_i \equiv G_i \left[\frac{x_i}{\rho_{gi}} + \frac{(1-x_i)}{\rho_{li}} \right] \tag{A.25}$$

The appropriate concentration parameter value of C_0 at the T-junction was found to be (Saba and Lahey, 1984),

$$C_o = 1.4 - 0.4 \left(\frac{\rho_{g1}}{\rho_{l1}} \right)^{0.5} \tag{A.26}$$

The drift-flux-velocity for churn-turbulent flow was used:

$$V_{gj} = 2.5 \left[\frac{(\rho_{l1} - \rho_{g1})\,\sigma g}{\rho_{l1}^2} \right]^{1/4} \tag{A.27}$$

Appendix B

Patents Aimed at Improvement of Two-Phase Distribution

B.1 Manifold design modifications

Osthues, Petz and Zeitvogel (1998 US Patent 5,806,586 by Ernst Flitsch GmbH and Co.) used a porous body inside the manifold to improve distribution of the two-phase flow, Figure B.1. The refrigerant was forced through the porous body, resulting in a dispersed liquid droplet flow, which was claimed to be easy to distribute evenly into the branch tubes of the heat exchanger.

A combined venturi distributor cone and refrigerant channel distribution arrangement was invented in US Patent 4,513,587 (Humpolik and Staffa, 1985). An insert in the inlet manifold acted as a venturi distributor, from which separate machined channels led the refrigerant to each branch tube, Figure B.2. Similar arrangements were also shown in US Patent 4,593,539 by Humpolik et al. (1986) and US Patent 4,430,868 by Kern et al. (1984).

Burk, Salzer and Wolf (1994, DE 4,319,192) suggested to use a header with reduction in cross-sectional area along the flow direction to improve the two-phase distribution (Figure B.3).

In US Patent 5,157,944 (Hughes, Struss and Boero, 1992) claimed that a double inlet to the distribution manifold would enhance the two-phase distribution, Figure B.4.

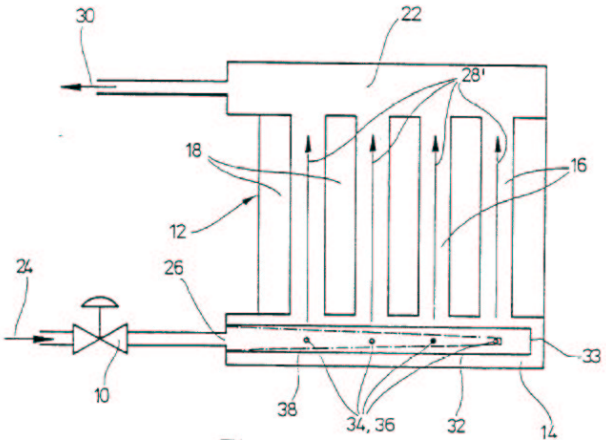

Figure B.1: Plate evaporator with refrigerant distributor made from a porous body (38), from US Patent 5,806,586 (Osthues, Petz and Zeitvogel, 1998).

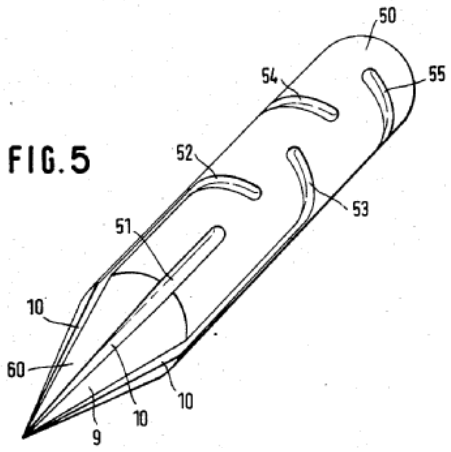

Figure B.2: Combined venturi distributor cone and flow channel arrangement from US Patent 4,513,587 (Humpolik and Staffa, 1985).

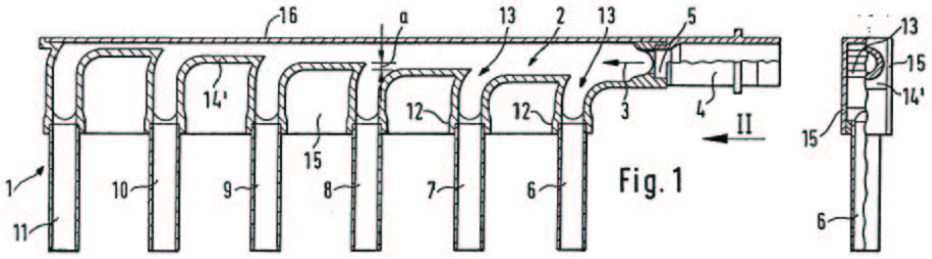

Figure B.3: Distribution manifold with decreasing cross-section, from DE 4,319,192 (Burk, Salzer and Wolf, 1994)

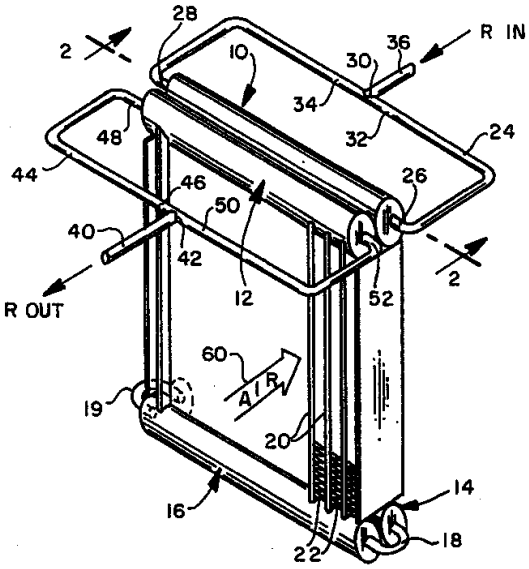

Figure B.4: Evaporator manifold with double inlet, from US Patent 5,157,944 (Hughes, Struss and Boero, 1992)

Hummel et al. (1985, US Patent 5,524,823) used a helical profiled insert inside a circular manifold to obtain improved two-phase distribution (Figure B.5). A venturi device at the inlet of the manifold distributed the two-phase flow to the helical flow channels.

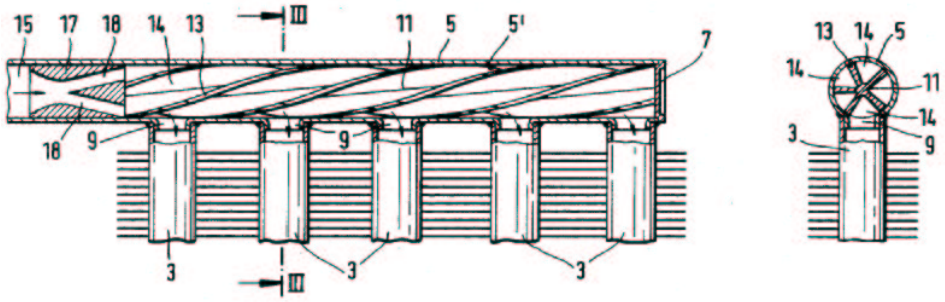

Figure B.5: Helical manifold insert, from US Patent 5,524,823 (Hummel et al., 1985)

B.2 Phase mixing and controlled mixture distribution

Reinke and Voss (1999, US Patent 5,190,167) showed a solution for distribution of two-phase flow into a horizontal evaporator manifold. A venturi distributor right after the expansion valve was feeding the flow into several distributing tubes that was connected to the manifold as shown in Figure B.6 a). The refrigerant was sprayed into the interior of the header, such that the header walls served as impingement distributors. A complete heat exchanger with distributor scheme is shown in Figure B.6 b).

A centrifugal swirl distributor (Figure B.7) was shown by Schneider and Byrd (1991 US Patent 5,059,226), while a rotating ”turbine” was used to distribute the two-phase flow in US Patent 5,832,744 (Dorste, Ens and Heffner, 1998), Figure B.8.

Samson et al. (1988) tested a ”fan header” based on the principle of symmetrical distribution of the two-phase flow into four branch tubes. The new design worked well (liquid was distributed within 16% of the equally distributed value) at inlet vapour fractions below 0.25. At higher inlet vapour fractions the performance deteriorated somewhat.

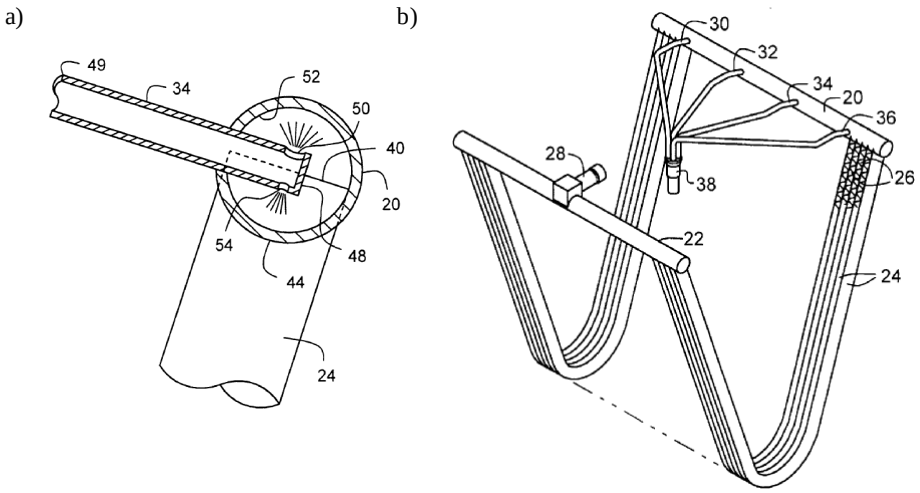

Figure B.6: Two-phase distribution system from US Patent 5,190,167 (Reinke and Voss, 1999). a) Manifold refrigerant injector. 20: manifold cross section, 24: heat transfer tube, 34: refrigerant injector. b) Evaporator with distributor arrangement.

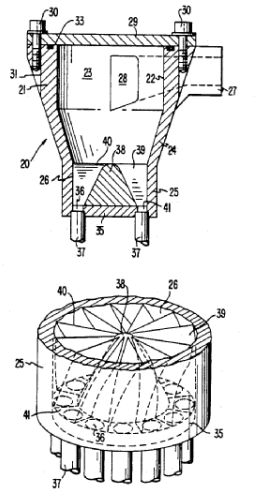

Figure B.7: Centrifugal swirl distributor from US Patent 5,059,226 (Shneider and Byrd, 1991). 27: inlet, 39: distributor vanes, 37: outlet tube.

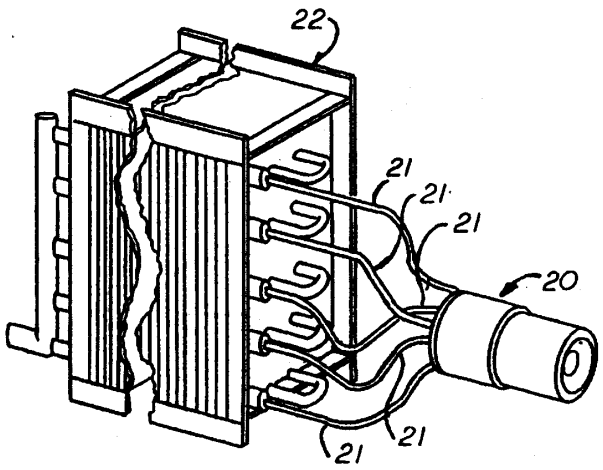

Figure B.8: Controlled two-phase distribution from US Patent 5,832,744 (Dorste, Ens and Heffner, 1998).

B.3 Phase mixers

Several types of phase mixers are shown in product literature and patents. A thorough overview of in-tube mixers used in the process industry is given in Baker (1991). Many static/motionless mixers consists of a series of stationary, flow-directing baffles. The two-phase flow is divided in two or more layers within each mixing element. These layers are continually and recombined until a homogeneous mixture is attained at the mixer exit. Some examples of static mixers are shown in Figure B.9.

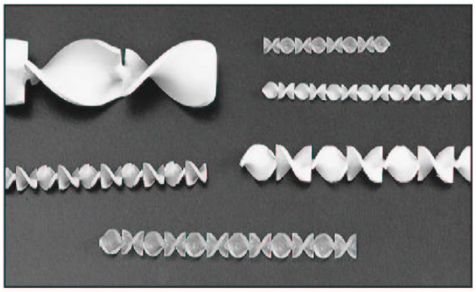

Figure B.9: Plastic spiral mixer elements (TAH industries Inc).

Mohn (US Patent 5,035,842, 1991) showed a flow mixer comprising a cylindrical

vessel with a gas/liquid diverter, an injection pipe and a gas/liquid ejector, Figure B.10. When entering the flow mixer, the liquid phase was continually drained to the bottom of the compartment and through the ejector. The gas phase was diverted to the top section of the compartment and via the injection pipe to the ejector. In the ejector nozzle, a turbulent shear layer was generated. Small pressure losses were achieved by utilizing this turbulent shear layer mixing process.

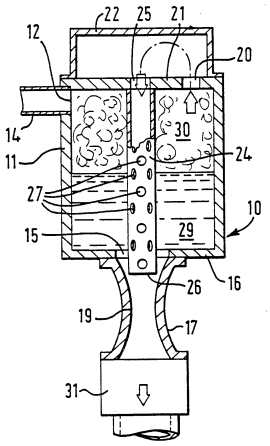

Figure B.10: Static mixer as shown in US Patent 5,035,842 (Mohn, 1991). 14: Inlet, 17: Ejector, 31: Outlet.

Li et al. (2002) performed an CFD-analysis using commercially available software to study the two-phase distribution and separation phenomena in existing and improved designs for refrigerant distributors.

B.4 Phase separation and liquid feeding of the evaporator

One solution for liquid feeding of the evaporator manifold was shown by Shimoya et al. (1995 US Patent 5,390,507 by Denso) where the flash vapour was condensed upstream of the evaporator inlet by internal heat transfer, Figure B.11.

Hanson and van Essen (US Patent 6,318,118, 2001) showed the system used by Beaver et al. (2000), where a separator was located in front of the evaporator. The flash gas from the expansion valve bypassed the evaporator.

The most common type of separator in refrigeration applications is the cyclone

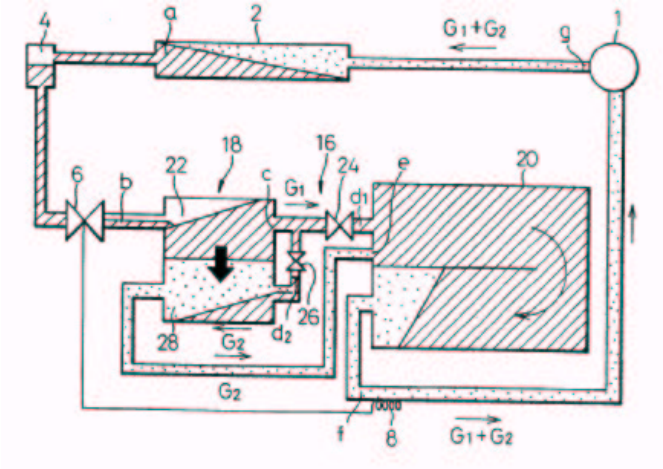

Figure B.11: Flash gas condensing, from US Patent 5,035,842 (Shimoya et al., 1995).

separator, which separates the liquid and the vapour due to gravity and centrifugal effects. Separation is obtained by the difference in density between the two phases. Examples of cyclone separators are shown by Haugen, Ohlsson and Persson (PTC/SE98/00368, 1998).

Kim and Lee (US Patent 4,370,868, 1983) showed an evaporator distribution arrangement based on initial separation of the two phases and controlled recombination of the phases into each refrigerant circuit in a plate evaporator. The phases were separated in a cyclone separator, Figure B.12, containing a float valve that prevented the vapour phase to reach the liquid inlets to the evaporator.

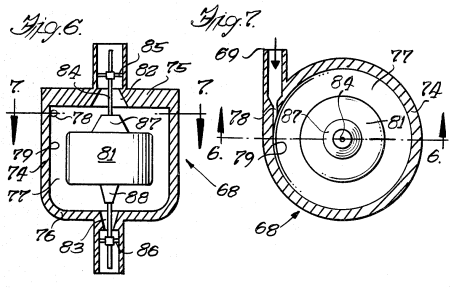

Figure B.12: Refrigerant phase separator with float valve, from US Patent 4,370,868 (Kim and Lee, 1993).

An ideal two-phase flow splitter should distribute vapour and liquid fractions evenly into the branch tubes, so that the vapour fraction is the same in the branches as in the main manifold line. Jones (1989 US Patent 4,824,614) showed a horizontal "flow splitting junction" for a two-phase fluid that used a combination of a static mixer (no moving parts), a multi-duct stratifier and a divider wall (guide vane), Figure B.13. It was claimed that the gas/liquid ratio of the inlet pipe was maintained in the splitting.

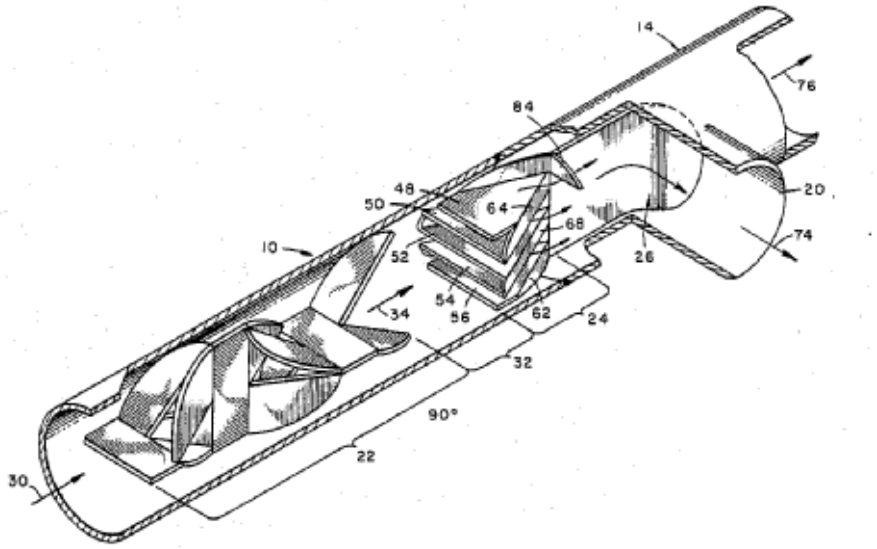

Figure B.13: Two-phase splitter as shown in US Patent 4,824,614 (Jones, 1989).

Hong and Griston (US Patent 5,810,032, 1998) proposed a number of designs for two-phase flow splitters based on impacting pipe tees. Mechanical modifications such as pre-separator vanes and nozzles in the exit arms were suggested. The patent also provided several references to technical literature on two-phase flow splitting.

Wurz and Zimmermann (US Patent 4,802,901, 1989) showed a separator based on a tube where the flow was led in a zig-zag pattern, and where trap pockets and guide vanes were provided for trapping liquid flowing along the wall of the tube. Several geometries were indicated for improved separation efficiency over a wide range of flow conditions, giving minimum pressure losses.

Godry and Hong (1998 US Patent 5,811,625) obtained single-phase liquid feeding of the evaporator manifold by only partly depressurization in the throttle valve. Pressure reduction into the two-phase region was done in flow restrictions at the

inlet of each branch tube, as shown in Figure B.14. The principle of using restrictions in the inlet of the individual heat exchanger channels are commonly used in large evaporators used in process industries (Holm et al., 2001).

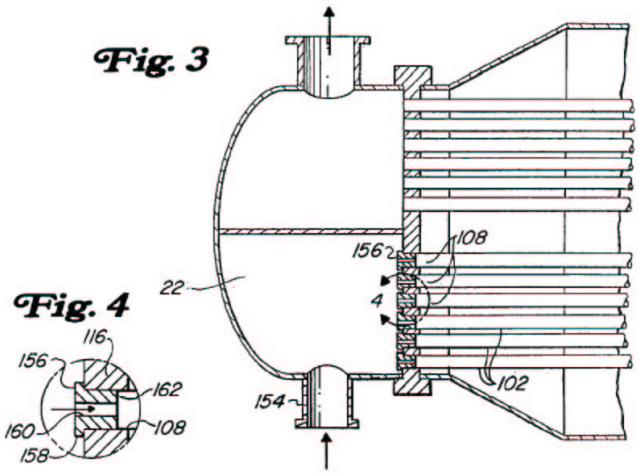

Figure B.14: Liquid feeding, from US Patent 5,811,625 (Godry and Hong, 1998).

Appendix C

Calibration measurements

C.1 Energy balance testing

Single phase testing allowed the refrigerant side enthalpies to be calculated directly based on temperature and pressure measurements. This allowed energy balances to be checked across the refrigerant preheater, condenser, test-section and the pipe section connecting the test section and the condenser. Once it was confirmed that deviations in heat balance between refrigerant and heating/cooling medium (electrical cable or water flow) was consistent with small heat losses or gains with the environment, simple empirical expressions were developed to predict the heat losses.

C.1.1 Tap-off condenser heat loss calibration measurements

During single-phase refrigerant testing, energy balances were checked across the tap-off condenser (see Figure 3.4 for annotations). The heat loss, $\dot{Q}_{leak,c}$, was computed based on the difference between energy gained by the water and that lost by the refrigerant using Equation 3.5. The water flowed in an annulus outside the refrigerant tube, and was always colder than the environment, resulting in a small amount of heat lost to the environment. The amount of heat loss was small, less than 30 W for temperature differences up to 15°C . Since some of the measurements had small refrigerant mass flow values (0.001 kg/s), a heat loss of 30 W would correspond to a change in calculated $x_{t,i}$ of approximately ± 0.17. Correlating the heat loss based on physical principles offered an opportunity to

reduce the experimental uncertainty. The model Equation C.1 was solved for an overall heat conductance, UA_c, of the insulation:

$$\dot{Q}_{leak,c} = UA_c \left(T_a - \overline{T_{w,c}}\right) \tag{C.1}$$

The overall conductance in Equation C.1 represents the total heat transfer resistance from the water to the ambient air (convection from the water, conduction through the pipe wall and the insulation and free convection to the air). The dominant resistance through the insulation was considered to be constant over the range of temperatures for the present tests. A series of single-phase tests were conducted to determine the overall conductance.

A linear regression curve was fit to the $\dot{Q}_{leak,c}$ versus $\left(T_a - \overline{T_{w,c}}\right)$ data. UA_c was then the slope of this curve. The resulting value was $UA_c = 2.4$ W/K. In Figure C.1 the measured heat loss data are compared to the predictions of the model. Most of the heat loss data were predicted within 15%, with worst error being 8W. Based on this agreement, the $\pm\, 2\sigma$ uncertainty in $\dot{Q}_{leak,c}$ was estimated at $\pm$15%.

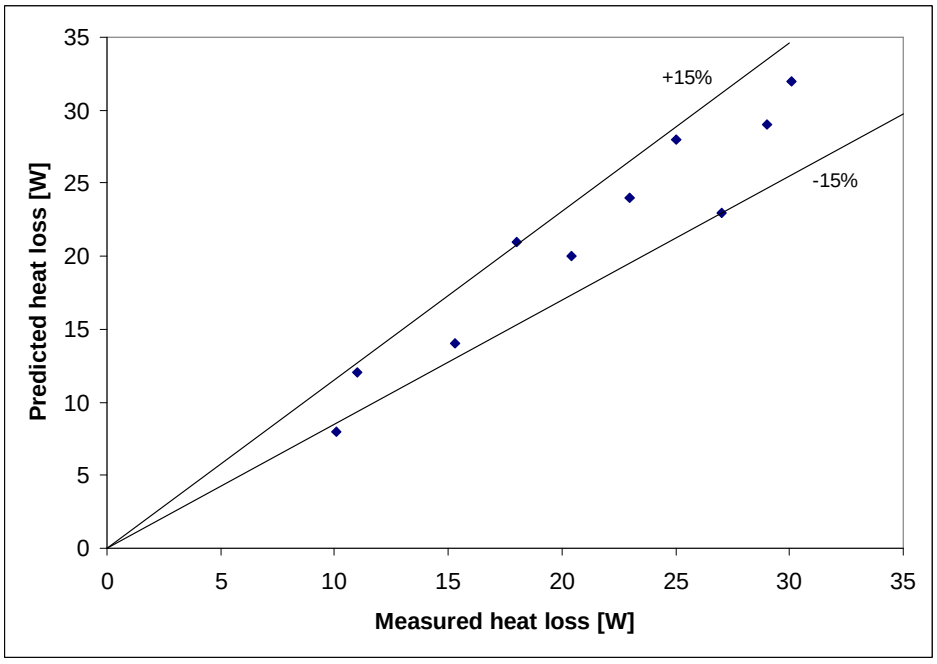

Figure C.1: Tap-off circuit condenser heat loss calibration.

C.1.2 Tap-off circuit tubing heat loss calibration measurements

Due to the high temperature in the tap-off circuit in measurements where the refrigerant was superheated in the test section, the heat loss could be significant. Therefore, the heat loss through the thermal insulated pipe connecting the test section and the tap-off circuit condenser, $\dot{Q}_{leak,t}$, was estimated by single-phase calibration experiments. A model equation was solved for the overall conductance, UA_t:

$$\dot{Q}_{leak,t} = UA_t \left(\overline{T_t} - T_a\right) \tag{C.2}$$

Following the same procedure as outlined in the previous section, the result of the linear regression was $UA_{leak,t} = 0.40$ W/K. Figure C.2 shows the measured heat loss data compared to the model predictions. A $\pm$ 2σ uncertainty in $\dot{Q}_{leak,t}$ was estimated at $\pm$10%.

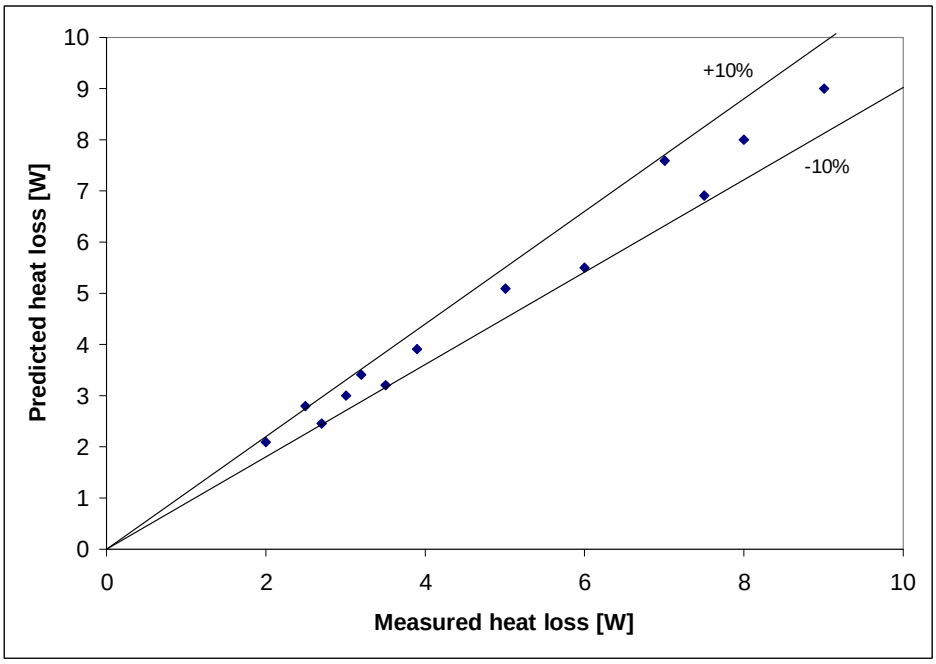

Figure C.2: Heat loss calibration for the tap-off circuit tubing.

C.1.3 Test section heat loss calibration measurements

The heat loss through the thermal insulation of the test section, $\dot{Q}_{leak,ts}$, was estimated the same way as shown in the two previous sections. The water was flowing

in annuli outside the refrigerant tubes and the heat loss was therefore modelled as a function of the average water temperature. Single-phase calibration experiments were used to find UA_{ts} in the following model equation:

$$\dot{Q}_{leak,ts} = UA_{ts}\left(\overline{T_{w,ts}} - T_a\right) \tag{C.3}$$

Following the same procedure as outlined in the previous section, the result of the linear regression was $UA_{leak,ts} = 0.55$ W/K. Figure C.2 shows the measured heat loss data compared to the model predictions. A $\pm\ 2\sigma$ uncertainty in $\dot{Q}_{leak,ts}$ was estimated at $\pm$15%.

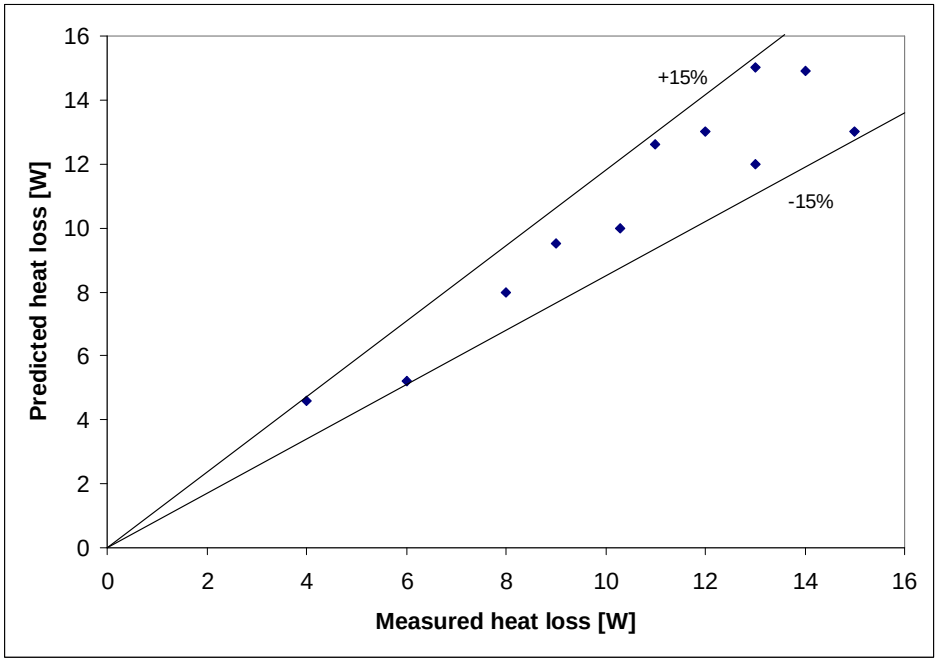

Figure C.3: Heat loss calibration for the test section.

C.2 Test section water flow calibration measurements

The total flow rate in the water circuit was distributed to ten parallel channels in the test section. The individual channel flow rates were calculated based on calibration measurements, where the flow rate was determined by collecting a sample of water for a fixed amount of time. The time was measured with a stopwatch, and was estimated to have an uncertainty of $\pm$0.2 s due to operator timing errors.

The water was measured using a graduated cylinder with an uncertainty of ± 0.01 litre. The individual channel flow rates are shown as fractions of the total water flow rate in Figure C.4. Twelve independent calibration tests was run during the entire period the measurements were taken to ensure that fouling in the water channels would not change the distribution between the water channels.

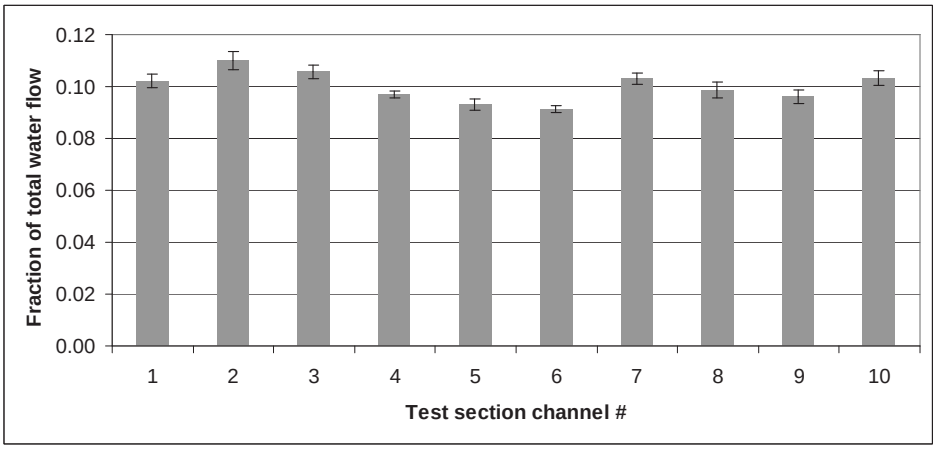

Figure C.4: Fraction of total water flow in test section channels. $\pm 2\sigma$ error bars are shown to indicate the deviation in the measurements.

The channel flow rate fraction of the total flow varied from 0.091 to 0.11 due to manufacturing differences in the annuli around the refrigerant tubes in the test section. The $\pm 2\sigma$ error in the measurements varied from 1.2% to 3.1% of measured value for the individual channels. In the uncertainty calculations, a value of 3.1% was used for all channels.

Appendix D

MPE-tube manifold geometry

Detailed drawings of the MPE-tube manifold used in the current work are given in the following Figures.

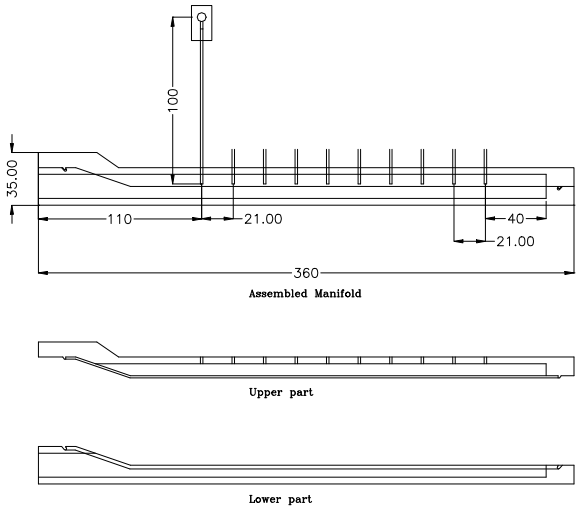

Figure D.1: Side-view of base-case MPE-tube manifold (M5). All measures are given in mm.

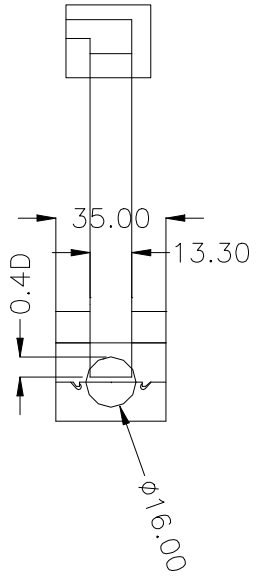

Figure D.2: Cross-sectional view of base-case MPE-tube manifold (M5). All measures are given in mm.

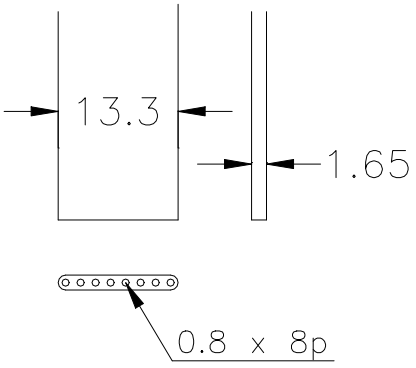

Figure D.3: Detailed view of MPE-tube used in manifolds M5 to M10. All measures are given in mm.

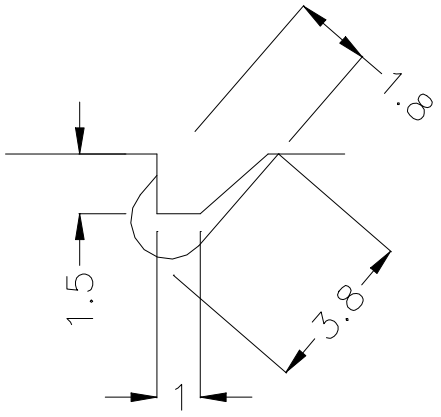

Figure D.4: Detailed view of O-ring groove used in connection of the MPE-tube manifold upper and lower parts. All measures are given in mm.

Appendix E

Additional Plots From Measurement Data Analysis - Upward Configuration

E.1 Branch tube vapour fraction as function of manifold gas mass flux, upward configuration

This Section contains the additional plots used to calculate the threshold values, $G_{g,m,lim}$, shown in Figure 5.41.

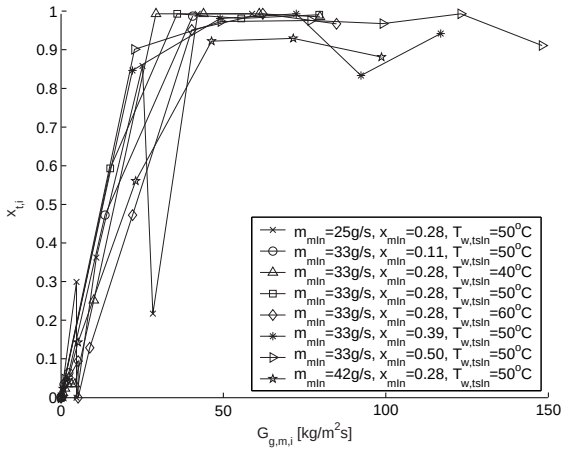

Figure E.1: Measured branch tube vapour fraction, $x_{t,i}$, as function of gas mass flux, $G_{g,m,i}$, at inlet of manifold T-junctions. Series with branch *No* 1 to 10 are shown from the right to the left (decreasing $G_{g,m,i}$). ID 12 mm manifold (M2). Refrigerant: HFC-134a, $T_{mIn} = 29.5°C$.

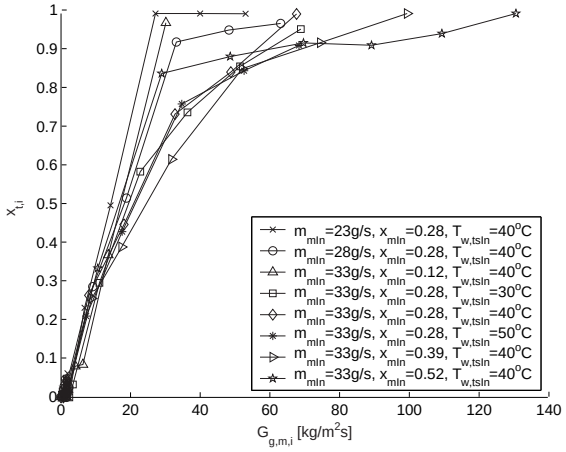

Figure E.2: Measured branch tube vapour fraction, $x_{t,i}$, as function of gas mass flux, $G_{g,m,i}$, at inlet of manifold T-junctions. Series with branch *No* 1 to 10 are shown from the right to the left (decreasing $G_{g,m,i}$). Manifold M5. Refrigerant: CO_2, $T_{mIn} = 18.7°C$.

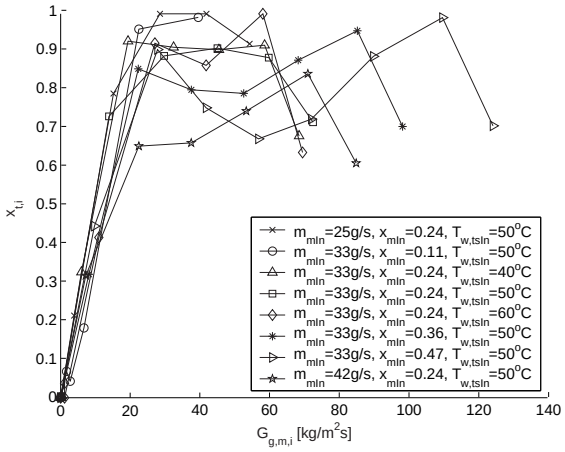

Figure E.3: Measured branch tube vapour fraction, $x_{t,i}$, as function of gas mass flux, $G_{g,m,i}$, at inlet of manifold T-junctions. Series with branch *No* 1 to 10 are shown from the right to the left (decreasing $G_{g,m,i}$). Manifold M5. Refrigerant: HFC-134a, $T_{mIn} = 29.5°C$.

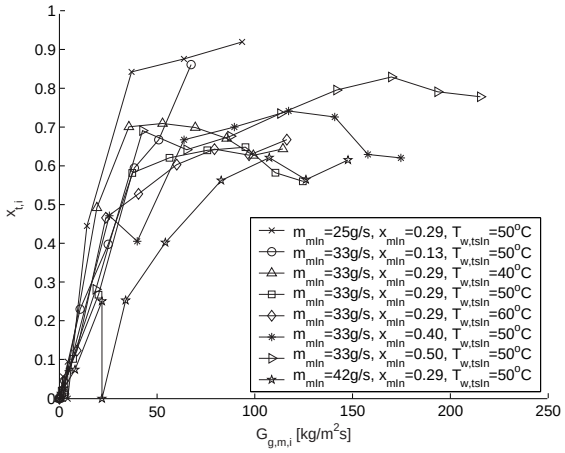

Figure E.4: Measured branch tube vapour fraction, $x_{t,i}$, as function of gas mass flux, $G_{g,m,i}$, at inlet of manifold T-junctions. Series with branch *No* 1 to 10 are shown from the right to the left (decreasing $G_{g,m,i}$). Manifold M6. Refrigerant: HFC-134a, $T_{mIn} = 29.5°C$.

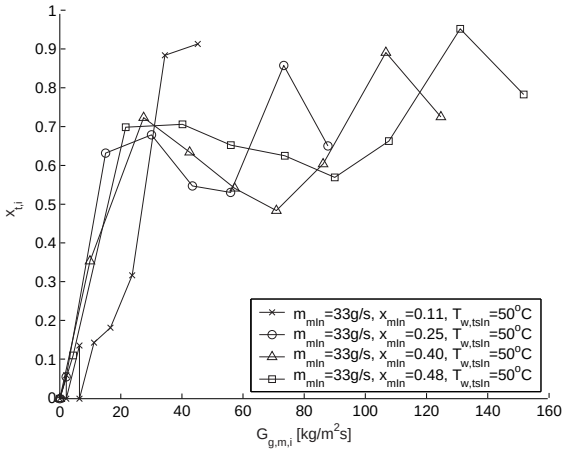

Figure E.5: Measured branch tube vapour fraction, $x_{t,i}$, as function of gas mass flux, $G_{g,m,i}$, at inlet of manifold T-junctions. Series with branch *No* 1 to 10 are shown from the right to the left (decreasing $G_{g,m,i}$). Manifold M7. Refrigerant: HFC-134a, $T_{mIn} = 29.5°C$.

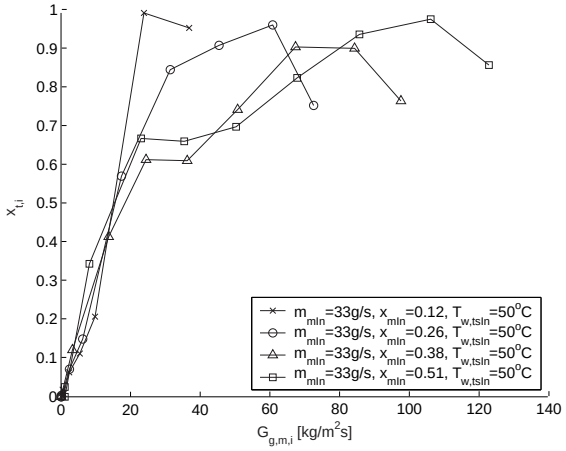

Figure E.6: Measured branch tube vapour fraction, $x_{t,i}$, as function of gas mass flux, $G_{g,m,i}$, at inlet of manifold T-junctions. Series with branch *No* 1 to 10 are shown from the right to the left (decreasing $G_{g,m,i}$). Manifold M8. Refrigerant: HFC-134a, $T_{mIn} = 29.5°C$.

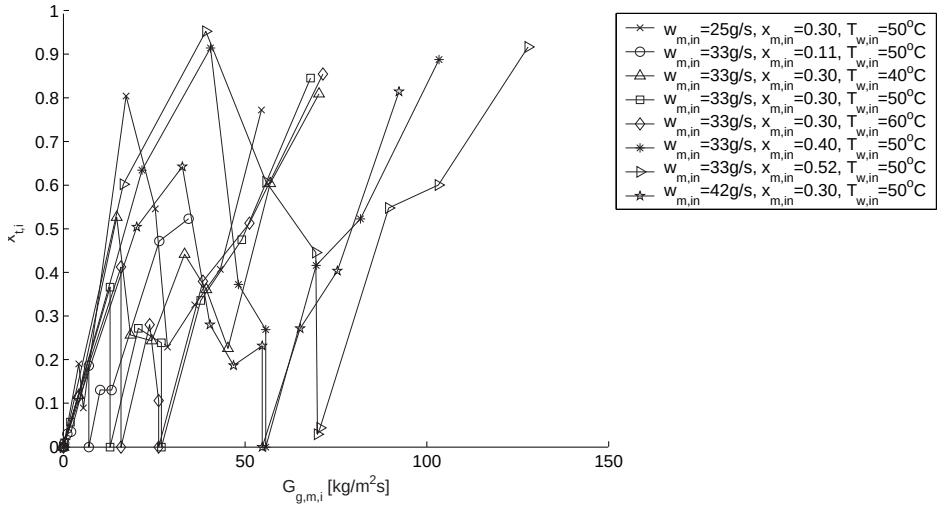

Figure E.7: Measured branch tube vapour fraction, $x_{t,i}$, as function of gas mass flux, $G_{g,m,i}$, at inlet of manifold T-junctions. Series with branch *No* 1 to 10 are shown from the right to the left (decreasing $G_{g,m,i}$). Manifold M9. Refrigerant: HFC-134a, $T_{mIn} = 29.5°$C.

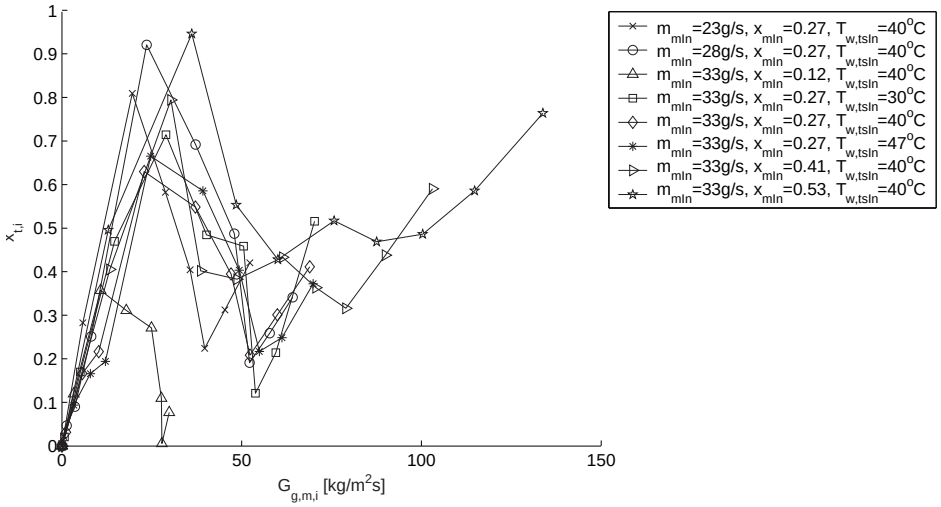

Figure E.8: Measured branch tube vapour fraction, $x_{t,i}$, as function of gas mass flux, $G_{g,m,i}$, at inlet of manifold T-junctions. Series with branch *No* 1 to 10 are shown from the right to the left (decreasing $G_{g,m,i}$). Manifold M9. Refrigerant: CO_2, $T_{mIn} = 18.7°$C.

E.2 New model - comparison to experimental results and existing correlations

The current Section contains the comparison of the literature T-junction models and the new empirical model to the measured branch tube vapour fractions in upward flow configuration. First, a single measurement series from each manifold measurement data set is shown in Section E.2.1. Next, the absolute deviations from the complete sets of measurement data series are shown in Section E.2.2. The deviation data is summarized in Figure 5.43.

E.2.1 Sample data series comparison

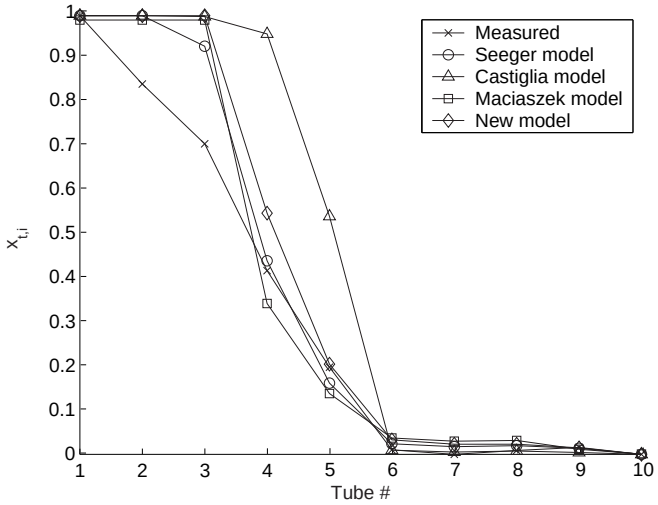

Figure E.9: Measured branch tube vapour fraction, $x_{t,i}$, compared to predictions using the Seeger, Castiglia, Maciaszek and the new model. ID 16 mm manifold (M1). Refrigerant: HFC-134a, $\dot{m}_{mIn} = 0.033$ kg/s, $x_{mIn} = 0.28$, $T_{mIn} = 29.5°$C, $T_{w,tsIn} = 50.0°$C.

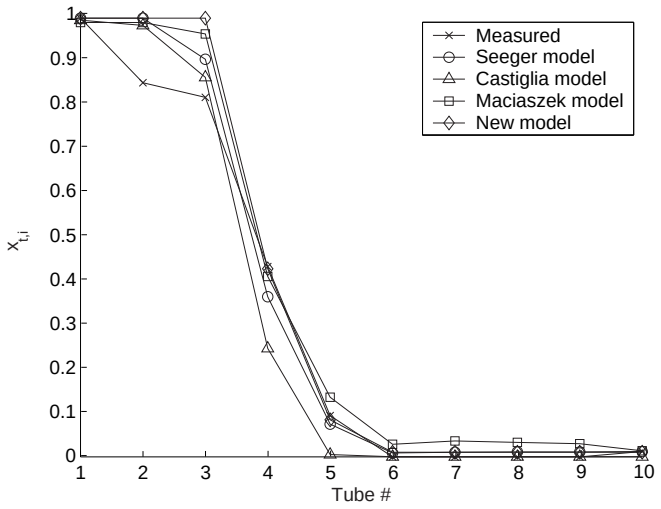

Figure E.10: Measured branch tube vapour fraction, $x_{t,i}$, compared to predictions using the Seeger, Castiglia, Maciaszek and the new model. ID 16 mm manifold (M1). Refrigerant: CO_2, $\dot{m}_{mIn} = 0.033$ kg/s, $x_{mIn} = 0.28$, $T_{mIn} = 18.7°$C, $T_{w,tsIn} = 40.0°$C.

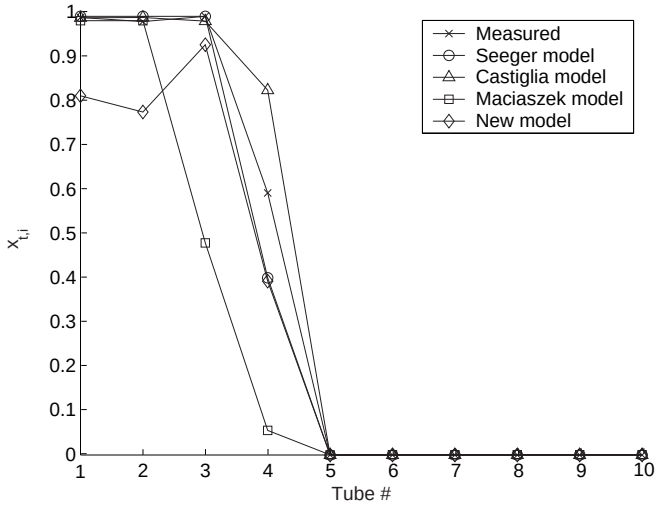

Figure E.11: Measured branch tube vapour fraction, $x_{t,i}$, compared to predictions using the Seeger, Castiglia, Maciaszek and the new model. ID 12 mm manifold (M2). Refrigerant: HFC-134a, $\dot{m}_{mIn} = 0.033$ kg/s, $x_{mIn} = 0.28$, $T_{mIn} = 29.5°$C, $T_{w,tsIn} = 50.0°$C.

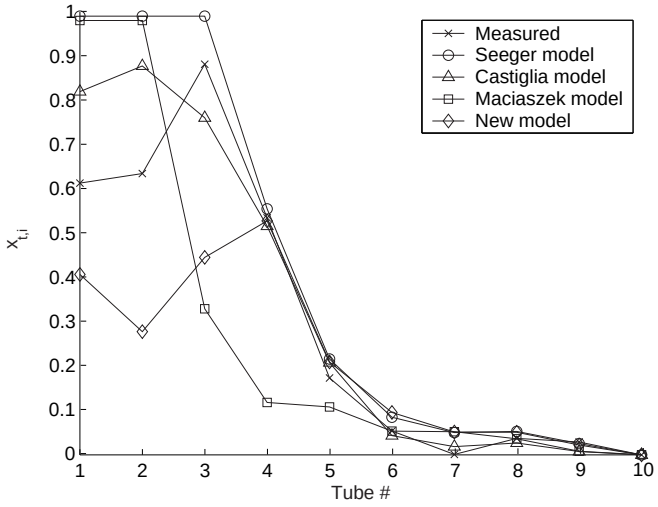

Figure E.12: Measured branch tube vapour fraction, $x_{t,i}$, compared to predictions using the Seeger, Castiglia, Maciaszek and the new model. ID 8 mm manifold (M3). Refrigerant: HFC-134a, $\dot{m}_{mIn} = 0.033$ kg/s, $x_{mIn} = 0.28$, $T_{mIn} = 29.5°$C, $T_{w,tsIn} = 50.0°$C.

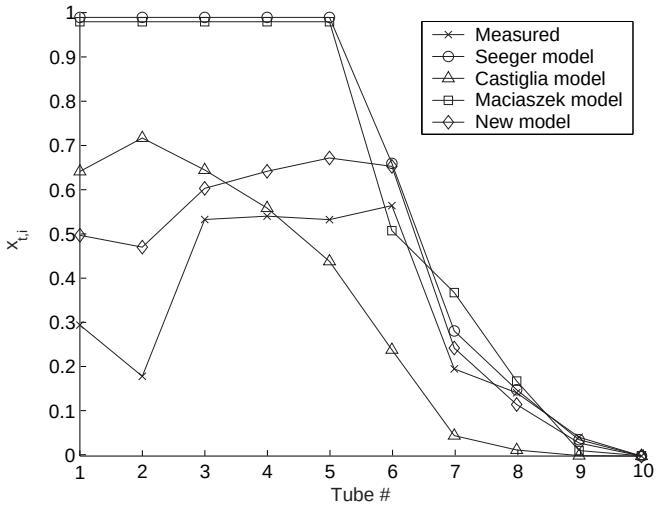

Figure E.13: Measured branch tube vapour fraction, $x_{t,i}$, compared to predictions using the Seeger, Castiglia, Maciaszek and the new model. ID 8 mm manifold (M3). Refrigerant: CO_2, $\dot{m}_{mIn} = 0.033$ kg/s, $x_{mIn} = 0.28$, $T_{mIn} = 18.7°$C, $T_{w,tsIn} = 40.0°$C.

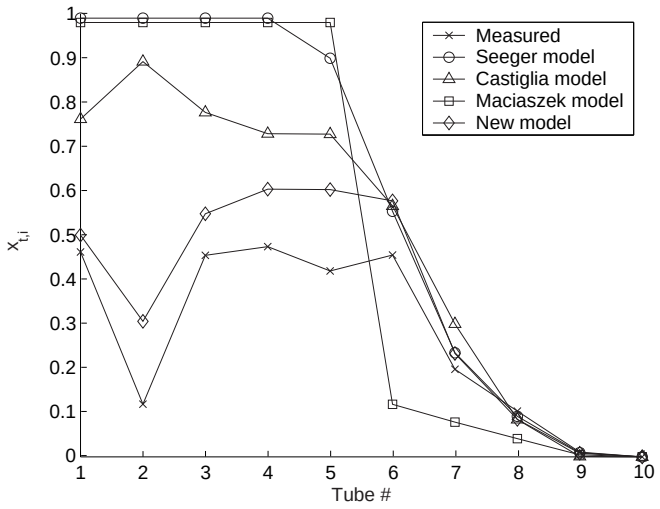

Figure E.14: Measured branch tube vapour fraction, $x_{t,i}$, compared to predictions using the Seeger, Castiglia, Maciaszek and the new model. Manifold M4 (ID 8 mm manifold with short inlet tube). Refrigerant: HFC-134a, $\dot{m}_{mIn} = 0.033$ kg/s, $x_{mIn} = 0.28$, $T_{mIn} = 29.5°$C, $T_{w,tsIn} = 50.0°$C.

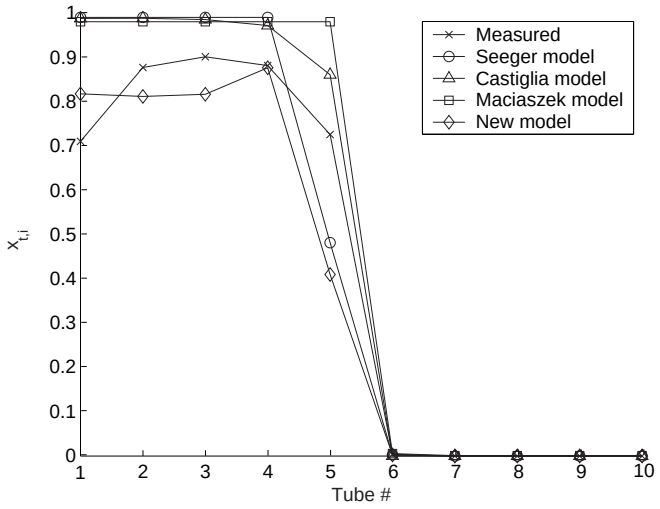

Figure E.15: Measured branch tube vapour fraction, $x_{t,i}$, compared to predictions using the Seeger, Castiglia, Maciaszek and the new model. Manifold M5 (base-case MPE-tube manifold). Refrigerant: HFC-134a, $\dot{m}_{mIn} = 0.033$ kg/s, $x_{mIn} = 0.28$, $T_{mIn} = 29.5°$C, $T_{w,tsIn} = 50.0°$C.

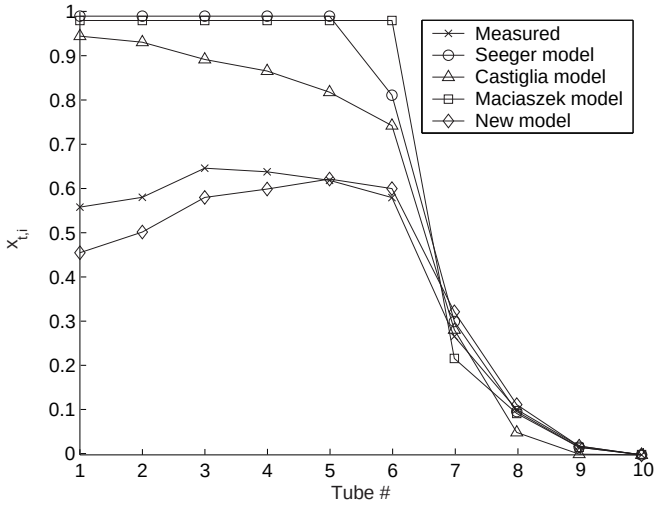

Figure E.16: Measured branch tube vapour fraction, $x_{t,i}$, compared to predictions using the Seeger, Castiglia, Maciaszek and the new model. Manifold M6 (MPE-tube manifold with insert ratio $r = 0.6$). Refrigerant: HFC-134a, $\dot{m}_{mIn} = 0.033$ kg/s, $x_{mIn} = 0.28$, $T_{mIn} = 29.5°$C, $T_{w,tsIn} = 50.0°$C.

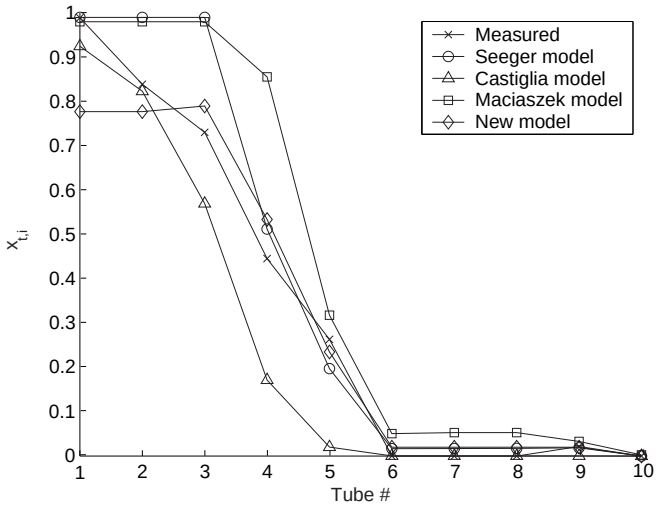

Figure E.17: Measured branch tube vapour fraction, $x_{t,i}$, compared to predictions using the Seeger, Castiglia, Maciaszek and the new model. Manifold M5 (base-case MPE-tube manifold). Refrigerant: CO_2, $\dot{m}_{mIn} = 0.033$ kg/s, $x_{mIn} = 0.28$, $T_{mIn} = 18.7°$C, $T_{w,tsIn} = 40.0°$C.

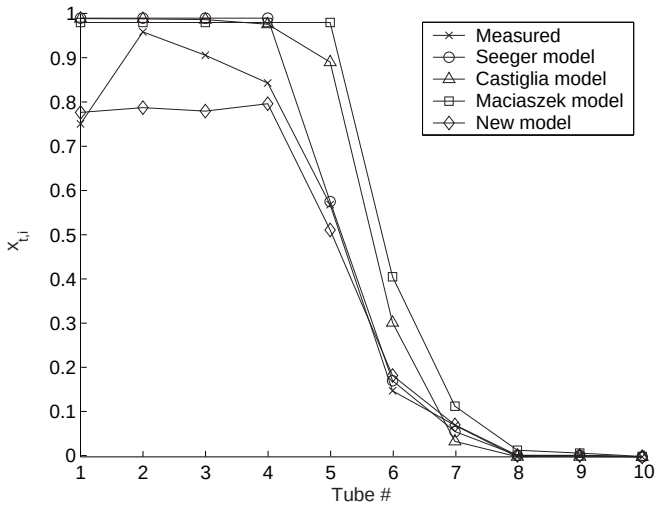

Figure E.18: Measured branch tube vapour fraction, $x_{t,i}$, compared to predictions using the Seeger, Castiglia, Maciaszek and the new model. Manifold M8 (MPE-tube manifold with 15 mm branch tube pitch). Refrigerant: HFC-134a, $\dot{m}_{mIn} = 0.033$ kg/s, $x_{mIn} = 0.28$, $T_{mIn} = 29.5°$C, $T_{w,tsIn} = 50.0°$C.

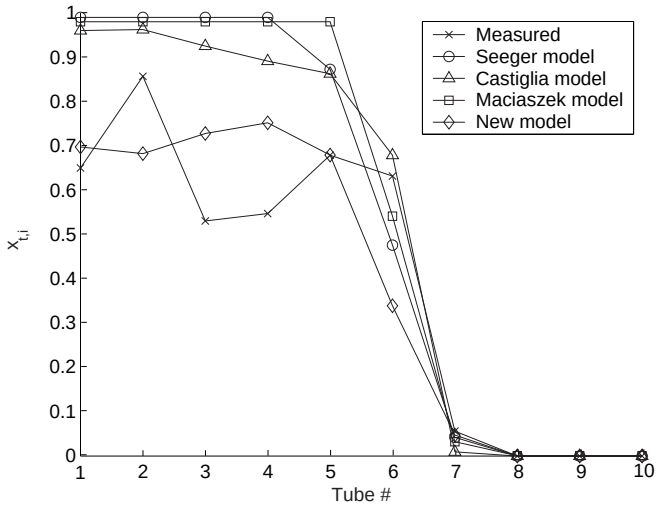

Figure E.19: Measured branch tube vapour fraction, $x_{t,i}$, compared to predictions using the Seeger, Castiglia, Maciaszek and the new model. Manifold M7 (MPE-tube manifold with baffle inserts). Refrigerant: HFC-134a, $\dot{m}_{mIn} = 0.033$ kg/s, $x_{mIn} = 0.28$, $T_{mIn} = 29.5°$C, $T_{w,tsIn} = 50.0°$C.

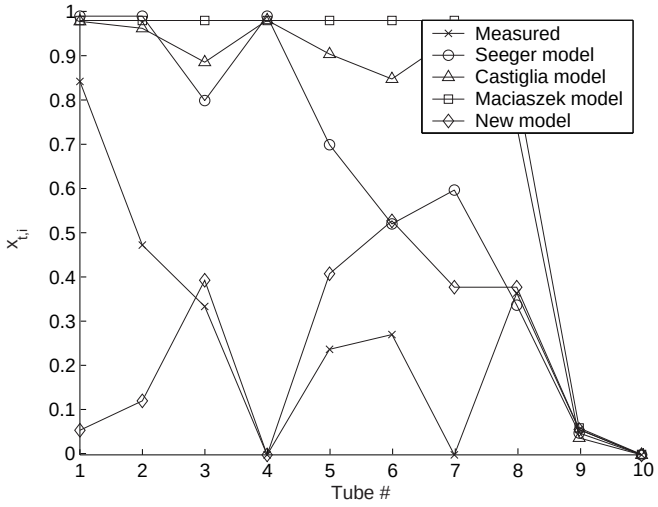

Figure E.20: Measured branch tube vapour fraction, $x_{t,i}$, compared to predictions using the Seeger, Castiglia, Maciaszek and the new model. Manifold M9 (MPE-tube manifold with spiral mixer insert). Refrigerant: HFC-134a, $\dot{m}_{mIn} = 0.033$ kg/s, $x_{mIn} = 0.28$, $T_{mIn} = 29.5°$C, $T_{w,tsIn} = 50.0°$C.

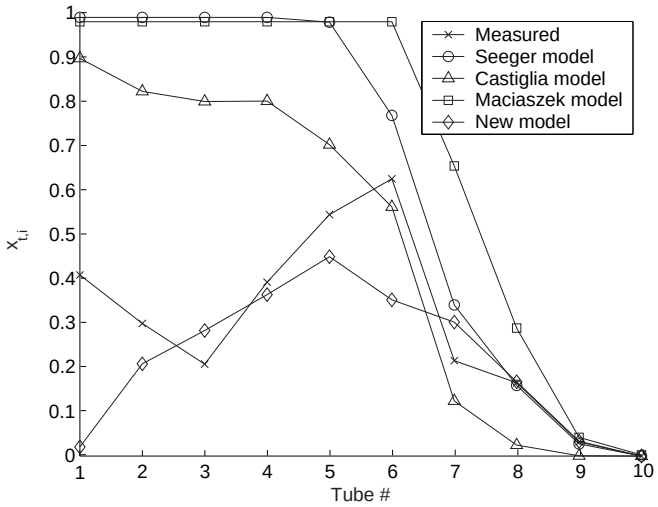

Figure E.21: Measured branch tube vapour fraction, $x_{t,i}$, compared to predictions using the Seeger, Castiglia, Maciaszek and the new model. Manifold M9 (MPE-tube manifold with spiral mixer insert). Refrigerant: CO_2, $\dot{m}_{mIn} = 0.033$ kg/s, $x_{mIn} = 0.28$, $T_{mIn} = 18.7°$C, $T_{w,tsIn} = 40.0°$C.

E.2.2 Absolute deviation between predicted and measured branch tube vapour fraction

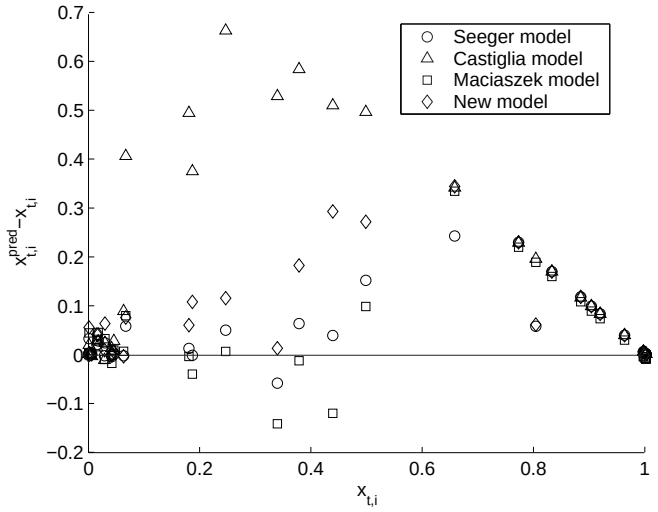

Figure E.22: Absolute deviation between predicted and measured branch tube vapour fraction. All measurement series using HFC-134a in the ID 16 mm manifold (M1) are shown.

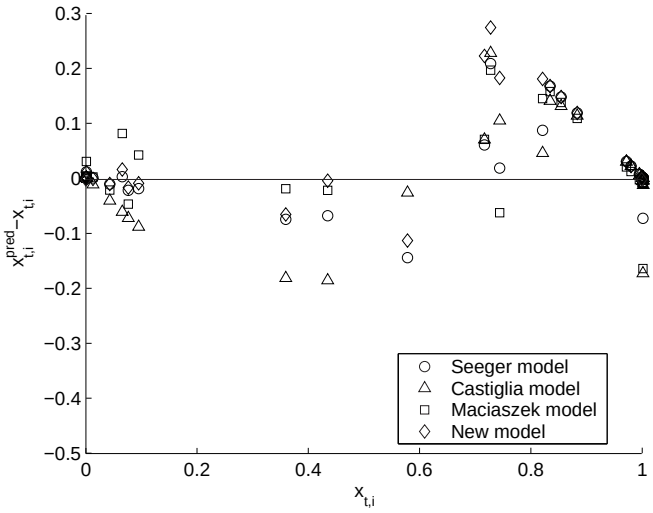

Figure E.23: Absolute deviation between predicted and measured branch tube vapour fraction. All measurement series using CO_2 in the ID 16 mm manifold (M1) are shown.

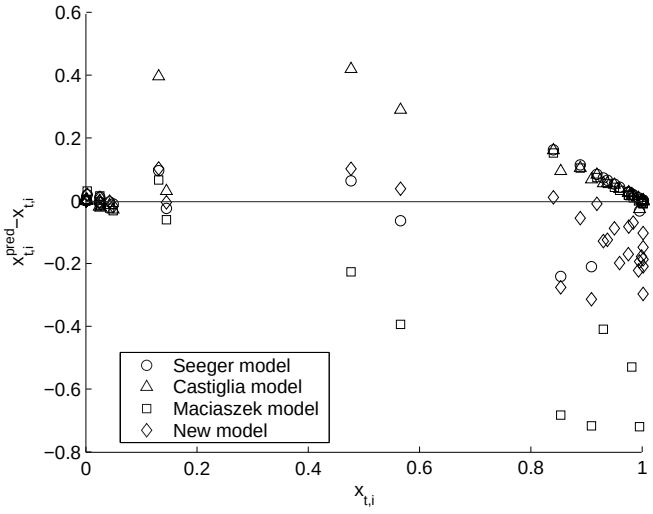

Figure E.24: Absolute deviation between predicted and measured branch tube vapour fraction. All measurement series using HFC-134a in the ID 12 mm manifold (M2) are shown.

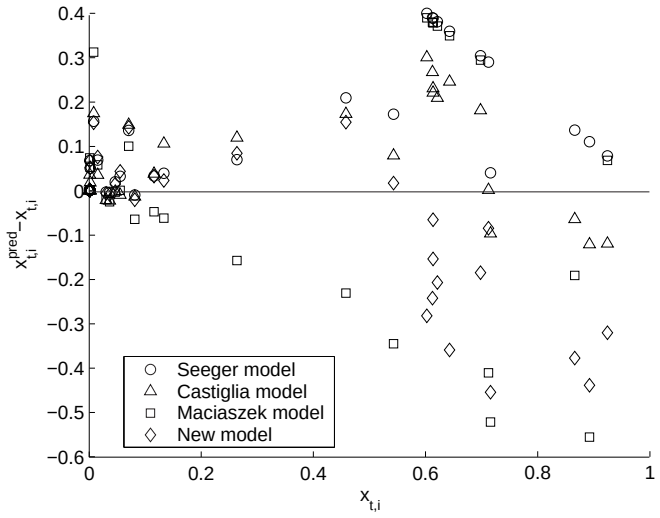

Figure E.25: Absolute deviation between predicted and measured branch tube vapour fraction. All measurement series using HFC-134a in the ID 8 mm manifold (M3) are shown.

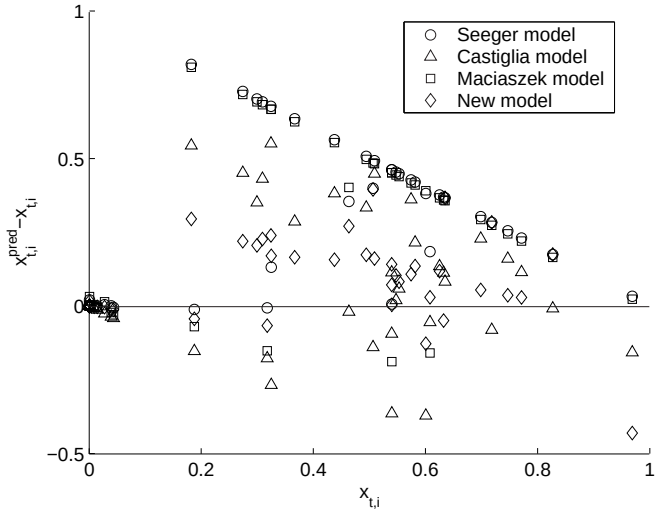

Figure E.26: Absolute deviation between predicted and measured branch tube vapour fraction. All measurement series using CO_2 in the ID 8 mm manifold (M3) are shown.

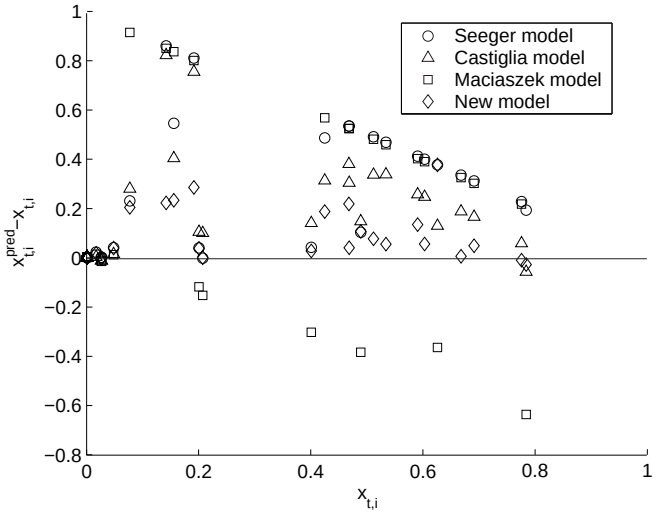

Figure E.27: Absolute deviation between predicted and measured branch tube vapour fraction. All measurement series using HFC-134a in manifold M4 (ID 8 mm manifold with short inlet tube) are shown.

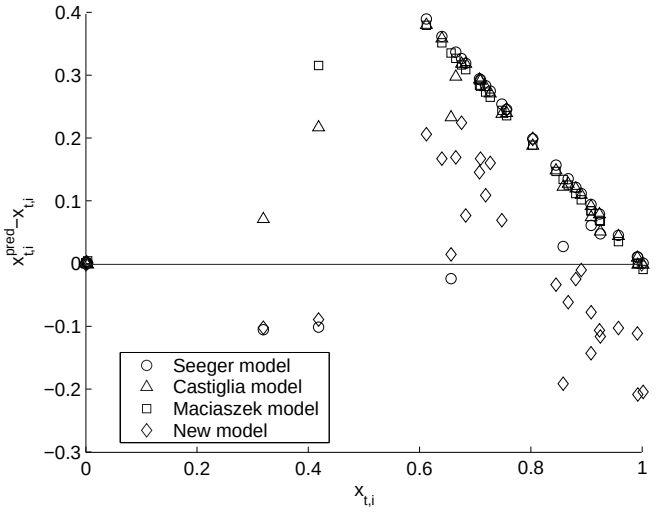

Figure E.28: Absolute deviation between predicted and measured branch tube vapour fraction. All measurement series using HFC-134a in manifold M5 (base-case MPE-tube manifold) are shown.

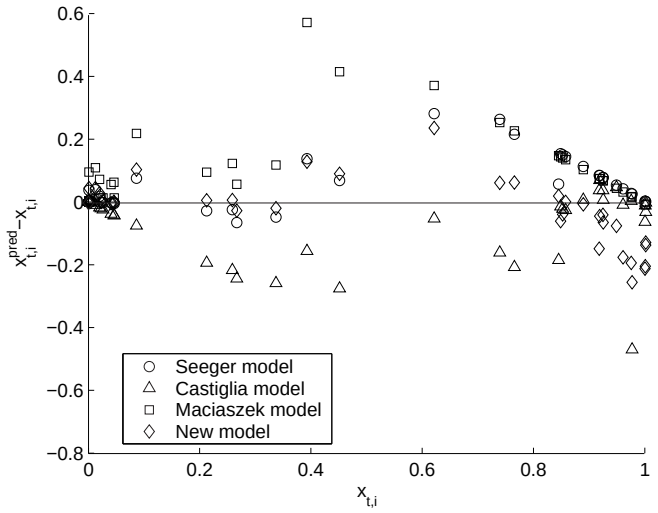

Figure E.29: Absolute deviation between predicted and measured branch tube vapour fraction. All measurement series using CO_2 in manifold M5 (base-case MPE-tube manifold) are shown.

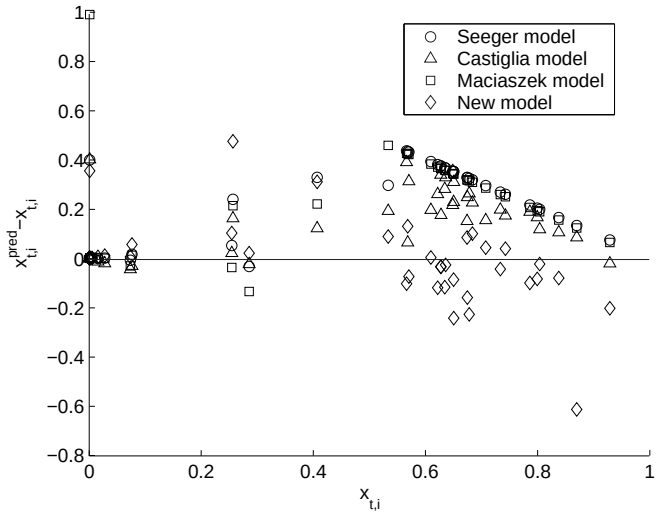

Figure E.30: Absolute deviation between predicted and measured branch tube vapour fraction. All measurement series using HFC-134a in manifold M6 (MPE-tube manifold with insert ratio $r = 0.6$) are shown.

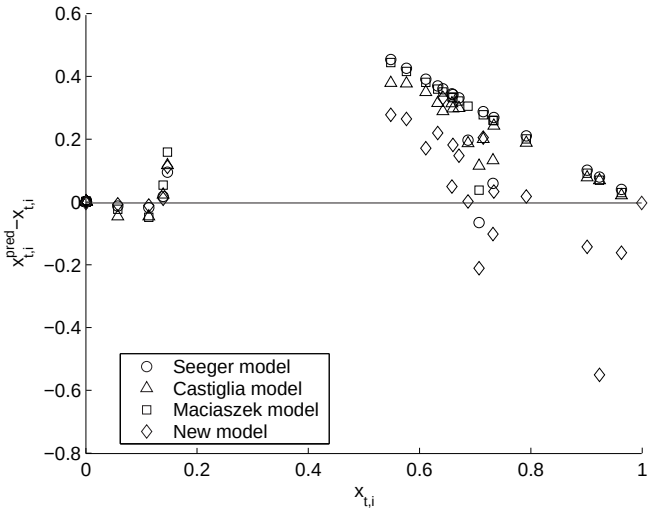

Figure E.31: Absolute deviation between predicted and measured branch tube vapour fraction. All measurement series using HFC-134a in manifold M7 (MPE-tube manifold with baffle inserts) are shown.

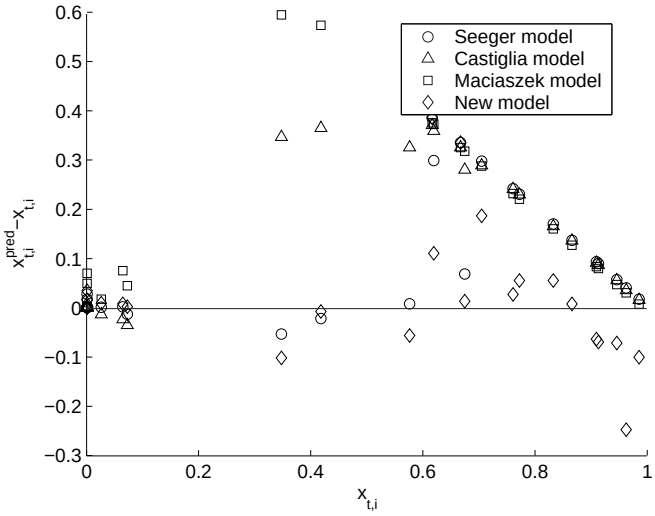

Figure E.32: Absolute deviation between predicted and measured branch tube vapour fraction. All measurement series using HFC-134a in manifold M8 (MPE-tube manifold with 15 mm branch tube pitch) are shown.

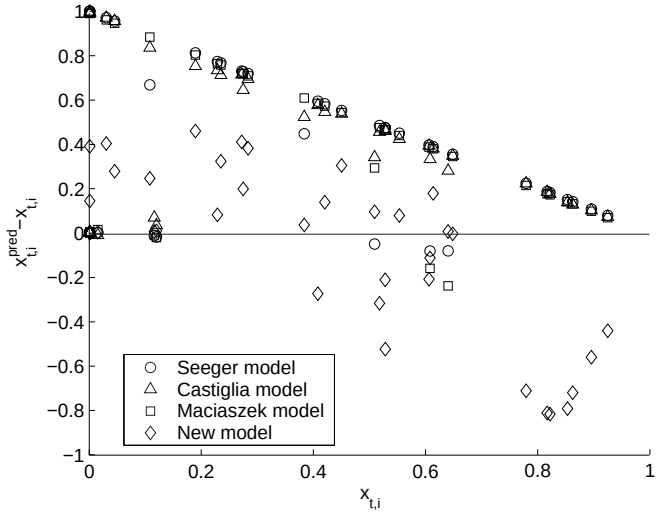

Figure E.33: Absolute deviation between predicted and measured branch tube vapour fraction. All measurement series using HFC-134a in manifold M9 (MPE-tube manifold with spiral mixer insert) are shown.

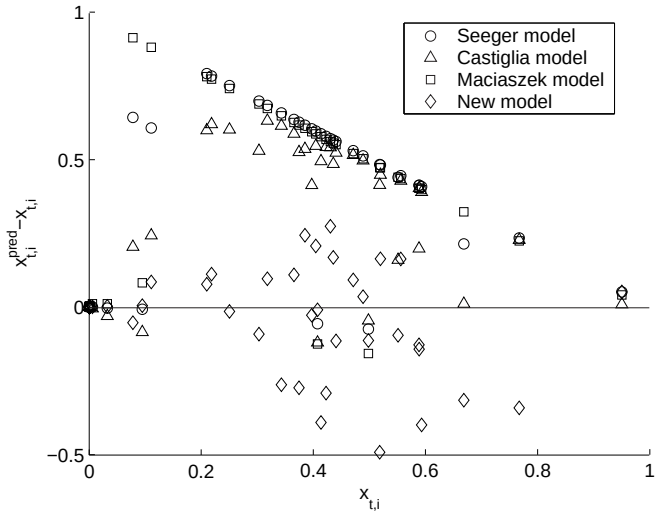

Figure E.34: Absolute deviation between predicted and measured branch tube vapour fraction. All measurement series using CO_2 in manifold M9 (MPE-tube manifold with spiral mixer insert) are shown.

Appendix F

Additional Plots From Measurement Data Analysis - Downward Configuration

F.1 Liquid take-off fraction in downward configuration

This Section contains plots used in the data analysis in Section 5.4.2. Liquid take-off fractions, $\dot{m}_{l,t,i}/\dot{m}_{l,m,i}$ are shown as function of dimensionless manifold mass flux values $G_{m,i}/G_{m,i,wavy}$. Lines calculated using the new regression model given by Equations 5.22 and 5.24 are also shown in the plots.

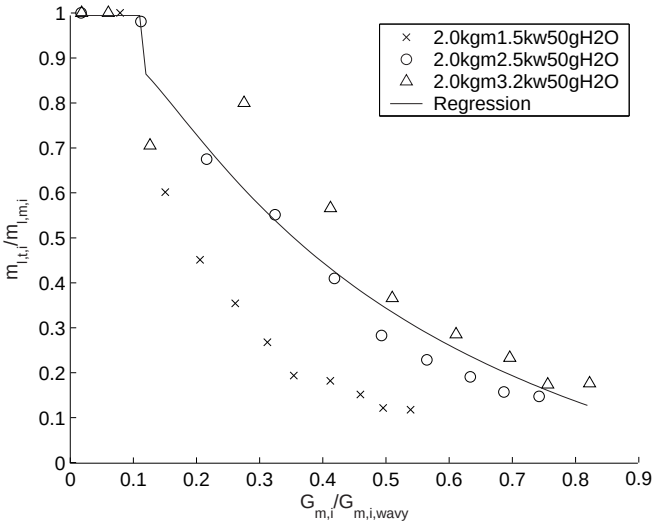

Figure F.1: Liquid take-off fraction, $\dot{m}_{l,t,i}/\dot{m}_{l,m,i}$, as function of dimensionless manifold mass flux. Values from all measurement series in the ID 16 mm manifold (M1) with HFC-134a are plotted together with the general manifold regression model (Equation 5.22).

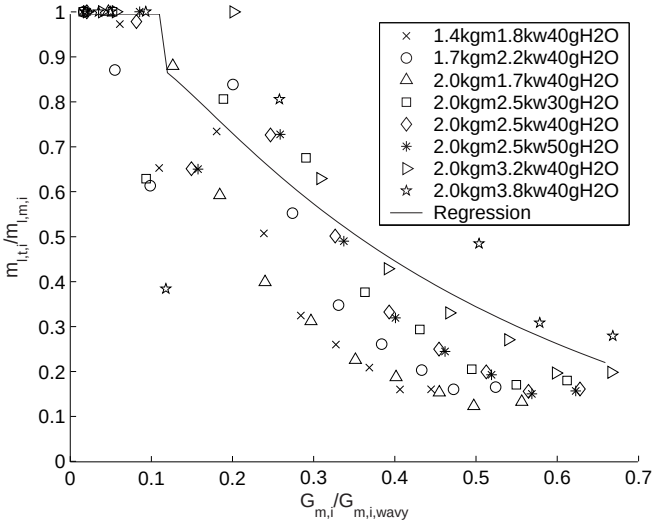

Figure F.2: Liquid take-off fraction, $\dot{m}_{l,t,i}/\dot{m}_{l,m,i}$, as function of dimensionless manifold mass flux. Values from all measurement series in the ID 16 mm manifold (M1) with CO_2 are plotted together with the general manifold regression model (Equation 5.22).

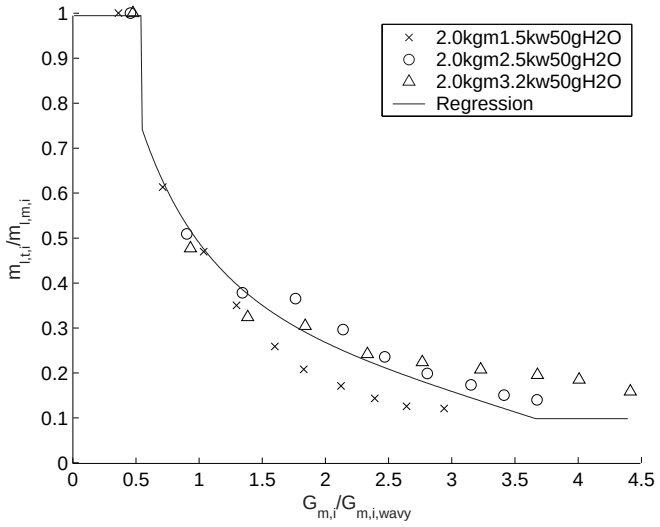

Figure F.3: Liquid take-off fraction, $\dot{m}_{l,t,i}/\dot{m}_{l,m,i}$, as function of dimensionless manifold mass flux. Values from all measurement series in the ID 8 mm manifold (M3) with HFC-134a are plotted together with the general manifold regression model (Equation 5.22).

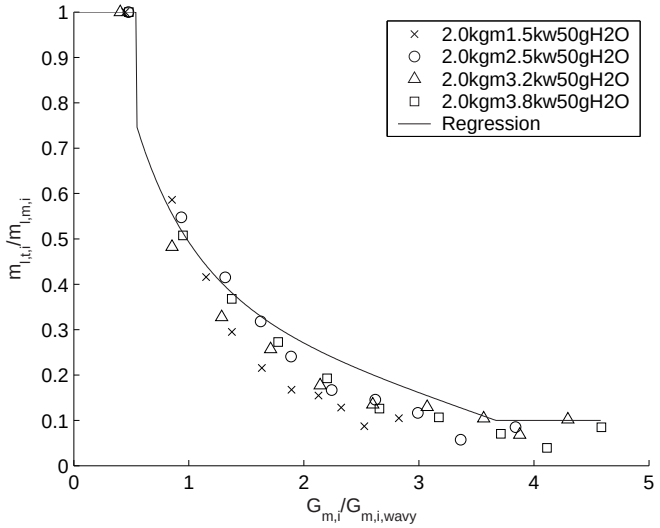

Figure F.4: Liquid take-off fraction, $\dot{m}_{l,t,i}/\dot{m}_{l,m,i}$, as function of dimensionless manifold mass flux. Values from all measurement series in the ID 8 mm manifold with short inlet tube (M4) with HFC-134a are plotted together with the general manifold regression model (Equation 5.22).

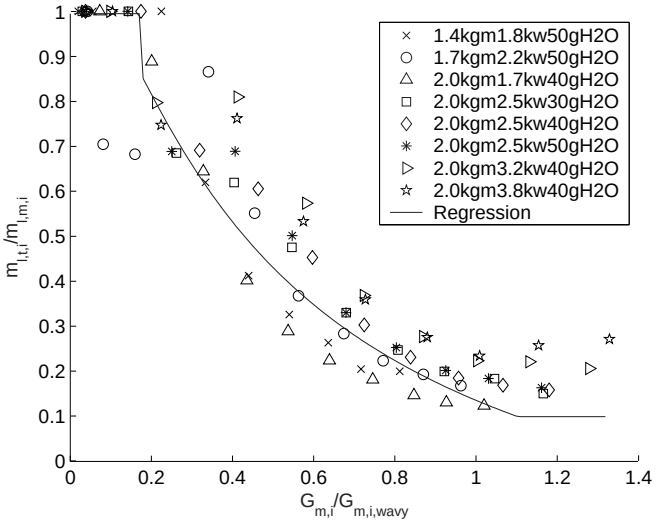

Figure F.5: Liquid take-off fraction, $\dot{m}_{l,t,i}/\dot{m}_{l,m,i}$, as function of dimensionless manifold mass flux. Values from all measurement series in the base-case MPE-tube manifold (M5) with CO_2 are plotted together with the general manifold regression model (Equation 5.22).

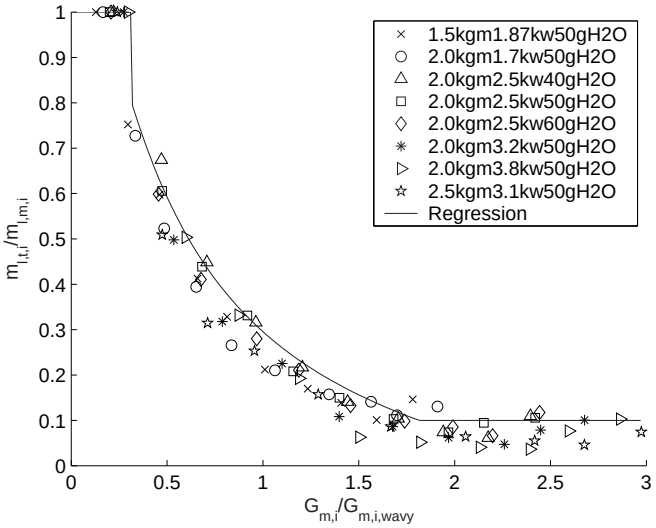

Figure F.6: Liquid take-off fraction, $\dot{m}_{l,t,i}/\dot{m}_{l,m,i}$, as function of dimensionless manifold mass flux. Values from all measurement series in the manifold M6 (MPE-tube manifold with insert ratio $r = 0.6$) with HFC-134a are plotted together with the general manifold regression model (Equation 5.22).

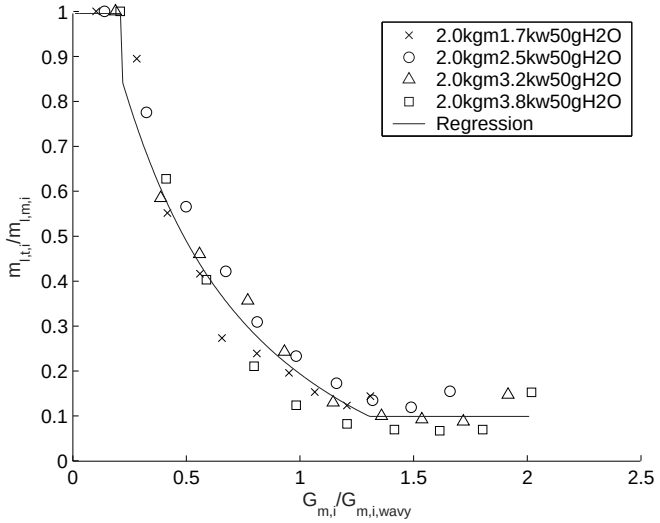

Figure F.7: Liquid take-off fraction, $\dot{m}_{l,t,i}/\dot{m}_{l,m,i}$, as function of dimensionless manifold mass flux. Values from all measurement series in the manifold M7 (MPE-tube manifold with baffle inserts) with HFC-134a are plotted together with the general manifold regression model (Equation 5.22).

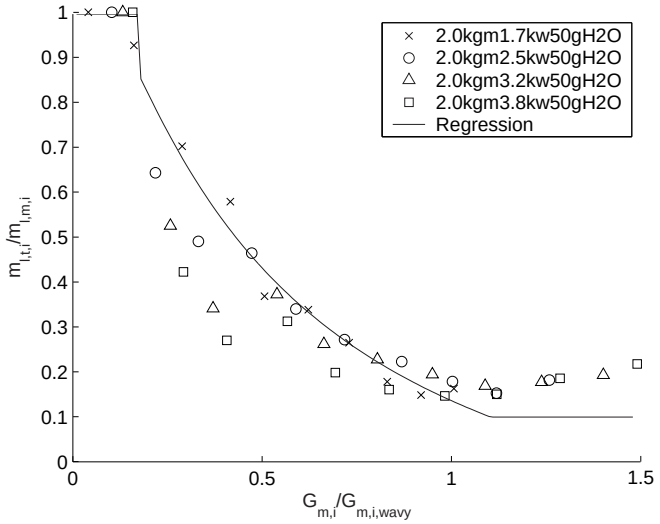

Figure F.8: Liquid take-off fraction, $\dot{m}_{l,t,i}/\dot{m}_{l,m,i}$, as function of dimensionless manifold mass flux. Values from all measurement series in the manifold M8 (MPE-tube manifold with 15 mm branch tube pitch) with HFC-134a are plotted together with the general manifold regression model (Equation 5.22).

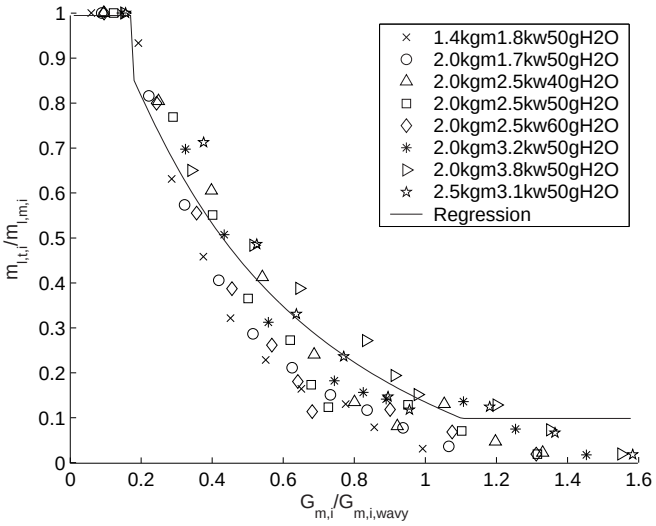

Figure F.9: Liquid take-off fraction, $\dot{m}_{l,t,i}/\dot{m}_{l,m,i}$, as function of dimensionless manifold mass flux. Values from all measurement series in the manifold M9 (MPE-tube manifold with spiral mixer insert) with HFC-134a are plotted together with the general manifold regression model (Equation 5.22).

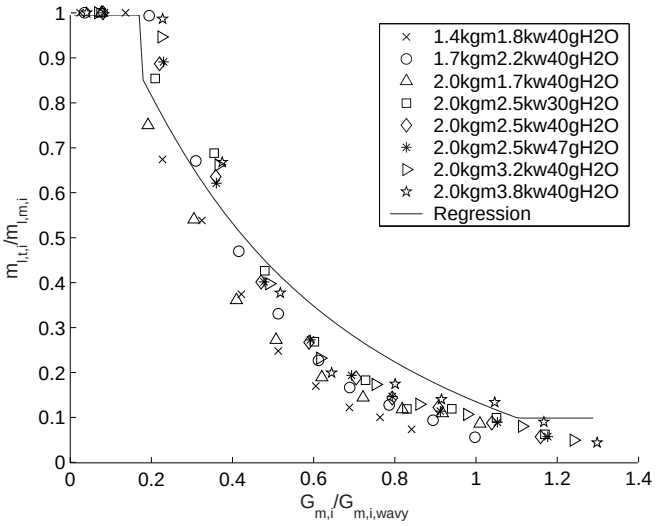

Figure F.10: Liquid take-off fraction, $\dot{m}_{l,t,i}/\dot{m}_{l,m,i}$, as function of dimensionless manifold mass flux. Values from all measurement series in the manifold M9 (MPE-tube manifold with spiral mixer insert) with CO_2 are plotted together with the general manifold regression model (Equation 5.22).

F.2 New model - comparison to experimental results and existing correlations

This Section contains the comparison of the T-junction models and the new empirical model to the measured branch tube vapour fractions in downward flow configuration. First, a single measurement series from each manifold measurement data set is shown in Section F.2.1. Next, the absolute deviations in the complete sets of measurement data are shown in Section F.2.2. The deviation data is summarized in Figure 5.54.

F.2.1 Sample data series comparison

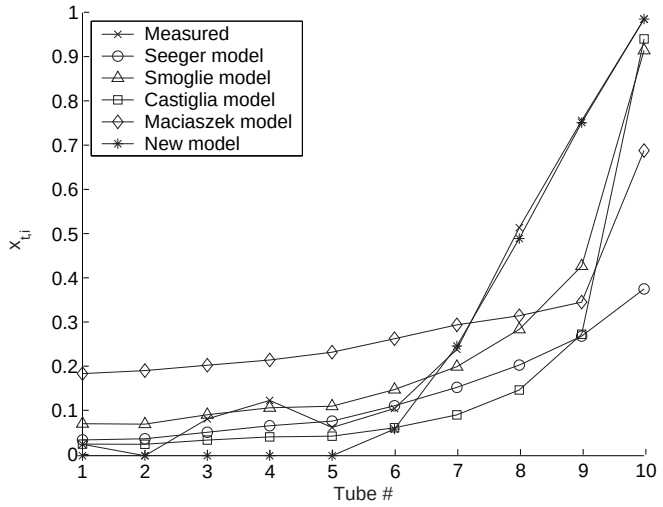

Figure F.11: Measured branch tube vapour fraction, $x_{t,i}$, compared to predictions using the Seeger, Smoglie, Castiglia, Maciaszek and the new model. ID 16 mm manifold (M1). Refrigerant: HFC-134a, $\dot{m}_{mIn} = 0.033$ kg/s, $x_{mIn} = 0.28$, $T_{mIn} = 29.5°$C, $T_{w,tsIn} = 50.0°$C.

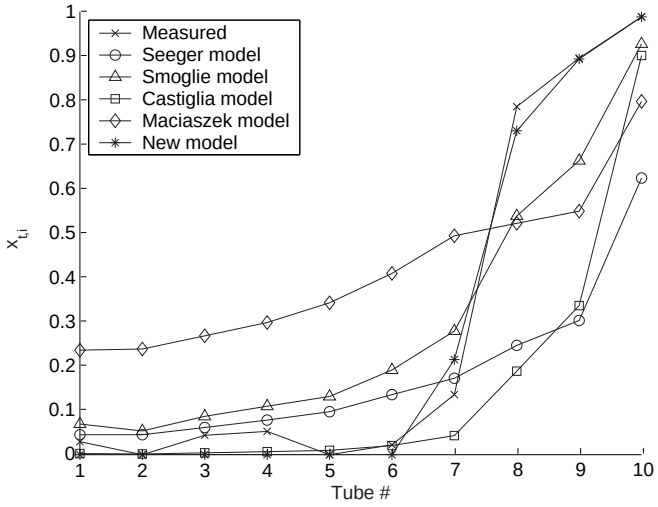

Figure F.12: Measured branch tube vapour fraction, $x_{t,i}$, compared to predictions using the Seeger, Smoglie, Castiglia, Maciaszek and the new model. ID 16 mm manifold (M1). Refrigerant: CO_2, $\dot{m}_{mIn} = 0.033$ kg/s, $x_{mIn} = 0.28$, $T_{mIn} = 18.7°$C, $T_{w,tsIn} = 40.0°$C.

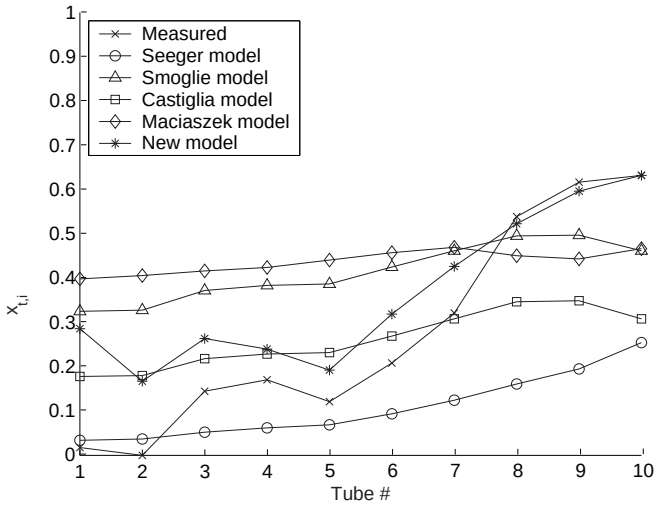

Figure F.13: Measured branch tube vapour fraction, $x_{t,i}$, compared to predictions using the Seeger, Smoglie, Castiglia, Maciaszek and the new model. ID 8 mm manifold (M3). Refrigerant: HFC-134a, $\dot{m}_{mIn} = 0.033$ kg/s, $x_{mIn} = 0.28$, $T_{mIn} = 29.5°$C, $T_{w,tsIn} = 50.0°$C.

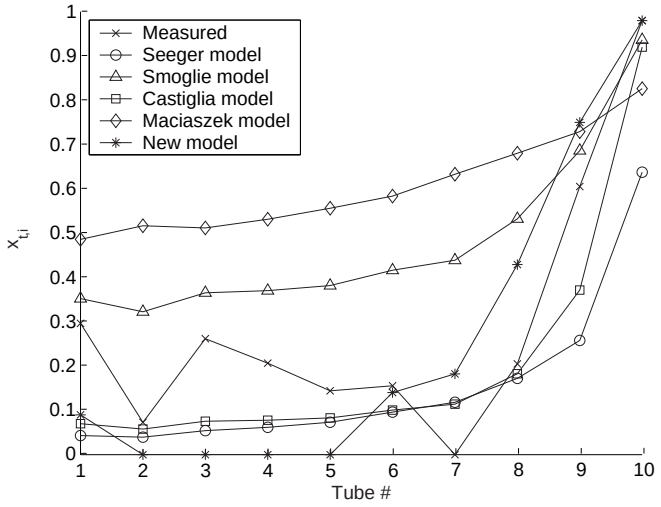

Figure F.14: Measured branch tube vapour fraction, $x_{t,i}$, compared to predictions using the Seeger, Smoglie, Castiglia, Maciaszek and the new model. ID 8 mm manifold (M3). Refrigerant: CO_2, $\dot{m}_{mIn} = 0.033$ kg/s, $x_{mIn} = 0.28$, $T_{mIn} = 18.7°$C, $T_{w,tsIn} = 40.0°$C.

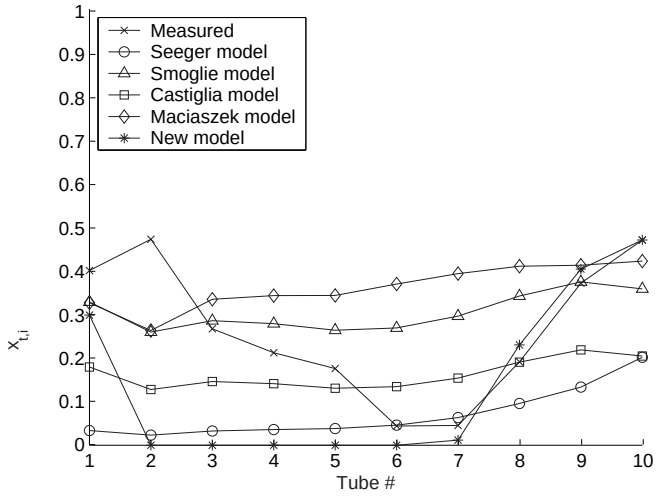

Figure F.15: Measured branch tube vapour fraction, $x_{t,i}$, compared to predictions using the Seeger, Smoglie, Castiglia, Maciaszek and the new model. ID 8 mm manifold with short inlet tube (M4). Refrigerant: HFC-134a, $\dot{m}_{mIn} = 0.033$ kg/s, $x_{mIn} = 0.28$, $T_{mIn} = 29.5°$C, $T_{w,tsIn} = 50.0°$C.

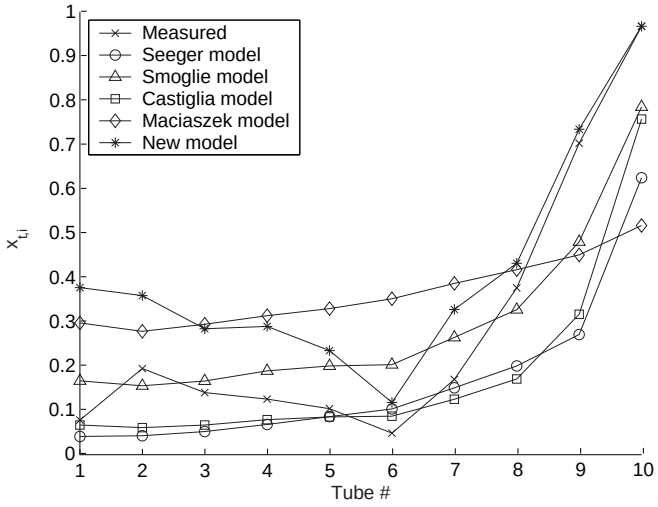

Figure F.16: Measured branch tube vapour fraction, $x_{t,i}$, compared to predictions using the Seeger, Smoglie, Castiglia, Maciaszek and the new model. Base-case MPE-tube manifold (M5). Refrigerant: HFC-134a, $\dot{m}_{mIn} = 0.033$ kg/s, $x_{mIn} = 0.28$, $T_{mIn} = 29.5^{\circ}$C, $T_{w,tsIn} = 50.0^{\circ}$C.

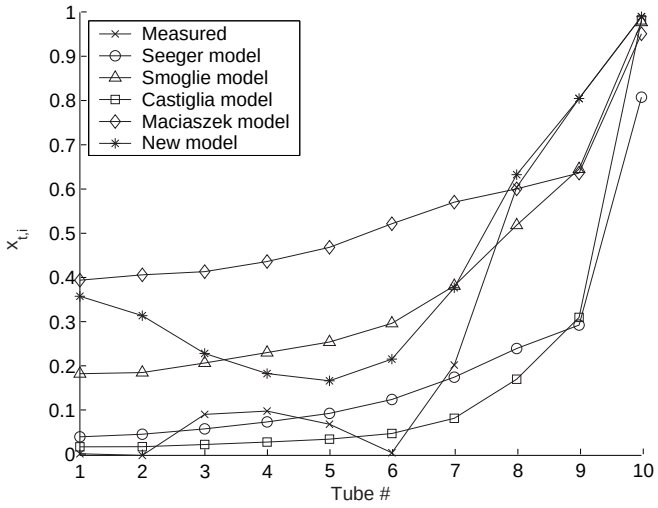

Figure F.17: Measured branch tube vapour fraction, $x_{t,i}$, compared to predictions using the Seeger, Smoglie, Castiglia, Maciaszek and the new model. Base-case MPE-tube manifold (M5). Refrigerant: CO_2, $\dot{m}_{mIn} = 0.033$ kg/s, $x_{mIn} = 0.28$, $T_{mIn} = 18.7^{\circ}$C, $T_{w,tsIn} = 40.0^{\circ}$C.

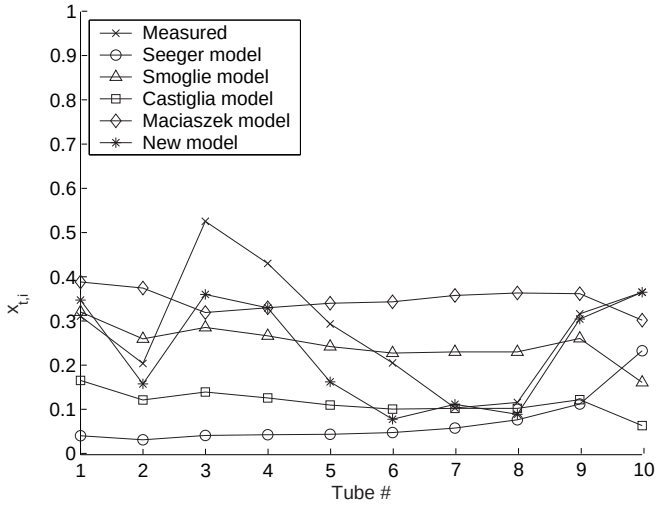

Figure F.18: Measured branch tube vapour fraction, $x_{t,i}$, compared to predictions using the Seeger, Smoglie, Castiglia, Maciaszek and the new model. Manifold M6 (MPE-tube manifold with insert ratio $r = 0.6$). Refrigerant: HFC-134a, $\dot{m}_{mIn} = 0.033$ kg/s, $x_{mIn} = 0.28$, $T_{mIn} = 29.5°$C, $T_{w,tsIn} = 50.0°$C.

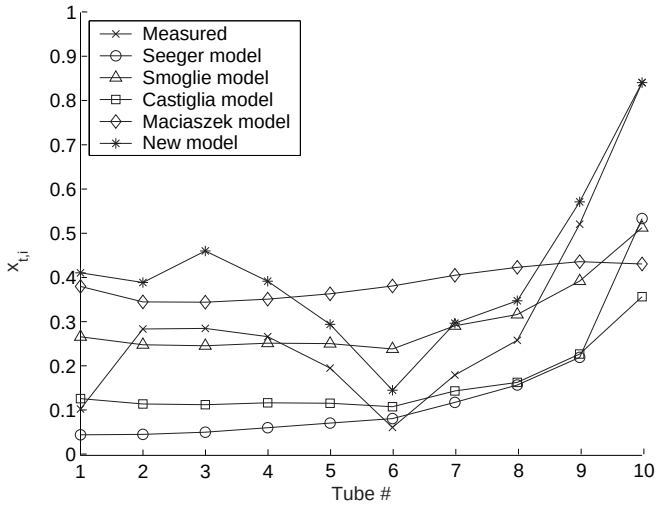

Figure F.19: Measured branch tube vapour fraction, $x_{t,i}$, compared to predictions using the Seeger, Smoglie, Castiglia, Maciaszek and the new model. Manifold M7 (MPE-tube manifold with baffle inserts). Refrigerant: HFC-134a, $\dot{m}_{mIn} = 0.033$ kg/s, $x_{mIn} = 0.28$, $T_{mIn} = 29.5°$C, $T_{w,tsIn} = 50.0°$C.

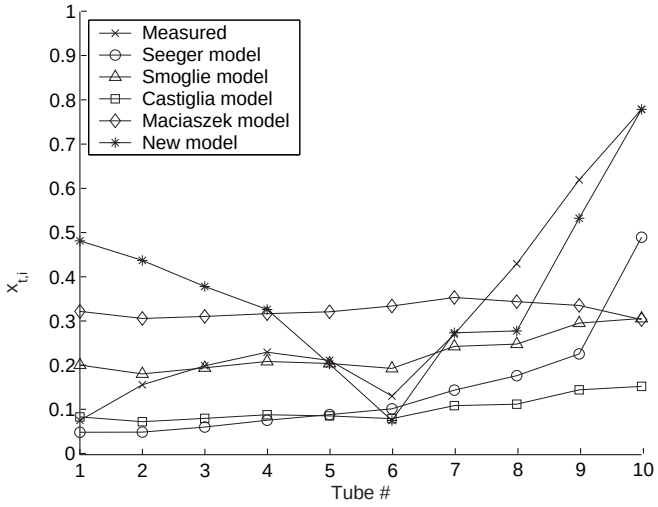

Figure F.20: Measured branch tube vapour fraction, $x_{t,i}$, compared to predictions using the Seeger, Smoglie, Castiglia, Maciaszek and the new model. Manifold M8 (MPE-tube manifold with 15 mm branch tube pitch). Refrigerant: HFC-134a, $\dot{m}_{mIn} = 0.033$ kg/s, $x_{mIn} = 0.28$, $T_{mIn} = 29.5°$C, $T_{w,tsIn} = 50.0°$C.

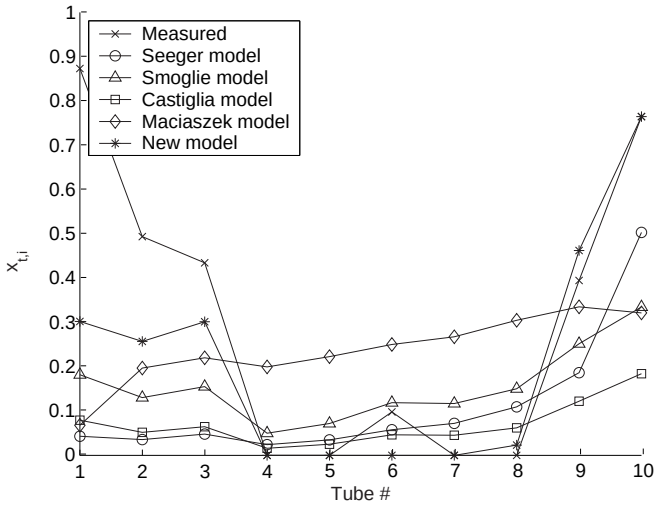

Figure F.21: Measured branch tube vapour fraction, $x_{t,i}$, compared to predictions using the Seeger, Smoglie, Castiglia, Maciaszek and the new model. Manifold M9 (MPE-tube manifold with spiral mixer insert). Refrigerant: HFC-134a, $\dot{m}_{mIn} = 0.033$ kg/s, $x_{mIn} = 0.28$, $T_{mIn} = 29.5°$C, $T_{w,tsIn} = 50.0°$C.

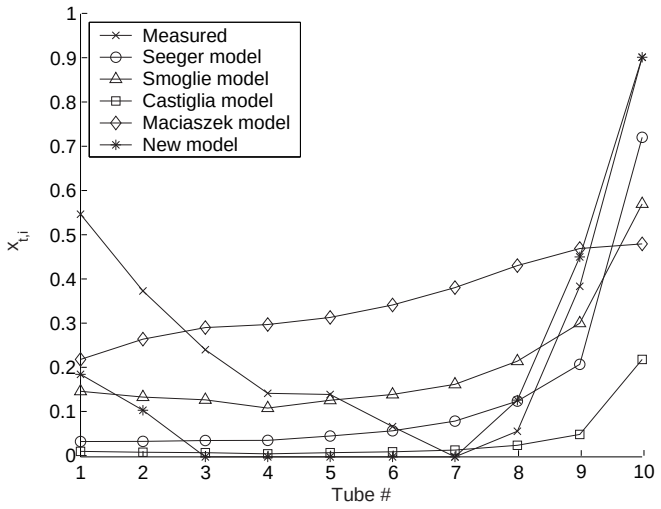

Figure F.22: Measured branch tube vapour fraction, $x_{t,i}$, compared to predictions using the Seeger, Smoglie, Castiglia, Maciaszek and the new model. Manifold M9 (MPE-tube manifold with spiral mixer insert). Refrigerant: CO_2, $\dot{m}_{mIn} = 0.033$ kg/s, $x_{mIn} = 0.28$, $T_{mIn} = 18.7°C$, $T_{w,tsIn} = 40.0°C$.

F.2.2 Absolute deviation between predicted and measured branch tube vapour fraction

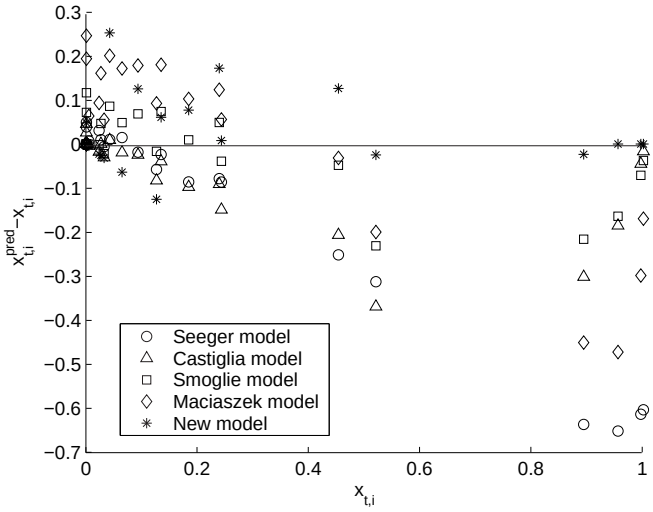

Figure F.23: Absolute deviation between predicted and measured branch tube vapour fraction. Values from all measurement series in the ID 16 mm manifold (M1) with HFC-134a are plotted.

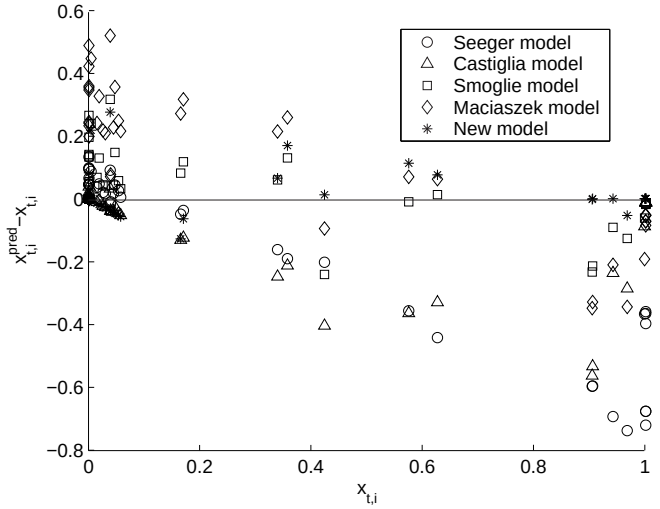

Figure F.24: Absolute deviation between predicted and measured branch tube vapour fraction. Values from all measurement series in the ID 16 mm manifold (M1) with CO_2 are shown.

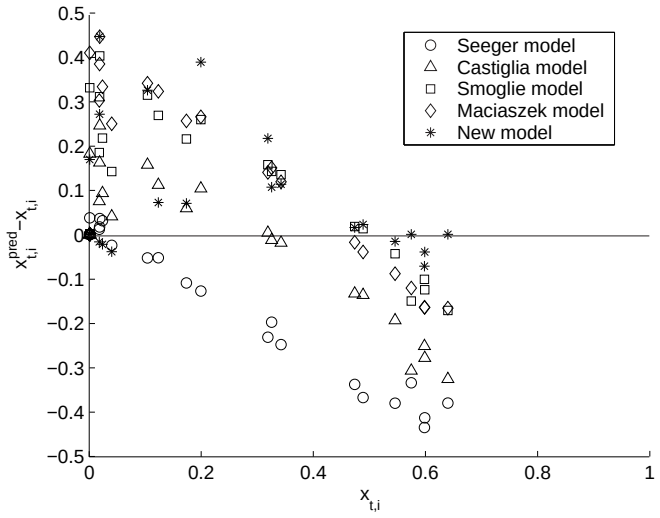

Figure F.25: Absolute deviation between predicted and measured branch tube vapour fraction. Values from all measurement series in the ID 8 mm manifold (M3) with HFC-134a are shown.

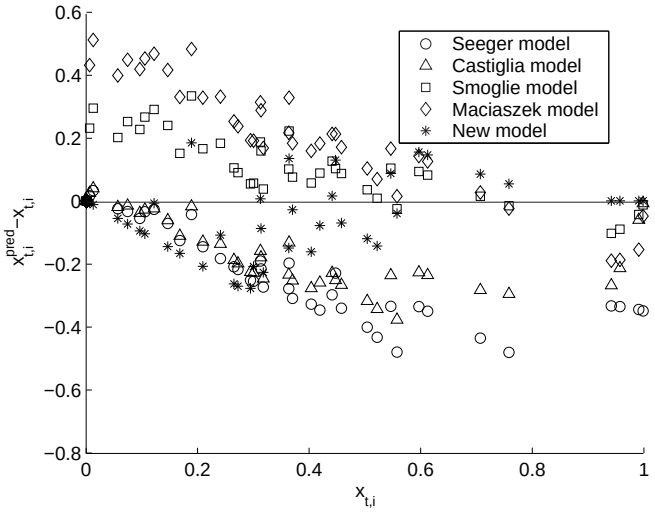

Figure F.26: Absolute deviation between predicted and measured branch tube vapour fraction. Values from all measurement series in the ID 8 mm manifold (M3) with CO_2 are shown.

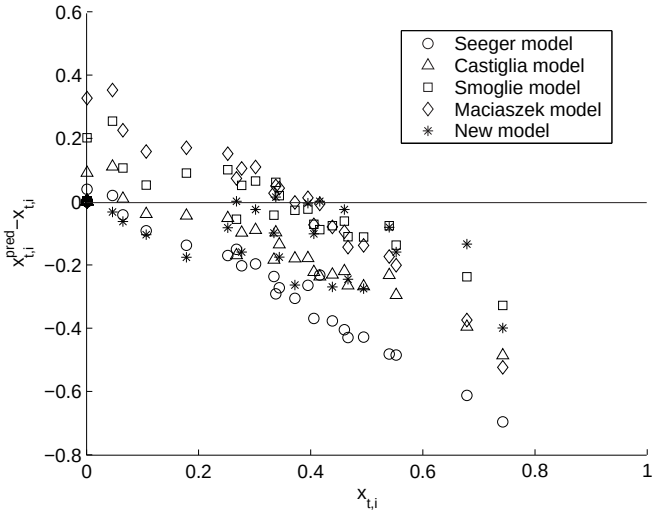

Figure F.27: Absolute deviation between predicted and measured branch tube vapour fraction. Values from all measurement series in the ID 8 mm manifold with short inlet tube (M4) with HFC-134a are shown.

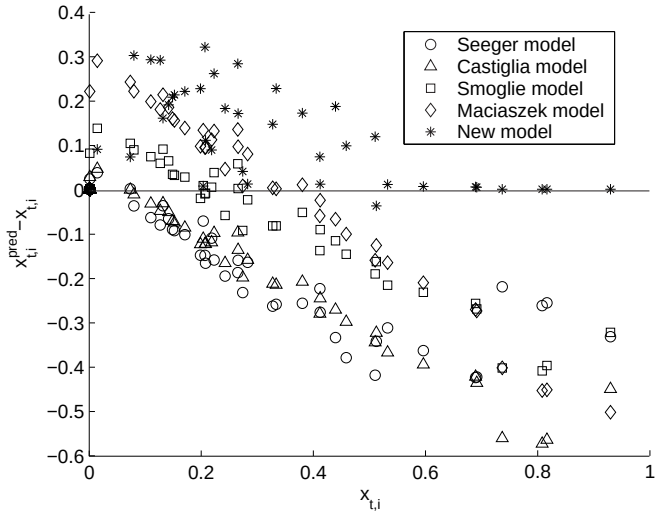

Figure F.28: Absolute deviation between predicted and measured branch tube vapour fraction. Values from all measurement series in the base-case MPE-tube manifold (M5) with HFC-134a are shown.

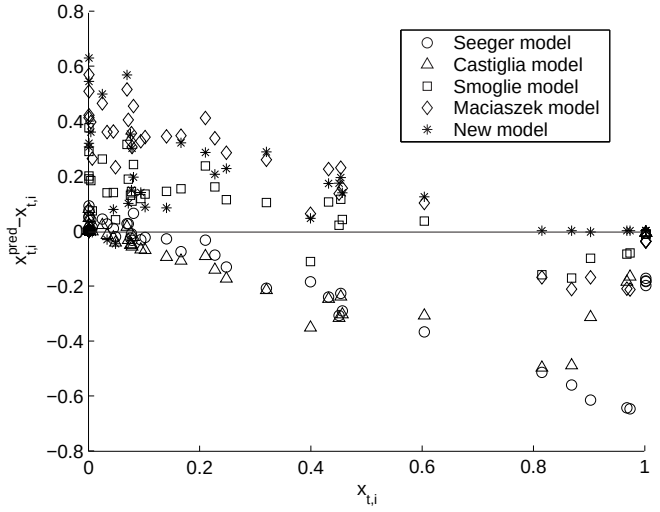

Figure F.29: Absolute deviation between predicted and measured branch tube vapour fraction. Values from all measurement series in the base-case MPE-tube manifold (M5) with CO_2 are shown.

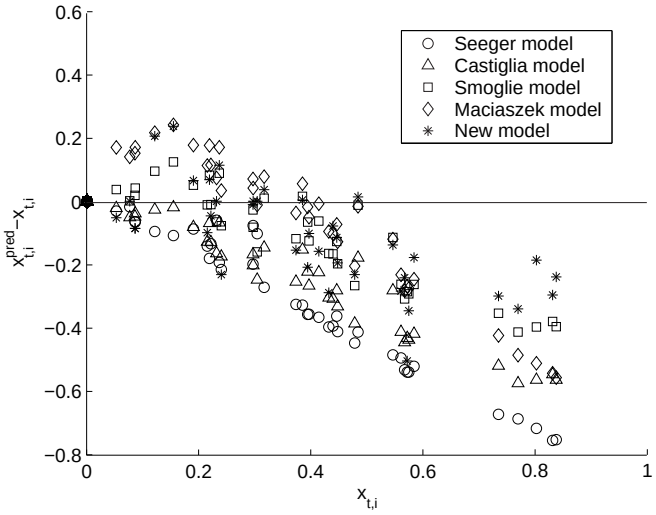

Figure F.30: Absolute deviation between predicted and measured branch tube vapour fraction. Values from all measurement series in the manifold M6 (MPE-tube manifold with insert ratio $r = 0.6$) with HFC-134a are shown.

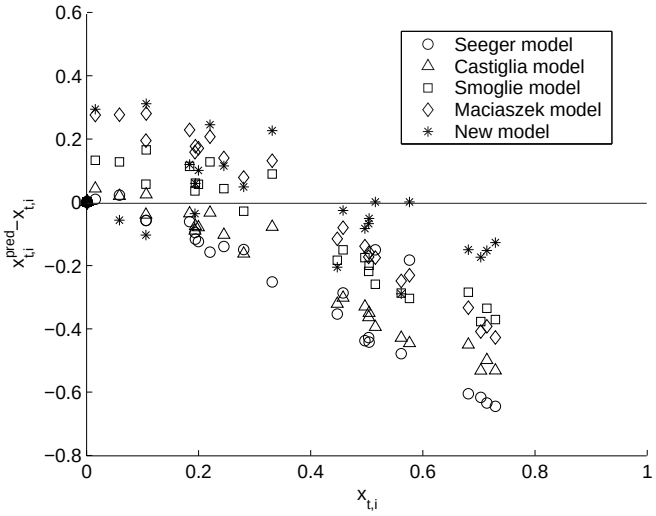

Figure F.31: Absolute deviation between predicted and measured branch tube vapour fraction. Values from all measurement series in the manifold M7 (MPE-tube manifold with baffle inserts) with HFC-134a are shown.

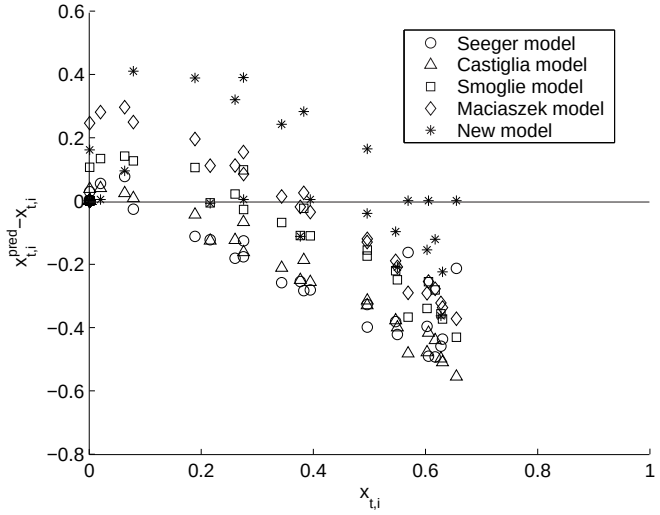

Figure F.32: Absolute deviation between predicted and measured branch tube vapour fraction. Values from all measurement series in the manifold M8 (MPE-tube manifold with 15 mm branch tube pitch) with HFC-134a are shown.

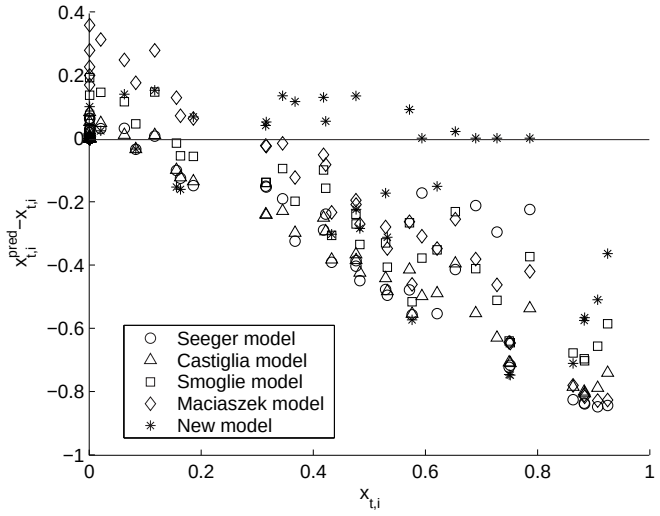

Figure F.33: Absolute deviation between predicted and measured branch tube vapour fraction. Values from all measurement series in the manifold M9 (MPE-tube manifold with spiral mixer insert) with HFC-134a are shown.

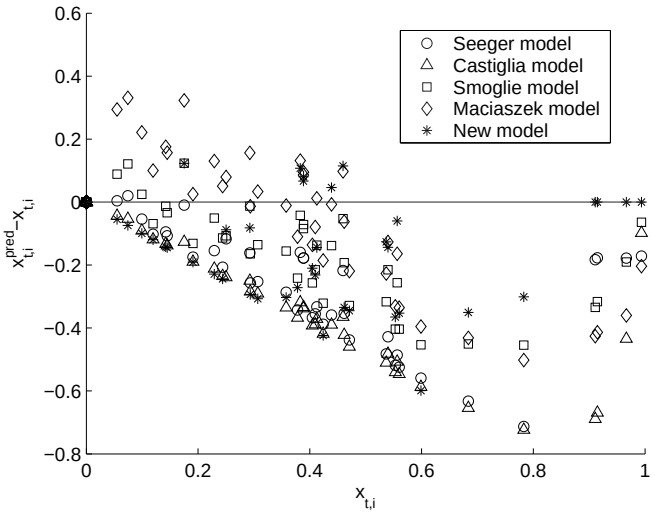

Figure F.34: Absolute deviation between predicted and measured branch tube vapour fraction. Values from all measurement series in the manifold M9 (MPE-tube manifold with spiral mixer insert) with HFC-134a are shown.